Numerical and experimental investigations on multiple air jets in counterflow for generating aircraft gas turbine engine inlet flow distortion patterns

Sivapragasam, M.

Award date:
2014

Awarding institution:
Coventry University
M S Ramaiah University of Applied Sciences

NUMERICAL AND EXPERIMENTAL INVESTIGATIONS ON MULTIPLE AIR JETS IN COUNTERFLOW FOR GENERATING AIRCRAFT GAS TURBINE ENGINE INLET FLOW DISTORTION PATTERNS

M. Sivapragasam

A thesis submitted in partial fulfilment of the University's requirements for the Degree of Doctor of Philosophy

JANUARY 2014

Coventry University

Research Carried out at

M. S. Ramaiah School of Advanced Studies

CERTIFICATE

This is to certify that the Doctoral Dissertation titled "Numerical and Experimental Investigations on Multiple Air Jets in Counterflow for Generating Aircraft Gas Turbine Engine Inlet Flow Distortion Patterns" is a bonafide record of the work carried out by Mr. M. Sivapragasam in partial fulfilment of requirements for the award of Doctor of Philosophy Degree of Coventry University

January-2014

Dr. M. D. Deshpande
Director of Studies
M. S. Ramaiah School of Advanced Studies, Bangalore

Dr. S. Ramamurthy
Supervisor
National Aerospace Laboratories, Bangalore

Prof. Peter White
Supervisor
Coventry University, UK

ACKNOWLEDGEMENTS

The research work started with the encouragement given by Dr. M. D. Deshpande, M. S. Ramaiah School of Advanced Studies. Since the start of this project, Dr. Deshpande has meliorated me with his sapient comments and moral support right through the successful completion. I express my gratitude to him.

The project took a meaningful direction because of Dr. S. Ramamurthy, National Aerospace Laboratories. He had continuously provided guidance that was necessary for the completion of this research. I thank him wholeheartedly in a sense of gratification.

The advice rendered by Professor Peter White, Coventry University helped me in many ways. I benefitted from his frequent visits to India. I thank him for his comments on this research and advice.

I thank the scientists and staff at the Closed-Circuit Centrifugal Compressor Test Rig (CLOCTER) Facility, Instrumentation Lab and Special Purpose Workshop at the Propulsion Division of the National Aerospace Laboratories for their tremendous support during the experimental programme.

TABLE OF CONTENTS

LIST OF TABLES

LIST OF FIGURES

NOMENCLATURE

Abbreviations

AEDC	Arnold Engineering Development Center
AIP	Aerodynamic Interface Plane
AIR	Aerospace Information Report
AJDG	Air Jet Distortion Generator
ARP	Aerospace Recommended Practice
CFD	Computational Fluid Dynamics
DI	Distortion Index
GCI	Grid Convergence Index
IDC	circumferential distortion parameter
IDR	radial distortion parameter
LDA	Laser Doppler Anemometry
LES	Large Eddy Simulation
MPR	multiple-per-rev
NASA	National Aeronautics and Space Administration
POD	Proper Orthogonal Decomposition
PRS	compressor pressure ratio at surge
RMSE	root-mean-square error
RSM	Reynolds Stress Model
SAE	Society of Automotive Engineers
S. D.	standard deviation
SIMPLE	Semi-Implicit Method for Pressure-Linked Equations
V/STOL	Vertical/Short Take-off and Landing
VTOL	Vertical Take-off and Landing

Symbols

A_1	area at station 1
A_2	area at station 2
A_3	area at station 3
A_j^*	area of the jet nozzle corresponding to choked condition
A_{p0}	parameter used in the calculation of r; $A_{p_o} = \left\{ \left[1 - \frac{p_0}{p_{01}} \right]_j - \left[1 - \frac{p_0}{p_{01}} \right]_{ave} \right\}_{target}$
A_R	area ratio
b	jet width
B	velocity-decay constant (see equation 4.19)
B_{p0}	parameter used in the calculation of r; $B_{p_o} = \left\{ \left[1 - \frac{p_0}{p_{01}} \right]_j - \left[1 - \frac{p_0}{p_{01}} \right]_{ave} \right\}_{achieved}$
c	model constant (in equation 4.21); c = 5.83
c'	constant of proportionality (in equation 4.9)
$C_{1\varepsilon}$	model constant in the k-ε equation
$C_{2\varepsilon}$	model constant in the k-ε equation
c_p	coefficient of pressure
C_p	specific heat at constant pressure
c_{p0}	total pressure loss coefficient
C_μ	constant of proportionality in the k-ε equation
d	diameter of the screen wire
D_0	diameter of confining duct
d_e	eddy diameter
d_h	diameter of hypothetical nozzle
D_h	hydraulic diameter
D_h	diameter of honeycomb cell
d_j	diameter of jet nozzle

F	fourth moment of the mass flow rate difference between the adjacent jets
f	friction factor
g	narrow gap between the eddy and the confining duct
I	turbulence intensity
i	counter indicating the ring number
k	turbulence kinetic energy
K	pressure loss in a component of the test facility
K_{D2}	distortion factor (developed by Pratt & Whitney)
K_{ex}	expansion loss coefficient in a diffuser
K_n	loss coefficient of the contraction section
K_θ (θ)	diffuser loss coefficient based on included diffuser angle θ
l	mesh size in the screen
l_c	length of the potential core
L_h	length of honeycomb cell
l_p	jet penetration length
m	mass flow rate in the jet at any axial station normal to the jet axis
M	momentum flux in the jet at any axial station normal to the jet axis
M	Mach number
m_0	mass flow rate at the jet exit
M_0	momentum flux at the jet exit
m_1	mass flow rate of the counterflow stream
M_1	Mach number at station 1
m_2	mass flow rate of the jet stream
$m_{2,j}$	jet mass flow rate
m_2/m_4	mass flow ratio
M_3	Mach number at station 3
m_4	mass flow rate at the duct exit, $m_4 = (m_1 + m_2)$
m_j	jet mass flow rate
n	number of sampling points
N	number of jets

$p_{0,\ ave}$	average total pressure in any plane of interest
$p_{0,\ face,\ ave}$	average total pressure in the plane
$p_{0,\ low,\ ave}$	average of the total pressures below the ring average total pressure
$p_{0,\ max}$	maximum total pressure in any plane of interest
$p_{0,\ min}$	minimum total pressure in any plane of interest
$p_{0,\ obtained}$	total pressure obtained at the end of a computational step
$p_{0,\ ring,\ ave}$	average total pressure in a ring
$p_{0,\ ring,\ ave}$	average total pressure in the ring
$p_{0,\ ring,\ min}$	minimum total pressure in a ring
$p_{0,\ target}$	target total pressure
$p_{0,\ z1}$	total pressure at $z/D_0 = 2.69$
$p_{0,\ z2}$	total pressure $z/D_0 = -2.47$
p_{01}	total pressure at the counterflow stream inlet
p_{02j}	jet exit total pressure
p_{02j}	total pressure at jet exit
p_{03}	total pressure at station 3
p_1	static pressure at the counterflow stream inlet
p_1	static pressure at station1
p_2	static pressure at station 2
p_3	static pressure at station 3
p_{atm}	atmospheric pressure
p_j	jet exit pressure
$p_{t,0}$	total pressure at the inlet of the duct
$p_{t,e}$	total pressure at the exit of the duct
p_w	wall static pressure
r_0	radial extent of jet boundary
Re	Reynolds number
Re_d	Reynolds number (based on a suitable hydraulic diameter)
r	linear correlation coefficient

r_j	radius of the jet nozzle
r_s	radial extent of stagnation streamsurface
T_{01}	total temperature at station 1
T_{02}	total temperature at station 2
U	relative velocity defined as $U = u_c + u_0$
u_0	counterflow velocity
u_1', v_1'	fluctuating velocity components at the inlet of the screen
u_2', v_2'	fluctuating velocity components at the exit of the screen
u_{avg}	mean axial velocity at the jet exit
$U_{b,m}$	impeller speed at the mean diameter
u_c	centreline velocity
u_j	jet velocity
u_{max}	maximum velocity in the neighbourhood of the jet
v_1	velocity at station 1
v_2	velocity at station 2
v_4	velocity at station 4
V_a	axial flow velocity at the impeller inlet
Z	momentum flux ratio
Z_c	momentum flux ratio for the compressible flow case
α	scaling factor
α	deflection coefficient
β	porosity of the screen
β_h	honeycomb porosity
Γ	defined as $\Gamma = \int_0^r r\,dr = \frac{r^2}{2}$
γ	ratio of specific heats
Δ	characteristic cross-sectional mixing area in the radial direction
δ^*	boundary-layer displacement thickness
Δp_0	total pressure rise from the impeller
$\Delta PC/P$	circumferential distortion intensity

$\Delta PR/P$	radial distortion intensity
$\Delta\varphi$	difference in mass flow rate between the adjacent jets
ε	turbulence kinetic energy dissipation rate
ε	roughness of the honeycomb cell
η	similarity variable, $\eta = \Gamma/\Delta$
η_j	value of η at the starting location of the jet similarity
θ	angle
θ	incidence angle
$\bar{\theta}$	circumferential distortion extent
θ_{crit}	critical angle
λ	non-dimensional value of mixing length in the jet
λ	honeycomb friction coefficient
λ_{p0}	total pressure loss parameter
μ_t	turbulent viscosity
ν_t	turbulence viscosity
ρ	density of the fluid
ρ_0	density of the counterflow stream
ρ_j	density of the jet stream
σ_k	model constant in the k-ε equation
σ_ε	model constant in the k-ε equation
φ	exit angle
φ	flow coefficient
ψ	streamfunction
ψ	pressure rise coefficient

ABSTRACT

The performance of an aircraft gas turbine engine is adversely affected by the non-uniform or distorted flow in the inlet duct. Inlet flow distortion lowers the surge margin of the engine's compression system with surge occurring at much lower pressure ratios at all engine speeds. The compressor and/or engine are subjected to ground tests in the presence of inlet distortion to evaluate its performance. The simplest method of simulating inlet distortion during these tests is by installing a distortion screen ahead of the engine on the test bed. The uniform inlet flow to the compressor becomes non-uniform with total pressure loss after passing through the distortion screen. Though the distortion screens offer a number of significant advantages, they have some disadvantages.

The air jet distortion system can alleviate many of the operational disadvantages encountered with the conventional distortion screens. The system consists of a number of air jets arranged in a circumferential array in a plane and issuing opposite to the primary air flow entering the engine. The jets interact with the primary stream and cause a local total pressure loss due to momentum exchange. The individual mass flow rates from the jets can be varied to obtain a required total pressure pattern ahead of the compressor at the Aerodynamic Interface Plane (*AIP*).

A systematic study of the flow field of confined, turbulent, incompressible, axisymmetric jet issuing into counterflow is covered in this research programme. The jet penetration length and the jet width are reduced compared to unconfined counterflow and a linear relationship between the velocity ratio and the jet length ceases to be valid.

The flow field of a circular compressible turbulent jet and then a system of four jets arranged circumferentially and issuing into a confined counterflow was studied experimentally and numerically. For the four jet system the mass flow rates in the four jets were equal in the first part of the study and in the second part they were unequal. The loss in total pressure due to the jet(s) interacting with the counterflow was quantified by a

total pressure loss parameter λ_{p0}. The total pressure loss increased with increasing mass flow ratio. The total pressure loss distribution was evaluated at several locations behind the jet injector(s). The total pressure non-uniformity quantified by Distortion Index (*DI*) was found to be highest at a location just downstream of the jet injector and at far downstream locations low values of *DI* were observed.

From the understanding gained with a single jet and four jets in counterflow a methodology was developed to generate a given total pressure distortion pattern at the *AIP*. The methodology employs computations to obtain the total pressure distortion at the *AIP* with quasi-one-dimensional inviscid analysis used as a starting point to estimate the mass flow rate in the jets. The inviscid analysis also provides a direction to the iterative procedure to vary the mass flow rate in the jets at the end of each computational step. The methodology is demonstrated to generate a given total pressure distortion pattern using four jets and is further extended to a larger number of jets, twelve and later twenty jets. The total pressure distortion patterns typical of use in aircraft gas turbine engine testing are generated accurately with a smaller number of jets than reported in the literature.

CHAPTER 1

INTRODUCTION

The performance of a modern fighter aircraft is heavily influenced by the performance of its propulsion system. These aircraft perform high angle of attack and high angle of sideslip manoeuvres, which puts severe demand on the gas turbine engine. The stable and safe operation of the aircraft and the gas turbine engine at all flight conditions is thus the most primary concern for the designer and the operator.

The engine compression system is particularly vulnerable to non-uniform or distorted flow in the inlet duct. The compressors are designed for uniform inlet flows and suffer from performance degradation due to non-uniform inflow conditions leading the compressor to aerodynamic instabilities like rotating stall and surge. The distortion in the inlet flow field can be in static or total pressures, or temperatures or velocities. The total pressure distortion is the most common type and also has the most deleterious effect on the performance of the compression system.

Many causes are attributed to the generation of total pressure distortion in the engine/compressor inlet; a few of them are described here. The duct geometry itself may present a non-uniform flow to the compressor. Moreover, during aircraft manoeuvres the flow in the inlet duct may separate off the walls and this may deliver a distorted flow to the compressor. The interaction of shockwave and boundary layer in the inlet of a supersonic aircraft causes boundary layer separation. The separated boundary layer essentially makes the flow non-uniform in the duct. Another case of inlet flow non-uniformity is caused by the ingestion of inlet or ground vortices into the engine when operated near a ground plane at static or near-static conditions. Aircraft with vertical take-off and landing (VTOL) capabilities present operational difficulties in the re-ingestion of hot exhaust gases into the engine. This causes a combined total pressure and total temperature distortion at the compressor face and severely reduces the engine surge margin. A further type of total pressure and total temperature distortion is due to hot gas ingestion from missiles and other armaments fired during combat.

The consequences of a compressor operating in a distorted flow field include performance degradation, unsteady blade forces, vibration and most importantly, a reduction in surge margin and loss of thrust when compared to a compressor with no distortion. This phenomenon is shown in Figure 1.1, (adapted from Williams and Surber 1993), which clearly indicates that the surge margin of the compressor has lowered, with surge occurring at lower pressure ratio for constant mass flow at all speeds.

Figure 1.1 Effect of inlet distortion on compressor performance (from Williams and Surber 1993).

Compressors are designed for uniform inlet flows and distortion always degrades their performance. More serious is the fact that inlet distortion triggers flow instability in the compression system and lowers its surge margin. The fluid dynamic aspect of this phenomenon is described here. The performance of a blade row in an axial compressor is determined by its velocity triangles constructed from the absolute, relative and circumferential velocity components together with the blade rotational speed. The radial component of velocity is also of considerable importance in low hub-to-tip ratio compressors. Inlet distortion induces perturbations in these velocity components as a

result of the complex flow field interaction between the inlet and the compressor, thus increasing the flow incidence to the blades. The already highly loaded blades stall and adversely affect the performance of the blade row. The stage velocity triangles are altered and this leads to re-matching of stages in a multistage compressor. These events initiate flow instability in the compressor and the machine eventually stalls or surges at a lower pressure ratio on a corrected speed line. The end result is the degraded compressor performance in terms of loss of airflow capacity at a corrected speed and a loss of efficiency with a marked loss in surge margin.

Figure 1.2 Typical distortion screens (from Beale, Cramer, and King 2002).

The compression system and/or the engine are thoroughly subjected to rigorous tests in ground-level test facilities in the presence of inlet distortion. These tests establish the compression system's response to such distorted conditions. The inlet flow distortion can be simulated by a number of methods. A comprehensive review of the various methods employed, including many methods presently under development/consideration is given by Beale, Cramer, and King (2002). The distortion screens and air jet distortion system are deemed most satisfactory and are widely employed. Some typical distortion screens are shown in Figure 1.2.

The air jet distortion system shown in Figure 1.3, (from AIR1419 1999: 175) consists of a number of air jets arranged in a circumferential array and issuing opposite to the primary air flow entering the engine/compressor. The jets mix with the incoming primary air flow, causing local momentum defect, which is proportional to the velocity of the jet. By individually adjusting the velocity in the jets a local total pressure loss is effected and a desired pressure distribution in the inlet can be obtained.

Figure 1.3 Schematic of air jet distortion system (from AIR1419 1999:175).

The development of such an air jet distortion system, which is the objective of this research, would require an understanding of the mechanism of total pressure loss caused by jets issuing into a counterflow primary stream. As indicated earlier the individual jet velocities can be set to obtain a required pressure distribution in the inlet. A methodology is evolved to achieve a prescribed total pressure distortion pattern employing multiple turbulent jets in counterflow.

A systematic study of the flow field of turbulent jets issuing into counterflow is embarked in this research programme. This dissertation is consequently arranged as follows: the relevant published literature pertaining to the present work is reviewed in

Chapter 2. It was realised that an improved understanding of the flow field of a jet in confined counterflow, and particularly that of multiple jets in confined counterflow was essential to devise a system of circumferential array of jets to simulate inlet distorted flow field. The problem definition, specific objectives, and the methodology employed to achieve these goals are described in Chapter 3.

The flow field of an axisymmetric incompressible turbulent jet issuing into an incompressible confined turbulent stream was computationally investigated and the solutions were compared with existing experimental results of a free jet issuing in a quiescent ambient and those of jet-in-counterflow configuration. Some fundamental differences and analogies between the free jet and jet-in-counterflow were elucidated; these findings are elaborated in Chapter 4. This study provided the basis for gaining an understanding into the characteristics of a turbulent jet issuing in an opposing stream.

A round compressible turbulent jet issuing into a confined counterflow was studied experimentally and numerically and the results are presented in Chapter 5. A system of four jets issuing into a confined counterflow was studied, again, by experiments and computations and the results are reported in Chapter 6. From the understanding gained with a single jet and four jets in counterflow a methodology has been developed to generate a given downstream total pressure pattern and demonstrated for several flow cases. These results are reported in Chapter 7. In the last chapter conclusions are drawn from the present study and some recommendations are made for further course of work.

CHAPTER 2
LITERATURE REVIEW

The performance of an aircraft gas turbine engine is adversely affected by the non-uniform or distorted flow in the inlet duct. The distortion in total pressure is the most common and also has the most deleterious effect on the compressor performance. Inlet flow distortion lowers the surge margin of the engine's compression system with surge occurring at much lower pressure ratios at all engine speeds. The compressor and/or engine are subjected to ground tests in the presence of inlet distortion to evaluate its performance. Of the various methods of distortion simulation in ground test facilities the distortion screen and the air jet distortion system are deemed most satisfactory.

In this chapter, the various methods of distortion simulation in engine test facilities are reviewed and the air jet distortion system is found to be a versatile means of distortion simulation. This system consists of a number of jets arranged in circumferential arrays in a plane and issuing opposite to the primary air flow ingested by the engine. The development of an air jet distortion system requires an understanding of the total pressure loss mechanism of turbulent jets in counterflow and particularly that of multiple jets in counterflow.

This chapter is arranged as follows in two major sub-sections: The relevant literature pertaining to methods of distortion simulation in engine test facilities are reviewed in the first section. The emphasis here is on the distortion screens and air jet distortion system. The limitations and capabilities of these techniques are identified and documented. The pertinent published work on turbulent jet in counterflow is reviewed next. The turbulent jet in counterflow configuration appears to be the least investigated in the jet-class of flows.

2.1 Methods of Inlet Total Pressure Distortion Generation

The general subject of inlet flow field distortion and its adverse effects on the performance and stability of the compression systems were reviewed by Longley and Greitzer (1992), and Sivapragasam and Ramamurthy (2009) (see also the references therein). The distorted flow field ahead of the compressor is simulated in ground test facilities by various methods. Several such techniques were examined by Beale, Cramer, and King (2002). In this section only the distortion screens and the air jet distortion system are considered.

2.1.1 Distortion Screens

Aerodynamic screens are used in a number of engineering applications to both remove and generate flow non-uniformities. The production of a uniform profile from arbitrary non-uniform upstream conditions is desired for wind-tunnel applications, and the production of a specified non-uniform profile from uniform upstream conditions is required for simulating test conditions. A general review on the subject of flow through screens can be found in Laws and Livesey (1978).

The distortion screens have long been commonly employed for simulating total pressure distorted inlet flow field in test facilities. The screens are simply wire meshes of various porosities secured to a frame and placed ahead of the engine/compressor. The screen porosities are chosen to produce the required pressure drop. The total pressure distortion can be either in circumferential or radial directions and such total pressure patterns are called ‘classical’ distortion patterns; the screens utilised to simulate such distorted flow fields are called ‘classical’ distortion screens. The total pressure distortion profile such as those occurring at flight conditions are termed ‘complex’ (or ‘composite’) distortion patterns and can have both circumferential and radial non-uniformities; the screens which can simulate such patterns are called ‘complex’ distortion screens. Examples of classical and complex distortion screens and their corresponding total pressure patterns they simulate are shown in Figure 2.1 (reproduced from Davis, Hale, and Klepper 2010: 148-149).

(a)

(b)

Figure 2.1 Typical distortion screens and their corresponding downstream total pressure pattern (a) 'classical' 180° distortion screen, and (b) 'complex' distortion screen (Davis, Hale, and Klepper 2010: 148-149).

Reid (1969) extensively employed distortion screens to study the performance of an axial compressor in distorted conditions. A critical angle, θ_{crit}, was defined which is the circumferential width of the distorted field at which its effect is felt on the compressor. It was also found that distortions of smaller circumferential widths did not have a significant effect on the stability of the compressor.

The design of screens to simulate the distorted flow field was discussed by Anderson (1983), Zhang and Gao (1983), and Cousins, Georges, and Rezaei (2003). Zhang and Gao call their distortion device as 'plate simulator', and Cousins *et al*.

employed what they term as “small metallic ‘fingers’”, which can, in fact, be considered to belong to the screen family. In spite of the design processes evolved some amount of trial-and-error is inevitable as the “screen design is in itself an art and a careful attention to detail is required if the desired pattern shapes… are to be achieved…” (AIR1419 1999: 43).

Several examples of the use of distortion screens are reported in the early Glenn (then Lewis) Research Center, Ohio, National Aeronautics and Space Administration work (see the reviews by Bowditch and Coltrin 1983, and Biesiadny *et al*. 1987). The distortion screens were also employed by Chen *et al*. (1985), Flitcroft, Dunham, and Abbott (1987), Cousins *et al*. (1994), Hah *et al*. (1998), Huang, Wu, and Du (2009), Salunkhe, Reddy, and Pradeep (2009), and Wadia (2010).

The distortion screens were also used to generate some kind of dynamic distortion by rotating them with reference to the rotor rotation. Such instances are reported in Longley *et al*. (1996), van Schalkwyk *et al*. (1998), Nie *et al*. (2006), and Salunkhe and Pradeep (2010 a, b).

The screens were utilised to study the adverse aeromechanical response, particularly with regards to high-cycle fatigue of the compression system. These studies are described in Manwaring and Fleeter (1990), Rabe, Bolcs, and Russler (1995), Manwaring *et al*. (1997), Hamed and Numbers (1997), and Wallace, King, and Kenyon (2004).

Despite the simplicity of not having any moving parts and not requiring frequent calibrations a distortion screen can generate only a set distortion pattern and hence need to be changed every time a different pattern is required.

2.1.2 Distortion Screen Development Programme at National Aerospace Laboratories

A research programme was undertaken at the Propulsion Division of National Aerospace Laboratories, Bangalore for the design and development of complex distortion screens to simulate total pressure distortion patterns ahead of aircraft gas turbine engines.

A series of systematic experiments were conducted to characterise the screen meshes of various porosities in terms of their loss coefficients and distortion parameters. A comprehensive database was generated for various mesh combinations in terms of porosity, loss coefficient and particularly, distortion parameters. Based on the experimental studies and the data bank accumulated, an inverse design methodology was developed to design a mesh combination for producing a prescribed total pressure distortion pattern. The methodology is described by Sankaranarayanan, Murugesan, and Rao (1994). This method was applied to produce a specific distortion pattern. The experimentally obtained total pressure contours matched well with the input design data.

During the course of this research programme, it was found that the distortion screen assembly made from wire mesh presented a number of fabrication and operational difficulties. The screen assembly was fabricated from a combination of wire meshes cut to the required shape and stitched and welded at the intersecting lines. This fabrication technique was particularly painstaking and required high skill. Due to different gauze wires welded near the joints, the mechanical strength of the joints was very weak. This required installation of additional thick mechanical guards to prevent the ingestion of wire mesh into the engine during test runs in case of their failure. Further, the welded regions created large blockage to the flow path and caused excessive pressure drop across them. Moreover, the porosity of the mesh calculated by the inverse method was not commercially available. This forced the use of mesh close to the design specification and settle for a compromise on the total pressure pattern obtained.

These difficulties were overcome by a new manufacturing technique adapted by Ramamurthy *et al.* (1998). In this technique, holes in the different porosity regions were cut on a single stainless steel sheet by a laser beam. By suitably selecting the holes size and web width, any required porosity could be achieved. The screens can be carefully designed to withstand the required mechanical strength by properly designing the web width. This avoided the need for guards downstream of the screen. Since this screen had no joints, the excessive flow blockage was eliminated.

In the meantime, many refinements to the inverse design methodology were incorporated. The aerodynamic characteristics of the screen designed by the new method and fabricated by the laser-cut technique were evaluated experimentally. It was observed that the laser-cut screen produced higher distortion compared to the one fabricated by the traditional wire mesh. This clearly indicated the advantage of using the laser-cut screen over the wire-mesh assembly.

During manufacturing of several laser-cut screens of various porosities and sizes, it was found that the thin stainless steel sheet had warped due to the tremendous heat generated by the cutting action of the laser beam. This problem was overcome by choosing to cut the square holes of required size by a water-jet. This method was highly successful in fabricating warp-free distortion screens for current research activities at the National Aerospace Laboratories.

Recently, Biswas *et al*. (2013) detected a fatigue failure in a complex distortion screen designed and manufactured by the method of Ramamurthy *et al.* (1998) reiterating the need for designing the screens for adequate mechanical strength.

2.1.3 Air Jet Distortion System

The air jet distortion system can alleviate many of the operational disadvantages encountered with the conventional distortion screens. The system consists of a number of air jets arranged in a circumferential array and issuing opposite to the primary air flow entering the engine. The jets interact with the primary stream and cause a local total

pressure loss due to momentum exchange. The individual mass flow rates from the jets can be varied to obtain a required total pressure pattern ahead of the compressor.

The Glenn Research Center, Ohio of the National Aeronautics and Space Administration developed an air jet distortion device which is described in Meyer, McAulay, and Biesiadny (1970). The jet array consisted of 54 flow nozzles which were uniformly distributed circumferentially and radially as shown in Figure 2.2. The nozzles were arranged in a pattern which repeated itself every 60º circumferentially. Each 60º sector was supplied with high pressure air through individual flow control valves. The steady state total pressure measurements were made by a standard 40 probe (8 rakes each with five probes) arrangement and unsteady pressure measurements were made with high-response transducers at 10 circumferential locations.

Both steady and dynamic distortions were simulated by this technique. The dynamic distortion was done by an oscillatory operation of the high-response servo-operated valves. This air jet system enabled variable-amplitude steady and sinusoidal dynamic distortions in circumferential and radial directions by controlling the secondary air distribution and flow rate. This system was later reported by Baumbick (1970) to produce dynamic total pressure distortion by pulsing the air jets. This system was employed by Braithwaite, Dicus, and Moss (1970) to evaluate the performance of a turbofan engine with inlet distorted conditions. They found that the air jet system produced distortion profiles comparable with the screen-induced distortion. Povolny (1970) also used the air jet system to simulate time-variant total pressure distortion for testing a turbofan engine installed with an afterburner.

Figure 2.2 Air jet distortion system developed at the NASA Glenn Research Center, Ohio, from Meyer *et al*. (1970).

An Air Jet Distortion Generator (AJDG) developed at the Arnold Engineering Development Center, Tennessee was described in Overall and Harper (1977) and McIlveen (1979). This system had the capability of generating a required total pressure pattern. The air jet system had a jet nozzle array of equally-spaced 56 jets arranged circumferentially as shown in Figure 2.3. The high pressure secondary air was supplied to the jets at the required pressure and temperature. A computerised air jet nozzle flow control system was interfaced to the total pressure distortion instrumentation and the valve actuators to supply high pressure air to the air jets. The measured distortion pattern was compared by this system with the required distortion pattern and it iterated upon the valve settings and varied the mass flow rate in the jets till the desired pattern was obtained to the specified accuracy. This technique was termed the 'dial-a-pattern' capability. This system was employed by Hubble and Smith (1979) for inlet flow distortion simulation ahead of a turbofan engine.

Figure 2.3 Air Jet Distortion Generator (AJDG) developed at the AEDC, Tennessee, from Overall and Harper (1977).

More recently, an Air Jet Distortion Generator was designed and developed by Naseri, Boroomand and Tousi (2012) to produce steady total pressure distortion patterns ahead of a micro-jet engine. This system was capable of only generating classical circumferential total pressure distortion patterns of 60º, 120º and 180º extent.

2.2 Turbulent Jet in Counterflow

A turbulent jet is a basic shear flow and has received extensive research attention (see, for example, Tennekes and Lumley 1972, Hinze 1975, Townsend 1980, Schlichting 1979, and Pope 2000). However, in many engineering applications the jet does not issue into a quiescent ambient stream but usually interacts with an external stream (see, Pai 1954, Abramovich 1963, and Rajaratnam 1976).

A turbulent jet issuing into a quiescent ambient stream is the most basic shear flow in the turbulent jet class and extensive measurements of the mean and turbulent flow fields was reported by Panchapakesan and Lumley (1993), and Hussein, Capp, and

George (1994). These measurements are now believed to be the most reliable measurements made in a turbulent free jet and are widely quoted.

When the jet and the external stream flow parallel to each other in the same direction the flow system is termed the co-flow jet. In this flow system the jet growth rate and entrainment characteristics are affected by the co-flowing stream. Such investigations were reported, for example, by Antonia and Bilger (1973), Perry and Tan (1984), Agüĭ and Hesselink (1988), Nickels and Perry (1996), and Villermaux and Rehab (2000).

When the jet issues normal to the freestream the jet in cross-flow situation is encountered. The jet flow structure is strongly modified by the cross-flow and large streamwise vortices appear which are responsible for the interesting kidney-shaped cross-section of the jet in the far field. These findings were described by Andreopoulos (1985), Fric and Roshko (1994), Kelso, Lim, and Perry (1996), Haven and Kurosaka (1997), and Rivero, Ferré, and Giralt (2001).

When the jet and the external stream flow opposite to each other the jet in counterflow configuration is observed. The jet flow field is dominated by a large recirculation pattern due to the interaction of the jet and counterflow. The literature pertinent to such flow system is reviewed here.

The earliest study of a turbulent jet in counterflow was reported by Arendt, Babcock, and Schuster (1956). They first demonstrated using dimensional analysis and experimental results that the jet length was linearly proportional to the velocity ratio between the jet and the counterflow.

The Helmholtz free-streamline theory was employed by Hopkins and Robertson (1967) to perform a kinematic simulation of the inviscid flow of a two-dimensional jet in opposing stream. Their results had restrictive practical value because of the grossly

simplifying assumptions made in the analysis. Moreover, their limited experimental results did not agree well with their analytical model.

Margason (1968) presented results, from flow visualization, of the flow path of a jet injected into the freestream at angles from 30º to 180º. The intention of these experiments was to study the interference between the jets and the freestream and its effect on the aerodynamic characteristics of V/STOL aircraft. The 180º case (jet in counterflow) is of interest here; the jet penetration distance was measured and plotted for different velocity ratios.

Some early Soviet researchers investigated the flow field of a jet in counterflow. The paper by Sekundov (1969) is the most notable amongst these and it also contains a review of the previous Soviet work. In this analytical work the velocity profiles were assumed to be piece-wise linear in the radial direction in the jet in various regions and these profiles were integrated resulting in a complicated expression for the jet length. Some experimental results were also presented in support of the analysis which was in reasonably good agreement.

A detailed description of the time-averaged features of the turbulent jet in counterflow was provided by Beltaos and Rajaratnam (1973). The velocity and length scales associated with this flow were estimated from dimensional arguments and some semi-empirical relations. From these results the geometry of the jet was reconstructed and was found to compare well with their experimental investigation. A simple linear relation between the jet length and velocity ratio was obtained. A comparison of this relation with experiments conducted by these and other authors was found to be satisfactory.

The turbulent jet in confined configuration was studied by Morgan, Brinkworth, and Evans (1976). The jet nozzles were enclosed by ducts of different diameters and thus various confinement ratios were achieved. These authors obtained an exceptionally high velocity ratio of about 160 in their experiments. They introduced an important

momentum parameter governing the jet length and found two regimes of interest, one associated with low jet momentum when the jet length is linearly proportional to the velocity ratio and another with high jet momentum where the jet length follows a one-third power law behaviour with the momentum ratio. They also arrived at a crucial conclusion that these jet length and momentum ratio relations are unaffected by the Reynolds number of the jet or that of the main stream when they are above 3000 and 10000, respectively.

Oron and Abuaf (1977) invoked the boundary layer approximation for the calculation of this flow field. Since the jet was unconfined the static pressure was assumed to be constant. The turbulence closure achieved by a mixing length turbulent viscosity hypothesis for free shear flows. This boundary layer-type solution was not valid near the stagnation region where the velocity changes sign. The agreement with experimental results in the remaining region was reported to be good.

The advent of Computational Fluid Dynamics in the early nineteen eighties spurred some activity in the investigation of the turbulent jet in counterflow. The first work to appear taking advantage of CFD was that of Peck (1981). The turbulent jet in an unconfined environment was numerically calculated by the two-equation $k - \varepsilon$ turbulence model. The predicted jet length was slightly underestimated when compared to experiments but was qualitatively correct. The centreline velocity along the jet axis and the radial velocity profiles in the jet compared well with experiments. It must be remarked that the computational grid used by Peck (1981) for the calculation of the axisymmetric flow field was 28 × 49 which is very coarse, especially comparing it with present-day CFD standards.

Elghobashi *et al*. (1981) also employed the $k - \varepsilon$ turbulence model to calculate the velocity, temperature and concentration fields of a non-reacting turbulent jet in confined opposing stream. The numerical calculations and experiments were conducted for both cold and hot air and CO jets. The predicted velocity field was in fair agreement with their

experiments but the agreement for the mean and fluctuating temperature and mean concentration was not convincing. First, the computational grid employed by the authors was 25 × 20 which is, in fact, quite coarse. Seondly, doubts were raised about the scalar turbulent diffusion equation used to solve for the scalar fields.

The turbulent jet in confined counterflow situation was numerically and experimentally investigated by Majumdar and Bhaduri (1981). The numerical simulation employed a stream function – vorticity formulation and an *ad hoc* effective viscosity was used to model turbulence. The confinement was varied by changing the jet nozzle diameter. The predicted axial and radial velocity components were not in good agreement with the experiments. However, the jet centreline velocity and jet length were in good agreement. The computational grid was 38 × 18, which is, again, coarse. Further, the use of the effective viscosity concept to model turbulence could have added to the discrepancy between numerical and experimental results.

More recently, two research groups, one at Technical University of Berlin (Yoda and Fiedler 1996) and another at The University of Hong Kong (Lam and Chan 1997) revived interest in this flow configuration. The former group appear to be concerned with the fundamental aspects of this flow system while the latter was interested in civil engineering applications of this flow. Interestingly enough, a collaborative research work between these groups was also reported as described in the next paragraphs.

Yoda and Fiedler (1996) presented experimental results of the turbulent jet in counterflow. The instantaneous flow visualisation images indicated the existence of a ‘stable’ jet at low velocity ratios with regular vortex shedding and at high velocity ratios flow becomes ‘unstable’ with significant velocity fluctuations in both axial and radial directions. A simple analytical model of this flow was provided by superimposing a turbulent jet with a uniform counterflow. The jet length predicted by this model agreed well with the experimental results obtained from time-averaged images. These results

were consistent with the earlier observations of the linearity of the jet length and velocity ratio relation. The mean concentration field was also studied in this work.

A flow visualisation study of the turbulent jet in counterflow was reported by Lam and Chan (1997). The jet penetration and its spreading was investigated. Again, a substantial fluctuation of the jet in both radial and axial directions was found and the fluctuations increased with increasing velocity ratio. The mean jet length was calculated from ensemble-averaged images. The mean jet length was also calculated by modelling the jet in counterflow as a contraction of the axial flow coordinates of a free jet. This model predicted the jet length reasonably well, but underestimated the length at low velocity ratios.

The jet length model prediction was followed up by Chan and Lam (1998). In this work the centreline velocity decay of a jet in counterflow was calculated using a flow advection hypothesis. The modelling was done in Lagrangian frame of reference and the potential core of the jet was 'compressed' by the counterflow. Beyond the potential core, the jet was advected backward by the counterflow. The proposed model predicted their measured mean centreline velocity decay well till and beyond the stagnation point. However, the model did not account for the effects of turbulence which can be very intense in the region of interaction between the jet and the counterflow.

The joint work between these groups was reported in Chan, Lam, and Bernero (1999). This study was primarily undertaken to resolve the differences in results that existed between the two laboratories. Their results were consolidated and a few additional experiments with the Technical University of Berlin apparatus were conducted at the University of Hong Kong. Apart from mean flow results and model predictions of these groups some results of the turbulence intensity characteristics along the jet centreline were also presented. An approximate similarity of the axial and radial turbulence intensity components along the jet length was obtained.

Bernero's (2000) doctoral dissertation contained some new results of this flow system. The flow field was visualised by various flow visualisation techniques and mean and fluctuating characteristics of the velocity and concentration fields were obtained and many of the results were consistent with earlier observations. The dynamics of the jet in counterflow was also studied and the 'stable' and 'unstable' regimes were observed. Further, a series of parametric studies was done to evaluate the effects of confinement, freestream turbulence level, initial jet momentum thickness, and jet inclination angle on the flow field. The control of this flow was attempted by both passive (by varying the nozzle shape) and active (by exciting the jet) means and found that flow control was possible only in the near field.

The mean velocity and concentration fields of a turbulent jet in counterflow was described by Tsunoda and Saruta (2003), and Tsunoda and Takei (2006). The flow field was evaluated by flow visualisation techniques and results were presented in terms of statistical characteristics for the concentration field.

Saghravani and Ramamurthy (2010) presented experimental results on the jet penetration length for varying confinements by using different nozzle diameters. They proposed a critical velocity ratio, beyond which the effects of confinement are felt on the jet and the departure from linear law was observed.

Torres *et al*. (2012) presented scaling factors for the mean concentration field of a turbulent jet in counterflow from their experiments. They proposed empirical relations for predicting the concentration decay in the jet in the axial and radial directions.

The available literature on turbulent jets in counterflowing stream was reviewed above and it serves well to summarise them in a tabular form as is done in Table 2.1. In this table, velocity ratio is the ratio of velocities between the jet and the counterflow stream. The confinement ratio indicates the ratio of the diameters of the duct confining the counterflow to the diameter of the jet nozzle. Thus, 'unconfined' refers to an

unbounded counterflowing stream. In many of the references above, however, the counterflow was confined in a duct or channel which is at a finite but sufficiently large distance.

Table 2.1 Summary of the literature review on turbulent jet in counterflow.

Sl. No.	Author(s)	Method	Velocity Ratio	Confinement Ratio	Comments
1.	Arendt, Babcock, and Schuster (1956)	Analytical, Experimental	Not available	Unconfined	Dimensional analysis, air jet with Pitot tube measurements
2.	Hopkins and Robertson (1967)	Analytical, Experimental	1 to 3 (analytical) and 1.2 to 1.6 (experimental)	Unconfined	Free-streamline theory, water used for counterflow and water and various liquids for jet
3.	Margason (1968)	Experimental	1.24 to 11.87	Unconfined	Flow visualisation – mixture of compressed air and water vapour jet
4.	Sekundov (1969)	Analytical, Experimental	2 to 15	10, 15, 30 and 100	Integral method, experimental technique not mentioned
5.	Beltaos and Rajaratnam (1973)	Analytical, Experimental	10.7 and 27.2	Unconfined	Semi-empirical and dimensional analysis, air jet with cylindrical Pitot probe
6.	Morgan, Brinkworth, and Evans (1976)	Experimental	2 to 160	8.3, 17, 43, 83	Flow visualisation – dyed water jet
7.	Oron and Abuaf (1977)	Analytical	6, 10 and 20	Unconfined	Boundary layer calculation
8.	Peck (1981)	Computational	0 to 22	Unconfined	Computation using $k-\varepsilon$ turbulence model
9.	Elghobashi *et al*. (1981)	Computational, Experimental	9 and 18 (cold jet), and 10. 2 and 20.4 (hot jet)	39.23	Computation using $k-\varepsilon$ turbulence model, air and CO jet, laser Doppler anemometer

10.	Majumdar and Bhaduri (1981)	Computational, Experimental	7.85 to 25.4	29, 38.67, 58	Computation using effective turbulent viscosity, air jet, single-hole cylindrical probe
11.	Yoda and Fiedler (1996)	Experimental, Analytical	1.3 to10	Unconfined	Flow visualisation – dyed water jet, laser-induced fluorescence, linear model for jet length
12.	Lam and Chan (1997), and Chan and Lam (1998)	Experimental, Analytical	2.5 to15	Unconfined	Flow visualisation – dyed water jet, planar laser-induced fluorescence, advection model for jet centreline velocity decay
13.	Chan, Lam, and Bernero (1999)	Experimental, Analytical	1.3 to 60	Unconfined	Flow visualisation – water jet, laser Doppler anemometer, advection model and uniform flow and jet superposition model for jet centreline velocity decay
14.	Bernero (2000)	Experimental, Analytical	1 to 30	Unconfined	Flow visualisation – water jet, laser Doppler anemometer, particle image velocimeter and laser-induced fluorescence, uniform flow and jet superposition model for jet centreline velocity decay
15.	Tsunoda and Saruta (2003), and Tsunoda and Takei (2006)	Experimental	2.9 to5.1	Unconfined	Flow visualisation – water jet, particle image velocimeter and planar laser-induced fluorescence
16.	Saghravani and Ramamurthy (2010)	Experimental	3 to 52	200, 100, 47.62, 32.26, 23.8	Flow visualisation – water jet, laser Doppler anemometer

17.	Torres *et al.* (2012)	Experimental	4 to 19	Unconfined	Flow visualisation – water jet, planar laser-induced fluorescence

A different type of counterflow jet flow system was developed by Strykowski and co-workers (Strykowski and Niccum 1991, Strykowski and Wilcoxon 1993) and its compressible counterpart by Strykowski, Krothapalli and Jendoubi (1996). In this arrangement a countercurrent mixing layer was established by applying suction right at the periphery of an axisymmetric jet nozzle. This set-up can be contrasted with the present one where the counterflow is applied at a far, but finite, distance from the jet nozzle (see Figure 4.1). Thus the dynamics of these two flow systems are different; despite this fact, these work are reviewed here for the sake of completeness. The experimental results of Strykowski and Niccum (1991) indicated the reduction of the decay rate of mean velocity along the jet centreline due to the presence of the counterflow. In the experiments of Strykowski and Wilcoxon (1993) self-excited global oscillations of the jet was established by the counterflow. They concluded that these oscillations are responsible for enhanced mixing between the jet and the surrounding fluid. Their later experiments with a supersonic jet (Strykowski, Krothapalli and Jendoubi 1996) revealed the presence of three-dimensional vortex structures in the countercurrent shear layer which are absent in co-flowing shear layers. These structures, they noted, were responsible for the enhanced diffusion of the shear layer with counterflow.

Further studies on this flow system were conducted by Asendrych and co-workers (Boguslawski *et al*. 2002, Asendrych and Favre-Marinet 2004, Asendrych 2007). In particular, the computations by Boguslawski *et al*. (2002) were discrepant with their experiments. Their numerical simulations showed that the turbulence level decreased because of the presence of the counterflow, whereas their experiments indicated rapid increase of turbulent diffusion caused by counterflow. It must be remarked here that their computational domain was covered by a 40 × 30 grid which is quite coarse to resolve the flow field under consideration. They have also mentioned that a rigorous grid independence study was not performed. A coarse grid causes excessive numerical

diffusion which must have led Boguslawski *et al*. (2002) to the observation noted above. Nevertheless, they concluded that the unsteady large scale structures in counterflow jets cannot be studied using classical turbulence modelling and advanced turbulence modelling like Large Eddy Simulation (LES) is required for resolving these features.

LES was, in fact, used to investigate the dynamics of the unconfined counterflow jet flow field (like in Figure 4.1, with $D_0/d_j \rightarrow \infty$) by Duwig and Revstedt (2009). Their study focussed on the large-scale coherent structures and fluctuation dynamics using Proper Orthogonal Decomposition (POD). They observed that the jet core length is compressed due to the counterflow and noted a flapping and rotation motion of the jet around the axis. More recently, Li *et al*. (2013) also performed LES to investigate the jet in unconfined counterflow arrangement. Their computations indicate the presence of large-scale vortex structures till near the stagnation point. The mean velocity decay along the jet centreline and the profiles of mean axial velocity at several radial locations were in good agreement with the experiments of Chan (1999). But the axial and radial fluctuating velocity components were only in reasonably good agreement.

Though it is true that LES is required to resolve the large-scale unsteady dynamics of the jet in counterflow, the mean flow field can be predicted accurately with classical turbulence models. The *k-ε* turbulence model is used in the present thesis for the prediction of the mean flow field. It will be shown later in Chapter 4 that the use of this model resulted in a good agreement with the available experimental data.

Several points are to be discussed in the light of the review above of the available literature. First, it is clear that the effects of confinement on the jet flow field are not thoroughly investigated, though some results were published. It appears, intuitively, that the physical characteristics of the jet like its length, width and growth rate would be affected by the presence of the confining duct. The jet entrainment rate is also likely to be altered. A systematic study of a turbulent jet in confined counterflow at various confinement ratios needs to be investigated.

Secondly, the effects of compressibility on the jet characteristics were not investigated. For example, Elghobashi *et al*. (1981) did consider a temperature difference between the jet and the counterflow; this ratio was about 1.1 in their study which was too small for any significant changes to be accounted. It would be interesting to study the effect of an initially compressible jet issuing into a counterflow at large density differences.

Another important observation is the lack of research on multiple jets issuing into counterflow. Though Beltaos and Rajaratnam (1976) suggested that "better mixing would be achieved if more than one outlet were used, through the interaction of the jets" and the study of "finding optimum spacing and configuration of the outlets" were recommended for further investigations none were carried out.

2.3 Summary

The distortion screens are the most preferred method of distortion simulation by virtue of its simplicity. Since the screens have no moving mechanical parts, they do not present complexity in manufacture. It is also relatively easy to employ the distortion screens. Once the screens are calibrated for their mass flow rate versus distortion characteristics, they can be used in different test facilities having similar engine configurations. The distortion screens are cheaper to develop and operate compared to other methods (see Bloch 1992 for a cost analysis and comparison).

The distortion screens have a few disadvantages though, arising mainly out of operational issues. Firstly, a screen can produce only a distinct distortion pattern. Since the engine operability evaluation consists of a number of distortion patterns to be simulated, each pattern simulation requires a different screen. This necessitates the need to interrupt the test process, uninstall the test hardware and change the screen every time another distortion pattern is to be simulated. The time and cost overruns associated with these interruptions are very high. Secondly, the screens are effective only over a narrow flow range below which they are ineffective and beyond which the holes in the screen

choke. The choking of holes presents a serious limitation as the mass flow through the engine cannot be increased any further. Moreover, the distortion screens essentially produce steady-state distortion pattern. However, if dynamic distortion conditions are to be simulated, the screens are grossly incapable of doing this. These considerations have led to the development of other means of inlet distortion simulation; albeit the screens are still widely employed.

With the several operational disadvantages with the distortion screens the air jet distortion system is a versatile system of generating total pressure distortion patterns. Both steady and unsteady total pressure distortion patterns can be generated by this system.

Also from the literature review it becomes clear that several issues are not addressed in the study of turbulent jets in counterflow stream. Addressing these issues would render this flow configuration even more amenable to practical applications as is demonstrated in this thesis for the design of an air jet distortion system. The study of a turbulent jet in confined counterflow, and that of an initially compressible jet in counterflow, and the fluid dynamic characteristics of multiple jets in counterflow are addressed in various chapters of this dissertation.

CHAPTER 3
PROBLEM DEFINITION AND METHODOLOGY

The performance of an aircraft gas turbine engine is adversely affected by the non-uniform or distorted flow in the inlet duct. Inlet flow distortion lowers the surge margin of the engine's compression system with surge occurring at much lower pressure ratios at all speeds. As mentioned in the previous chapter on literature review though the distortion screens are commonly employed for distortion simulation they have several operational disadvantages. An air jet distortion system can overcome these difficulties. The air jet distortion systems at NASA Glenn and AEDC have demonstrated this but with a large number of jets, 54 and 56, respectively. Also, in the NASA Glenn system a setting of the air jets was made and the consequent distorted total pressure field is used at the engine *AIP*. The AEDC system, on the other hand, had a limited provision to arrive at the jet settings to generate a desired total pressure distortion pattern. However, it used an ad-hoc feedback system to adjust the jet air flow to achieve a desired total pressure that was measured.

Hence there is a need to come up with a method to generate a complex total pressure distortion field using air jet systems. It is desirable that this method should be achieved by a systematic direct method, rather than a trial-and-error method, and preferably with a smaller number of jets. In the present study an effort is made to develop a methodology so that any set total pressure distortion field is achieved and it is demonstrated with only twenty jets.

3.1 Aim and Specific Objectives

The aim of this research is to numerically and experimentally investigate the total pressure loss mechanism and flow distortion created by multiple turbulent air jets in counterflow and develop a methodology for achieving prescribed inlet flow distortion for aircraft gas turbine engine testing. The specific research objectives are:

1. To review the various methods of distortion simulation in aircraft gas turbine engine test facilities and identify their capabilities and limitations.

2. To review the influence of turbulent jets in counterflow on total pressure loss mechanism.
3. To carry out steady-state computational and experimental investigations on total pressure loss and distortion index due to a *single* turbulent jet in counterflow.
4. To carry out steady-state computational and experimental investigations on total pressure loss and distortion index due to *multiple* turbulent jets in counterflow.
5. To develop a methodology to achieve prescribed total pressure distortion using multiple turbulent jets in counterflow.

3.2 Methodology

The methodology adopted for the conduct of this research project is listed below:

1. Literature survey on distortion simulation methods: The various methods of distortion simulation in an aircraft gas turbine engine test facility were reviewed and their capabilities and limitations identified.
2. Literature survey on jets in counterflow: The effects of fluid mixing and total pressure loss of jets issuing in counterflow were reviewed.
3. Single jet in counterflow studies: Computational studies were undertaken to gain understanding into mechanism of fluid mixing influencing the total pressure loss due to a single jet in counterflow. The computational results were compared with experimental results and total pressure losses estimated.
4. Multiple jets in counterflow studies: Computational analysis were done to investigate the total pressure loss, distortion index and its spatial decay downstream caused by the multiple jets in counterflow. The computational results were compared against experimental results.
5. Development of methodology to achieve prescribed distortion: The results obtained from previous phases were collated and were used to develop a methodology to achieve prescribed total pressure distortion. This methodology was validated computationally.

CHAPTER 4

COMPUTATION OF AXISYMMETRIC INCOMPRESSIBLE TURBULENT JET IN CONFINED COUNTERFLOW

In this chapter an axisymmetric jet issuing into a counterflowing stream is investigated computationally. A series of parametric computations were performed for different duct-to-jet diameter ratios and for various jet-to-counterflow velocity ratios. All time-averaged calculations were performed with the k-ε turbulence model using the ANSYS FLUENT flow solver. The results are presented in terms of the velocity profiles in the jet, the decay of velocity along the jet centreline, pertinent velocity and length scales, and turbulence characteristics, among others. Comparisons with available experimental data are made wherever possible.

4.1 Description of the Flow Field

A steady, incompressible, turbulent jet of velocity u_j issues from a nozzle of diameter d_j into a steady uniform stream of velocity u_0 ($u_j > |u_0|$) confined within a duct of diameter D_0 as shown in Figure 4.1. The direction of freestream velocity is opposite to that of the jet. The ratio of jet-to-counterflow velocity is u_j/u_0 and the ratio of the diameters of the confining duct and the jet nozzle is D_0/d_j.

The jet penetrates into the counterflow stream up to a certain distance, then interacts with the freestream and deflects backwards. This length, measured on the jet axis, from the nozzle exit till where the axial velocity becomes zero is termed the penetration length, l_p. The axial extent of the jet can be divided into three distinct regions (Sekundov 1969). The region immediately downstream of the jet nozzle consists of a developing jet with the potential core of the jet and persists downstream for a few nozzle diameters. In the potential core the velocity is uniform and equal to u_j. The jet beyond the developing region, in region 2, qualitatively behaves like a free jet. The jet thickness increases with distance from the nozzle. (A similarity solution exists in this region for the unconfined counterflow case. In the present study this similarity solution was modified to represent the results of the confined jet cases also. The analysis is presented in

Appendix 1). The jet and the counterflow stream interact intensely in region 3 and this region is characterized by a highly turbulent field of flow.

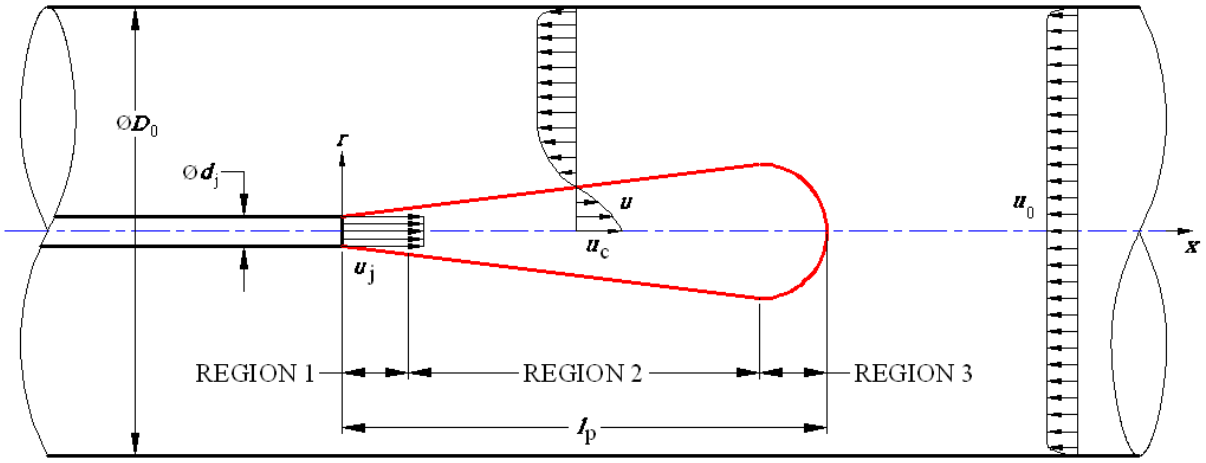

Figure 4.1 Schematic description of the flow field. The jet-to-counterflow velocity ratio is u_j/u_0; the diameter ratio is D_0/d_j.

4.2 Computational Procedure

The Reynolds-averaged Navier-Stokes (RANS) equations are used in the present thesis. The compressible, three-dimensional form of the equations is listed below.

$$\frac{\partial \rho}{\partial t} + \frac{\partial}{\partial x_i}(\rho u_i) = 0$$

$$\frac{\partial}{\partial t}(\rho u_i) + \frac{\partial}{\partial x_j}(\rho u_i u_j) = \frac{\partial p}{\partial x_i} + \frac{\partial}{\partial x_j}\left[\mu\left(\frac{\partial u_i}{\partial x_j} + \frac{\partial u_j}{\partial x_i} - \frac{2}{3}\delta_{ij}\frac{\partial u_l}{\partial x_l}\right)\right] + \frac{\partial}{\partial x_j}\left(-\rho\overline{u_i' u_j'}\right)$$

$$\frac{\partial}{\partial t}(\rho E) + \frac{\partial}{\partial x_i}\left[u_i(\rho E + p)\right] = \frac{\partial}{\partial x_j}\left[k_{eff}\frac{\partial T}{\partial x_j} + u_i(\tau_{ij})_{eff}\right] + S_h \qquad (4.1)$$

where, u_i and u_i' are the mean and fluctuating velocity components, ρ is the fluid density, μ is the viscosity, p is the pressure and k_{eff} is the effective thermal conductivity. The Reynolds stresses are related to the mean velocity gradients by (see, for example, Versteeg and Malalasekara 2007)

$$-\rho\overline{u_i' u_j'} = \mu_t\left(\frac{\partial u_i}{\partial x_j} + \frac{\partial u_j}{\partial x_i}\right) - \frac{2}{3}\left(\rho k + \mu_t\frac{\partial u_i}{\partial x_i}\right)\delta_{ij} \qquad (4.2)$$

where, μ_t is the turbulent viscosity and δ_{ij} is the Kronecker delta function. Two additional transport equations, one for the turbulence kinetic energy, k, and another for its dissipation rate, ε, are also solved using the standard k-ε turbulence model. The model equations are

$$\frac{\partial}{\partial t}(\rho k)+\frac{\partial}{\partial x_i}(\rho k u_i)=\frac{\partial}{\partial x_j}\left[\left(\mu+\frac{\mu_t}{\sigma_k}\right)\frac{\partial k}{\partial x_j}\right]+G_k+G_b-\rho\varepsilon-Y_M+S_k$$

$$\frac{\partial}{\partial t}(\rho\varepsilon)+\frac{\partial}{\partial x_i}(\rho\varepsilon u_i)=\frac{\partial}{\partial x_j}\left[\left(\mu+\frac{\mu_t}{\sigma_\varepsilon}\right)\frac{\partial \varepsilon}{\partial x_j}\right]+C_{1\varepsilon}\frac{\varepsilon}{k}\left(G_k+C_{3\varepsilon}\,G_b\right)-C_{2\varepsilon}\,\rho\frac{\varepsilon^2}{k}+S_\varepsilon\,. \qquad (4.3)$$

The turbulence viscosity is calculated in this model as,

$$\mu_t=\rho C_\mu\frac{k^2}{\varepsilon} \qquad (4.4)$$

where C_μ is a constant. The model constants are assigned the following values (Launder and Spalding 1972):

$C_{1\varepsilon}$ = 1.44, $C_{2\varepsilon}$ = 1.92, C_μ = 0.09, σ_k = 1.0, σ_ε = 1.3.

The governing equations were solved numerically using the commercial finite-volume method based code ANSYS FLUENT. Spatial discretization was carried out by a second-order upwind differencing scheme. Pressure-velocity coupling was achieved by the SIMPLE algorithm (Patankar 1980).

In the present chapter, the incompressible, axisymmetric version of the RANS was employed for the computations, and comparisons with available experimental data were made. This is because, as was discussed in Chapter 2, much of the available experimental data on jets in counterflow configuration consider the incompressible jet flow case only. However, in Chapters 5 to 7, the full compressible, three-dimensional form of the RANS was solved, because in the present thesis the eventual application is to use multiple jets in counterflow arrangement where the mass flow rates in the individual jets can be altered. To this effect, a circular sonic jet issuing into a confined counterflow studied in Chapter 5 and four circular sonic jets issuing into a confined counterflow

studied in Chapter 6, and later with 12 and 20 jets in Chapter 7, necessitated the need for solving the compressible, three-dimensional form of the RANS.

Some select calculations were also carried out with the Reynolds Stress Model (RSM) of turbulence. This model calculates the individual Reynolds stresses using seven differential equations, and these stresses are used to obtain closure of the Reynolds-averaged momentum equation (Launder *et al*. 1975, Launder 1989). The decay of axial velocity along the jet centreline is shown in Figure 4.2. It can be seen that there is no significant difference between the results from these two turbulence models. In fact, the jet penetration length, l_p/d_j, (see Section 4.3.3 later for an extensive discussion) was estimated to be 20.55 from the *k*-*ε* model, and 20.48 with the RSM model. The simulation time on an Hewlett-Packard HP Z800 Workstation with Intel Xeon processor of 12 GB RAM and 3.47 GHz was 13 minutes for 2500 iterations using the standard *k*-*ε* turbulence model and 18 minutes 40 seconds for 2500 iterations for the RSM turbulence model. More importantly, the residuals for the standard *k*-*ε* turbulence model were 2×10^{-5}, whereas for the RSM turbulence model they were only 6×10^{-4}. It may also be mentioned that the rate at which the residuals decrease in case of the standard *k*-*ε* turbulence model were steeper as iteration progresses and hence more encouraging. Thus, the standard *k*-*ε* turbulence model was found to be a sufficient approximation without having to resort to the more elaborate RSM turbulence model. Hence, all calculations reported in this thesis were carried out with the standard *k*-*ε* turbulence model in conjunction with the standard wall-function approach (Launder and Spalding 1974) for near-wall treatment.

Though it was mentioned in Chapter 2 that advanced turbulence modelling like Large Eddy Simulation (LES) is required to resolve the unsteady large scale structures in counterflow jets, in the present thesis interest is only in the time-averaged mean flow field. Hence, the standard *k*-*ε* turbulence model is employed as discussed above, and also as will be seen in the subsequent sections the use of this model resulted in a good agreement with the available experimental data. Further, the eventual aim in this thesis is

to develop a methodology to generate a target non-uniform total pressure field and the use of RANS approach should not impede with the development of this methodology.

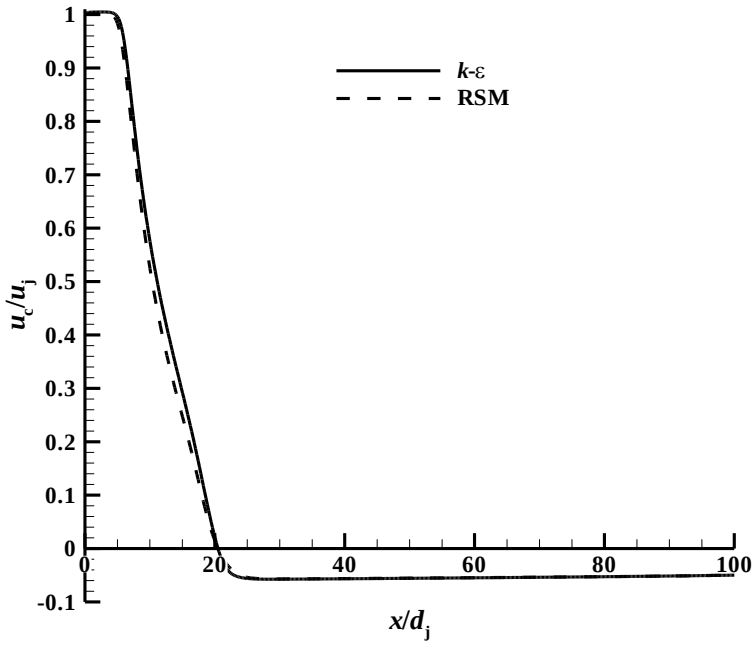

Figure 4.2 Decay of axial velocity along the jet centreline using the standard *k-ε* and RSM turbulence models; $D_0/d_j = 10$; $u_j/u_0 = 20$.

An axisymmetric structured grid was devised for the computations. The computational domain for the numerical solution consisted of 1000 axial × 25 radial (axis to wall) cells for $D_0/d_j = 3$; 1000 × 45 for $D_0/d_j = 5$; 1000 × 95 for $D_0/d_j = 10$; 1000 × 145 for $D_0/d_j = 15$; 1000 × 325 for $D_0/d_j = 30$; and 5200 × 510 for $D_0/d_j = 100$. The number of computational cells was chosen after a careful grid independence study. This study was conducted for the $D_0/d_j = 10$, $u_j/u_0 = 20$ case with 52,000 (coarse grid), 95,000 (medium grid) and also with 150,000 (fine grid) grid points. The decay of axial velocity along the jet centreline and also the axial velocity at one streamwise location, $x/d_j = 10$, are shown in Figures 4.3(a) and (b), respectively, for these three grids. It can be seen that a significant difference in the results between these grids are not seen.

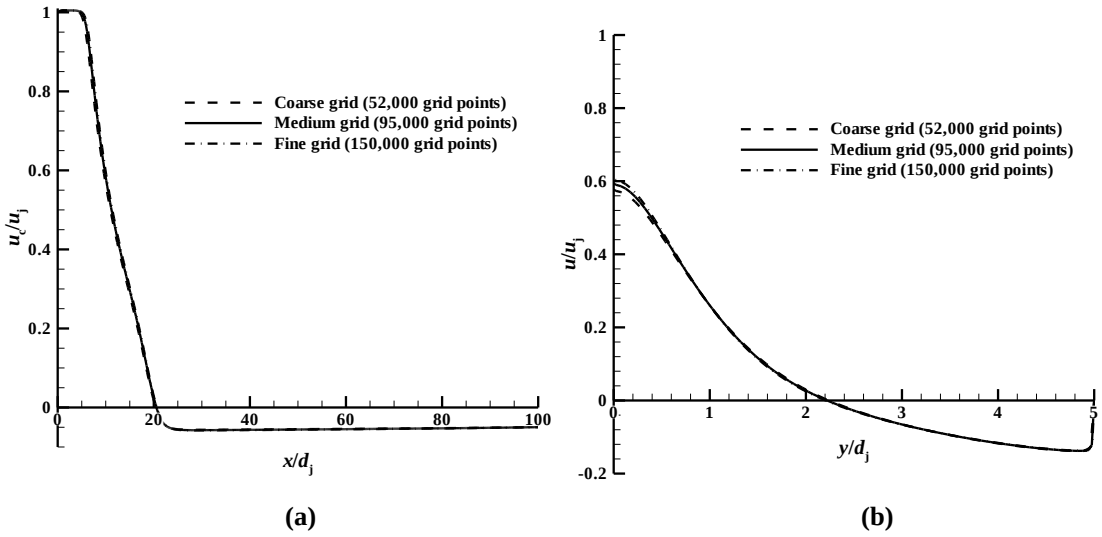

Figure 4.3 (a) Decay of axial velocity along the jet centreline and (b) axial velocity at one streamwise location, x/d_j = 10, for D_0/d_j = 10; u_j/u_0 = 20.

Further, the Grid Convergence Index (see Celik *et al*. 2008) was calculated and the numerical uncertainty in the calculation of jet penetration length in terms of the discretization error was 0.99 % and 1.45 % for the fine and medium grids, respectively. The apparent order of the numerical method was calculated to be about 1.65. Since the medium grid had a reasonably low value of discretization error it was employed and grids for the other cases were constructed with similar grid spacing, particularly in the jet penetration region, thus ensuring an acceptably low discretization error.

The convergence of the residuals of the various parameters was set to 10^{-7}. The convergence history of the residuals for each of the conserved variables for a typical flow case, D_0/d_j = 10; u_j/u_0 = 20, is shown in Figure 4.4(a). Also, the jet penetration length, l_p/d_j, was calculated at intermediate levels of convergence and the results are plotted in Figure 3(b). It is noted that the jet length does not vary below a convergence level of 10^{-5}. However, the calculations were continued till a convergence level of 10^{-7} to verify this convergence. Based on these observations the convergence level in all the following computations was maintained to be at least 10^{-5}.

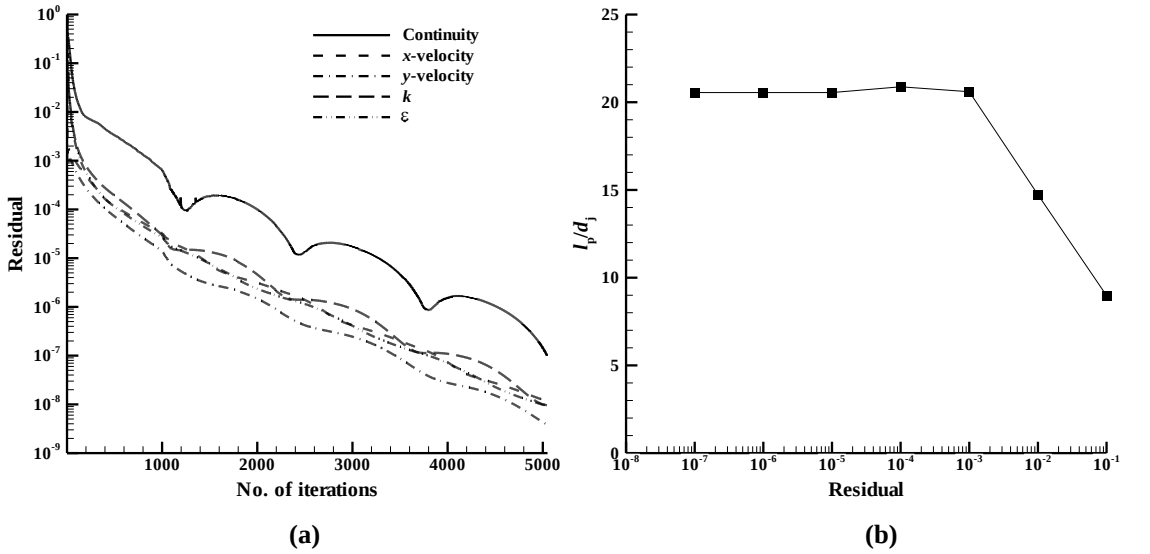

Figure 4.4 (a) Convergence history of residuals of the conserved variables and (b) jet penetration length at various levels of convergence, for $D_0/d_j = 10$; $u_j/u_0 = 20$.

All calculations were carried out in double-precision arithmetic. The simulation time on the HP Z800 Workstation was 3 minutes 50 seconds for 1000 iterations using single-precision arithmetic and 5 minutes 05 seconds for 1000 iterations using double-precision arithmetic. However, while using single-precision arithmetic, the residuals for the continuity equation do not drop below about 7×10^{-4} even up to 10,000 iterations. But while using double-precision arithmetic the residuals drop off to 10^{-7} in about 5000 iterations (see Figure 4.4(a)). Hence, the subsequent calculations were all carried out in double-precision arithmetic.

The Reynolds number (*Re*) of the counterflow stream (based on D_0 and u_0) varied from 10^4 to 3×10^5 and that of the jet (based on d_j and u_j) varied from 6×10^3 to 6×10^4. The values of Reynolds number used in the present computations meet the requirements stipulated by Morgan *et al*. (1976) for results being independent of Reynolds number. Some select calculations also verified that the present results were independent of the Reynolds number.

4.3 Results and Discussion

4.3.1 Velocity Field

The mean streamlines in the flow field are shown in the top half of Figure 4.5, for a diameter ratio of 10 and a velocity ratio of 20. The jet originating from the nozzle and penetrating into the counterflow stream can be clearly seen. The flow field is dominated by a large recirculation region as observed in this figure. The flow field can be reckoned into three parts different from those shown in Figure 4.1. There is a toroidal shaped eddy in the jet region. The flow from the jet penetrates this eddy, wraps around and returns backwards. The counterflow stream is distinct from the jet flow, the two streams being separated by a dividing stream surface. The counterflow stream does not come in contact with this eddy. This picture is for a steady flow and in turbulent flows mixing, of course, takes place. The profiles of axial velocity in the radial direction at various locations are shown in the bottom half of Figure 4.5.

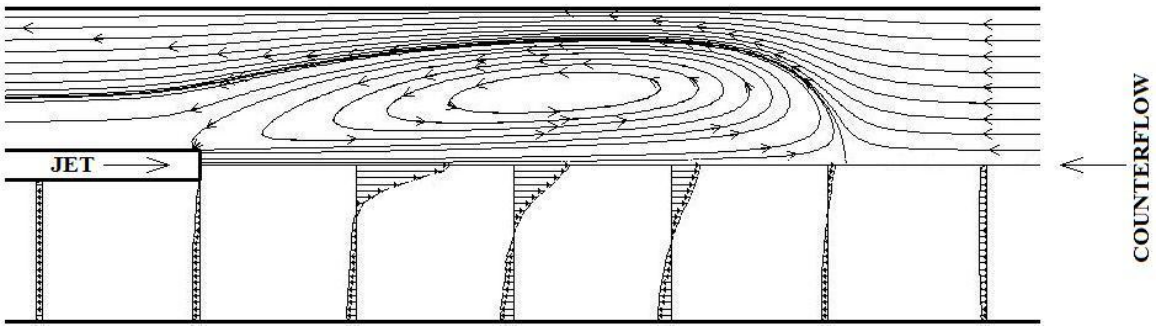

Figure 4.5 Streamlines in the flow field are shown in the top half of this figure. The profiles of axial velocity in the radial direction at various locations are shown in the bottom half; D_0/d_j = 10 and u_j/u_0 = 20.

The radial distribution of axial velocity in the jet at various streamwise locations can be plotted using the self-similarity hypothesis. Beltaos and Rajaratnam (1973) gave the following expression for the self-similarity of the velocity profiles in the jet in unconfined counterflow estimated from a potential flow solution of a point source in a uniform stream

$$\frac{u-u_0}{u_c-u_0}=\left[1+0.59\left(\frac{y}{b}\right)^2\right]^{-3/2}. \qquad (4.5)$$

In the above relation the local excess velocity ($u - u_0$) is normalised by the excess velocity at the jet centreline ($u_c - u_0$); the radial coordinate is normalised by the local jet width b. The jet width is defined as the radial distance where the local excess velocity equals one-half of the centreline excess velocity. It is to be noted that self-similarity of velocity profiles may be expected and also it is found only in region 2 (see Figure 4.1).

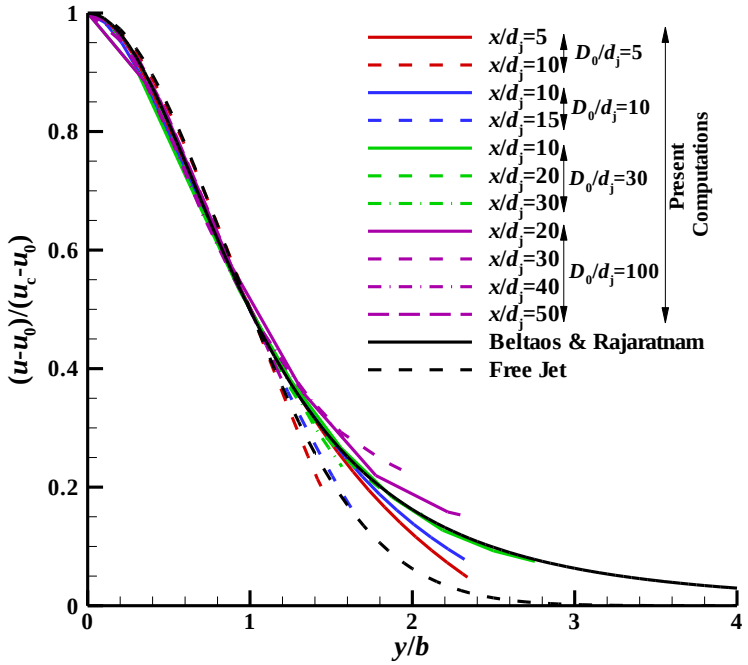

Figure 4.6 Self-similarity of axial velocity profiles at several streamwise locations. The velocity ratio u_j/u_0=20 for all diameter ratios. The empirical expression of Beltaos and Rajaratnam (1973) for unconfined counterflow jet and the velocity distribution for a free circular jet are also plotted for comparison.

The velocity profiles at several axial locations from the computational analysis are plotted in Figure 4.6 for different diameter ratios for a velocity ratio of 20. The analytical curve is valid for infinite counterflow and the computational results in fact compare well for the highest diameter ratio of 100 considered here.

The velocity distribution in a circular jet issuing into stagnant ambient air calculated by Tollmien (see Abramovich 1963 for details) is also plotted in Figure 4.6 for reference. The velocity distribution compares well with that of a free jet near the axis till about y/b is unity. The inner region near the axis of the jet is free from the influence of the counterflow and behaves much like a free jet. Away from the jet axis the counterflow influences the jet and departure from the free jet behaviour is observed. It is clear that the jet in counterflow spreads faster than a jet in quiescent ambient.

4.3.2 Potential Core

The potential core of the jet is the region immediately close to the nozzle where the velocity is uniform and equal to u_j. The potential core persists downstream a few nozzle diameters. It is indicated as region 1 in Figure 4.1 and it is a right circular cone with the nozzle exit as the base and its apex located on the jet axis.

The length of the potential core for a circular jet issuing into quiescent ambient is about 6.2 d_j (Or, Lam, and Liu 2011) and is independent of the jet velocity. However, the length of this potential core is reduced in a jet in counterflow configuration because the jet is "compressed" by the counterflow (Chan and Lam 1998). They proposed that this length is,

$$l_c \propto \frac{u_j - u_0}{u_j + u_0} \tag{4.6}$$

with the constant of proportionality equal to 6.2. Though they did not present experimental data to verify this relationship, Bernero (2000) suggested that the constant of proportionality is 5 based on his experiments.

The potential core length calculated from the present computational analysis is plotted in Figure 4.7. This length is predicted to be smaller than the unconfined case and for high diameter ratios and high velocity ratios it remains constant at about 4.8 d_j. When calculated as a fraction of the jet penetration length (described in detail in the next

section) it is seen that the potential core occupies a considerable proportion of the jet length for low diameter ratios at all velocity ratios. But as the diameter ratio increases the potential core prevails for less than 20% of the jet length for high velocity ratios.

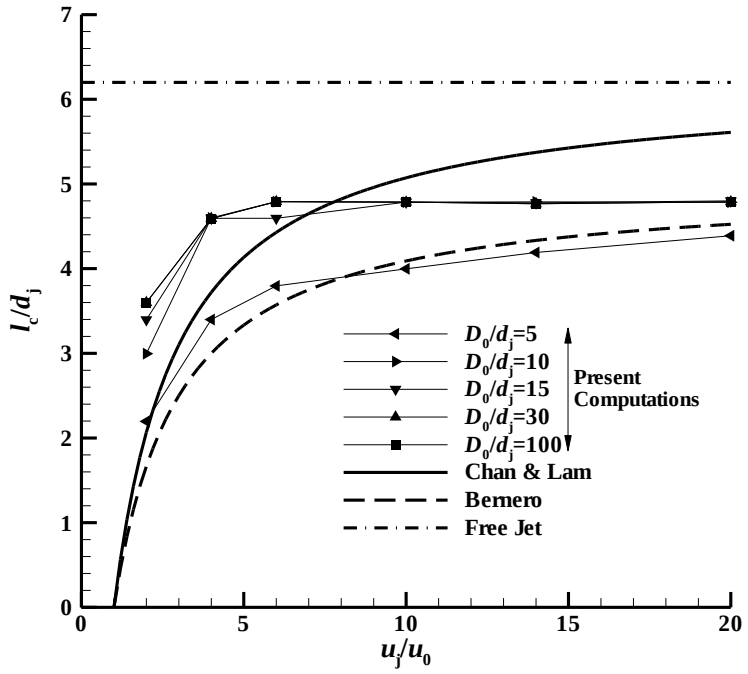

Figure 4.7 Potential core length of the jet; this length modelled by Chan and Lam (1998) and Bernero (2000) for unconfined counterflow is shown for comparison. The potential core length is constant for a round jet and is shown by a dashed straight line.

4.3.3 Jet Penetration Length

The jet penetration length, l_p, is defined as the length of the jet from the nozzle exit to a point on the axis where the axial velocity becomes zero. The penetration length depends on the jet-to-counterflow velocity ratio, u_j/u_0, and on the duct-to-jet diameter ratio, D_0/d_j. Thus in the non-dimensional form

$$\frac{l_p}{d_j} = f\left(\frac{u_j}{u_0}, \frac{d_j}{D_0}\right) \quad . \tag{4.7}$$

For an unconfined counterflow case this relation reduces to

$$\frac{l_p}{d_j} = f\left(\frac{u_j}{u_0}\right) \quad . \tag{4.8}$$

It is possible to evaluate this functional form from dimensional analysis itself by taking jet momentum as a parameter. This leads to a linear relation (see also Arendt *et al*. 1956, and Beltaos and Rajaratnam 1973)

$$\frac{l_p}{d_j} = c' \frac{u_j}{u_0}. \tag{4.9}$$

The value of the linearity constant *c* is quoted by various investigators (Arendt *et al*. 1956, Beltaos and Rajaratnam 1973, Morgan *et al*. 1976, Yoda and Fiedler 1996, Chan and Lam 1998, Bernero 2000) to be in the range from 2.4 to 2.9. Several factors might have contributed for this variation in *c'*. Some of them are, (i) different boundary conditions at the jet exit and the counterflow stream inlet, (ii) different values of turbulence intensity in the two streams and (iii) influence of the confining duct for larger values of u_j/u_0. It may be noted, however, that the variation in *c* is not substantial.

To allow a direct comparison of the jet penetration length from the present computational results with available experimental data several computations were carried out for the diameter ratios employed in Morgan *et al*. (1976). The results are shown in Figure 4.8. A reasonably good agreement with the experimental data was observed.

The presence of the external bounding walls causes departure from the linear jet penetration length – velocity ratio relation. In fact, the effect of confinement is to reduce the penetration length of the jet compared to the unconfined case. This behaviour can also be seen in Sekundov (1969), Majumdar and Bhaduri (1981), Bernero (2000) and Saghravani and Ramamurthy (2010).

The penetration length evaluated from the present computations with the diameter ratios mentioned earlier is shown in Figure 4.9(a).

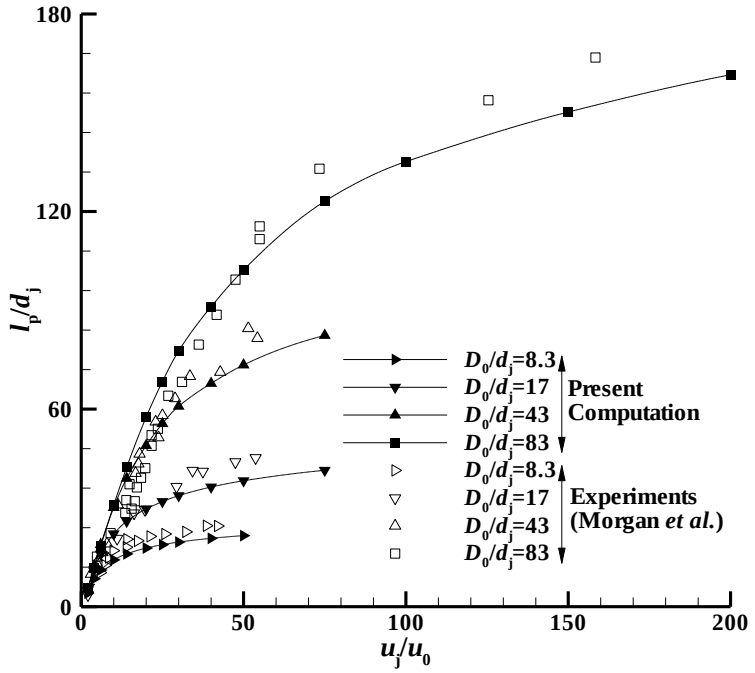

Figure 4.8 Jet penetration length estimated from the present computations compared with the experiments of Morgan *et al*. (1976).

A remarkable collapse of the penetration length data was achieved in Morgan *et al*. (1976) by plotting l_p/D_0 as a function of jet-to-counterflow momentum flux ratio. This ratio is

$$Z = \left(\frac{u_j \, d_j}{u_0 \, D_0} \right)^2 , \tag{4.10}$$

since density, ρ, is constant. From their experimental results they divided the flow into two distinct regimes based on the momentum flux ratio; see Figure 4.10(a). When the counterflow momentum flux is high compared to the jet momentum flux ($\sqrt{Z} < 0.5$) the penetration length is linearly related to the velocity ratio.

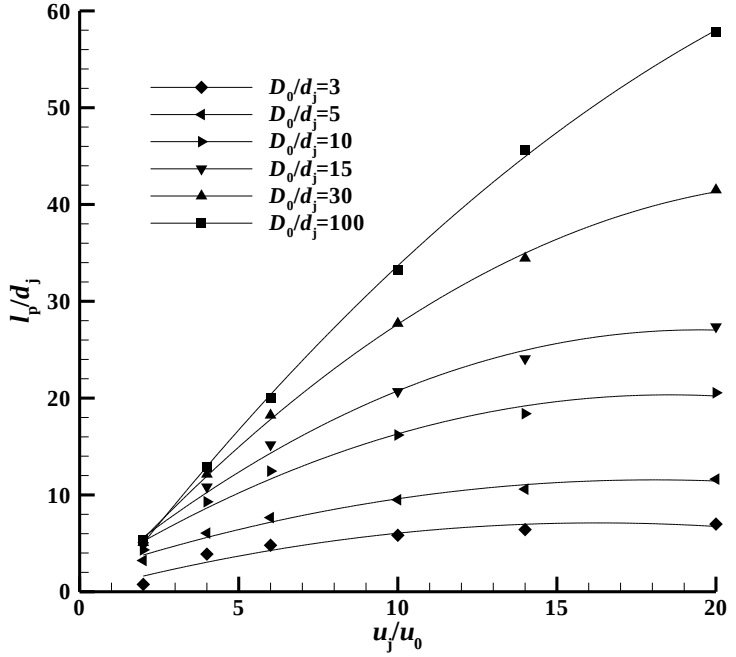

(a)

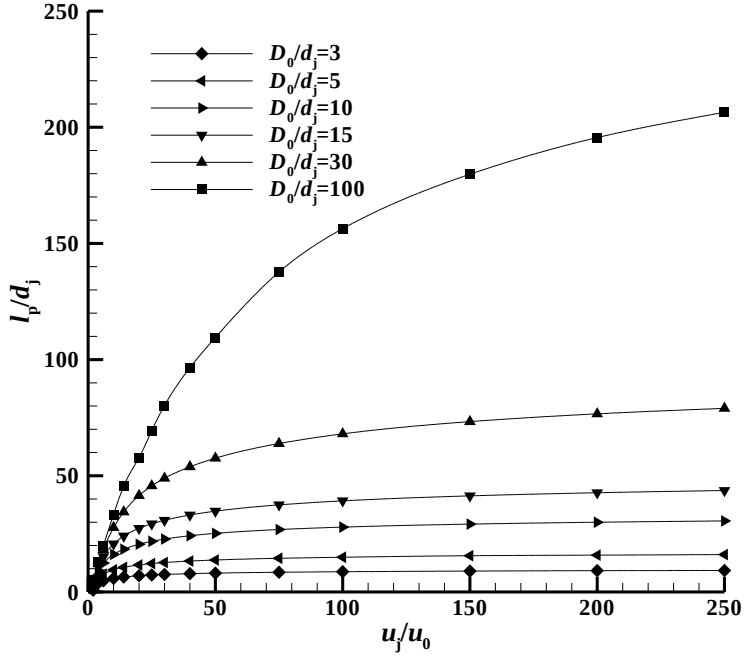

(b)

Figure 4.9 Jet penetration length. (a) Initial computational results (b) subsequent computational results for extended values of u_j/u_0.

This relationship is of the form

$$\frac{l_p}{D_0} = 2.9\left(\frac{u_j\, d_j}{u_0\, D_0}\right), \tag{4.11}$$

which reduces back to the earlier form

$$\frac{l_p}{d_j} = 2.9\,\frac{u_j}{u_0} \tag{4.12}$$

for the unconfined case given by equation (4.9). The linearity constant, *c*, is chosen here to be 2.9 as against 2.5 suggested in Morgan *et al*. (1976). It may be noted that as the jet length increases the effect of confinement is felt which reduces the value of this constant *c*. Hence the data either experimental or computational for large values of velocity ratios is likely to under-predict this constant. This may partly explain a lower value for this constant in Morgan *et al*. (1976).

As the value of *Z* increases further, the influence of confinement becomes effective for a range of

$$0.5 < \sqrt{Z} < 1.5. \tag{4.13}$$

Morgan *et al*. (1976) identify this to be a transitional zone and for $\sqrt{Z} > 1.5$ suggest a one-third power law, and then the penetration length is given by

$$\frac{l_p}{D_0} = 1.8\left(\frac{u_j\, d_j}{u_0\, D_0}\right)^{1/3}. \tag{4.14}$$

The authors did not provide any explanation as to why data should collapse so neatly with the modified coordinates and also to such a simple relation for the confined case with $\sqrt{Z} > 1.5$. The two regimes of Morgan *et al*. (1976) were also reiterated by one of these authors elsewhere (Brinkworth 1999). In the present study, first a dimensional analysis is carried out using jet momentum flux, counterflow stream velocity u_0 and the diameters D_0 and d_j which leads to the relation

$$\frac{l_p}{D_0} = f\left(\frac{u_j\, d_j}{u_0\, D_0}\right) . \qquad (4.15)$$

This explains the data collapse as first indicated in Morgan *et al*. (1976). However, the present observations made in the present study differ qualitatively from those in Morgan *et al*. (1976).

Also shown in Figure 4.10(a) is the criterion for the jet expanding in counterflow of infinite extent. Sekundov (1969) indicated that the flow field may be considered to be unconfined if $D_0/l_p \geq 2$. This limit is shown in Figure 4.10(a) and the data points below this line are for unconfined flow.

As the effect of confinement increases the penetration length appears to follow the one-third power law beyond the transitional zone. However, a closer examination of the results in Figure 4.10(a) in the high jet momentum regime reveals that the agreement with the one-third power law is not satisfactory, particularly in the presence of significant confinement where the power appears to drop gradually to less than 1/3. This raised an important question as to whether, if at all, a power-law behaviour would govern the jet penetration length at high momentum ratios. The jet penetration length behaviour was investigated at very high momentum ratios; the velocity ratio was increased up to 250 which corresponded to a momentum flux ratio of about 7,000 for a diameter ratio of three.

The extended computational results are plotted in Figure 4.10(b). It is now clear that the one-third power law is not valid for high momentum flux ratios. More importantly, there is no distinct regime 2 unlike a clearly identified regime 1. The experiments of Morgan *et al*. (1976) had covered a momentum flux ratio up to about 25 and within this range they inferred the one-third power law approximating their experimental data.

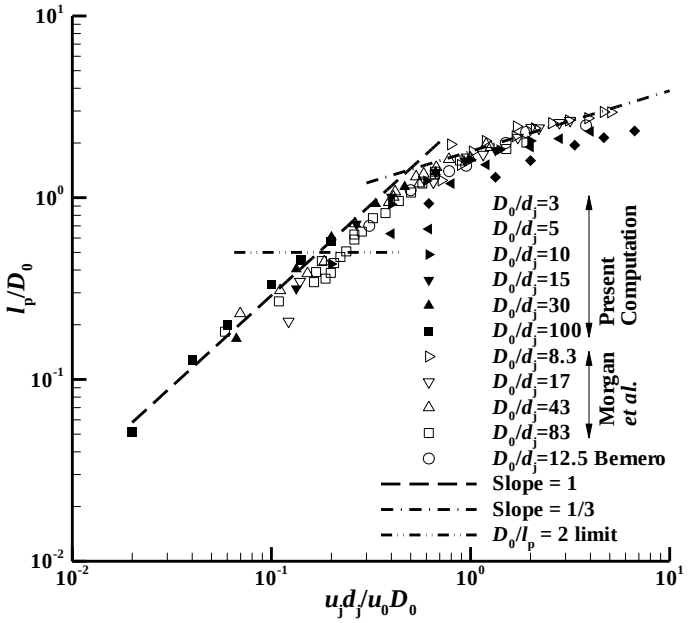

(a)

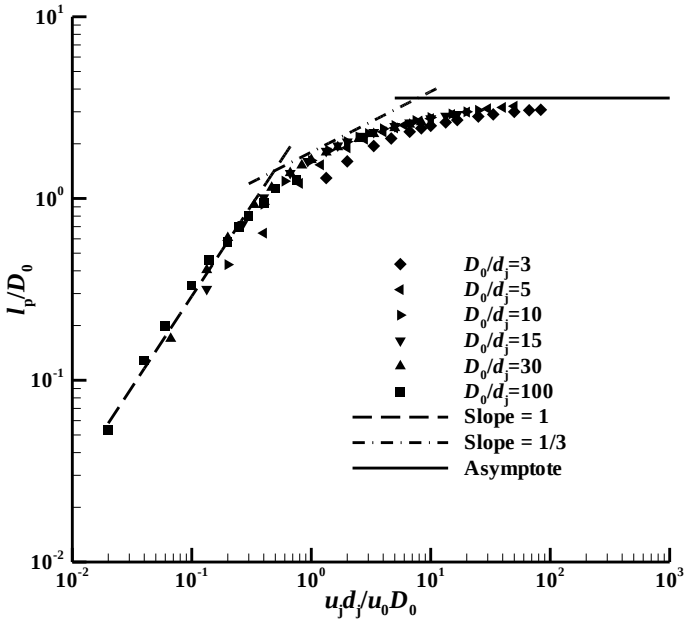

(b)

Figure 4.10 Jet penetration length as a function of the jet-to-counterflow momentum flux ratio parameter. (a) Initial computational results compared with the experimental data. (b) Extended computational results with the linear and one-third power law. The asymptotic limit for the jet penetration length of about 3.57 D_0 is also depicted.

However, as is evident from the present investigation the slope of this curve continuously decreases and asymptotically tends to zero. The asymptotic value for the maximum jet penetration length is estimated to be 3.57 times the diameter of the enclosing duct. This value was obtained by averaging the asymptotic limits for each of the D_0/d_j cases which were themselves estimated by extrapolating the present computational results.

The prediction from dimensional analysis for data collapse as seen from Eq. 4.10 has some scatter observed in Figure 4.10(b) for intermediate values of momentum flux ratios. This is because of the length of the potential core which is part of the jet penetration length. The potential core length is fairly constant (see Figure 4.7) and unaffected by the counterflow and its length is a substantial part of the penetration length. The potential core length was not part of the dimensional analysis made earlier and hence it is equivalent to another parameter being introduced in the problem leading to the scatter.

The fact that the jet penetration length does not increase indefinitely can be seen readily from Figure 4.9(b) where the jet length is plotted as a function of the velocity ratio. The curves for each of the diameter ratios considered do, indeed, tend to a constant value.

The existence of an asymptotic limit for the jet penetration length can also be explained referring to the mean streamline pattern in Figure 4.5. There is a toroidal shaped eddy in the jet region. The flow from the jet penetrates this eddy, wraps around and returns backwards. The counterflow stream is distinct from the jet flow, the two streams being separated by a dividing stream surface. The counterflow stream does not come in contact with this eddy. As the jet momentum flux increases the eddy length increases and the dividing stream surface is pushed forward. This forward force is proportional to the jet momentum and is independent of the penetration length l_p. The force on the dividing stream surface in the negative direction scales like $(u_0^2 d_e^2)$ as long

as the eddy diameter d_e is small compared to D_0. Since d_e grows with l_p the rate of growth of both these scales should slow down once d_e becomes comparable to D_0. Then the reverse jet flow and the counterflow stream have to pass through a narrower and longer annular region. The additional force in the negative direction scales like $(u_0 D_0^2 l_p / g^2)$, where g is the narrow gap $(D_0 - d_e)/2$. Because of this sharp increase, eventually it is not possible for the jet to push the eddy forward no matter how high the momentum. There is no such restriction in the unconfined case.

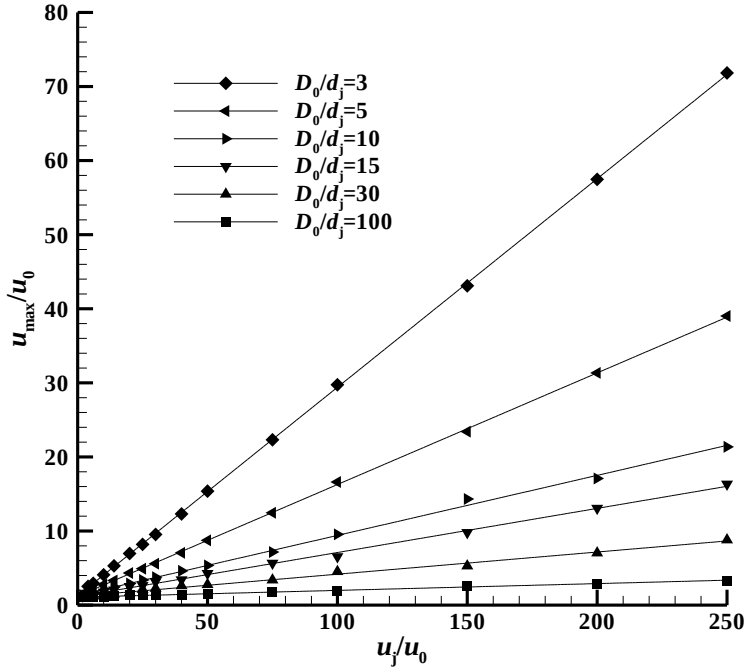

Figure 4.11 Maximum counterflow velocity in the neighbourhood of the jet, u_{max}, non-dimensionalised by the counterflow stream velocity u_0, is plotted for different u_j/u_0. It can be seen that this ratio grows linearly and indefinitely.

The counterflow stream passes through an annular converging – diverging geometry formed by the dividing stream surface. The pressure drop in the counterflow mainly occurs in the converging part but the minimum pressure value occurs slightly towards the downstream side of the throat (left side of the throat in Figure 4.5). The maximum velocity in this neighbourhood u_{max} non-dimensionalised by u_0 grows linearly in u_j/u_0 for all diameter ratios D_0/d_j as shown in Figure 4.11. This interesting observation

can be explained from the fact that a higher u_j results in a higher return flow and also higher velocity from counterflow due to a narrower gap thus leading to higher u_{max}/u_0 and hence the indefinite growth.

The data shown in Figure 4.11 can be represented by the following approximation:

$$\frac{u_{max}}{u_0} = 0.85\left(\frac{d_j}{D_0}\right)\left(\frac{u_j}{u_0}\right) + 1.2\,. \tag{4.16}$$

It is interesting to note that u_{max}/u_0 is linear in d_j/D_0 and u_j/u_0.

The observation of Morgan *et al*. (1976) that high momentum jets are sternly restrained by the counterflow stream and the confining duct is correct. The present results strengthen it further by qualifying that the restraining of the jet is to a finite penetration length no matter how high the jet momentum flux.

4.3.4 Jet Width

The jet width is the radial distance where the local excess velocity equals one-half the centreline excess velocity. Beltaos and Rajaratnam (1973) gave an empirical relation for the jet half-width *b* using dimensional arguments. Their expression was

$$\frac{b}{l_p} = 0.2\,\frac{x/l_p}{\sqrt{\left(\dfrac{2.24}{x/l_p}\right)^{2/3} - 1}}\,. \tag{4.17}$$

The experimental results compiled by Beltaos and Rajaratnam (1973) and the results of Lam and Chan (2002) closely follow this relation for unconfined counterflow.

The results from the present computational analysis for u_j/u_0 = 20 are shown in Figure 4.12 along with the empirical equation. It might be noted that at low diameter ratios the results do not compare well with the empirical expression. This is because of the effect of confinement of the duct. However, for large diameter ratios the

computational results do, in fact, tend towards the empirical relation for the unconfined case.

The jet spread rate is linear for a circular jet in stagnant ambient fluid as indicated by various measurements (see, for example, Panchapakesan and Lumley 1993 and Hussein *et al*. 1994); this spreading rate is also plotted in Figure 4.12. It is evident that the jet in counterflow grows faster than a free jet.

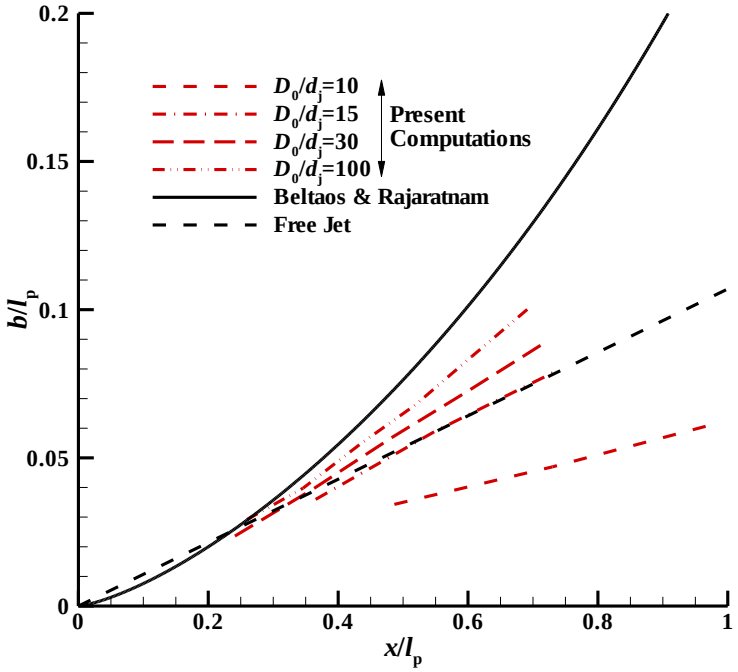

Figure 4.12 Growth of jet width along the jet; the expression of Beltaos and Rajaratnam (1973) for unconfined jet is shown by a continuous line. The jet width growth for a free jet is also plotted for comparison.

4.3.5 Jet Boundary and Stagnation Stream Surface

The jet boundary is the locus of points where the axial velocity becomes zero. The stagnation stream surface is considered to represent the radial extent of the mixing region and is the line along which the net momentum flux is zero. This stream surface should satisfy

$$\int_0^{r_s} 2\,\pi\, r\, u\, dr = 0\,. \qquad (4.18)$$

The stagnation stream surface has remained elusive because of the difficulty in determining it experimentally. Beltaos and Rajaratnam (1973) calculated the jet boundary and the stagnation stream surface from dimensional and semi-empirical arguments, whereas Bernero (2000) used the concentration distribution from flow visualisations to calculate the radial extent of the mixing region.

The maximum values of r_0/l_p and r_s/l_p from the present computations are plotted in Figures 4.13(a) and (b). As the diameter ratio increases the computational results tend towards the values of 0.18 l_p and 0.3 l_p, respectively derived in Beltaos and Rajaratnam (1973). However, the maximum width of the jet boundary and stagnation stream surface occur at approximately 70 % and 65 % of the penetration length, respectively, as against the corresponding 77 % and 75 % obtained by Beltaos and Rajaratnam (1973).

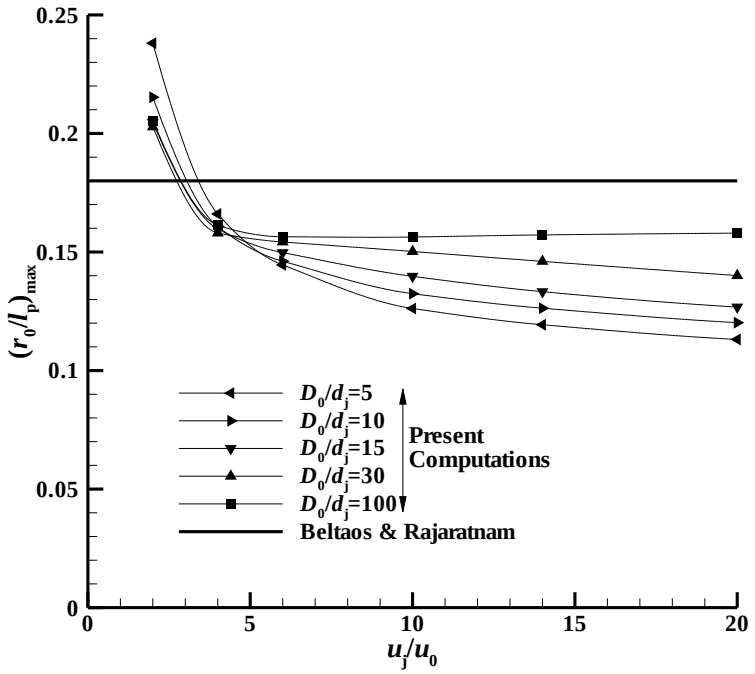

(a)

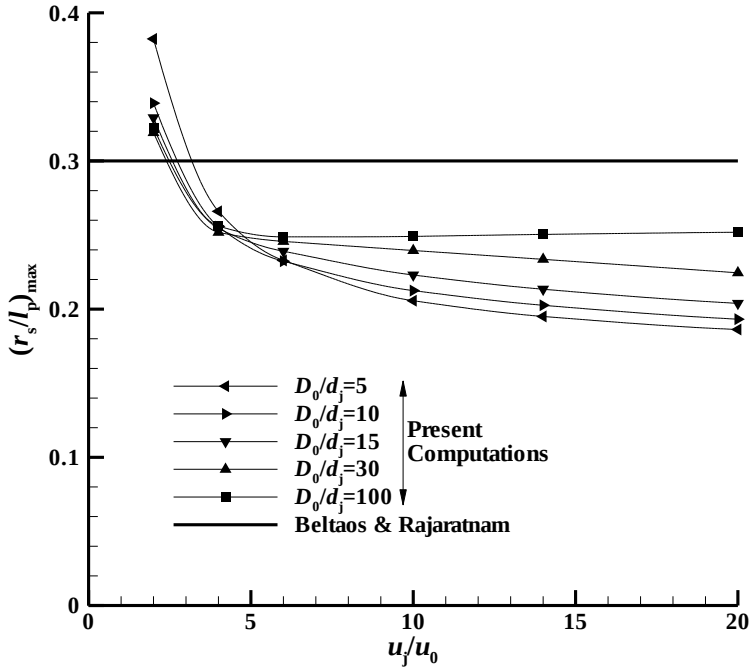

(b)

Figure 4.13 Maximum width of the (a) dividing and (b) stagnation streamlines. The maximum widths are compared with the values of Beltaos and Rajaratnam (1973) for unconfined counterflow.

4.3.6 Centreline Velocity Decay

The mean velocity variation with axial distance along the jet centreline for a round jet in ambient medium is given by (see, for example, Pope 2000)

$$\frac{u_c}{u_j} = \frac{B}{x/d_j} \tag{4.19}$$

where B is an empirically determined velocity-decay constant. Panchapakesan and Lumley (1993) obtained the decay constant as 6.06 and Hussein *et al*. (1994) as 5.8 and 5.9 from LDA and hot-wire measurements, respectively.

The centreline velocity decay along the jet in counterflow is very much alike the jet in still medium in region 2 (see Figure 4.1) but with a different constant B. A drastic change from the free jet behaviour is observed in region 3 where the jet and the counterflow interaction are intense. Beltaos and Rajaratnam (1973) postulated a simple

decay curve and assumed a decay constant value of 5.83. Yoda and Fiedler (1996) modelled this flow superimposing a turbulent jet and uniform counterflow using the same decay constant of Beltaos and Rajaratnam (1973).

Chan and Lam (1998) proposed a more comprehensive analytical model supported by their experimental observations. They hypothesised that the potential core of the jet in counterflow is reduced and the jet flow field is advected backwards by the counterflow. The centreline velocity is determined from

$$u_{\mathbf{c}} = \frac{u_{\mathbf{j}}\, l_{\mathbf{c}}}{x^*} + u_0 \log\left(\frac{u_{\mathbf{j}}\, l_{\mathbf{c}}}{x^*} - u_0\right) - u_0 \log\left(u_{\mathbf{j}} - u_0\right) \quad ; \quad x^* > l_{\mathbf{c}}. \tag{4.20}$$

The axial coordinate x should start from an origin shifted by a distance d_{v}, which is given as, $d_{\mathbf{v}} = \frac{u_0}{u_0 + u_j} 6.2\, d_{\mathbf{j}}$. (The length of the potential core of the jet in stagnant ambient medium is 6.2 d_{j}). Now, $x^* = x + d_{\mathrm{v}}$. The potential core length for a jet in counterflow l_{c} is given by, $l_{\mathbf{c}} = 6.2\, d_{\mathbf{j}} \frac{u_{\mathbf{j}}}{u_{\mathbf{j}} + u_0}$.

Bernero (2000) extended Yoda and Fiedler's (1996) idea of superimposing a turbulent jet and uniform counterflow and suggested the following model

$$\left(\frac{u_{\mathbf{c}} - u_0}{u_{\mathbf{j}}}\right)\frac{l_{\mathbf{p}}}{d_{\mathbf{j}}} = \left(\frac{c}{2}\right)\frac{1 + \sqrt{1 - x/l_{\mathbf{p}}}}{x/l_{\mathbf{p}}}. \tag{4.21}$$

He too assumed c = 5.83 as suggested by Beltaos and Rajaratnam (1973).

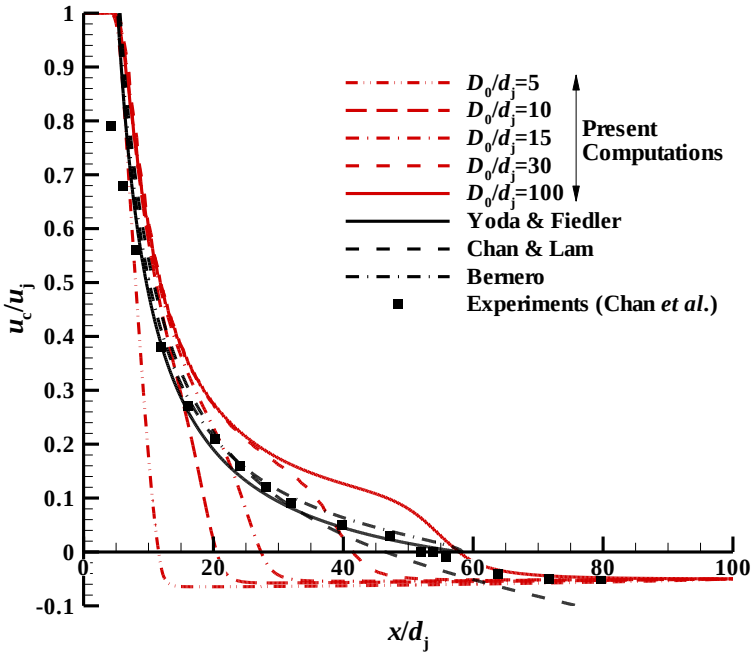

Figure 4.14 Decay of axial velocity along the jet centreline from present computations plotted for all diameter ratios. The analytical models of Yoda and Fiedler (1996), Chan and Lam (1998), Bernero (2000) and the experiments of Chan *et al.* (1999) for unconfined counterflow are plotted for comparison. u_j/u_0=20 for all cases.

The results from the present computational analysis are indicated in Figure 4.14 along with the various models described in the previous paragraphs. The effect of the confining duct is obviously seen in this figure. Yet again, good comparison is obtained at large diameter ratios.

The discrepancy between the present computation and experiments may be due to the extreme difficulty in both modelling and measuring the flow field interaction between the jet and the counterflow beginning at approximately 70% of the penetration length. Moreover, these models do not account for the effect of flow confinement.

An alternative scale proposed by Beltaos and Rajaratnam (1973) is also useful in representing the centreline velocity decay data presented in Figure 4.14. The centreline

excess velocity ($u_c - u_0$) normalised by u_j and multiplied by the non-dimensional penetration length (l_p/d_j) is chosen as the ordinate. The relation is,

$$\left(\frac{u_c - u_0}{u_j}\right)\frac{l_p}{d_j} = \frac{5.83}{x/l_p} \text{ for } x/l_p \le 0.7 \text{, and}$$

$$\left(\frac{u_c - u_0}{u_j}\right)\frac{l_p}{d_j} = \frac{0.104}{\left[\left(\frac{x/l_p - 0.8}{l_p}\right)\right]^2} \text{ for } x/l_p \ge 1. \qquad (4.22)$$

They indicated a smooth curve should join these two regimes.

The results are shown in Figure 4.15. Apart from helping the centreline velocity decay curves for different diameter ratios collapse into single curve, the choice of these scales also serves to introduce a useful working model for the velocity decay for a jet in confined counterflow for the entire range of diameter ratios from the present computational results.

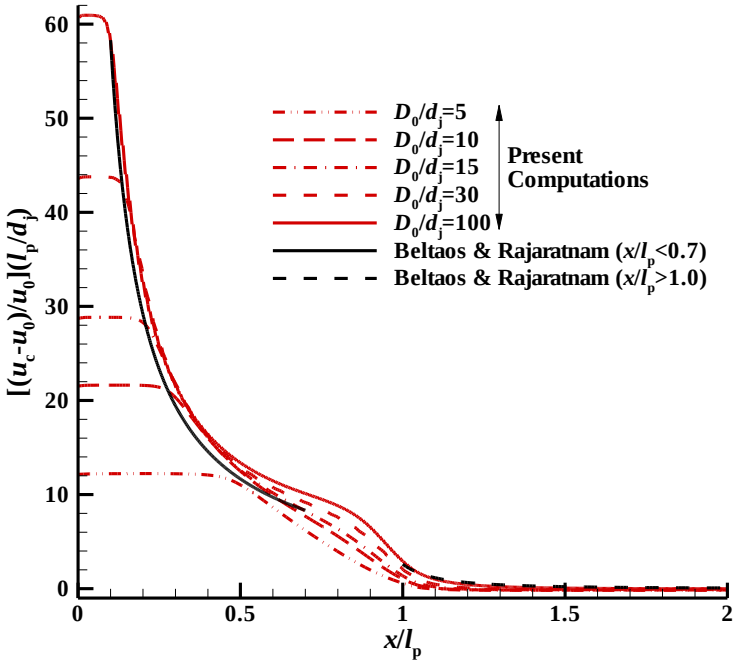

Figure 4.15 Decay of axial velocity along the jet centreline plotted using the scaling arguments suggested by Beltaos and Rajaratnam (1973); u_j/u_0=20.

Further insight into the centreline velocity decay can be gained by resorting to a logarithmic plot. Such a plot would be useful in investigating any power law behaviour they may obey. In Figure 4.16 the centreline velocity decay for different velocity ratios at a constant diameter ratio of 10 from the computational results are plotted. Also in the same figure the centreline mean velocity decay for a free jet is plotted.

From this figure it is immediately obvious that no constant decay exponent can be assigned. The rate of decay is quite rapid for small velocity ratio and decreases with increasing velocity ratio. In fact, for high velocity ratios the decay rate in region 2 approximately complies with the decay rate for a free jet. Finally it should be noted that the centreline velocity decay is faster than a free jet for all velocity ratios.

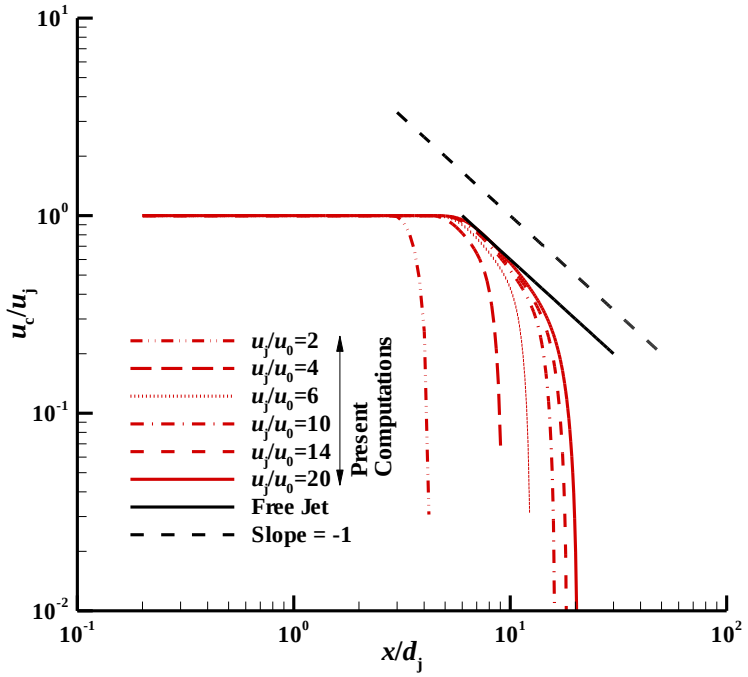

Figure 4.16 Decay of axial velocity along the jet centreline D_0/d_j = 10. Plotted on alogarithmic scale a x^{-1} variation is observed in region 2 of the jet.

4.3.7 Entrainment

The mass flow rate in the jet at any axial station normal to the jet axis is given by

$$m = \int_0^{r_0} 2\,\pi\,\rho\,u\,r\,dr\,, \qquad (4.23)$$

and that from the nozzle is denoted by m_0. The mass flow rate increases with axial distance from the nozzle because the fluid from the surrounding ambient medium is entrained into the jet.

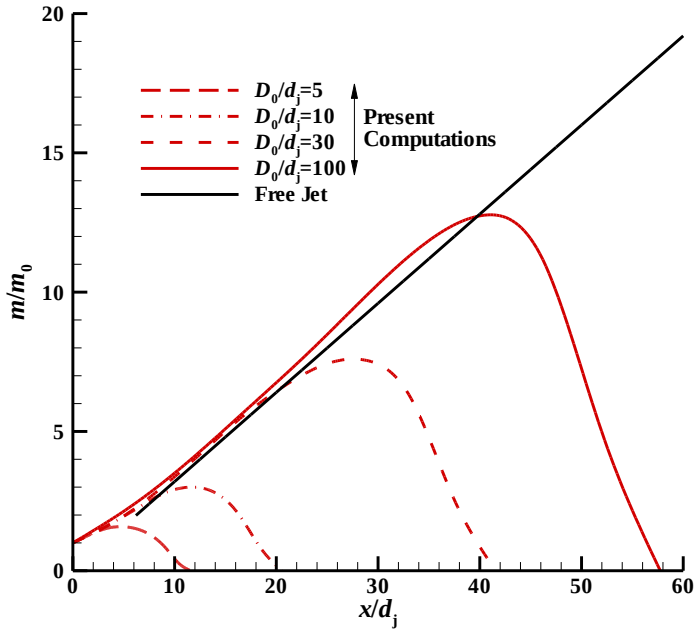

Figure 4.17 Entrainment rate for a jet in confined counterflow for all diameter ratios; u_j/u_0=20. The entrainment rate for free jet from Ricou and Spalding (1961) is also plotted.

The entrainment rates for the jet in counterflow configuration were calculated from the computational results and are presented in Figure 4.17 together with the entrainment rate for a free circular jet given by Ricou and Spalding (1961). It can be seen that the mass flow rate of the jet increases with distance from the nozzle entraining the ambient counterflowing stream. The entrainment rate reaches a maximum at about 70% penetration length beyond which it decreases in region 3. The presence of the external

bounding wall impedes the entrainment rate and as the diameter ratio increases the jet length increases and more mass flow is entrained into the jet.

It is also clear that the entrainment rate of a jet in counterflow stream upto about 0.7 l_p is identical to the circular jet entrainment rate. This is particularly intersesting, because, in spite of the the fact that the jet has entrained the counterflow fluid which has negative momentum its entrainment rate is same as that for a jet in free ambient.

From the classical theory of jets it is known that the momentum flux is conserved in the axial direction (Schlichting 1979). But, it is now well known that the axial momentum is not conserved (see, for example, Schneider 1985), rather diminishes (though slowly) in the streamwise direction. The momentum remaining invariant is a consequence of assuming the axial pressure gradient to be zero. For the free jet case, in general, a weak pressure gradient exists in the axial direction because of the entrainment of the surrounding fluid. And, for jets in streams with pressure gradients the momentum flux cannot be assumed constant.

With a jet issuing into a counterflow the momentum flux increases in the axial direction. The momentum flux in the jet at any axial station normal to the jet axis is given by

$$M = \int_0^{r_0} 2\,\pi\,\rho\,u^2\,r\,dr \tag{4.24}$$

and that at the jet exit is denoted by M_0. The calculated rates of momentum increase are shown in Figure 4.18. The momentum flux increases in the streamwise direction till about 0.7 l_p after which it reduces.

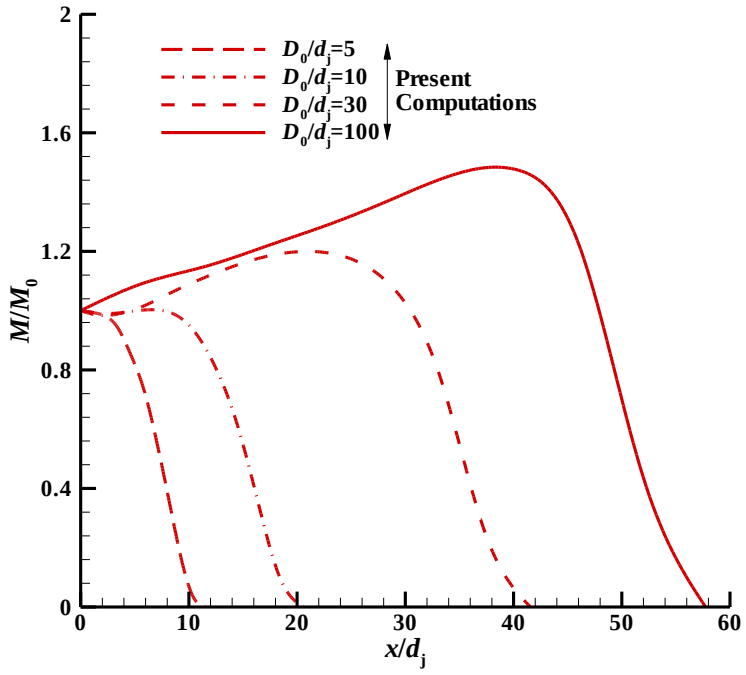

Figure 4.18 Momentum flux variation along the jet centreline; u_j/u_0=20.

4.3.8 Wall Pressure Distribution

The pressure distribution on the external confining walls would indicate the jet interaction with the wall and can show the effect of containment of the bounding walls. A coefficient of pressure was defined as,

$$c_p = \frac{p_w - p_j}{\frac{1}{2}\rho u_j^2} \tag{4.25}$$

where, p_w is the wall static pressure, and p_j is the jet exit pressure. This pressure coefficient is plotted in Figure 4.19 for various diameter ratios in the region close to the jet where the pressure variation can be the most revealing.

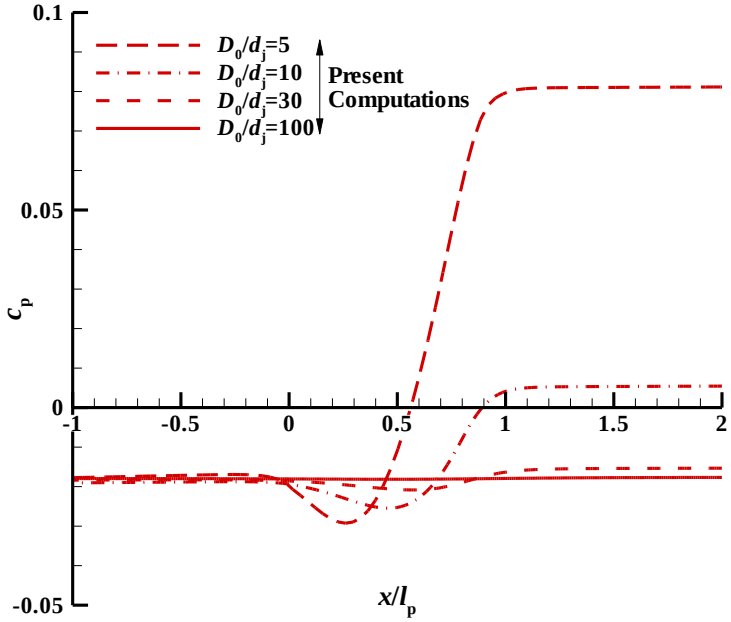

Figure 4.19 Wall pressure distribution in the region close to the jet; u_j/u_0=20.

It is evident that at the low diameter ratios the jet in fact interacts with the wall causing the wall pressure to drop drastically. The pressure variation near the jet nozzle is due to the decrease in area because of the presence of the jet tube. The wall confinement has a significant effect on the flow field in the jet and in the duct close to the jet as illustrated in various instances in this chapter. As is obvious the wall pressure distribution is essentially invariant at the highest diameter ratio implying the wall has no effect on the flow field.

4.3.9 Total Pressure Loss

The loss in total pressure due to the jet mixing with the counterflow stream was quantified by a non-dimensional total pressure loss coefficient, which is defined as

$$c_{p0} = \frac{p_{t,0} - p_{t,e}}{\frac{1}{2}\rho u_j^2} \tag{4.26}$$

where $p_{t,0}$ and $p_{t,e}$ are the total pressures at the inlet and exit of the duct, respectively.

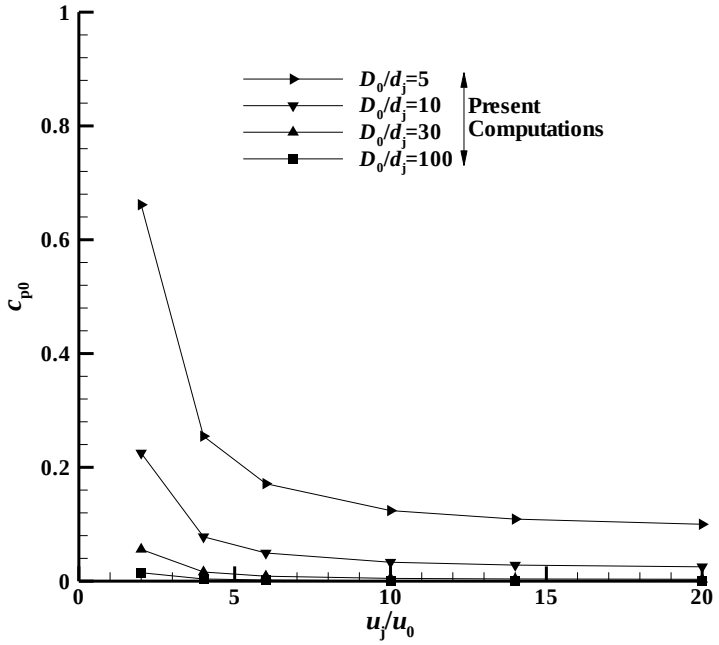

Figure 4.20 Total pressure loss coefficient for all velocity ratios and diameter ratios.

The loss coefficients evaluated from the computations are shown in Figure 4.20. The total pressure loss is high at low diameter ratios and at large diameter ratios the total pressure loss is very meagre, only a few percent of the inlet dynamic head.

4.3.10 Centreline Turbulence Intensity

The turbulence intensity is a measure of the turbulent velocity fluctuations and is defined as the ratio of the root-mean-square of the velocity fluctuation to mean flow velocity

$$I = \frac{u'}{u_{avg}}. \tag{4.27}$$

The turbulence intensity at the jet exit and the counterflow stream inlet was input to the computations. The turbulent kinetic energy, *k*, is calculated as

$$k = \frac{3}{2}\left(u_{avg} I\right)^2. \tag{4.28}$$

For the present calculations u_{avg} is the mean axial velocity at the jet exit and the counterflow stream inlet.

The variation of turbulence intensity along centreline is plotted in Figure 4.21 for various diameter ratios. It is observed that two distinct peaks appear; they are also found to be independent of the velocity ratio. This behaviour was also reported in the computations of Elghobashi *et al*. (1981) and was observed in the experiments of Tsunoda and Saruta (2003). The first peak is associated with the basic instability of the jet at the end of the potential core and the second peak near the maximum penetration length is due to the backward deflection of the jet by the opposing counterflow resulting in intense turbulent activity. This second peak is a peculiar characteristic of this particular flow configuration. After the second peak the turbulence intensity decays to the counterflow free stream turbulence level.

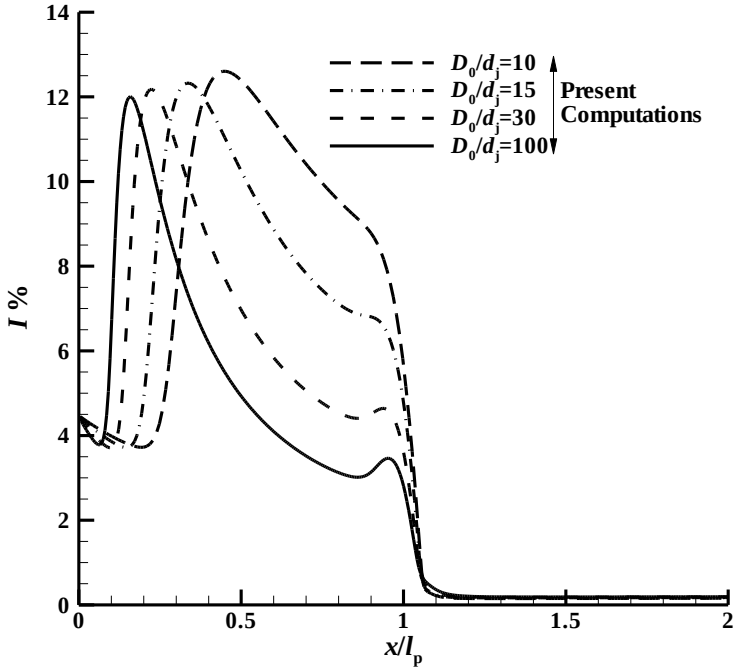

Figure 4.21 Turbulence intensity along the jet centreline; u_j/u_0=20.

4.4 Summary

An incompressible turbulent jet issuing into a uniform confined counterflow stream was computationally investigated. A series of parametric numerical studies was carried out for different annular-to-jet diameter ratios and various jet-to-counterflow velocity ratios. It was observed that the jet in confined counterflow behaves differently from the jet in infinite counterflow. The jet penetration length and the half-width of the jet are reduced and a linear relationship between the velocity ratio and penetration length ceases to be valid. The computed centreline velocity decay compares well with the analytical model for the highest diameter ratio. The peculiar two peaks in the computed centreline turbulence intensity are also consistent with experimental observations from the literature.

Even though the final application in this thesis involves multiple compressible jets, the study was started with a single incompressible jet to understand the flow interactions and study the influence of various parameters. Now we are in a position to take up the study of a compressible jet both computationally and experimentally.

CHAPTER 5

SINGLE JET IN CONFINED COUNTERFLOW – COMPUTATIONS AND EXPERIMENTS

In Chapter 4 an axisymmetric, incompressible turbulent jet issuing into confined counterflow was computationally investigated for several values of confinement. In this chapter a circular, compressible turbulent jet issuing into confined counterflow is investigated computationally and experimentally. A set of computations and experiments were performed for a fixed duct-to-jet diameter ratio covering various jet-to-counterflow mass flow ratios. The time-averaged numerical calculations were done with a *k-ε* turbulence model using a commercial flow solver. The computational results were compared with the experimental results obtained from a specially-built test facility.

5.1 Description of the Flow Field

A schematic illustration of the flowfield under consideration is depicted in Figure 5.1. The station numbering is as shown in Figure 5.1. The counterflow stream (far ahead of the jet) is numbered 1, the jet exit plane 2, a plane one-duct diameter downstream of the jet exit where the total pressure distortion is evaluated is 3 and the (far downstream, combined jet and counterflow stream) outlet is 4. In this study station 3 is considered to be the Aerodynamic Interface Plane (*AIP*). This is the station used to define the total pressure distortion between the inlet and engine (ARP 1420, 2002).

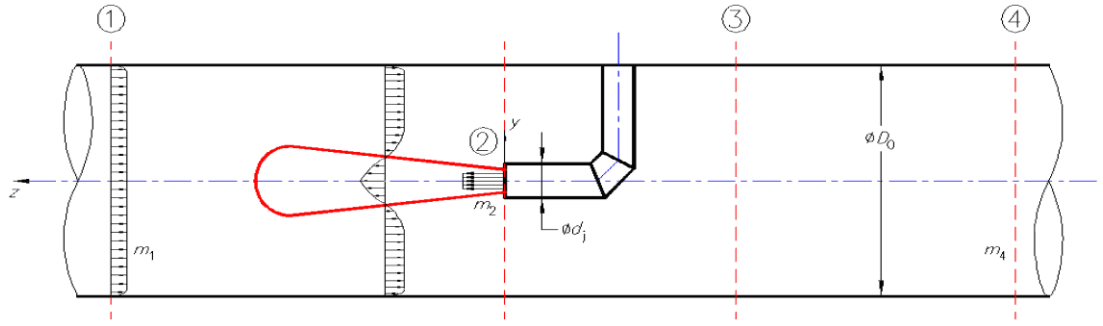

Figure 5.1 Schematic description of the flow field of a single jet in confined counterflow.

A steady, compressible, turbulent jet of uniform velocity u_j and density ρ_j issues from a nozzle of internal diameter d_j into a steady, turbulent, uniform counter stream of

velocity u_0 ($u_j > u_0$), density ρ_0, and confined within a duct of diameter D_0. In the present investigation D_0 = 102 mm and d_j = 10 mm. The mass flow of the counterflow stream is $m_1 = \pi/4\ D_0^2\ \rho_0\ u_0$ and that at the jet exit is $m_2 = \pi/4\ d_j^2\ \rho_j\ u_j$. The mass flow ratio is defined as the ratio of the jet mass flow to the total mass flow, m_2/m_4, where $m_4 = (m_1 + m_2)$.

5.2 Computational Procedure

The governing equations for mass, momentum and energy conservation for a turbulent flow field namely, the Reynolds-averaged Navier-Stokes equations were solved numerically using the software ANSYS FLUENT. The time-averaged computations were performed for one duct-to-jet diameter ratio (D_0/d_j = 10.2) and covering jet-to-counter-flow mass flow ratios (m_2/m_4) ranging from 0.090 to 0.332. The counterflow stream inlet and the combined flow outlet were placed at 4.9 D_0 and -4.9 D_0 from the jet exit, respectively.

The total and static pressure boundary conditions were specified at the counterflow inlet and the jet exit. The pressure boundary conditions at the jet exit corresponded to sonic jet exit velocity. In the air jet distortion system of NASA (Meyer *et al*. 1970) also the jets were choked. In all the studies reported in this thesis henceforth the jet(s) remained choked. The exit static pressure was specified at the outlet boundary (station 4). The total temperature was specified (and equal) at the inlets and the outlet. On the main duct walls and on the walls of the jet stem the no-slip boundary condition was imposed.

All computations were performed by a *k-ε* turbulence model. The turbulence viscosity is calculated in this model as,

$$\nu_t = C_\mu \frac{k^2}{\varepsilon} \tag{5.1}$$

where C_μ is a constant. The model constants are assigned the following values (Launder and Spalding 1972):

$C_{1\varepsilon} = 1.44$, $C_{2\varepsilon} = 1.92$, $C_{\mu} = 0.09$, $\sigma_k = 1.0$, $\sigma_{\varepsilon} = 1.3$.

The turbulence intensity at the counterflow stream inlet and jet exit were 0.3 % and 2.0 %, respectively based on the mean axial velocity at these locations. They were obtained from measurements by a hot-wire anemometer and were imposed as turbulence boundary conditions for the computations.

The pressure-velocity coupling was achieved by the SIMPLE algorithm (Patankar 1980). All calculations were carried out in double-precision arithmetic.

The three-dimensional computational grid consisted of 718,935 cells. The number of computational cells was chosen after a grid independence study. This study was conducted for the $m_2/m_4 = 0.200$ case with 419,100 (coarse grid), 718,935 (medium grid) and also with 1,194,102 (fine grid) grid points. The Grid Convergence Index (see Celik *et al*. 2008) was calculated and the numerical uncertainty in the calculation of total pressure loss λ_{p0} (see equation 5.3) in terms of the discretization error is 0.90 % and 0.57 %, and in the calculation of Distortion Index *DI* (see equation 5.4) is 0.96 % and 0.85 % for the fine and medium grids, respectively. Since the medium grid had a reasonably low value of discretization error it was chosen and all computations reported in this chapter are for this grid.

5.3 Experimental Procedure

An experimental facility was designed and built to investigate the characteristics of the counterflow jet and the flow arrangement is shown schematically in Figure 5.2. The design and calibration of the test facility is described in Appendix 3.

The counterflow stream is supplied by the blower, passing through the settling chamber which consists of honeycomb and turbulence reduction screens and a contraction. The counterflow mass flow can be controlled by a conical throttle at the exit of the straight duct which can be moved axially by means of a lead screw and a nut.

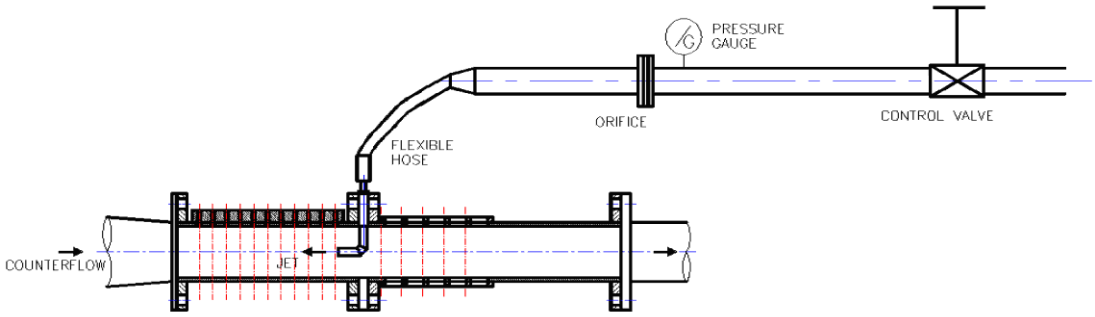

Figure 5.2 Test section showing the jet supply arrangement and locations for measuring velocity profiles in the jet and downstream total pressure profiles.

For the jet system high-pressure air was sourced from a central Compressed Air Facility controlled through a manual gate-valve and metered by a standard orifice plate (ISO 5167-2: 2003). The orifice upstream and downstream pressure tapings were at D_0 and $D_0/2$, respectively. The orifice upstream pressure was measured with a Druck (model PDCR 821, 150 psig range, ± 0.1 % accuracy) pressure transducer and the orifice differential pressure was measured with a BLH (model HLD, 20" water column range) differential pressure cell. These pressure transducers were calibrated before experiments.

The jet issues from a stem protruding into the confining duct and flows opposite to the air from the blower. The jet mass flow can be varied by operating a control valve. By adjusting the counterflow and jet mass flow the required mass flow ratio can be obtained.

The test section has provision for measuring velocity profiles in the jet (see Section A3.4). The velocity profiles were measured by traversing a three-hole wedge probe. The design of the wedge probe is based on Manickam and Murugesan (1978) and is shown in Figure 5.3 and a close-up photograph of the probe is depicted in the inset. The wedge probe was installed on a manually-operated micrometer traverse mechanism. The wedge probe can be radially traversed at nine axial locations in front of the jet. At each of these locations the wedge probe was traversed inside the confining duct first with the probe facing the jet. When the probe is traversed facing the jet the jet velocities are

correctly measured whereas the counterflow velocities are not registered since the probe is not aligned to this stream. Now the probe is rotated 180º and traversed facing the counterflow stream; the jet velocities are not registered during this traverse. The two velocity profiles thus obtained were superposed and the points of intersection identified; the velocity profile at a given axial location was obtained by this method.

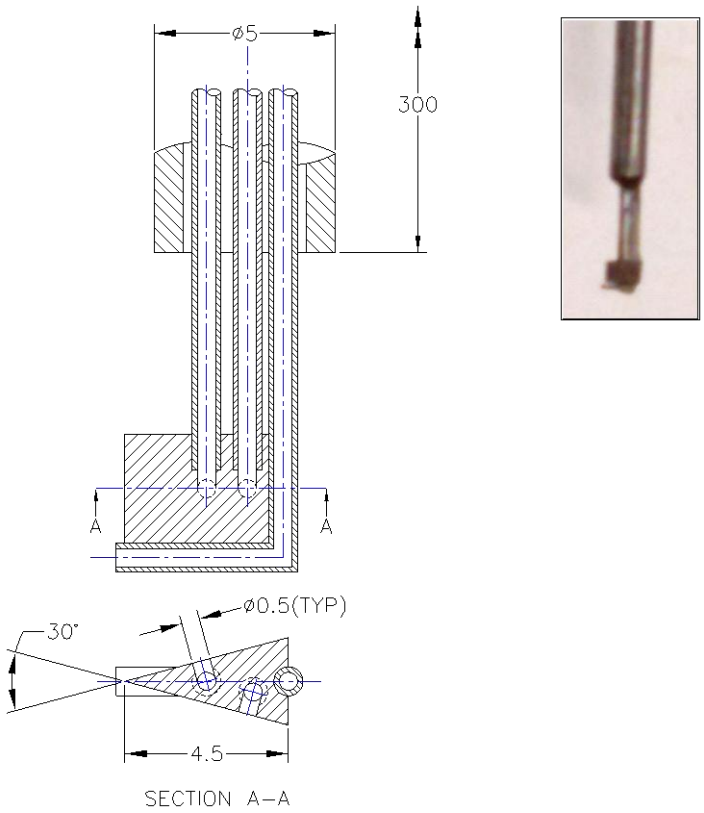

Figure 5.3 Sectional view of the wedge probe; dimensions are in mm. A photograph of the probe head is shown in the inset.

The wedge probe measurements were made only in the subsonic regime of the jet due to difficulties is making satisfactory measurements in the supersonic regions; see Rathakrishnan (2009) for a discussion on issues concerned while making pressure measurements in supersonic flow. Zaman (1999) and Yüceil and Ötügen (2002) in their measurements in supersonic free jets with pressure probes avoided the supersonic zones of the jet.

The total pressure loss due to the jet in counterflow arrangement was estimated from total pressure measurements made at five axial locations behind the jet injection stem as shown in Figure 5.2 and also Figure 5.10. The total pressure measurements were made by forty total pressure probes. These probes were arranged in eight equi-angularly spaced rakes, each rake consisting of five probes located at the centres of equal annular ring areas of the main duct. The orientation of the probes is shown in Figure 5.4 and is in accordance with ARP 1420 (2002). The total pressure rakes can be installed at one of the five axial locations downstream the jet injection.

The pressures were measured by two numbers of ESP-32HD miniature electronic differential pressure scanners of ± 45 kPa range with an accuracy of ± 0.03 % FS. Each of these pressure scanners consisted of 32 pressure sensors and all the 64 pressure sensors were calibrated individually in the pressure range of interest prior to experimentation.

The signals from the transducers were acquired by an Agilent 34970A Data Acquisition / Switch Unit through RS-232 interface and an on-line data acquisition program was written in LabVIEW (National Instruments) to acquire and process the experimental data.

The uncertainties in the experimental data were estimated by the method of Kline and McClintock (see Holman 2001: 51-60). The uncertainty in m_2/m_4 is estimated to be about 0.5 % and that in λ_{p0} and *DI* are 0.6 % and 1.2 %, respectively. For the wedge probe the uncertainty in the velocity measurement is about 0.8 %.

For each mass flow ratio the experiments were conducted in two stages; in the first stage the velocity profiles upstream of the jet was measured and in the next stage the total pressure profiles downstream of the jet were measured.

Figure 5.4 Locations where total pressures are measured behind the jet injector. This arrangement is in accordance with AIR1419 (1999).

5.4 Results and Discussion

5.4.1 Velocity Field

The velocity profiles at several axial locations in the duct were measured by a three-hole wedge probe as described in Section 5.3. The velocity profiles are shown in Figure 5.5 for m_2/m_4 = 0.130. The velocity profiles at each axial location are non-dimensionalised by the local centreline velocity. In general, the computational results agree reasonably well with the experiments. The small disagreement in the velocity profiles was also reported in Majumdar and Bhaduri (1981) who attributed this to the approximations in the turbulence model. A small asymmetry is also noticed in the present experimentally obtained velocity profiles. This, perhaps, might have been due to the non-uniform jet exit velocity profile; it may be noted that the jet exits from a jet injector which is first perpendicular to the duct axis and after a 90º bend the injector axis

coincides with the duct axis (see Figure 5.2). This type of jet injector arrangement was also used by Morgan *et al*. (1976) in their experiments.

The jet geometry is also shown in Figure 5.5. It is constructed from the computational data and is the locus of $u = 0$. The stagnation point is on the jet axis and its distance from the jet exit is the jet penetration length (see next section for further discussion).

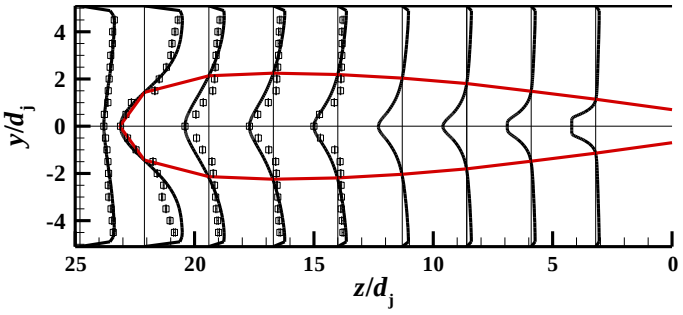

Figure 5.5 Profiles of axial velocity at several locations in the duct. The continuous curves are from computations and open symbols are experimental data. The geometry of the jet is also shown in this figure.; m_2/m_4 = 0.130.

The radial distribution of axial velocity in the jet at various streamwise locations is again plotted applying the self-similarity hypothesis of Beltaos and Rajaratnam (1973); see equation 4.5.

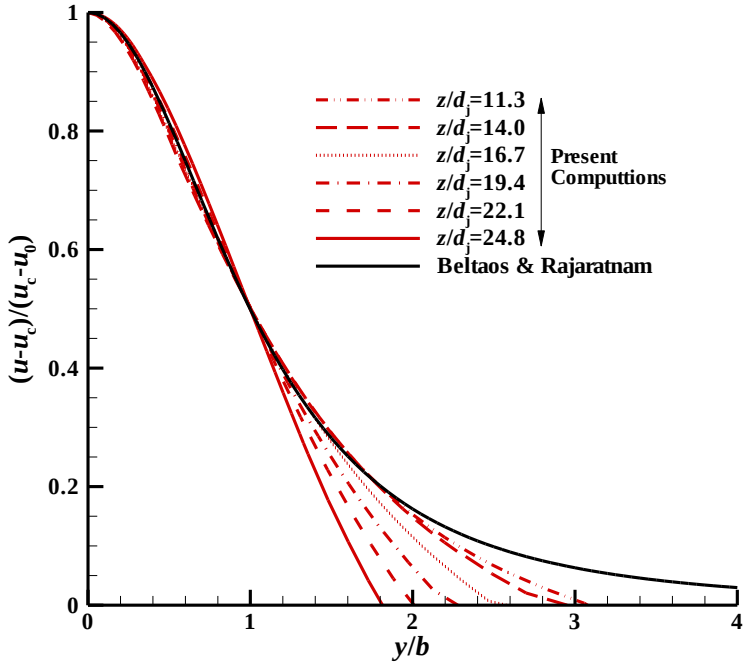

Figure 5.6 Velocity profiles at several axial locations in the jet plotted using the self-similarity hypothesis (equation 4.5); m_2/m_4 = 0.230. The velocity profile in a jet in unconfined counterflow (Beltaos and Rajaratnam 1973) is also shown for comparison.

The velocity profiles at several axial locations from the computational analysis are plotted in Figure 5.6 for m_2/m_4 = 0.230. The velocity distribution compares well with the unconfined case till about y/b is unity indicating the effect of confinement is not felt near the jet axis. However, away from the axis the confining duct has a strong effect and influences the jet growth. It is clear that the jet propagation in the confined duct is slower than in unconfined situation.

5.4.2 Jet Penetration Length

The jet penetration length, l_p, is defined as the length of the jet from the nozzle exit to a point on the axis where the axial velocity becomes zero. The penetration length evaluated from the present computations is shown in Figure 5.7(a). The penetration length increases as the mass flow ratio increases.

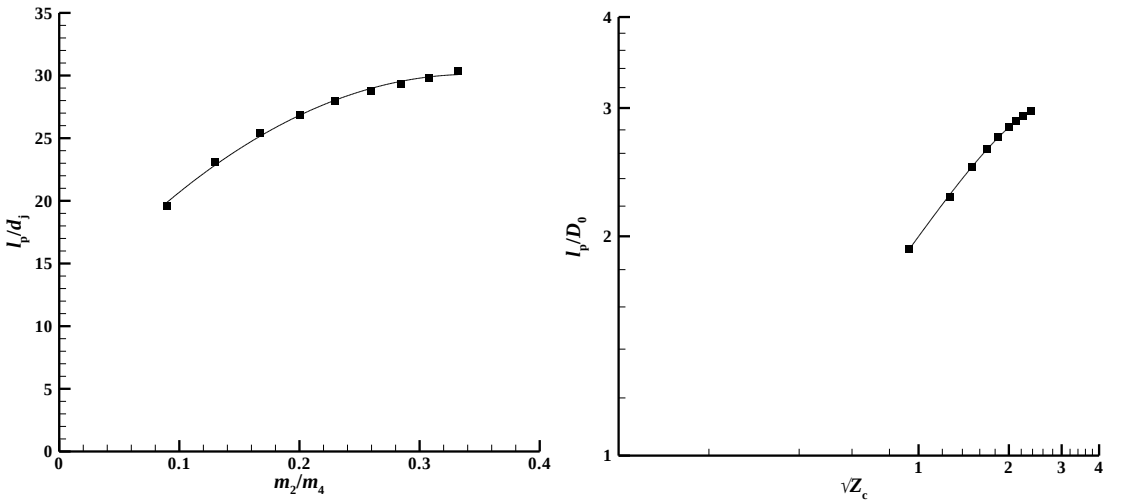

(a) **(b)**

Figure 5.7 Jet penetration length (a) as a function of m_2/m_4 and (b) as a function of momentum parameter (equation 5.2).

Morgan *et al*. (1976) defined a momentum parameter for the incompressible jet case (equation 4.10). This parameter for the compressible jet can be written as,

$$Z_c = \frac{\rho_j}{\rho_0}\left(\frac{u_j\, d_j}{u_0\, D_0}\right)^2, \qquad (5.2)$$

where ρ_j and ρ_0 are the densities of the jet and the counterflow stream, respectively. This momentum parameter can also be used to present the jet penetration length as shown in Figure 5.7(b). The values of diameter ratio and mass flow ratios used in the present study fall in the high jet-momentum regime (Morgan *et al*. 1976).

5.4.3 Centreline Mach Number Distribution

The variation of Mach number along the jet centreline for different values of mass flow ratios is plotted in Figure 5.8. The sonic jet exits into the counterflow stream and since the jet exit pressure is higher than the pressure of the counterflow stream near the nozzle an underexpanded jet scenario is formed. Thus the jet expands further on exit into the duct resulting in the well-known shock-cell structure in the study of supersonic jets. The potential core is determined by the necessity of pressure being equal in the outermost

portion of the flow within the shock structure and the surrounding ambient stream (Donaldson and Snedeker 1971). The core dissipates due to viscosity and downstream of the core the velocity decay is similar to the incompressible counterflow jet case. The Mach number reduces till the stagnation point and then slightly increases and eventually reaches the counterflow stream value. The peak Mach number in the shock-cell increases with increasing mass flow ratio which amounts to increasing pressure ratio.

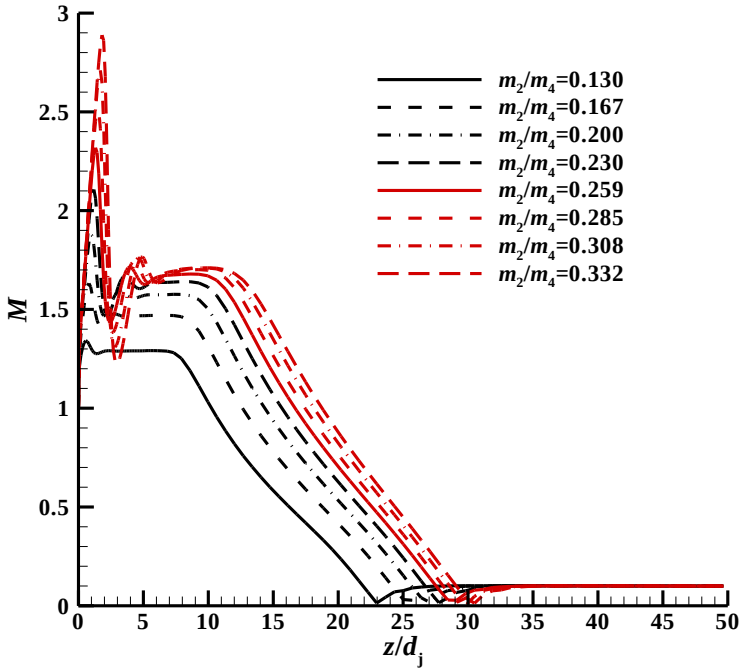

Figure 5.8 Variation of Mach number along the jet centreline for different values of mass flow ratio m_2/m_4.

The characteristic features of the underexpanded jet in confined counterflow stream explained above can be seen in Figure 5.9 for $m_2/m_4 = 0.230$ which corresponds to $p_{02j}/p_1 = 5.40$. The shock-cell just downstream of the jet exit is clearly visible in this figure.

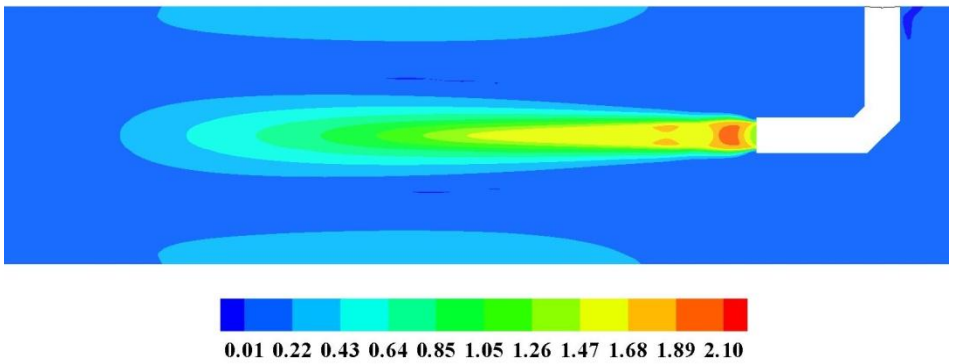

Figure 5.9 Contours of Mach number; m_2/m_4 = 0.230. The shock-cell structure at the jet exit can be clearly seen.

5.4.4 Total Pressure Loss Distribution

The contours of total pressure loss downstream of the jet injector is shown in Figure 5.10 for m_2/m_4 = 0.130. The total pressure loss is expressed in terms of 1 - (p_0/p_{01}). A good agreement between the computations and experiments is obtained. The wake behind the jet injector is clearly seen in the contours. The width of this wake increases downstream. At the most downstream location of the measurement (z/D_0 = -2.47) it can be seen that total pressure loss distribution is more uniform than at z/D_0 = -0.82. At far downstream locations it is expected that the flow would eventually become uniform.

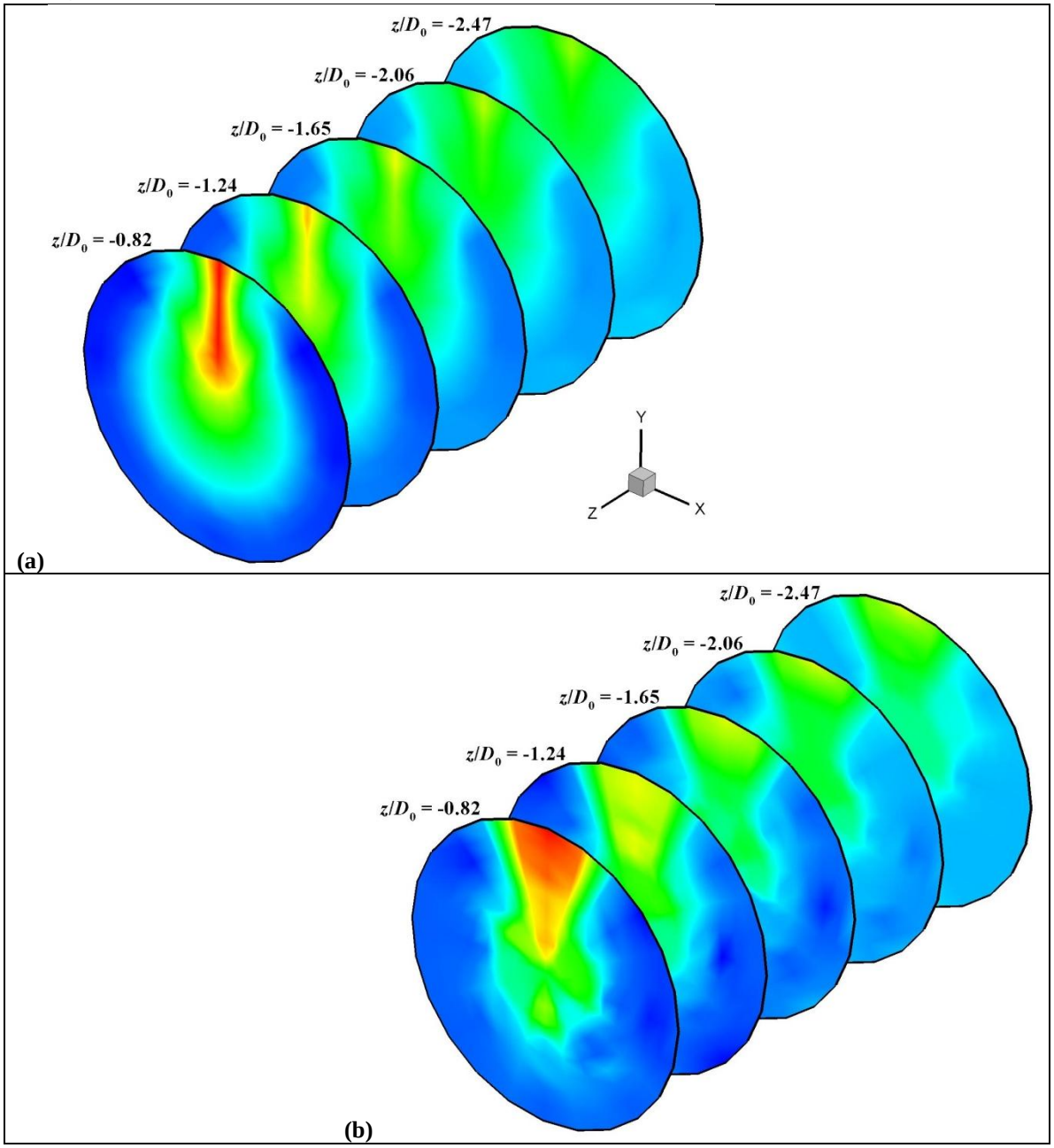

Figure 5.10 Contours of total pressure loss expressed as 1 – (p_0/p_{01}) at several locations behind the jet injector. (a) Computations and (b) experiments; m_2/m_4 = 0.130.

5.4.5 Total Pressure Loss

The loss in total pressure due to the jet mixing with the counterflow stream was quantified by a non-dimensional total pressure loss parameter, which is defined as

$$\lambda_{p0} = 1 - \frac{p_{0,z1}}{p_{0,z2}} \tag{5.3}$$

where $p_{0,\,z1}$ and $p_{0,\,z2}$ are the total pressures at $z/D_0 = 2.69$ and $z/D_0 = -2.47$, respectively.

The inlet total pressure was measured in the experimental facility by a Pitot probe located at the centre of the inlet duct (at $z/D_0 = 2.69$) at and the exit total pressure was calculated as the average total pressure of the forty measurements made with the total pressure rakes (at $z/D_0 = -2.47$).

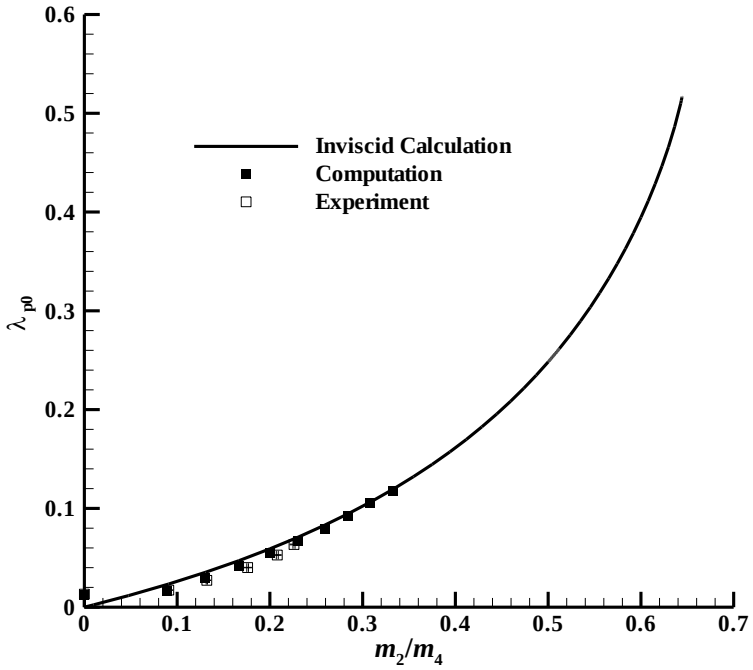

Figure 5.11 Total pressure loss λ_{p0} (equation 5.3) plotted as a function of m_2/m_4. The continuous curve is from quasi-one-dimensional inviscid analysis. The error bars on the experimental data are shown for the open symbols.

The total pressure loss evaluated numerically and obtained from experiments is shown in Figure 5.11. Also shown in this figure is the total pressure loss estimated from a

quasi-one-dimensional inviscid analysis of the flow system solving the steady-state continuity, momentum, and energy equations. This analysis is described in Appendix 2.

It can be seen that the computational and experimental results agree well. The numerical and experimental results indicate a non-zero total pressure loss when the jet mass flow is zero because of the presence of the jet injector protruding into the duct. The jet stem occupies about 10 % of the cross-sectional area of the duct.

5.4.6 Total Pressure Distortion

The total pressure non-uniformity can be quantified by means of a parameter Distortion Index *DI*, which is defined as, (see, for example, Seddon and Goldsmith 1999)

$$DI = \frac{p_{0,\max} - p_{0,\min}}{p_{0,ave}} \tag{5.4}$$

where $p_{0,\,\max}$ and $p_{0,\,\min}$ are the maximum and minimum total pressures, respectively, and $p_{0,\,ave}$ is the average total pressure in any plane of interest. The total pressures were measured by forty total pressure probes, arranged circumferentially in eight rakes each having five probes (see Figure 5.4).

The distortion indices were calculated from the forty total pressure measurements from the experiments and similarly from the computations. The distortion indices obtained at several locations downstream of the jet injector are shown in Figure 5.12. The computational results agree reasonably well with the experimental data.

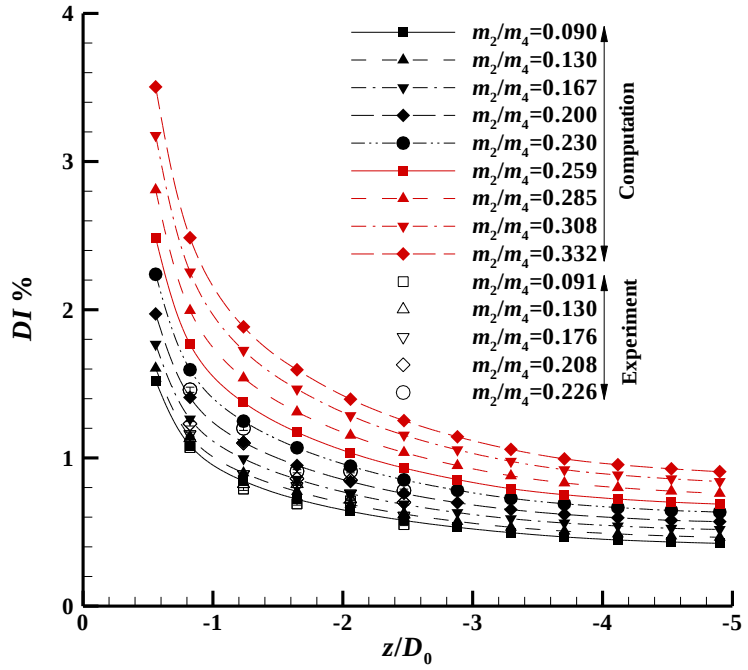

Figure 5.12 Distortion Index (*DI*) at several locations behind the jet injector plotted for different values of m_2/m_4. The error bars on the experimental data are shown for the open symbols.

The distortion index increases with an increase in the mass flow ratio. The highest distortion index occurs at a plane just downstream of the jet injector for all mass flow ratios. At far downstream locations low values of distortion index are observed.

5.4.7 Total Pressure Distribution and Distortion at Aerodynamic Interface Plane

The total pressure distribution and distortion parameters at the Aerodynamic Interface Plane (*AIP*) are examined in this section for three typical mass flow ratios m_2/m_4 = 0.130 (*DI* = 1.013 %), 0.230 (*DI* = 1.409 %) and 0.332 (*DI* = 2.170 %). To quantify total pressure distortion at the *AIP* two more distortion descriptors are used in addition to the Distortion Index (*DI*) already defined in equation 5.4. This is necessary because though the *DI* is a gross quantity indicating the non-uniformity and is a useful descriptor for comparative purposes (Seddon and Goldsmith 1999), it does not distinguish between circumferential and radial distortion components.

The circumferential and radial total pressure distortion are defined as (Hubble and Smith 1979; see also Hercock and Williams 1974 for a general description of most distortion parameters in common use)

$$IDC = \frac{p_{0,ring,ave} - p_{0,ring,\min}}{p_{0,\,face,ave}} \tag{5.5}$$

and

$$IDR = \frac{p_{0,\,face,ave} - p_{0,ring,ave}}{p_{0,\,face,ave}} \quad , \tag{5.6}$$

respectively, where $p_{0,\,face,\,ave}$ is the average total pressure in the plane and $p_{0,\,ring,\,ave}$ and $p_{0,\,ring,\,min}$ are the average and minimum total pressures in a ring, respectively. It may be noted that there are as many values of *IDC* and *IDR* as the number of rings. *IDC* is always positive with a larger value indicating a larger loss and hence lower total pressure. *IDR* values for all rings together sum to zero.

The total pressure loss contours represented by $[1 - (p_0/p_{01})]$, the ring-wise total pressure loss distribution and the circumferential and radial distortion parameters for the three mass flow ratios are plotted in Figure 5.13(a) to (c). The total pressure loss increases with increasing mass flow ratio (as was also seen in Figure 5.11) resulting in a corresponding loss in the ring total pressure distribution. The circumferential total pressure distribution is nearly uniform and the dip in total pressure distribution in the rings is due to the wake from the jet injector. The circumferential and radial distortion increases with increasing mass flow ratio. For all the three cases the *IDC* increases from the innermost ring (hub) to the outermost ring (tip). The radial distortion is highest at the hub and lowest in ring number 4 for all the mass flow ratios.

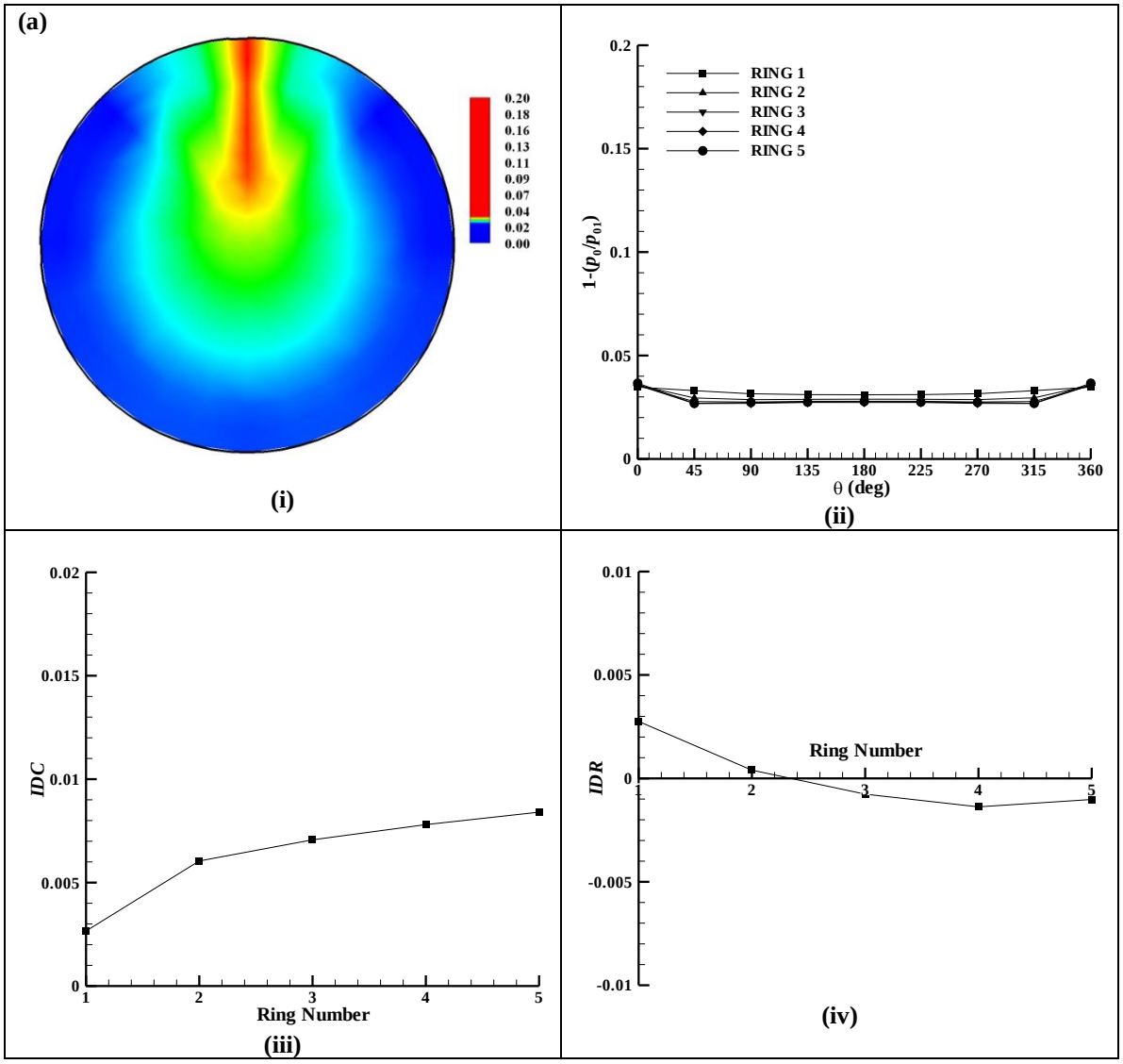
(a)
0.20
0.18
0.16
0.13
0.11
0.09
0.07
0.04
0.02
0.00
(i)
RING 1
RING 2
RING 3
RING 4
RING 5
1-(p0/p01)
θ (deg)
(ii)
IDC
Ring Number
(iii)
IDR
Ring Number
(iv)

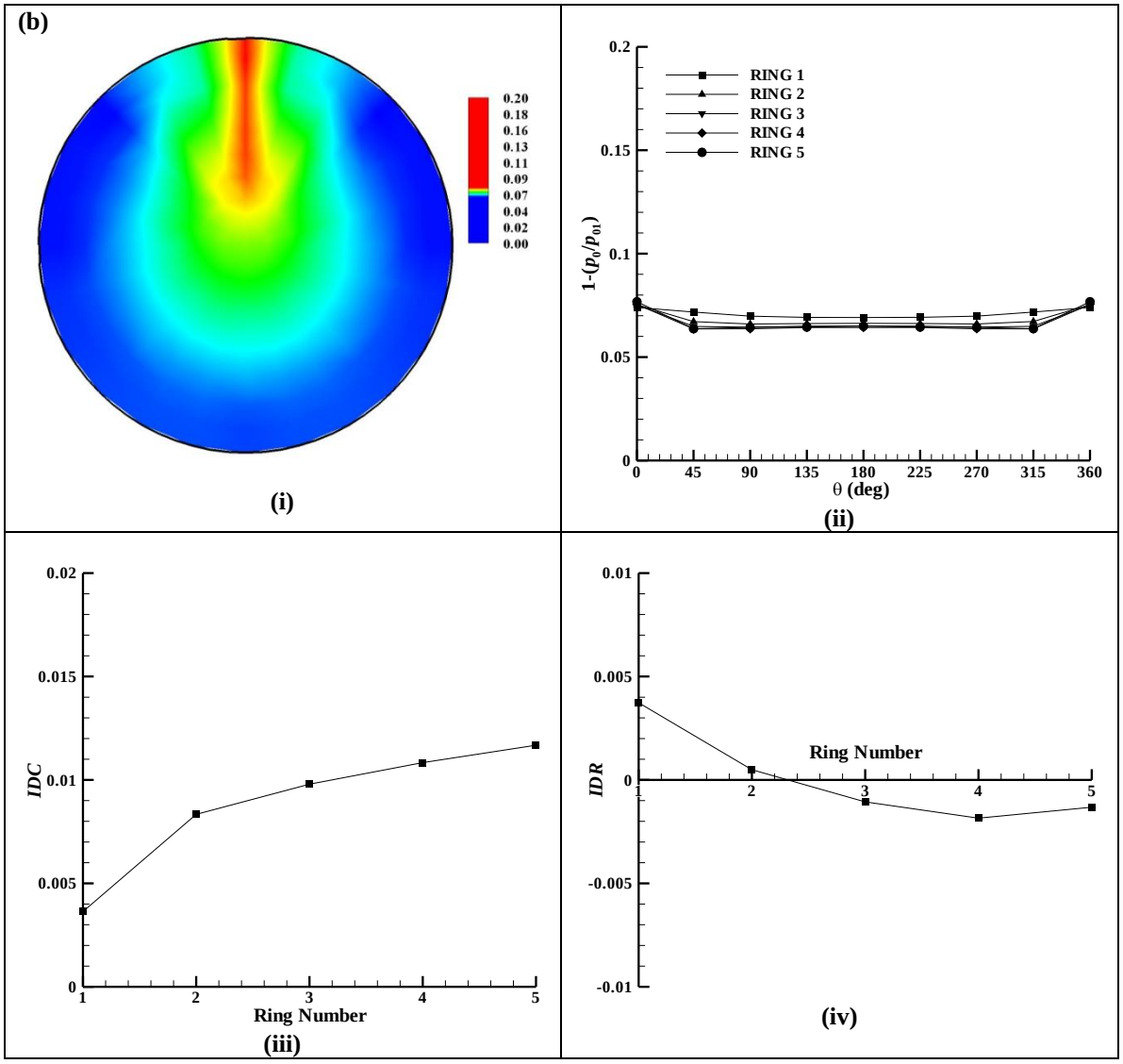
(b)
0.20
0.18
0.16
0.13
0.11
0.09
0.07
0.04
0.02
0.00
(i)
RING 1
RING 2
RING 3
RING 4
RING 5
1-(P0/P01)
θ (deg)
(ii)
IDC
Ring Number
(iii)
IDR
Ring Number
(iv)

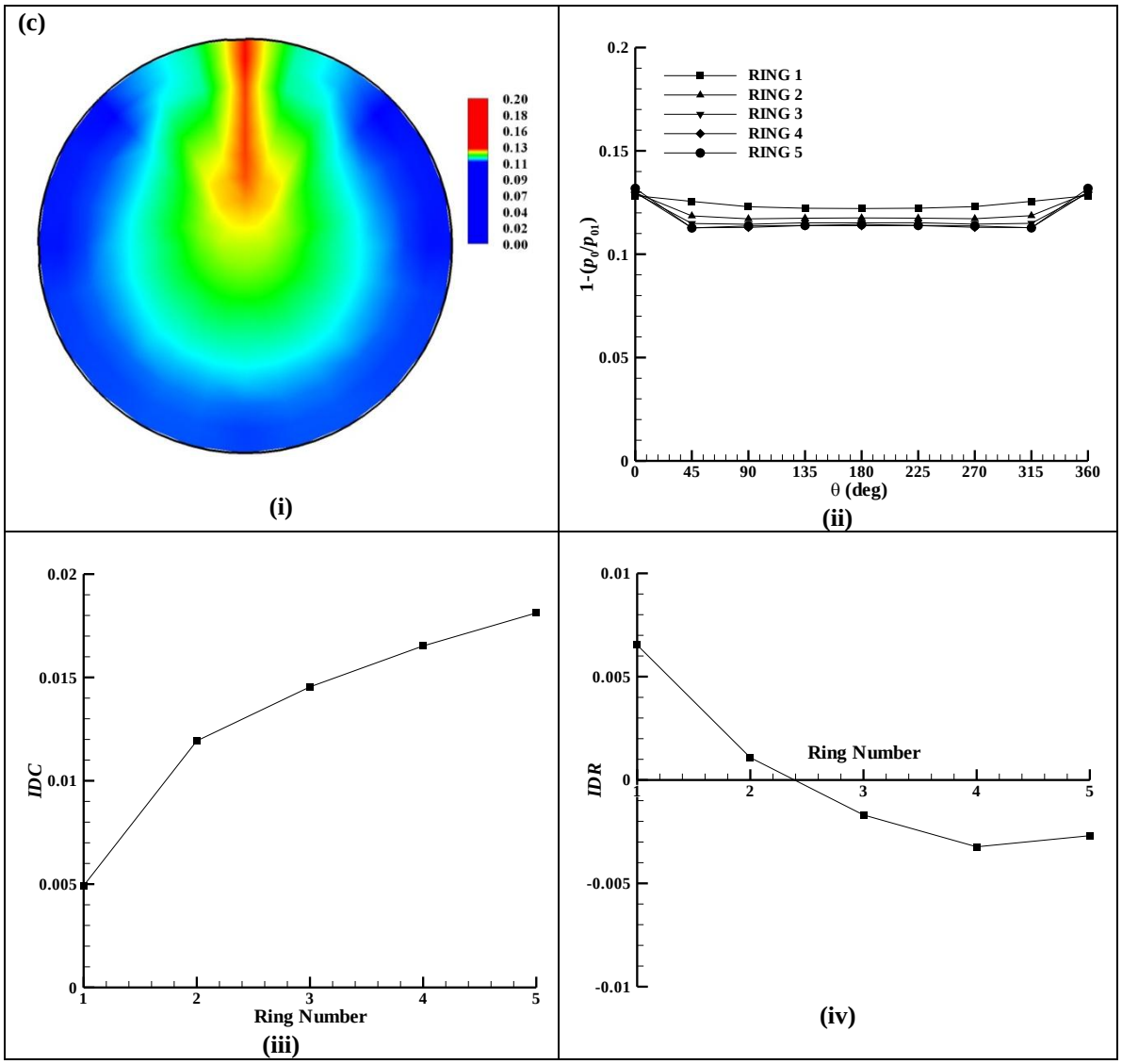

Figure 5.13 Distortion parameters at the *AIP* for (a) m_2/m_4 = 0.130, (b) m_2/m_4 = 0.230 and (c) m_2/m_4 = 0.332. In these figures (i) contours of total pressure loss [1 – (p_0/p_{01})], (ii) distribution of total pressure loss in each of the five rings, (iii) the circumferential distortion parameter *IDC* and (iv) the radial distortion parameter *IDR* in the rings.

5.5 Summary

The mean flow field of a single jet in confined counterflow was computationally and experimentally investigated. The jet velocity field and the total pressure field downstream of the jet injector were obtained for different values of mass flow ratio m_2/m_4 ranging from 0.090 to 0.332. The computational and experimental results were in good comparison. The total pressure loss λ_{p0} increased with increasing mass flow ratio. The distortion parameters at the *AIP* were evaluated for three mass flow ratio cases. The *DI* increased with an increase in mass flow ratio at all the downstream planes. At the highest mass flow ratio in this study m_2/m_4 = 0.322 the *DI* at z/D_0 = - 0.82 was about 3.504 % and decreased to about 0.907 % at z/D_0 = - 4.9.

The total pressure distribution and total pressure distortion parameters at the *AIP* were examined for three mass flow ratios m_2/m_4 = 0.130, 0.230 and 0.332. The total pressure loss increased with increasing mass flow ratio. The circumferential total pressure distribution was nearly uniform for all the mass flow ratio cases and the dip in the total pressure distribution at one circumferential location was due to the wake from the jet stem. The circumferential and radial distortion parameters also increased with increase in mass flow ratio.

The present study with a single jet enables us to take up the practical case with four jets which involves an increased number of parameters since the mass flow rate in each jet can be independently varied. The consequent flow field is non-axisymmetric. Even though the number of jets required for the present application will be increased to twelve and then twenty it will be seen that the study of the case with four jets in the next chapter is very fruitful since all the mass flow rate permutations can be easily counted and a more complete parametric study be performed.

CHAPTER 6

FOUR JETS IN CONFINED COUNTERFLOW – COMPUTATIONS AND EXPERIMENTS

In Chapter 5 a compressible turbulent jet issuing into confined counterflow was studied. In the present chapter flow due to four jets circumferentially arranged and issuing into confined counterflow is investigated computationally and experimentally. A series of computations and experiments were performed for a fixed duct-to-jet diameter ratio covering various jet-to-counterflow mass flow ratios and different values of mass flow rates in each jet. The steady numerical calculations were done with a k-ε turbulence model using a commercial flow solver. The computational results were compared with the experimental results obtained from a specially-built test facility.

6.1 Description of the Flow Field

A schematic illustration of the flowfield is depicted in Figure 6.1. The station numbering is done as shown in Figure 6.1. The counterflow stream (far ahead of the jet) is numbered 1, the jet exit plane 2, a plane one-duct diameter downstream of the jet exit where the total pressure distortion is evaluated is 3 and the (far downstream, combined jet and counterflow stream) outlet is 4. The Aerodynamic Interface Plane (*AIP*) is at station 3.

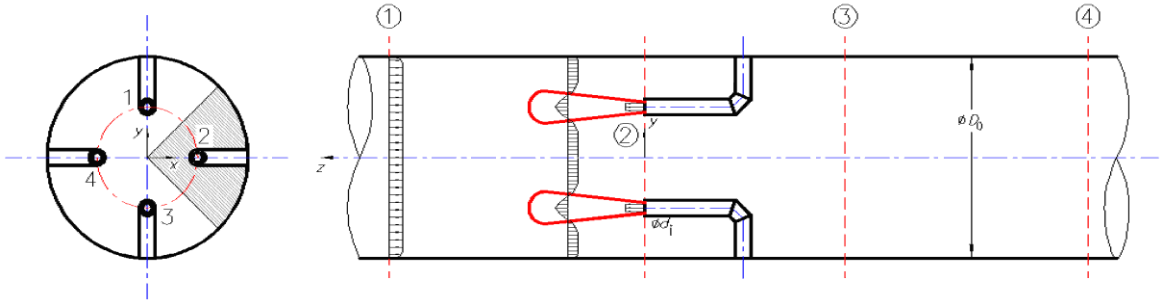

Figure 6.1 Schematic description of the flow field for four circumferentially arranged jets in confined counterflow.

A steady, compressible, turbulent jet of uniform velocity u_j and density ρ_j issues from a nozzle of internal diameter d_j into a steady, turbulent, uniform counter stream of velocity u_0 ($u_j > u_0$), density ρ_0, and confined within a duct of diameter D_0. In the present investigation D_0 = 102 mm and d_j = 7.5 mm. The diameters of the four jets were equal. The four jets are arranged circumferentially at a radial location of $D_0/4$ each jet representing a sector (see Figure 6.1). The boundary layer thickness is expected to be small compared to the diameter of the duct and hence need not have to be accounted for while fixing the radial jet location. Subsequent computations (Section 6.2) show that this assumption is right. In a computation involving only the counterflow stream in the presence of the jet injectors but with no jet mass flow rate injection, the ratio of boundary-layer displacement thickness to the duct diameter δ^*/D_0 on the confining duct wall at the axial location of the jet injectors ($z/D_0 = 0$) is only 0.017. This procedure is followed while locating twelve (Figure 7.15) and twenty jets (Figure 7.24) also in their radial positions.

The mass flow of the counterflow stream is $m_1 = \pi/4\ D_0^2\ \rho_0\ u_0$ and that at the jet exit is $m_{2,j} = \pi/4\ d_j^2\ \rho_j\ u_j$. The total mass flow rate from the jets is $m_2 = \sum_{j=1}^{N} m_{2,j}$, where N = 4 in the present chapter.

The mass flow ratio is defined as the ratio of the jet mass flow to the total mass flow, m_2 / m_4, where $m_4 = (m_1 + m_2)$.

6.2 Computational Procedure

The governing equations for mass, momentum and energy conservation for a turbulent flow field namely, the Reynolds-averaged Navier-Stokes equations were solved numerically using the software ANSYS FLUENT. The time-averaged computations were performed for one duct-to-jet diameter ratio (D_0/d_j = 13.6) and jet-to-counterflow mass flow ratios (m_2/m_4) ranging from 0.055 to 0.197 for equal mass flow rates in the jets and from 0.19 to 0.352 for varying mass flow rates in the jets. The counterflow stream inlet

and the combined flow outlet were placed at 4.9 D_0 and – 4.9 D_0 from the jet exit, respectively.

The three-dimensional computational domain consisted of 962,189 cells. The grid spacing was similar to that employed for the single jet case in Section 5.2. The total and static pressure boundary condition were specified at the counterflow inlet and the jet exit. The pressure boundary conditions at the jet exit corresponded to sonic jet exit velocity. The exit static pressure was specified at the outlet boundary. The total temperature was specified (and equal) at the inlets and the outlet. On the main duct walls and on the walls of the jet stem the no-slip boundary condition was imposed.

The computations conducted were similar to the single jet case with turbulence closure achieved by a k-ε turbulence model. All calculations were carried out in double-precision arithmetic.

6.3 Experimental Procedure

The test section of the test facility was suitably modified to accommodate the four jet system. The modified test section is shown in Figure 6.2.

The four jets were supplied with high-pressure air from a central Compressed Air Facility controlled through a manual valve. The mass flow rates through the jets were calculated by measuring the wall static pressure in the jet supply lines. The wall static pressure was calibrated against the mass flow rate using a Micro Motion Coriolis type mass flow meter (model R050, maximum flow rate capacity is 400 kg/hr, with an accuracy of ± 0.75 % of mass flow rate). The four supply lines for the jets were individually calibrated. The static pressure in the jet supply lines were measured by a Statham (model PA-208TC, 0 to 150 psia pressure range, ± 0.1 % accuracy) pressure transducer in conjunction with a Scani-Valve (model 48J4-1052).

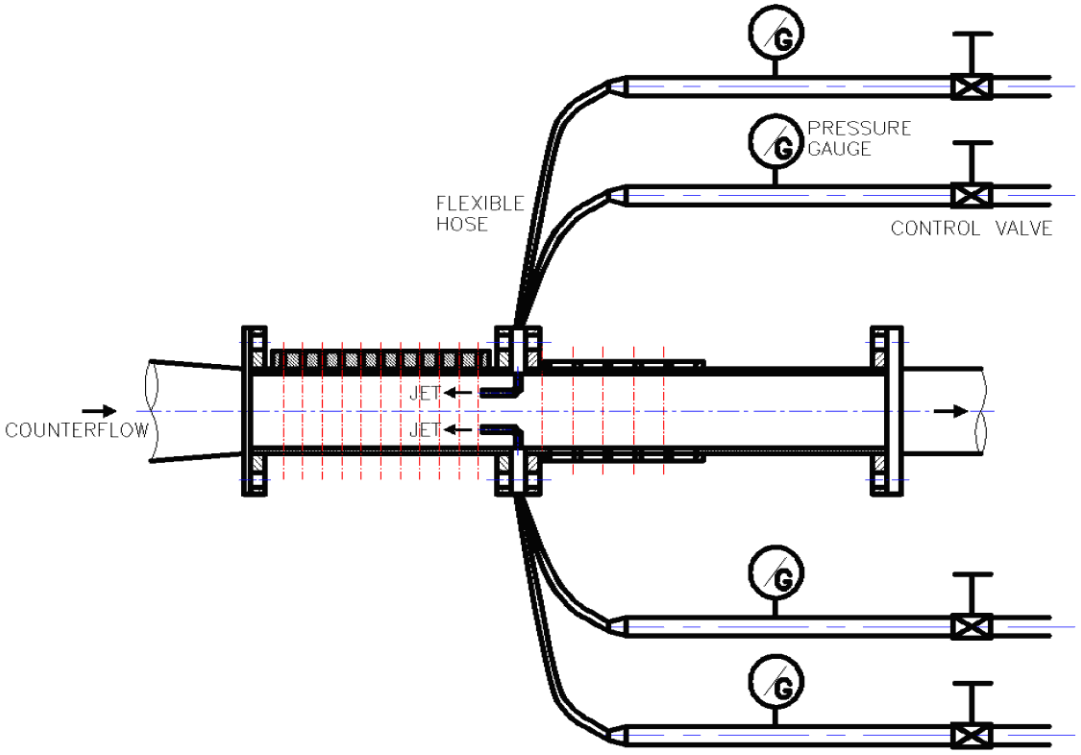

Figure 6.2 Test section showing the air supply arrangement for the jets and the locations for measuring the velocity profiles in the jet and total pressure profiles behind the jet injector.

The velocity profiles in the jets were measured with a three-hole wedge probe shown in Figure 5.3. The procedure of measuring the velocity profiles in the jets is as described in Section 5.3. However, by traversing the probe in such a manner the velocity profiles in jets 1 and 3 only can be obtained. To obtain the velocity profiles in jets 2 and 4 the upstream portion of the test section (identified as A in Figure A3.3) was rotated by 90º and the wedge probe was traversed.

The total pressure loss was calculated from total pressure measurements made at various axial locations behind the jet injectors. The total pressure measurements were made by forty total pressure probes as described in Section 5.3.

The total and static pressures were measured by two numbers of ESP-32HD miniature electronic differential pressure scanners and data was acquired by an Agilent

34970A Data Acquisition / Switch Unit through RS-232 interface. An on-line data acquisition program was written in LabVIEW (National Instruments) to acquire and process the experimental data.

The uncertainty in m_2/m_4 is estimated to be about 0.5 % and that in λ_{p0} and *DI* are 0.6 % and 1.2 %, respectively. The uncertainty in the velocity measurement using the wedge probe is about 0.8 %.

The experiments were conducted in two stages – first to measure the velocity profiles in the jets and then to measure the total pressure distribution.

The results are presented in the next sections in two categories – one when the mass flow rate through all the jets were equal and other when the jets had unequal mass flow rates.

6.4 Results and Discussion

6.4.1 Equal Mass Flow Rates in the Jets

6.4.1.1 Velocity Field

The velocity profiles at several axial locations in the duct were measured by a three-hole wedge probe as described in Section 6.3. The non-dimensional velocity profiles are shown in Figure 6.3 for $m_2/m_4 = 0.165$. The computational results agree well with the experiments. The geometries of the jets constructed from the computational data are also shown in Figure 6.3 which are the loci of $u = 0$.

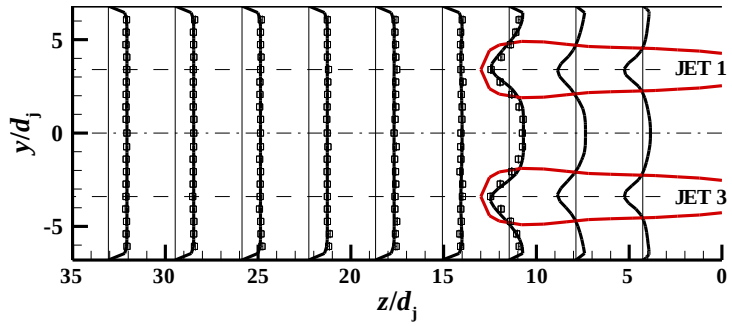

(a)

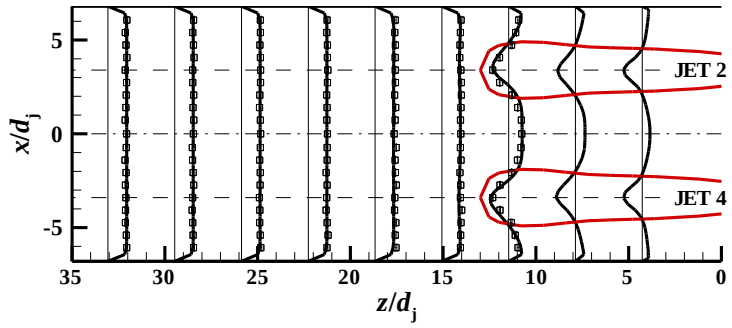

(b)

Figure 6.3 Profiles of axial velocity at several locations in the duct; (a) jets 1 and 3 (b) jets 2 and 4. The continuous curves are from computations and open symbols are experimental data; m_2/m_4 = 0.165. The geometries of the jets are also shown in this figure. The error bars on the experimental data are shown for the open symbols.

6.4.1.2 Jet Penetration Length

The jet penetration length, l_p, is defined as the length of the jet from the nozzle exit to a point on the jet axis where the axial velocity becomes zero. The penetration length evaluated from the present computations is shown in Figure 6.4(a). Since equal mass flow rates were injected from all the four jets it should suffice to show the penetration length of one jet only. The jet length is also plotted in terms of the momentum parameter defined in equation 5.2 as shown in Figure 6.4(b). The values of diameter ratio and mass flow ratios fall in the high jet momentum regime (see Morgan *et al*. 1976).

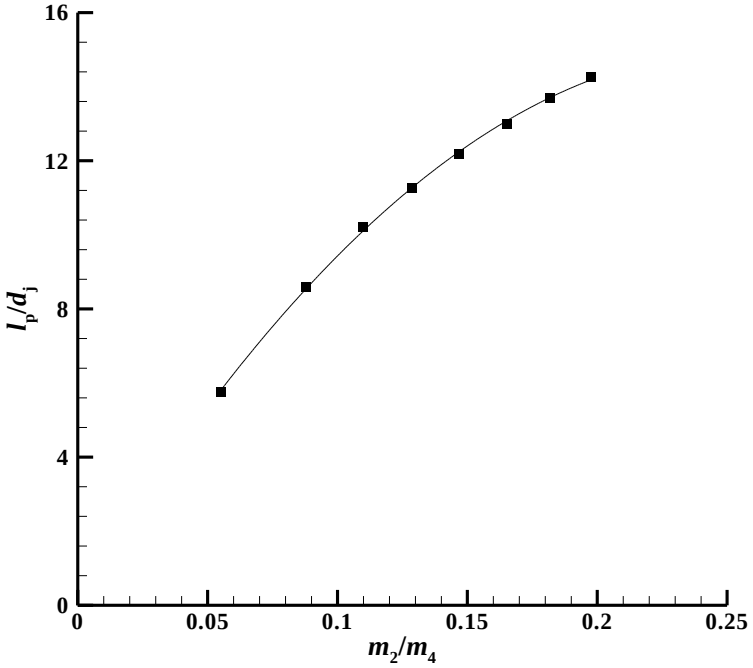

(a)

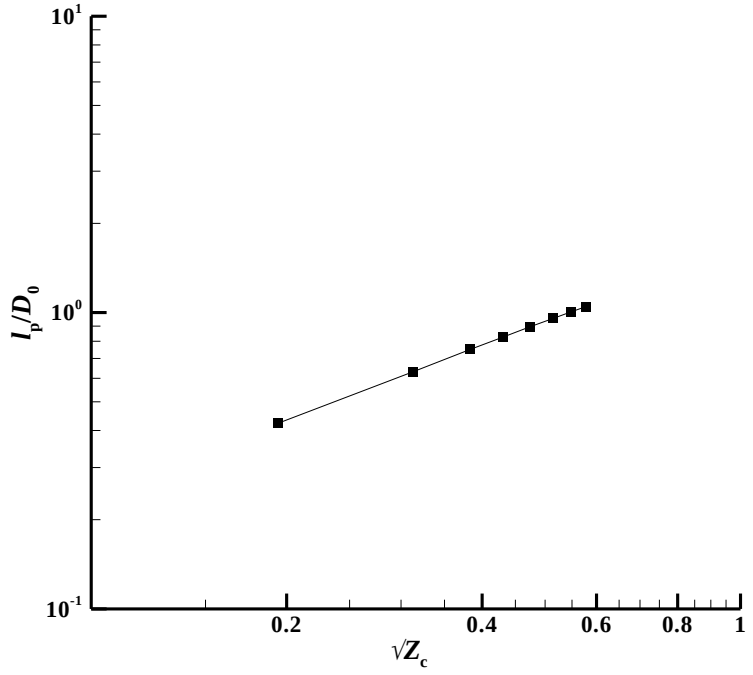

(b)

Figure 6.4 Jet penetration length as a function of (a) mass flow ratio and (b) as a function of momentum parameter (equation 5.2). The jet length is shown for one jet only as the mass flow rate in the four jets are equal.

6.4.1.3 Centreline Mach Number Distribution

The variation of Mach number along one of the jet's centreline for different values of mass flow ratios is plotted in Figure 6.5. The sonic jet exits into the counterflow stream and since the jet exit pressure is higher than the pressure of the counterflow near the nozzle an underexpanded jet scenario is formed. Thus the jet expands further on exit into the duct resulting in the well-known shock-cell structure in the study of free jets. The peak Mach number in the shock-cell increases with increasing mass flow ratio which amounts to increasing pressure ratio. The Mach number along the jet centreline reduces till the stagnation point and then increases and eventually reaches the counterflow stream value.

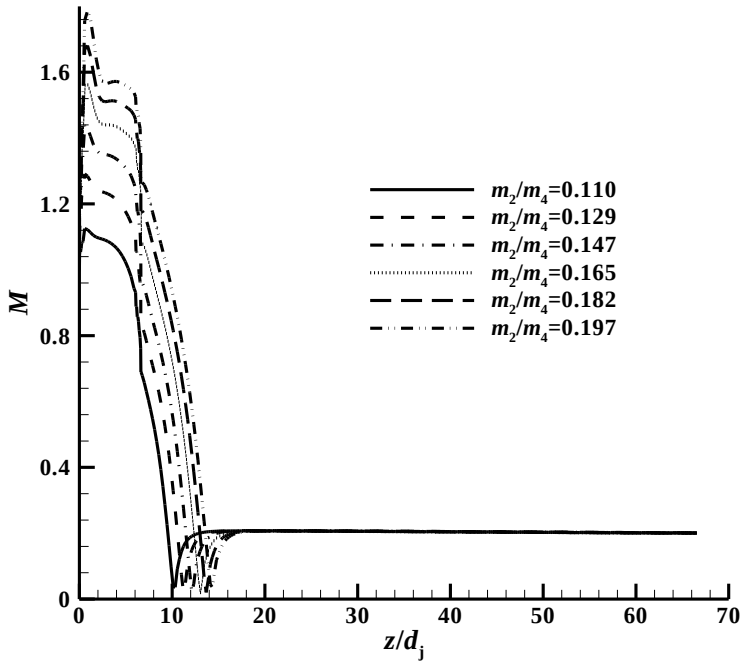

Figure 6.5 Variation of Mach number along the jet centreline. This variation is shown for one jet only as the mass flow rate in the four jets were equal.

The contours of Mach number are shown in Figure 6.6 for m_2/m_4 = 0.165 for which p_{02}/p_1 = 3.21. The shock-cell just downstream of the exit of the jets is clearly visible in this figure.

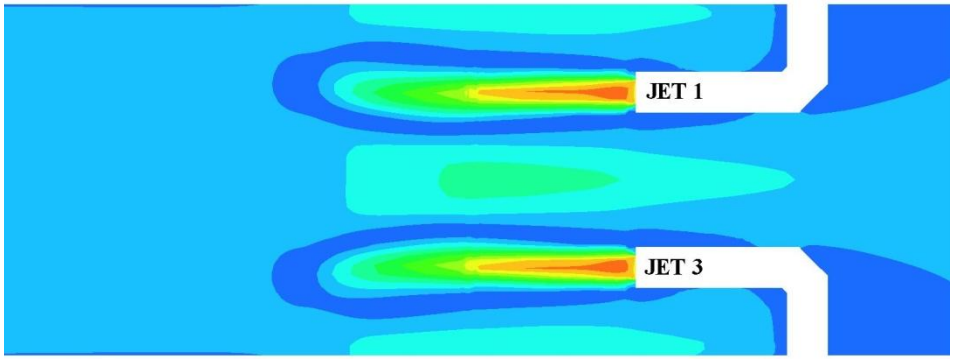

(a)

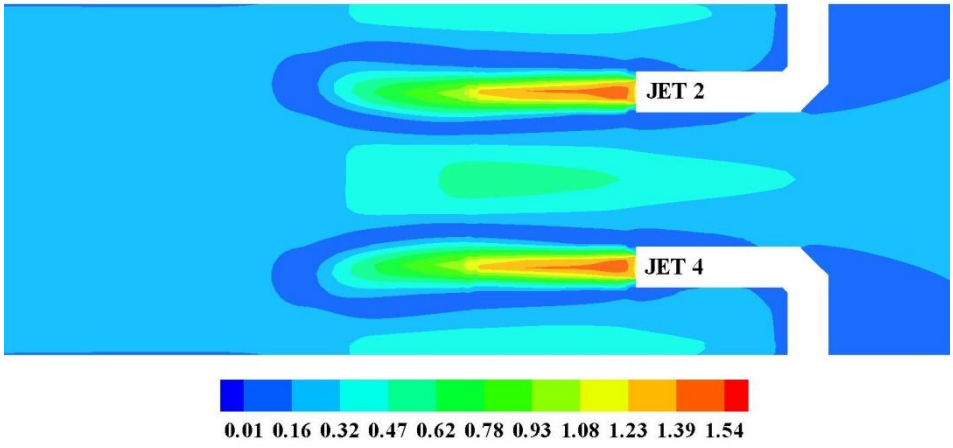

(b)

Figure 6.6 Contours of Mach number; m_2/m_4 = 0.165. (a) Jets 1 and 3 (b) jets 2 and 4.

6.4.1.4 Total Pressure Loss Distribution

The contours of total pressure loss downstream of the jet injectors is shown in Figure 6.7 for m_2/m_4 = 0.165 from both the computations and experiments. The total pressure loss is expressed in terms of 1 - (p_0/p_{01}). The wake behind the jet injectors is distinctly seen in the contours. At the most downstream location of the measurement (z/D_0 = - 2.47) it can be seen that total pressure is more uniform than at z/D_0 = - 0.82.

The total pressure loss is high behind the jet injectors and very low values of losses are found in regions between the wakes of the jet struts. These low loss regions are due to the effect of confinement of the outer duct. The effect of confinement is, perhaps, more vivid in the Mach number contours at z/D_0 = - 0.82 from the computational data as

shown in Figure 6.8. The high Mach number regions between the wakes of the jet are clearly due to the effect of the confining duct which constrains the radial expansion of the flow. This observation is important because the downstream circumferential total pressure (or Mach number) distribution is intrinsically connected to the number of jets and their arrangement and has a bearing on the design of an air jet distortion system. This statement is further elaborated below.

The circumferential total pressure and Mach number distribution at z/D_0 = - 0.82 is shown in Figure 6.9(a); only rings 1, 3 and 5 are shown for brevity (see Figure 5.4 for the location of the rings and Figure 6.1 for the location of the jets). The total pressure distribution is uniform in the innermost ring (ring 1). For the other rings the peak values occur in between the wakes and the dips are behind the jet injectors. This 'V' shaped distribution is characteristic of the four jet system. Of course, the amplitude of the dips and peaks can be varied by varying the mass flow ratios in the jets, which is discussed later in Section 6.4.2.3. However, the 'V' shaped distribution is not altered. It thus becomes clear that to obtain total pressure distributions as required for gas turbine testing a four jet system would not suffice. The number of jets has to be increased and these issues are discussed further in Chapter 7.

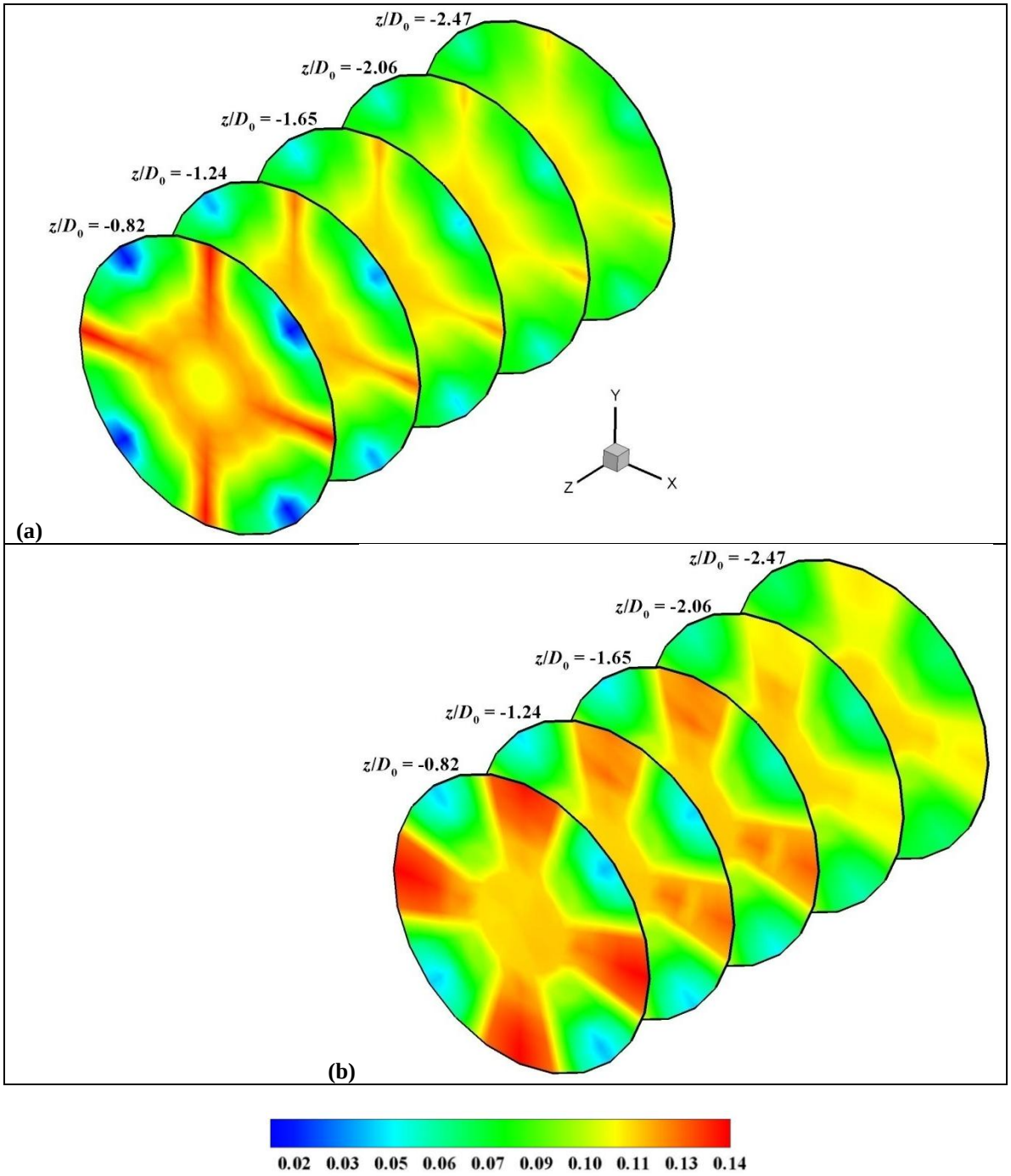

Figure 6.7 Contours of total pressure loss expressed as 1 – (p_0/p_{01}) at several locations behind the jet injectors. (a) Computations and (b) experiments; m_2/m_4 = 0.165.

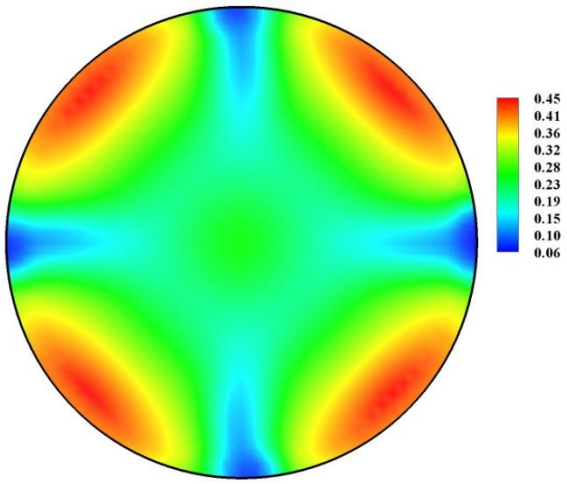

Figure 6.8 Contours of Mach number at z/D_0 = - 0.82; m_2/m_4 = 0.165. The regions of high Mach number are due to the effect of the confining duct.

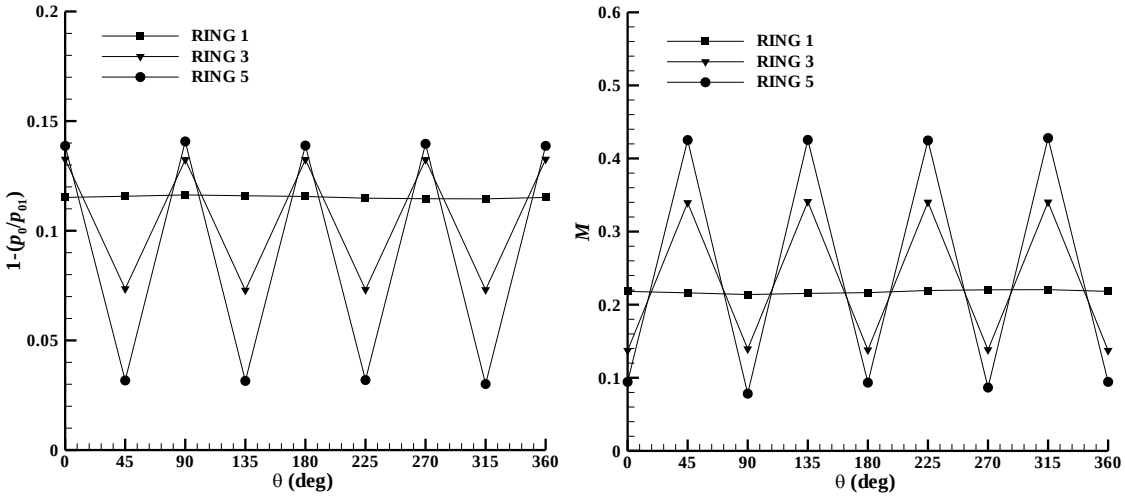

(a) **(b)**

Figure 6.9 (a) Total pressure loss and (b) Mach number distribution in rings 1, 3 and 5 at z/D_0 = - 0.82; m_2/m_4 = 0.165.

6.4.1.5 Total Pressure Loss

The loss in total pressure due to the jets mixing with the counterflow stream was quantified by a non-dimensional total pressure loss parameter which was defined in equation 5.3.

The total pressure loss evaluated numerically and obtained from experiments is shown in Figure 6.10. The agreement is good. The total pressure loss estimated from a from a quasi-one-dimensional control-volume analysis of the flow system solving the inviscid, steady-state continuity, momentum, and energy equations, as described in Appendix 2, is also shown in this figure. In this analysis it is only the total mass flow rate from the four jets m_2 that decides the total pressure loss for a given inlet Mach number. The other two methods in this figure account for the change in total pressure loss for different mass flow rates in the jets.

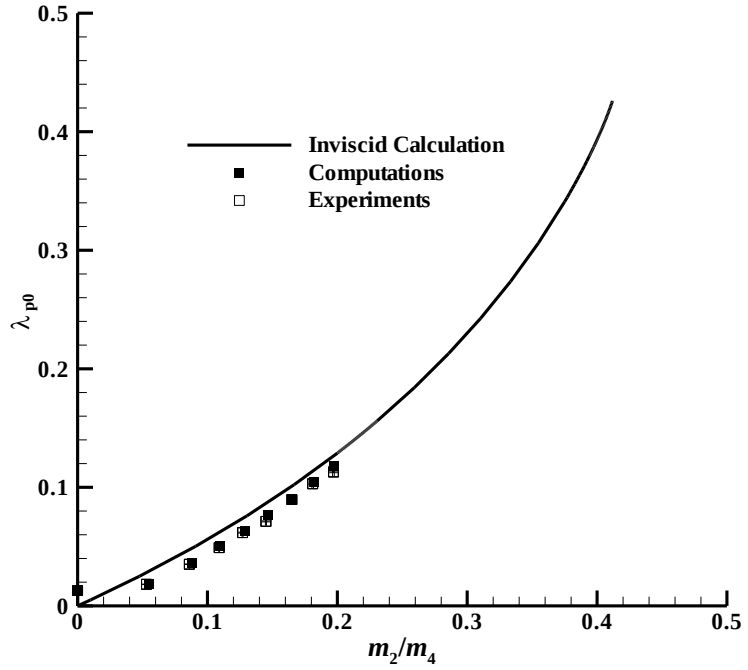

Figure 6.10 Total pressure loss λ_{p0} (equation 5.3) plotted as a function of m_2/m_4. The continuous dark curve is from one-dimensional inviscid analysis. The error bars on the experimental data are shown for the open symbols.

6.4.1.6 Total Pressure Distortion

The total pressure non-uniformity is quantified by Distortion Index *DI*, which is defined in equation 5.5. The distortion indices were calculated from the forty total pressure measurements from the experiments and similarly from the computations. The

distortion indices obtained at several locations downstream of the jet injector are shown in Figure 6.11. The computational results agree well with the experimental data.

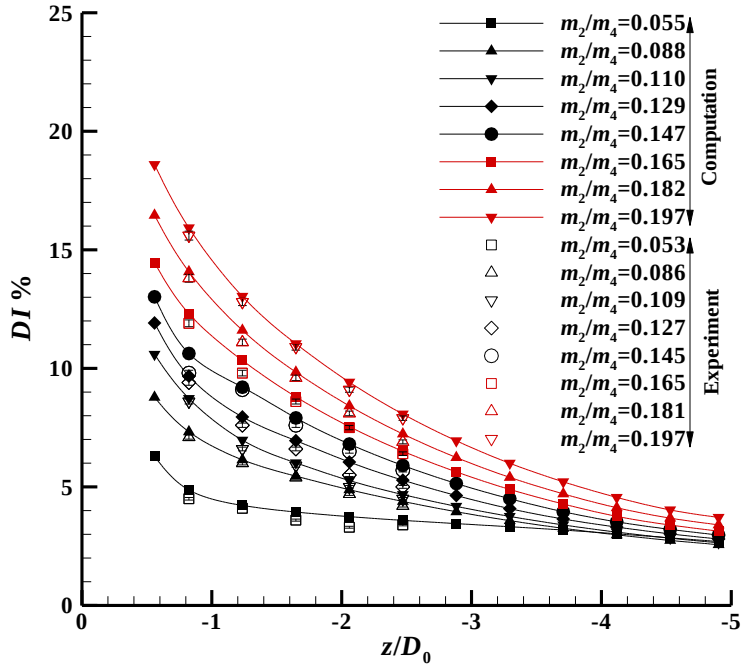

Figure 6.11 Distortion Index (*DI*) at several locations behind the jet injectors plotted for different values of m_2/m_4. The error bars on the experimental data are shown for the open symbols.

The distortion index increases with an increase in the mass flow ratio. The highest distortion index occurs at a plane just downstream of the jet injector for all mass flow ratios. At far downstream locations low values of distortion index are observed.

6.4.1.7 Total Pressure Distribution and Distortion at Aerodynamic Interface Plane

The total pressure distribution and distortion at the Aerodynamic Interface Plane (*AIP*) is examined in this section for three typical mass flow ratios m_2/m_4 = 0.110 (*DI* = 7.619 %), 0.165 (*DI* = 11.254 %) and 0.197 (*DI* = 14.291 %).

The total pressure contours represented by [1 – (p_0/p_{01})], the ring-wise total pressure loss distribution and the circumferential and radial distortion parameters for the three mass flow ratios are plotted in Figure 6.12(a) to (c). In general, the total pressure

loss increases with increase in mass flow ratio (as was also seen from Figure 6.10) resulting in larger peak to dip amplitude in the ring-wise pressure distribution. The pressure distribution is uniform in the innermost ring (ring 1); this is due to the geometry of the flow system as the jet stems do not extend till and beyond ring 1. The circumferential distortion parameter *IDC* for all the rings (including ring 1) increases with increase in mass flow ratio. *IDC* is found to be highest at the outermost ring for all mass flow ratios except m_2/m_4= 0.110 where it is highest in ring 4. The radial distortion parameter *IDR* also increases with increasing mass flow ratio and the highest *IDR* is found in ring 1 except for m_2/m_4 = 0.110 where it is highest in ring 2.

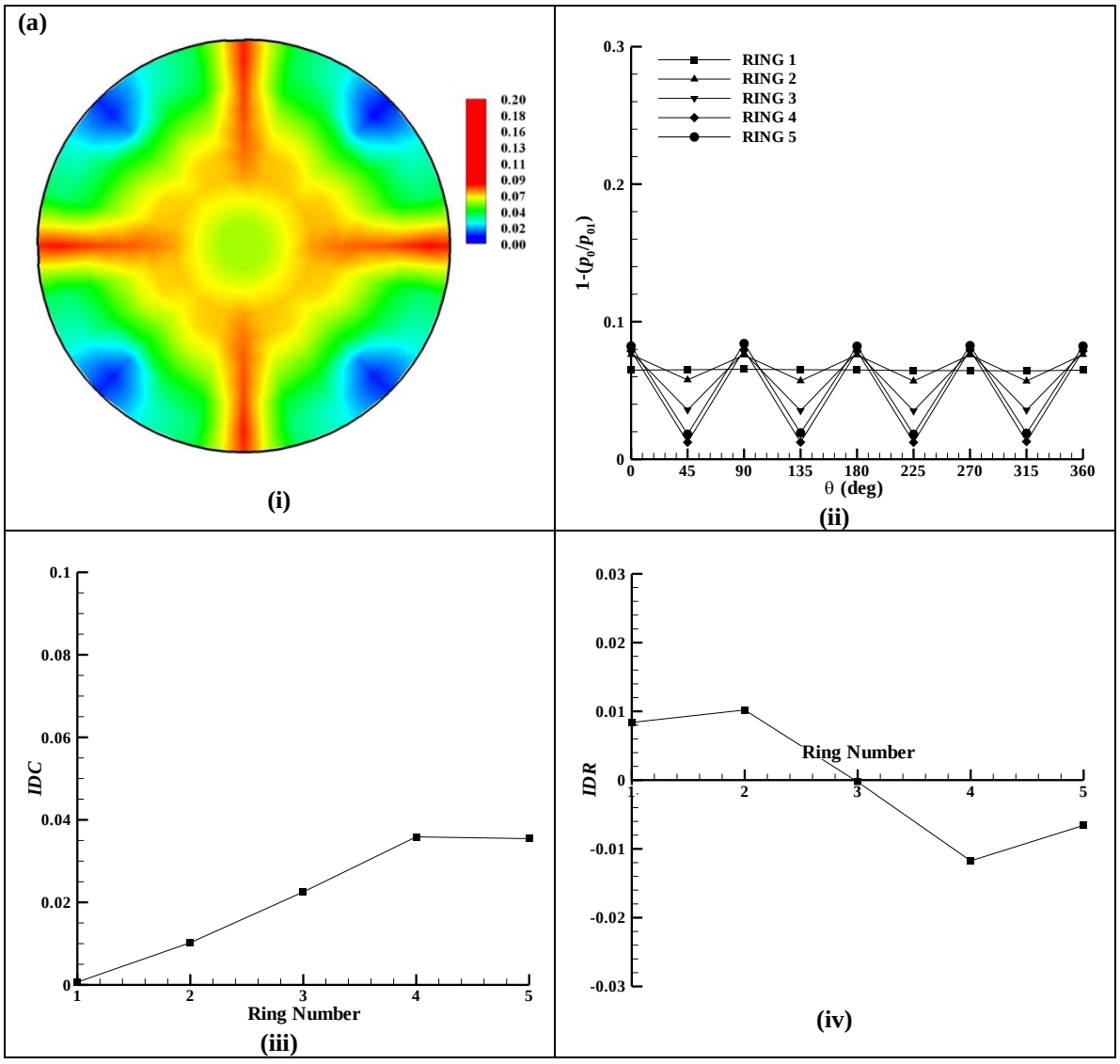

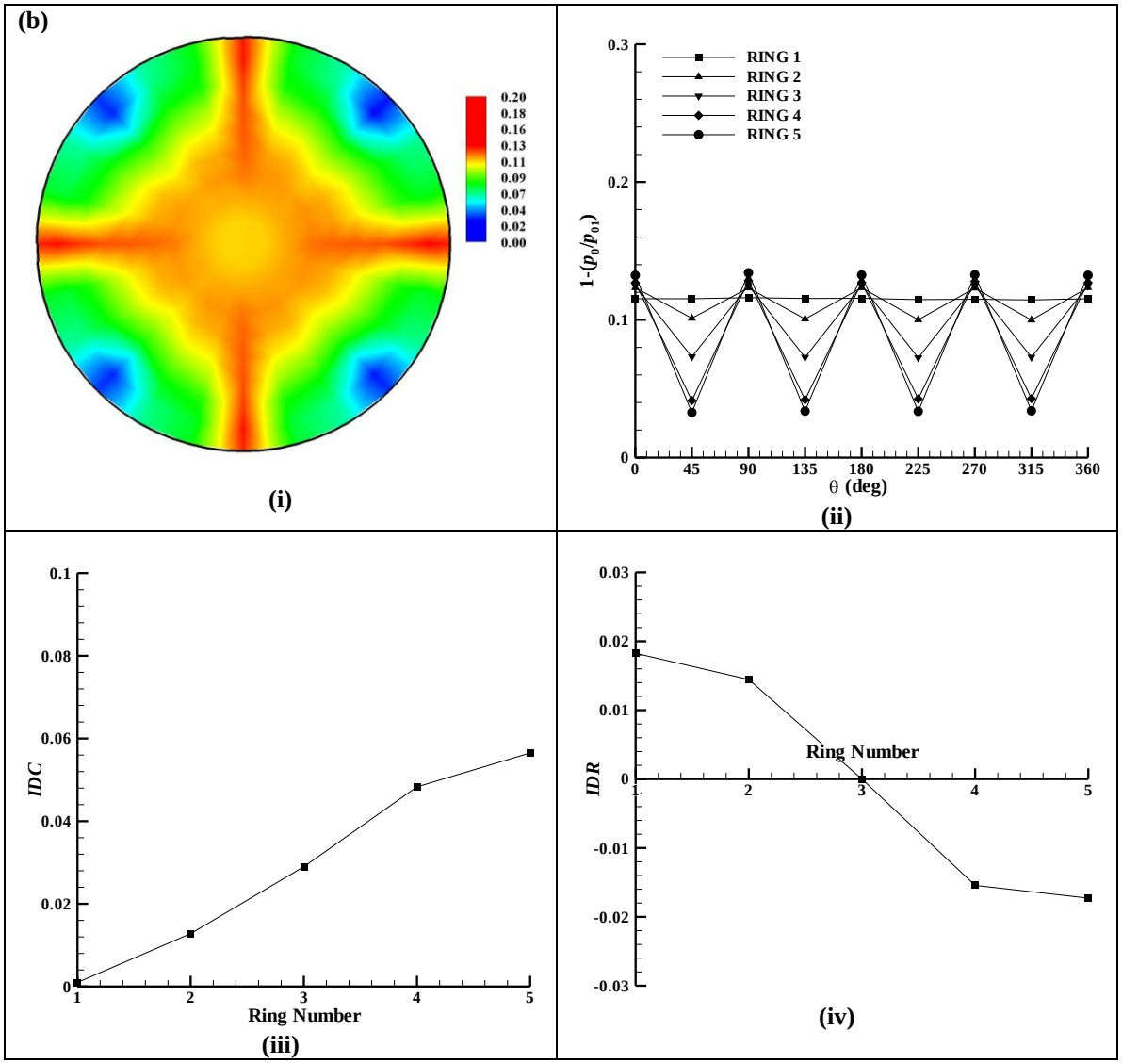
(b)
0.20
0.18
0.16
0.13
0.11
0.09
0.07
0.04
0.02
0.00
(i)
RING 1
RING 2
RING 3
RING 4
RING 5
1-(p0/p01)
θ (deg)
(ii)
IDC
Ring Number
(iii)
IDR
Ring Number
(iv)

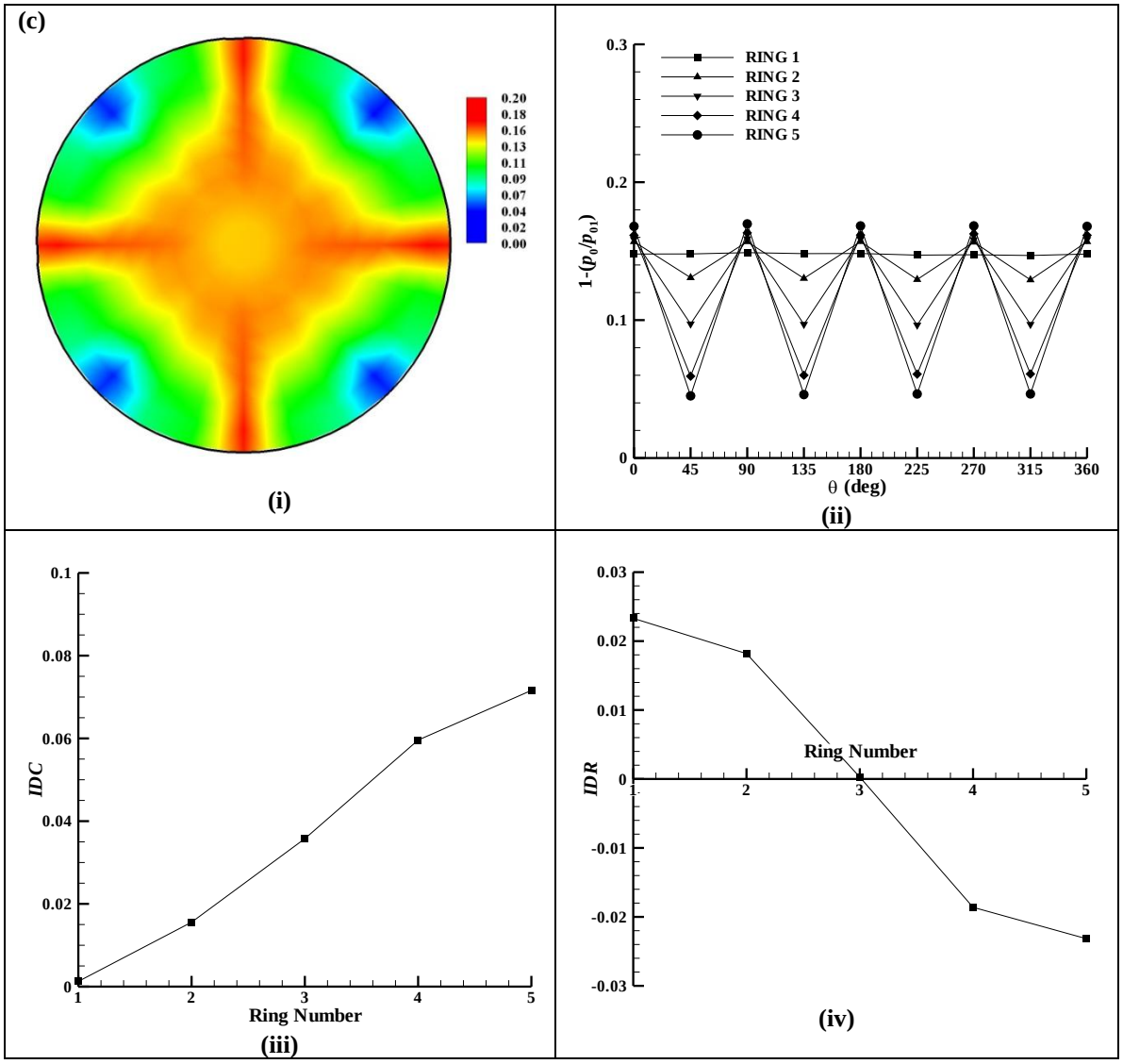

Figure 6.12 Distortion parameters at the *AIP* for (a) m_2/m_4 = 0.110, (b) m_2/m_4 = 0.165 and (c) m_2/m_4 = 0.97. In these figures (i) contours of total pressure loss [1 – (p_0/p_{01})], (ii) distribution of total pressure loss in each of the five rings, (iii) the circumferential distortion parameter *IDC* and (iv) the radial distortion parameter *IDR* in the rings.

6.4.2 Unequal Mass Flow Rates in the Jets

The potential capability of the air jet distortion system in producing non-uniform total pressure patterns can greatly be tapped by injecting unequal mass flow rates in the jets. In this section results are presented for such flow cases with the four jet system.

For a given number of jets in the system the possible permutations of mass flow rates amongst the jets in very large. A strategy is to be adapted to keep the mass flow rate combinations to a realisable level. Let a (large) value of mass flow rate in one of the jets be 100 %. Then the mass flow rates in the other jets can be fractions of the mass flow rate in one jet, say, 100 %, 75 %, 50 % and 25 %, respectively. Thus for a four jet system with each one being set at any one of the four settings (100 %, 75 %, 50 % and 25 %) the total number of combinations is 4^4 = 256. The four settings chosen are arbitrary since the intermediate values and zero are not included; but the purpose here is to establish a procedure. Even with only four jets this is a very large number to perform any kind of parametric study. However, by a careful look at the physical arrangement of the four jets and the permutations of mass flow rates in the four jets one can eliminate those which can be obtained by rotation and mirror symmetry. It is found that only 55 sets out of these 256 sets are unique.

For example, if the mass flow rates in the four jets are arranged as {100 % : 75 % : 50 % : 25 %}, this permutation is the same as {75 % : 50 % : 25 % : 100 %}, {50 % : 25 % : 100 % : 75 %} and {25 % : 100 % : 75 % : 50 %} due to same cyclic order. This situation is illustrated graphically in Figure 6.13(a). Also consider the combination {100 % : 75 % : 50 % : 25 %} which is the same set as {50 % : 75 % : 100 % : 25 %} or {100 % : 25 % : 50 % : 75 %} due to mirror symmetry; this is depicted in Figure 6.13(b).

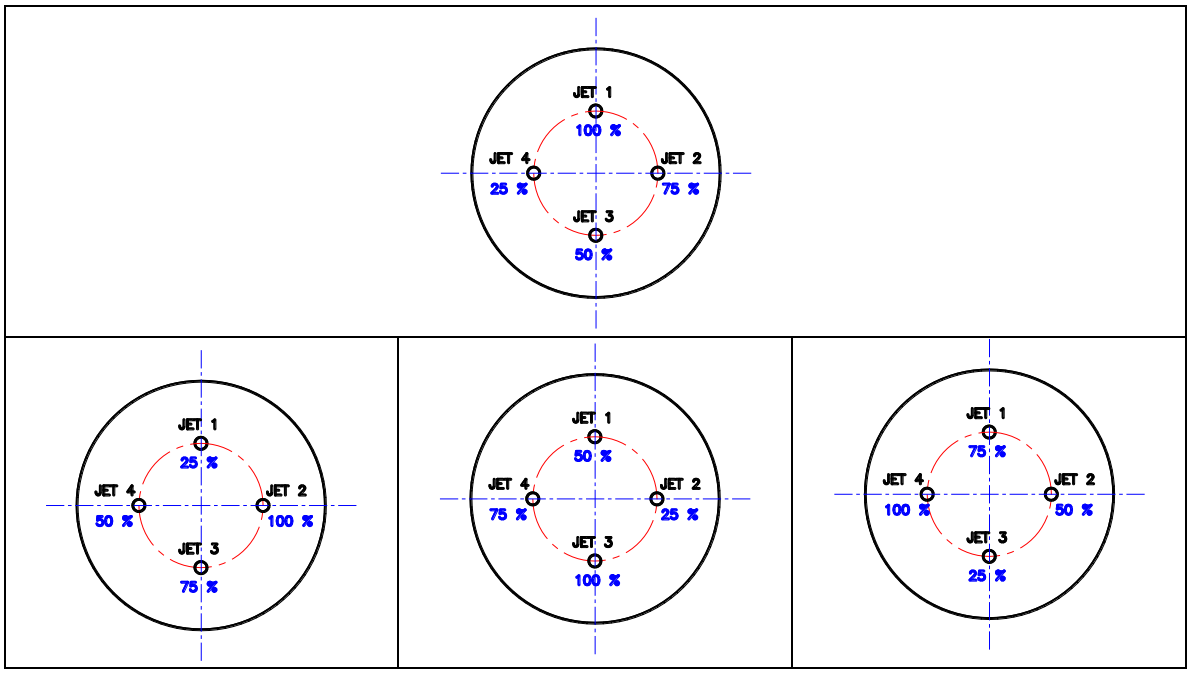

(a)

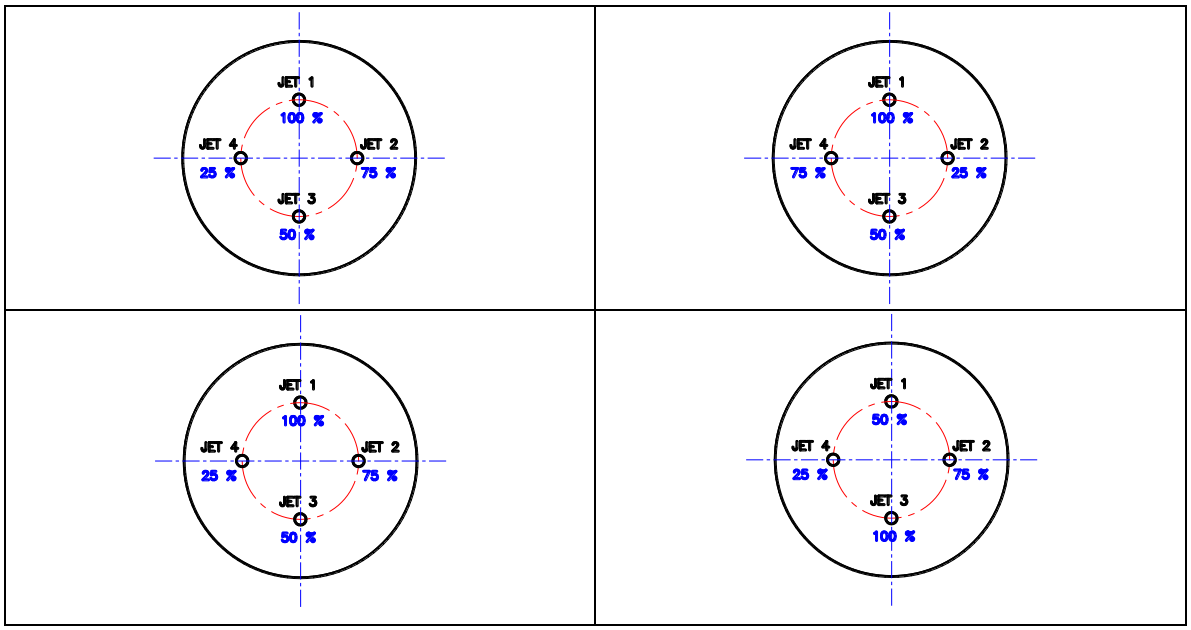

(b)

Figure 6.13 Physical arrangement of the four jets and their mass flow rates exhibiting (a) cyclic degeneracy and (b) mirror symmetry.

Starting with this small set with four jets and each jet having any one of the only four flow rates 100 %, 75 %, 50 % and 25 % enabled us to count and infer that of the 256 permutations only 55 of them are unique. The total mass flow rate in this set has the lowest value of 100 (all four jets having 25 % flow rate) and the highest value of 400 (all four jets having 100 % flow rate). It is easy to see that there are only 13 combinations of total flow rates from 100 to 400. Corresponding to each combination of total mass flow rate there are different permutations of individual jet mass flow rates, totalling to 55 as mentioned above; the histogram in Figure 6.14 gives the details.

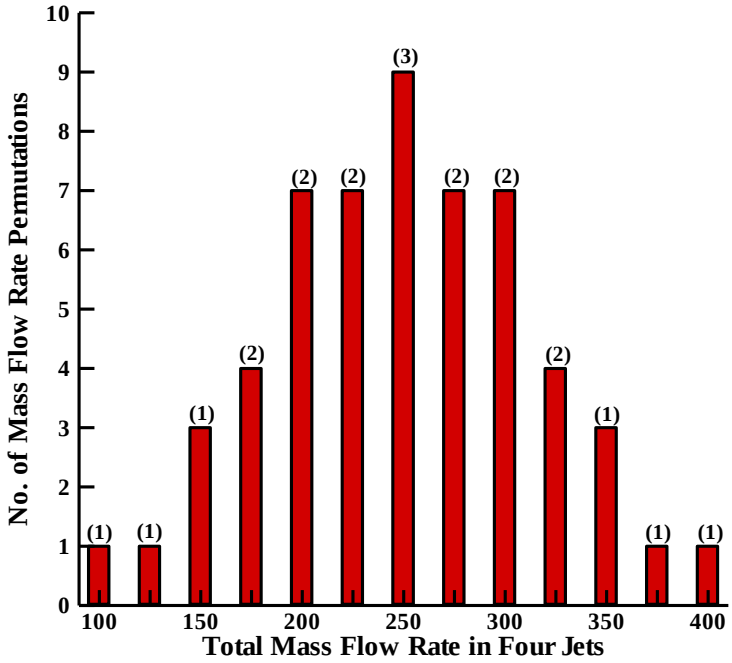

Figure 6.14 Histogram showing the number of cases for each total mass flow rate. The numbers in parantheses above each of the 13 bars indicate the number of flow cases chosen for computation summing to 21.

From the 55 permutations of mass flow rates 21 sets were chosen for computations. The mass flow rate in the jets was summed and sample sets were picked from each total mass flow rate case based on a ranking scheme where the fourth moment of the mass flow rate difference between the adjacent jets were calculated. The highest

and lowest moment sets were selected and some intermediate sets were also chosen. The fourth moment is calculated as

$$F = \sum \left(\frac{\Delta \phi^4}{4} \right)^{1/4} \tag{6.1}$$

where $\Delta\varphi$ is the difference in mass flow rate between the adjacent jets.

The total of 21 sets chosen from each total mass flow rate case is shown in the histogram in Figure 6.14. The number of sets chosen from each case for computation is shown in parentheses above the bars. These 21 sets are representative of the 55 sets which are the only unique sets from the 256 permutations. The selected 21 cases and their mass flow ratios are listed in Table 6.1. In this table the total pressure loss and distortion index at the *AIP* are also listed which were evaluated from computations. It may be mentioned that the cases 1, 7, 16 and 21 listed in this table have equal mass flow rates in the four jets.

Table 6.1 The flow cases chosen for computations and their overall total pressure loss and distortion index from computations are listed.

Sl. No.	Inlet Mach number, M_1	Inlet mass flow rate, m_1 (kg/s)	Jet mass flow rate, m_{2j} %				Total jet mass flow rate, m_2 (kg/s)	Mass flow ratio, m_2/m_4	Total pressure loss, λ_{p0}	Distortion Index, *DI* % at the *AIP*
			Jet 1	Jet 2	Jet 3	Jet 4				
1.	0.175	0.621	25	25	25	25	0.084	0.119	0.046	5.132
2.	0.186	0.659	50	25	25	25	0.105	0.137	0.063	8.896
3.	0.214	0.754	75	25	25	25	0.126	0.143	0.083	14.632
4.	0.257	0.895	100	25	25	25	0.147	0.141	0.108	22.063
5.	0.184	0.652	50	50	50	25	0.147	0.184	0.095	13.170
6.	0.248	0.864	100	25	50	25	0.168	0.163	0.125	21.350
7.	0.178	0.632	50	50	50	50	0.168	0.210	0.113	10.257
8.	0.244	0.852	100	25	75	25	0.190	0.182	0.144	21.058
9.	0.186	0.660	75	50	50	50	0.190	0.223	0.131	14.327
10.	0.220	0.773	100	75	50	25	0.211	0.214	0.154	27.495
11.	0.253	0.881	100	25	100	25	0.211	0.193	0.166	27.290
12.	0.188	0.668	75	75	50	50	0.211	0.240	0.149	17.432
13.	0.231	0.811	100	50	100	25	0.232	0.222	0.180	24.799
14.	0.185	0.658	75	75	75	50	0.232	0.261	0.166	18.276
15.	0.217	0.765	100	75	100	25	0.253	0.249	0.192	23.893
16.	0.178	0.633	75	75	75	75	0.253	0.286	0.182	17.511
17.	0.212	0.749	100	100	100	25	0.275	0.268	0.208	32.021
18.	0.183	0.651	100	75	75	75	0.275	0.296	0.203	23.597
19.	0.198	0.699	100	100	100	50	0.296	0.297	0.223	29.269
20.	0.182	0.646	100	100	100	75	0.317	0.329	0.239	27.320
21.	0.175	0.622	100	100	100	100	0.338	0.352	0.256	26.316

6.4.2.1 Velocity Field

The velocity profiles at several axial locations in the duct are plotted in Figure 6.15 for m_2/m_4 = 0.214 (Sl. No. 10 in Table 6.1); the mass flow rates in the jets are $m_{2,1}$ = 0.085, $m_{2,2}$ = 0.063, $m_{2,3}$ = 0.042 and $m_{2,4}$ = 0.021 kg/s. The computational results agree reasonably well with the experiments. The geometries of the jets constructed from the computational data are also shown in Figure 6.15 which are the loci of u = 0.

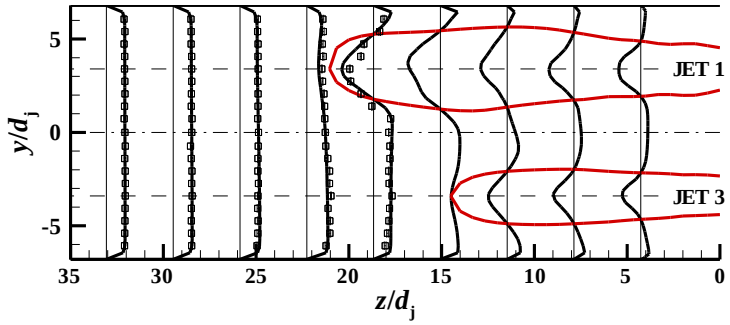

(a)

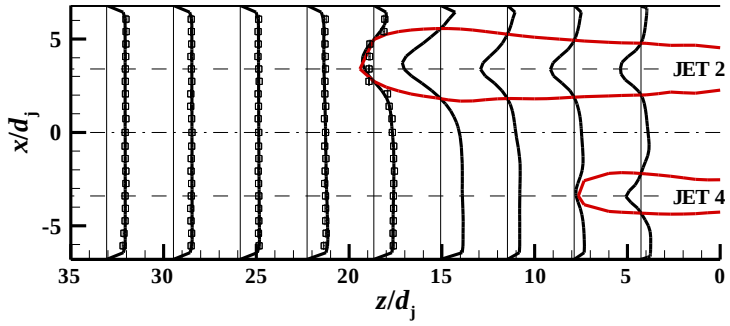

(b)

Figure 6.15 Profiles of axial velocity at several locations in the duct; (a) jets 1 and 3 (b) jets 2 and 4. The continuous dark curves are from computations and open symbols are experimental data. The geometry of the jet is also shown in this figure. The error bars on the experimental data are shown for the open symbols.

6.4.2.2 Centreline Mach Number Distribution

The Mach number variation along the centreline of the four jets is plotted in Figure 6.16 for m_2/m_4 = 0.214. The nozzles are choked and each sonic jet exits into the counterflow stream as an underexpanded jet and expands further on exit into the duct

resulting in the shock-cells. The peak Mach number in the shock-cell increases with increasing mass flow ratio which amounts to increasing pressure ratio. The Mach number along the jet centreline reduces till the stagnation point and then increases and eventually reaches the counterflow stream value.

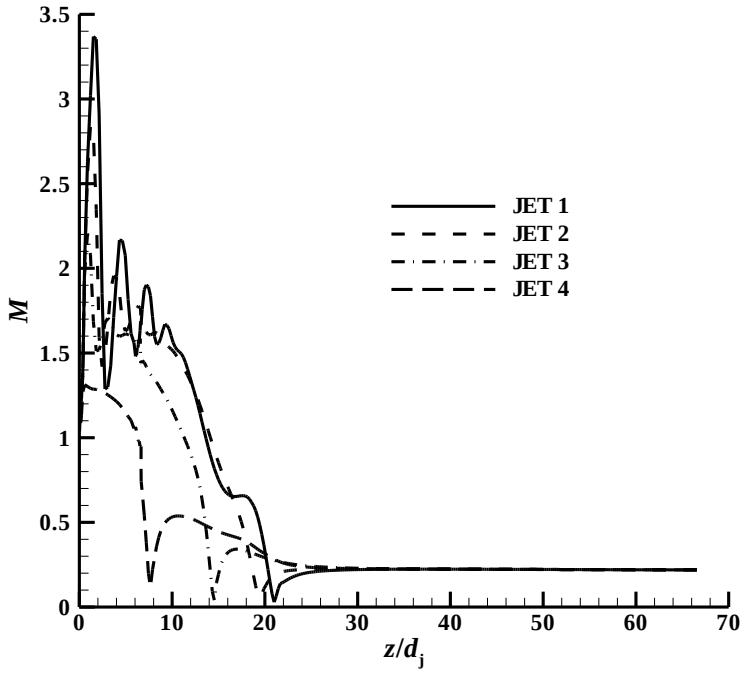

Figure 6.16 Variation of Mach number along the jet centreline. This variation is shown for the four jets for m_2/m_4 = 0.214.

The mass flow rates in the jets are listed in Section 6.4.2.1 and their corresponding pressure ratios (p_{02}/p_1) are 8.10, 6.06, 4.03 and 1.99. The contours of Mach number are shown in Figure 6.17 for this mass flow ratio. The shock-cell just downstream of the exit of the jets is clearly visible in this figure.

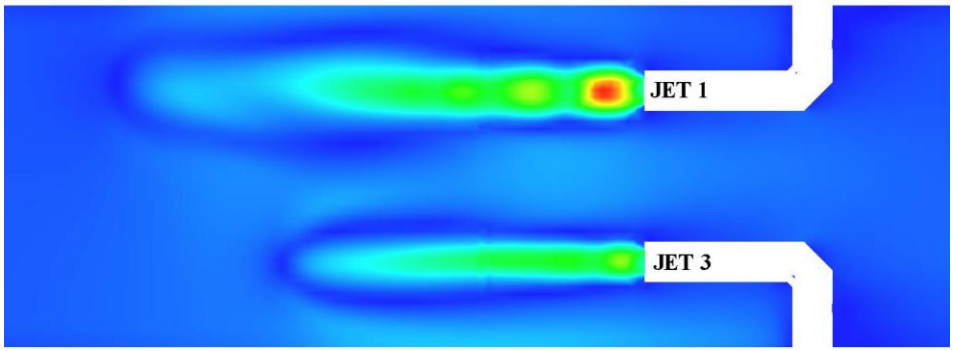

(a)

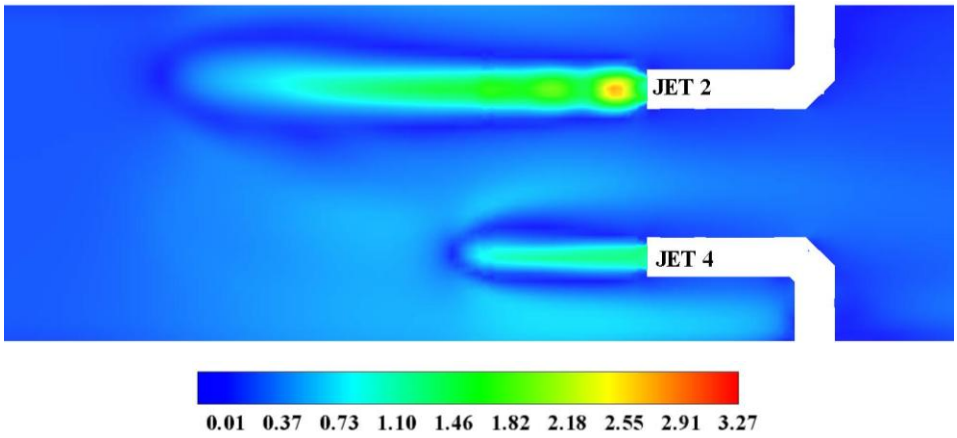

(b)

Figure 6.17 Contours of Mach number; m_2/m_4 = 0.214. (a) Jets 1 and 3 (b) jets 2 and 4.

6.4.2.3 Total Pressure Loss Distribution

The contours of total pressure loss downstream of the jet injectors in terms of 1-(p_0/p_{01}) is shown in Figure 6.18 for m_2/m_4 = 0.214 from both the computations and experiments. The wake behind the jet injectors is clearly seen in the contours. At the most downstream location of the measurement (z/D_0 = - 2.47) it can be seen that total pressure is more uniform than at z/D_0 = - 0.82.

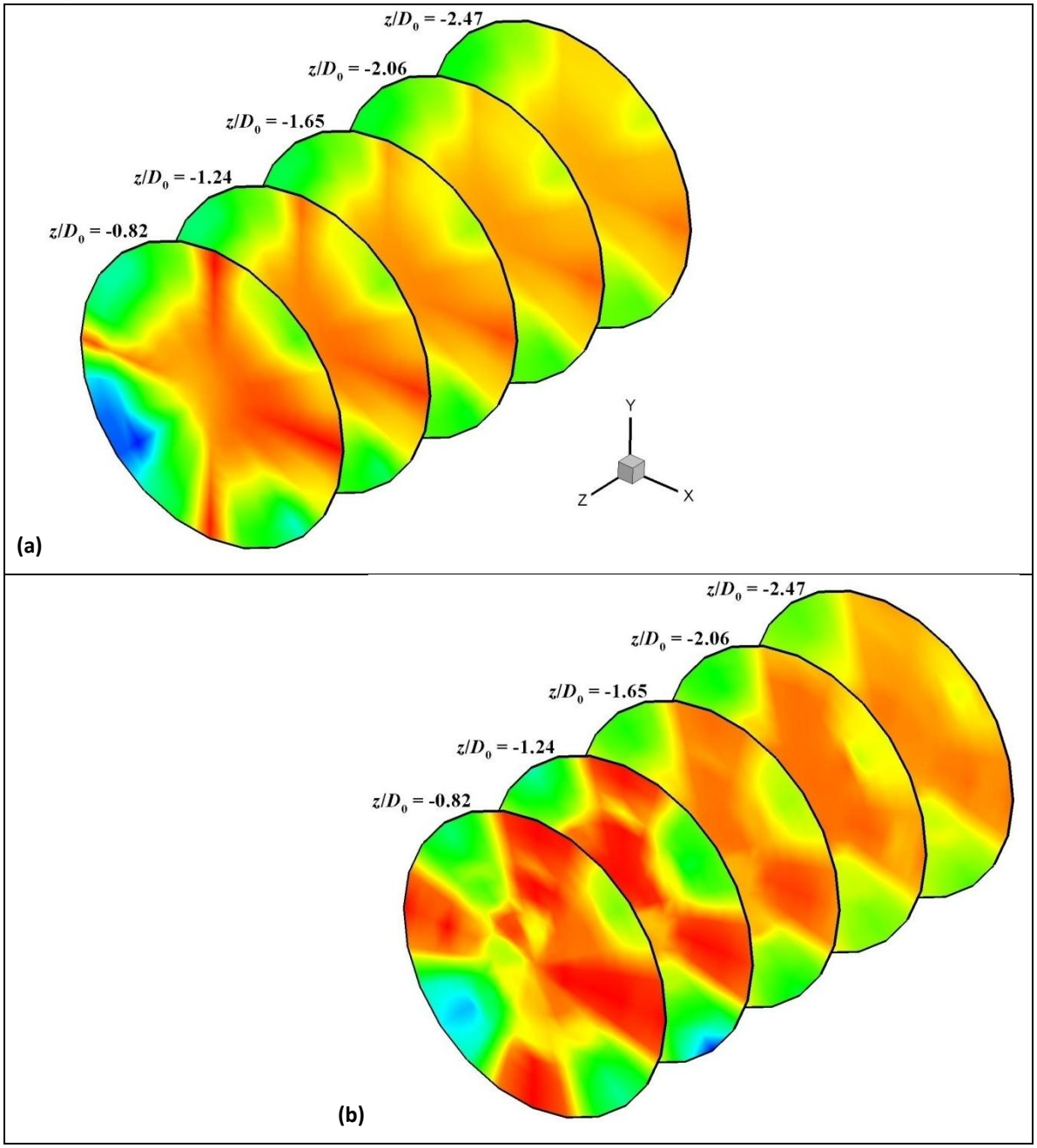

Figure 6.18 Contours of total pressure loss expressed as 1 – (p_0/p_{01}) at several locations behind the jet injector (a) computations and (b) experiments; m_2/m_4 = 0.214.

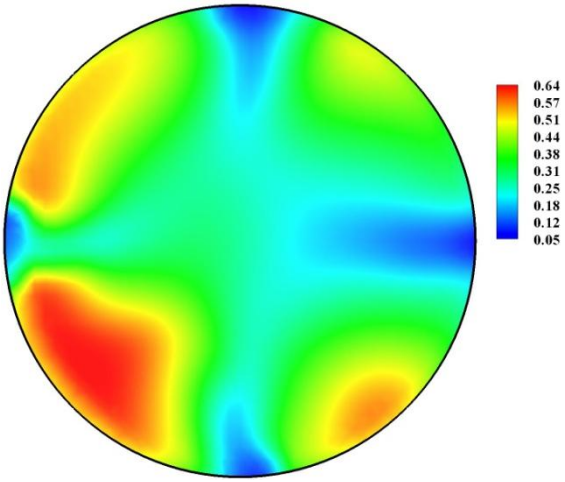

Figure 6.19 Contours of Mach number at z/D_0 = - 0.82; m_2/m_4 = 0.214. The regions of high Mach number are due to the effect of the confining duct. (See Figure 6.8 for Mach number distribution with equal mass flow rates in the jets.)

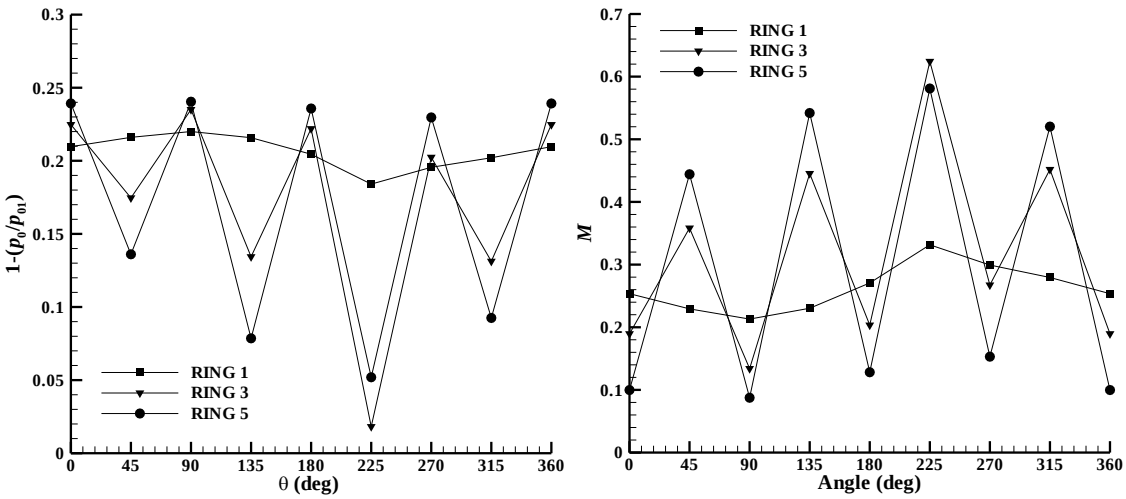

(a) **(b)**

Figure 6.20 (a) Total pressure loss and (b) Mach number distribution in rings 1, 3 and 5 at z/d_j = - 11.2; m_2/m_4 = 0.165.

Following the discussions in Section 6.4.1.4, the Mach number contours at z/D_0 = - 0.82 from the computational data are shown in Figure 6.19. The high Mach number regions between the wakes of the jet are clearly due to the effect of the confining duct which constrains the radial expansion of the flow. The circumferential total pressure and

Mach number distribution at z/D_0 = - 0.82 are shown in Figure 6.20 in rings 1, 3 and 5. As compared to Figure 6.9 the amplitudes from the dips to peaks are altered by varying the mass flow rates in the jets. However, the 'V' shaped characteristic distribution is unaffected.

6.4.2.4 Total Pressure Loss

The loss in total pressure due to the jets mixing with the counterflow stream was quantified by a non-dimensional total pressure loss parameter defined in equation 5.3.

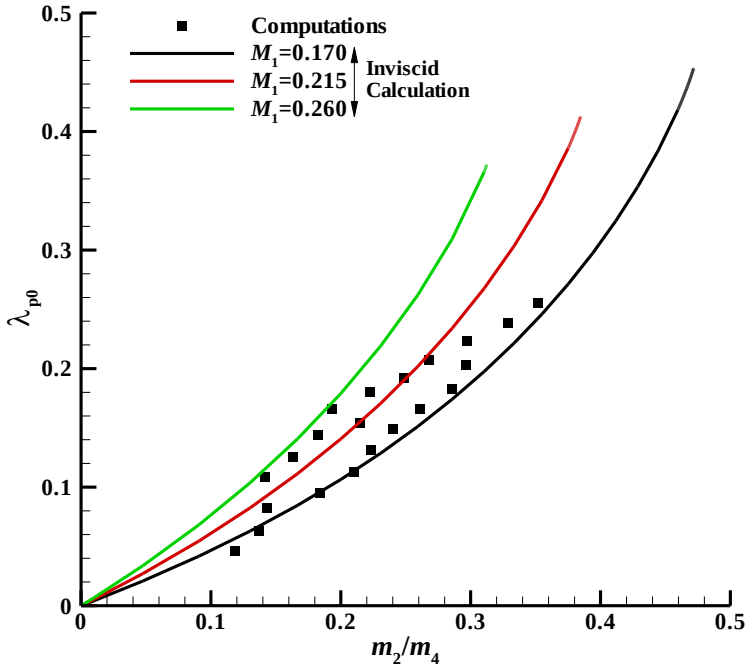

Figure 6.21 Total pressure loss λ_{p0} (equation 6.1) plotted as a function of m_2/m_4 for the 21 computations. The continuous dark curves are from one-dimensional inviscid analysis.

The total pressure loss evaluated from computations is shown in Figure 6.21. The scatter seen in this plot is because the inlet Mach number for each of these cases was different (see Table 6.2). Also shown in the same figure is the total pressure loss estimated from a quasi-one-dimensional control-volume analysis of the flow system solving the inviscid, steady-state continuity, momentum, and energy equations, as

described in Appendix 2. The total mass flow rate from the four jets is m_2 and used for the analysis. The total pressure loss increases with an increase in mass flow ratio. The total pressure loss is also higher at a higher inlet Mach number for a given mass flow ratio.

For a given total mass flow rate m_2 from the four jets we have a unique total pressure loss given by the inviscid calculations as shown in Figure 6.21. However, each value of m_2 allows different permutations of jet mass flow rates and associated total pressure distribution at the *AIP*. The computations in Figure 6.21 allow evaluation of this total pressure distribution at the *AIP*. This information aids in examining the types of total pressure distribution that can be generated at the *AIP*. Further it also helps how to invert the problem, i.e. for a given target total pressure distribution at the *AIP* how to select a jet mass flow rate permutation that can achieve the closest desirable total pressure distribution.

In the next chapter it will be shown how this idea can be utilised to generate a total pressure distribution within the specified constraints and further how its accuracy can be improved by increasing the number of jets and allowing a continuous variation of mass flow rate in each jet.

6.4.2.5 Total Pressure Distortion

The total pressure non-uniformity quantified in terms of Distortion Index *DI*, (equation 5.5) obtained at several locations downstream of the jet injector are shown in Figure 6.22. The distortion index increases with an increase in the mass flow ratio. The highest distortion index occurs at a plane just downstream of the jet injector for all mass flow ratios. At far downstream locations low values of distortion index are observed. A further important observation is that the distortion values are larger than those obtained with injecting equal mass flow rates in the jets (see Figure 6.11).

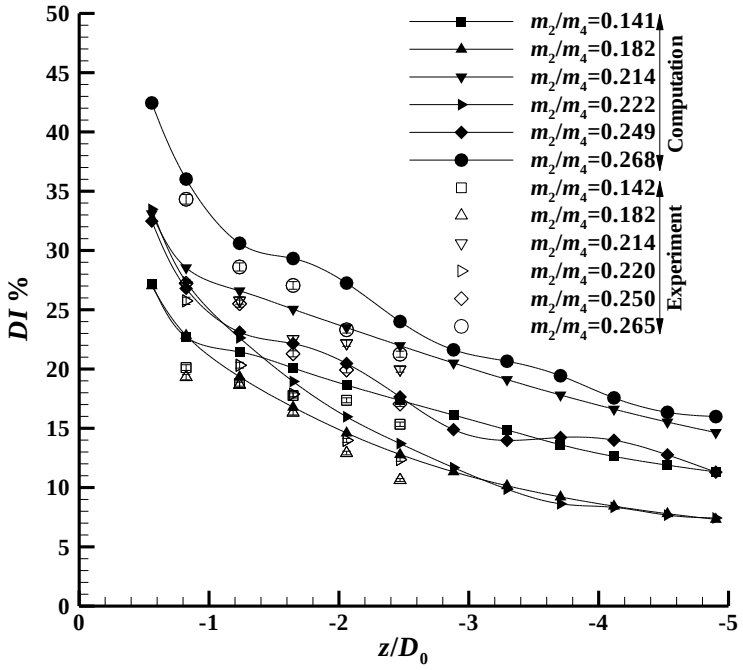

Figure 6.22 Distortion Index (*DI*) at several locations behind the jet injector plotted for different values of m_2/m_4. The error bars on the experimental data are shown for the open symbols.

6.4.2.6 Total Pressure Distribution and Distortion at Aerodynamic Interface Plane

The total pressure distribution and distortion at the Aerodynamic Interface Plane (*AIP*) is examined in this section for three typical mass flow ratios m_2/m_4 = 0.141 (*DI* = 22.063 %), 0.214 (*DI* = 27.495 %) and 0.268 (*DI* = 32.012 %).

The total pressure contours represented by [1 – (p_0/p_{01})], the ring-wise total pressure loss distribution and the circumferential and radial distortion parameters for the three mass flow ratios are plotted in Figure 6.23(a) to (c). In general, the total pressure loss increases with increase in mass flow ratio (as was also seen from in Figure 6.21) resulting in steeper dips in the ring-wise pressure distribution. The pressure distribution is nearly uniform in the innermost ring (ring 1). The circumferential distortion parameter *IDC* for all the rings increases with increase in mass flow ratio. *IDC* is found to be highest at the outer rings for all mass flow ratios. The radial distortion parameter *IDR* also increases with increasing mass flow ratio and the highest *IDR* is found in ring 1.

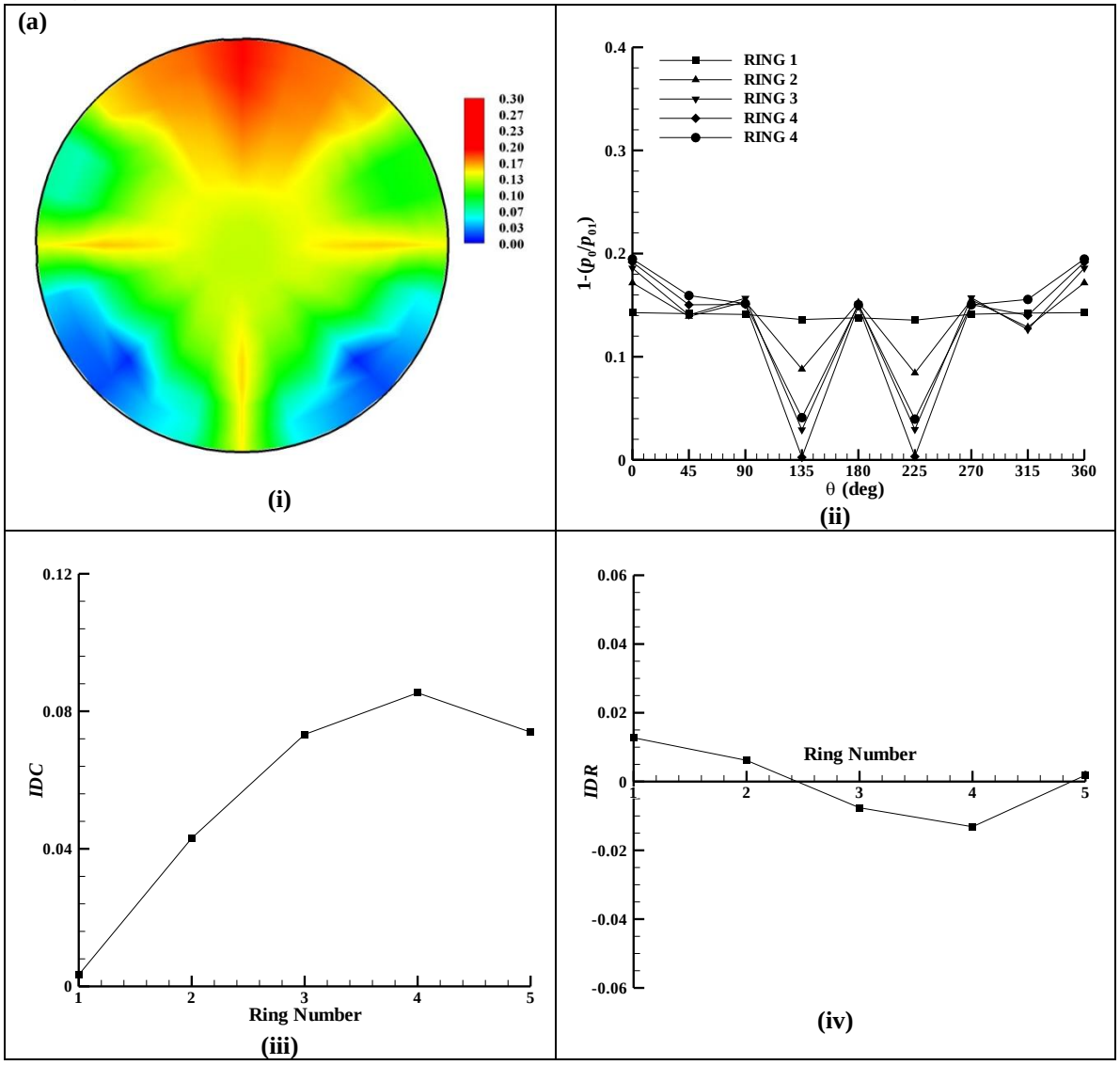
(a)
0.30
0.27
0.23
0.20
0.17
0.13
0.10
0.07
0.03
0.00
(i)
RING 1
RING 2
RING 3
RING 4
RING 4
1-(p0/p01)
θ (deg)
(ii)
IDC
Ring Number
(iii)
IDR
Ring Number
(iv)

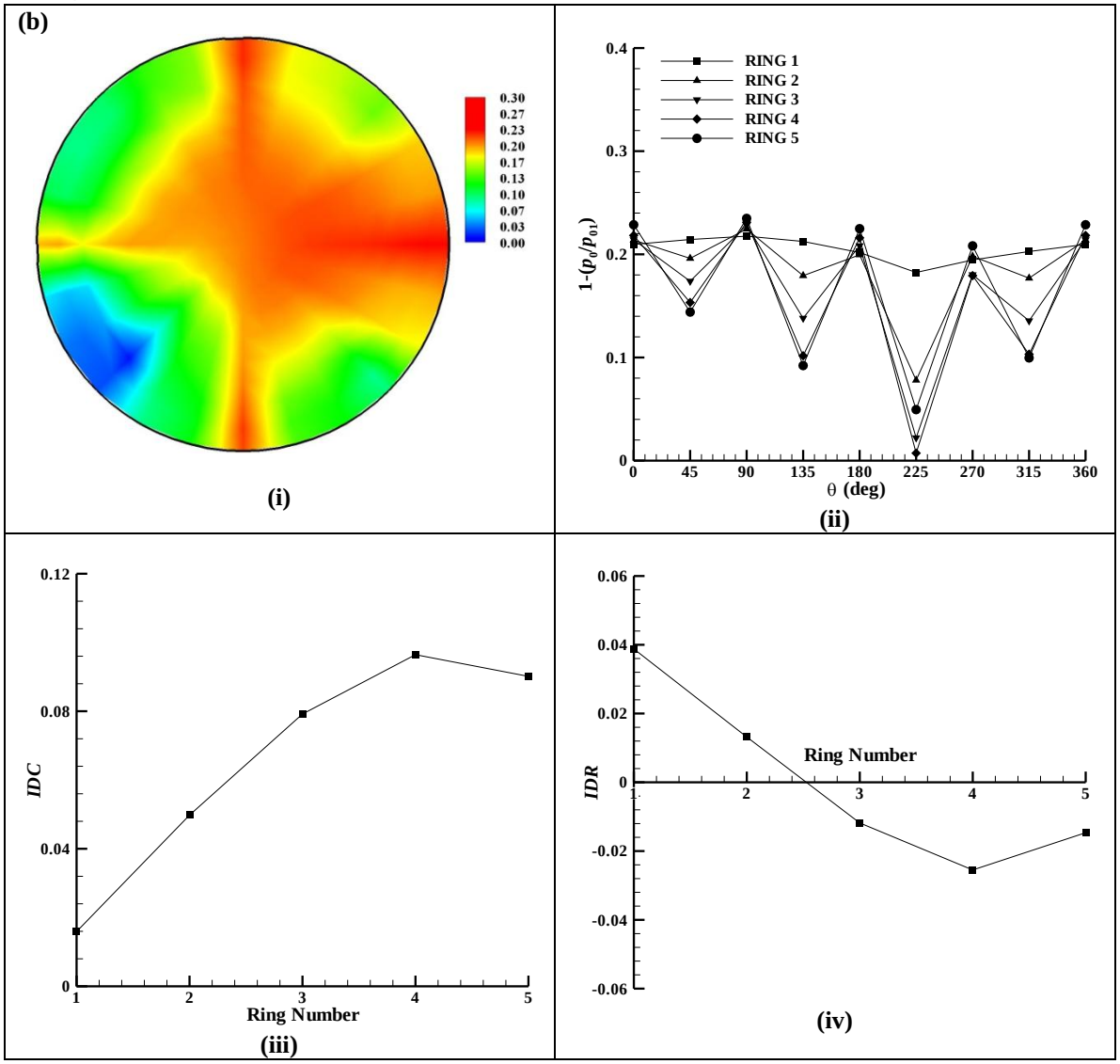
(b)
0.30
0.27
0.23
0.20
0.17
0.13
0.10
0.07
0.03
0.00
(i)
RING 1
RING 2
RING 3
RING 4
RING 5
$1-(p_0/p_{01})$
θ (deg)
(ii)
IDC
Ring Number
(iii)
IDR
Ring Number
(iv)

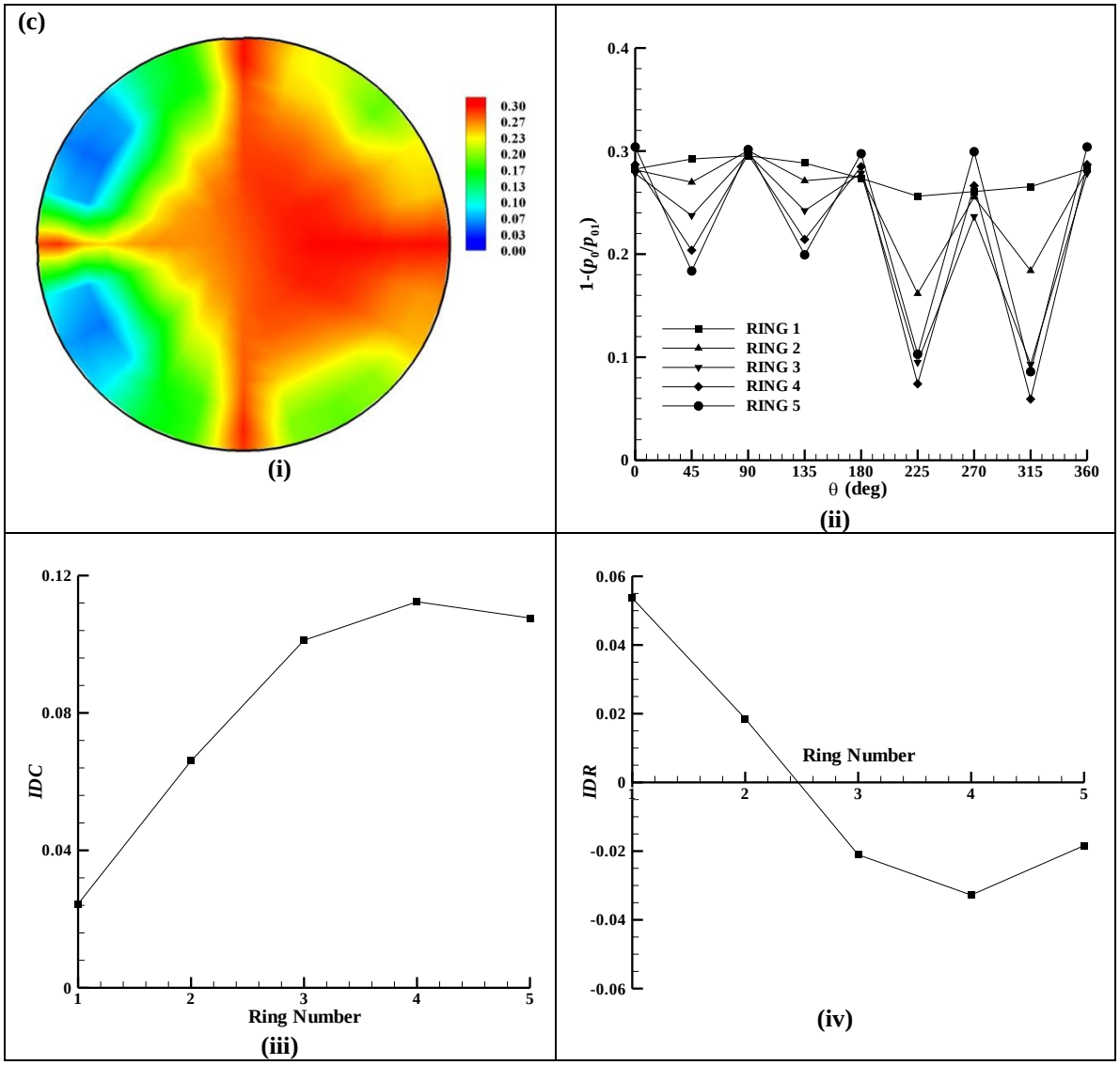

Figure 6.23 Distortion parameters at the *AIP* for (a) m_2/m_4 = 0.141, (b) m_2/m_4 = 0.214 and (c) m_2/m_4 = 0.268. In these figures (i) contours of total pressure loss [1 – (p_0/ p_{01}), (ii) distribution of total pressure loss in each of the five rings, (iii) the circumferential distortion parameter *IDC* and (iv) the radial distortion parameter *IDR* in the rings.

6.5 Summary

The mean flow field of four circumferentially arranged jets in confined counterflow was studied computationally and experimentally. For selected sets of jet mass flow rates from all possible permutations the non-repetitious cases are identified and experiments and computations were done for a select representative class. The velocity field and the total pressure field downstream of the jet injectors were obtained for different values of inlet Mach number M_1 and mass flow ratio m_2/m_4 ranging from 0.190 to 0.352. The mass flow rates in the four jets were equal in the first part of the study and in the second part they were unequal.

The total pressure loss parameter λ_{p0} increased with increasing mass flow ratio. Distortion Index (*DI*) was found to be highest at a location just downstream of the jet injector and at far downstream locations low values of *DI* were observed. The *DI* increased with an increase in mass flow ratio at all the planes. At the highest mass flow ratio for the equal mass flow rates in the jets m_2/m_4 = 0.197 the *DI* at z/D_0 = - 0.82 was about 18.596 % decreased to about 3.713 % at z/D_0 = - 4.9. Correspondingly for the unequal mass flow rates in the jets, with m_2/m_4 = 0.193 the *DI* at z/D_0 = - 0.82 was about 29.285 % decreasing to about 8.988 % at z/D_0 = - 4.9.

The total pressure distribution and total pressure distortion parameters at the *AIP* were examined for three typical mass flow ratios m_2/m_4 = 0.110, 0.165 and 0.197 with equal mass flow rates in the jets and m_2/m_4 = 0.110, 0.214 and 0.268 with unequal mass flow rates in the jets. The total pressure loss increases with increasing mass flow ratio resulting in steeper dips in the ring-wise total pressure loss distribution. The circumferential and radial distortion parameters also increased with increase in mass flow ratio.

The present study with four jets should enable us now to develop a methodology to generate a given total pressure distortion pattern. It is true that for achieving a good representation of the distortion field one needs more number of jets. But first the

methodology will be developed in the next chapter with only four jets since it is easier to understand and control a system with fewer parameters. After establishing a methodology it will be demonstrated subsequently with twelve and twenty jets.

CHAPTER 7

DEVELOPMENT OF A METHODOLOGY TO GENERATE A PRESCRIBED TOTAL PRESSURE DISTORTION PATTERN

The flow fields of single and multiple jets in confined counterflowing stream were investigated in Chapters 5 and 6, respectively. The total pressure loss and downstream total pressure distortion due a single jet and four jets were evaluated. With the successful modelling of these flow systems we are now in a position to develop a methodology to generate a prescribed total pressure distortion pattern. The method is based on the computational procedure for multiple jets in counterflow and the quasi-one-dimensional inviscid analysis is used as the starting point to estimate the overall total pressure loss. This method is described in Section 7.2. The methodology thus developed is demonstrated to generate given total pressure distortion patterns using four jets. The methodology is further extended to a larger number of jets, twelve and later twenty jets, and the total pressure patterns typical of use in aircraft gas turbine engine testing are successfully simulated.

7.1 Limits of Operation from Inviscid Analysis

The methodology developed here to generate a given total pressure distortion pattern is based on a one-dimensional evaluation of the total pressure loss due to the jet flow into a counterflowing stream as described in Appendix 2. Before the methodology is described it is prudent to investigate the regimes and limits of operation of this system in an inviscid framework. The results presented here are for the four jet system with D_0 = 102 mm and d_j = 7.5 mm. The total mass flow rate from the four jets is used for calculating the total pressure loss because it is uniquely determined by the mass flow ratio (m_2/m_4) and the inlet Mach number (M_1).

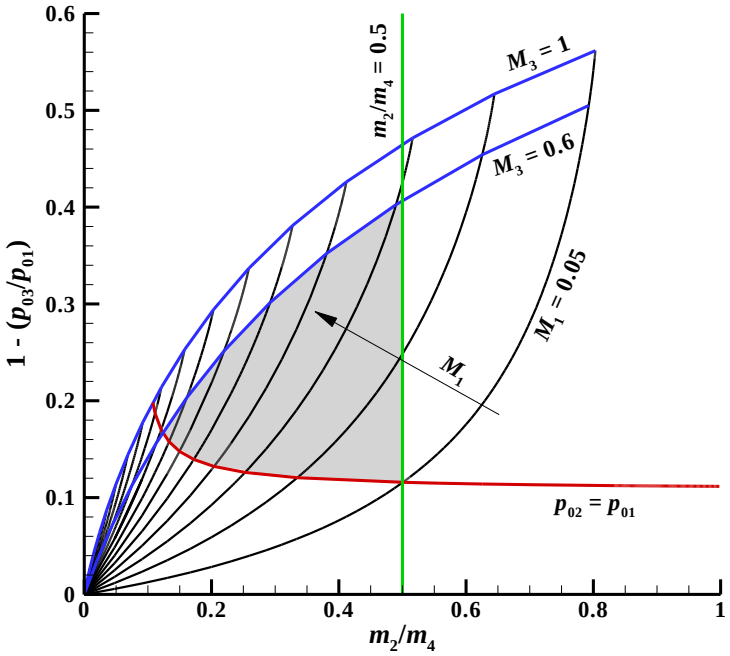

(a)

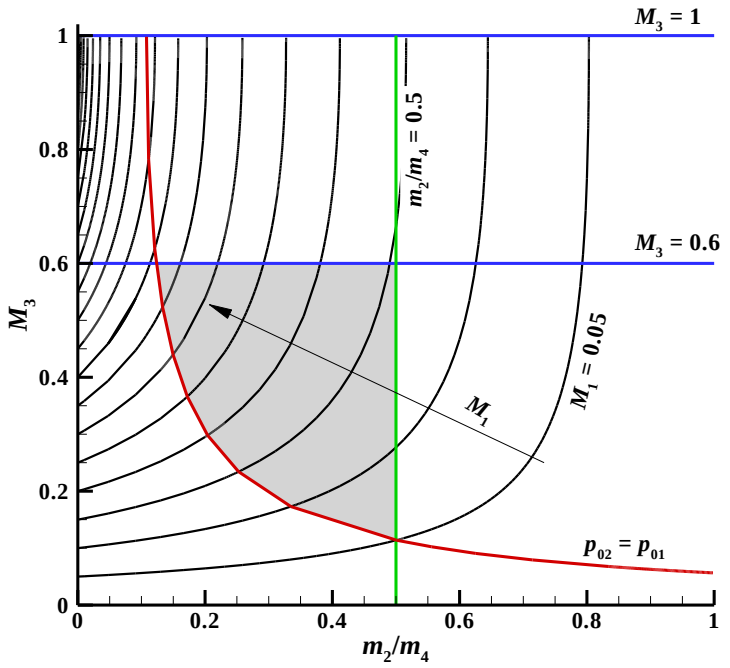

(b)

Figure 7.1 Variation of (a) total pressure loss and (b) exit Mach number (M_4) as a function of mass flow ratio m_2/m_4 for different values of inlet Mach number (M_1); $\delta M_1 = 0.05$.

The calculations were conducted for a series of inlet Mach numbers (M_1) ranging from 0.05 to 1 ($\delta M_1 = 0.05$) and various mass flow ratios (m_2/m_4). The total pressure loss due to the jets in counterflow is shown in Figure 7.1 (a). Several interesting and important observations can be immediately made from this figure. The $M_3 = 1$ limit is shown at the top of this plot. This limit places a constraint on the meaningful solutions that can be obtained from the inviscid analysis. The $M_3 = 0.6$ limit is also shown in this figure. This limit assumes importance as the mean Mach number at the inlet to the compressor face is usually below 0.6 (Serovy 1985, Walsh and Fletcher 2004) to avoid very high relative Mach number at the rotor tip and attendant excessive losses (Saravanamuttoo, Rogers and Cohen 2001). The vertical line showing the $m_2/m_4 = 0.5$ limit is also depicted in this plot. This is quite a liberal limit as it is not expected to inject more than 50 % of the total mass flow rate from the jets. Another limiting curve is the $p_{02} = p_{01}$ curve; this follows from the fact the flow system under consideration cannot exist if the total pressure in the jet is less than the total pressure in the counterflow stream (Sekundov 1969). As $m_2/m_4 \rightarrow 1$, the total pressure loss asymptotically becomes about 0.112, because, though $m_1 \rightarrow 0$ in the $m_2/m_4 \rightarrow 1$ limiting process, p_{01} (and p_{02}) remain finite leading to this asymptotic value.

Now, the exit Mach number (M_3) is plotted in Figure 7.1 (b). It is mentioned in Appendix 2 that the exit velocity can correspond to either subsonic or supersonic solution and only the subsonic solution is considered. The results are plotted here for subsonic exit Mach number till M_3 becomes unity. All the limits described above are also depicted in this figure. These limits yield the restrictions on the possible values of total pressure loss and exit Mach number and the solution space is shown by a shaded region in the figure.

7.2 Methodology

The methodology to generate a given total pressure distortion pattern is described in this section. The inputs required for this method are the average Mach number M_3 and the required total pressure distribution at the *AIP*. (It may be mentioned here that in the inviscid analysis station 3 is not defined. However, in the methodology detailed below

the flow properties at station 4 from the inviscid analysis are used at station 3 which is the *AIP*.)

The procedure to simulate a given total pressure distribution is as follows:

1. From the given total pressure distribution the average total pressure loss $[1 - (p_{03}/p_{01})]_{ave}$ is formed. It may be noted that p_{01} is uniform.
2. The inlet Mach number (M_1) is evaluated from M_3 and $[1 - (p_{03}/p_{01})]_{ave}$ from Figure 7.2.

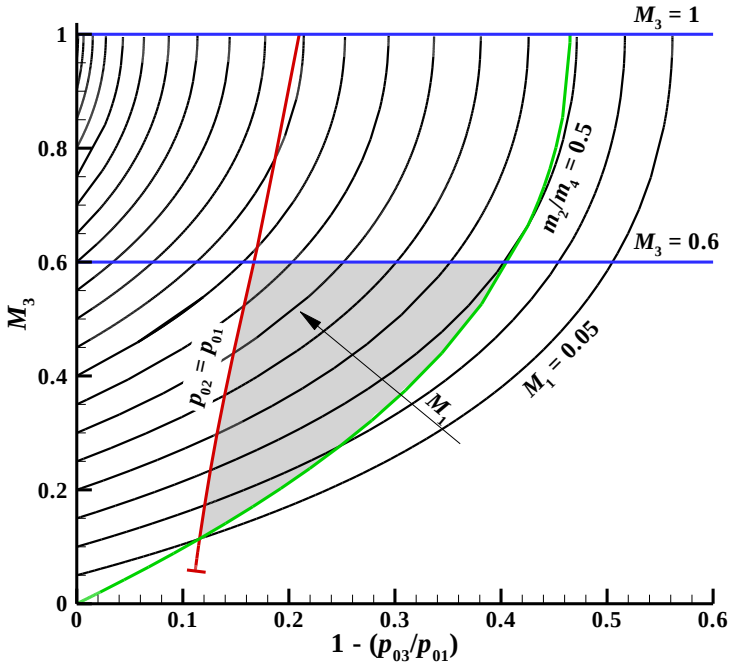

Figure 7.2 Variation of average Mach number M_3 as a function of total pressure loss for different values of inlet Mach number (M_1); $\delta M_1 = 0.05$.

3. The inlet mass flow rate m_1 can be calculated from M_1 by assuming inlet total pressure (p_{01}) and total temperature (T_{01}) using isentropic relations.
4. The mass flow ratio (m_2/m_4) required to exert the required total pressure loss can be estimated from Figure 7.1(a). It has to be ensured that $m_2/m_4 < 0.5$ and all the constraints discussed in Section 7.1 are met.
5. Now that the overall mass flow ratio (m_2/m_4) is known and thus the total mass flow rate m_2 in the jets, the task at hand is to distribute this mass flow rate amongst the jets. This is done by the following steps:

a) The flow field is divided into a number of streamtubes equal to the number of jets and each streamtube has one jet issuing into the counterflowing stream. It is assumed that there is no flow across these streamtubes.

b) Since M_1 which is uniform is known from step (2) the local mass flow rate in each of the jets $m_{2,\,j}$ is calculated to effect desired pressure loss in the streamtube. The calculation is similar to the one done for the entire flow field, the only difference being that the calculations are now done for individual streamtubes.

c) The jets are assumed to be choked[1] and from $m_{2,\,j}$ and the diameter of the jet d_j the jet total pressure is calculated from

$$\frac{m_{2,j}}{A_j^*} = 0.0404\,\frac{p_{02j}}{\sqrt{T_{02}}}$$

which is obtained from isentropic relations (see Shapiro 1953: 84-85).

d) At this stage it is ensured that $p_{02j} > p_{01}$ meeting Sekundov's (1969) criterion so that the jet penetrates into the counterflow stream.

e) A computational simulation is now performed with the parameters obtained from the previous steps.

f) The total pressure distribution at the *AIP* obtained from computations is compared with the target total pressure distribution.

g) The difference between the obtained and required total pressure loss is employed to vary the mass flow rates in the jets. The mass flow rate is varied from the current mass flow rate by an amount equal to the difference of the previous and current total pressure loss multiplied by the slope of the $[1 - (p_{03}/p_{01})]$ versus $m_{2,j}$ curve for the corresponding inlet Mach number (M_1).

h) With the new mass flow rate steps (c) to (g) are repeated till convergence.

[1] The calculations can be easily extended to unchoked nozzles using the same method described here. However, in the present thesis it is assumed that the jets are always choked.

7.3 Examples

The methodology developed to generate a given total pressure distribution was described above in Section 7.2. In the present section this methodology is demonstrated using two example flow cases using the four jet system. In fact, these flow cases are the ones for which computations were already done in Section 6.4.2. By using a total pressure distribution which is known a priori and employing the methodology developed here it can be readily asserted if the scheme can reproduce the known total pressure distribution.

7.3.1 Example 1

Consider the total pressure distribution shown in Figure 7.3. It was obtained from computations (Sl. No. 16 in Table 6.1). This flow case had equal mass flow rates in the jets thus leading to a periodic characteristic 'V' shaped total pressure distribution described in Section 6.4.1.4. Since this problem is designed using the known mass flow rates in the jets is serves as a good test case for the methodology to retrieve the total pressure distribution. The sample points for total pressure distribution are at a radius of $D_0/2$ at the *AIP*.

The number of sampling points in that radius was chosen to be eight (equi-angularly spaced). It was initially thought that four sampling points can be selected with each sampling point corresponding to each jet. However, a careful look at the total pressure distributions that were obtained in Section 6.4.1.4 (see, for example, Figure 6.9 (a)) reveals that with four sampling points only the peaks (or the dips) in the total pressure distribution could be considered and completely ignoring the dips (or the peaks). Thus, to account for the characteristic peaks and dips in the total pressure distribution a total of eight sampling points are considered.

The scheme is started with the given total pressure distribution in Figure 7.3 and the required average Mach number at the *AIP*, $M_3 = 0.259$. From the given total pressure distribution, $[1 - (p_{03}/p_{01})]_{ave} = 0.213$. M_1 is evaluated to be 0.111 from these data and

from $[1 - (p_{03}/p_{01})]_{ave}$ and M_1, m_2 is calculated as 0.312 kg/s. This mass flow rate is to be distributed amongst the jets.

Now, the flow field is divided into four streamtubes with each streamtube having a jet issuing into the counterflow stream. Since eight sampling points are considered and only four jets are available to achieve the desired total pressure distribution the total pressure losses are suitably averaged and used to calculate the mass flow rate in the individual jets. The average of three adjacent total pressure losses are used to evaluate the mass flow rate in the jets; for example, the mass flow rate in jet 1 (located at θ = 0º) is estimated using the average of total pressure loss at locations 0º, 45º and 315º. Thus the total pressure loss at eight locations can be reduced to four average losses commensurate with the number of jets.

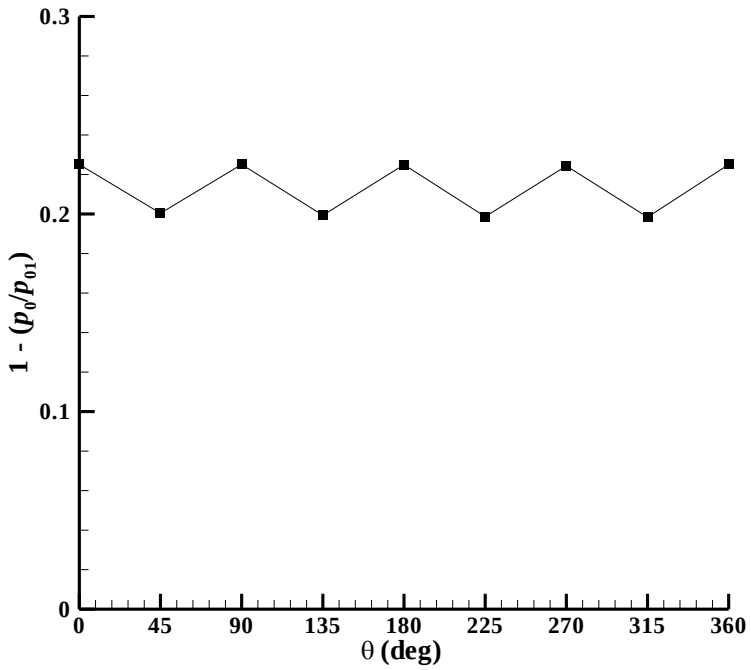

Figure 7.3 Target total pressure loss distribution at the *AIP* corresponding to Example 1.

Since M_1 is known which is uniform, and from the four average total pressure losses the mass flow rate in each jet can be easily calculated. At this stage it is not even

strictly necessary that the mass flow rates from the individual jets sum up to the total jet mass flow rate, though both would be quite close. The total pressure in the jet can be calculated with the jet mass flow rate and the jet diameter assuming a jet exit total temperature. It has to be stringently ensured that $p_{02j} > p_{01}$ for the jet to penetrate into the counterflow stream.

For the present flow case, as was earlier calculated, $M_1 = 0.111$ and the averaged four total pressure losses are equal to 0.209 each resulting in $m_{2,\,j} = 0.076$ kg/s. The jet total pressure calculated is 7.408 kPa assuming the jet exit temperature is 300 K.

With the parameters thus obtained a computation is done as per the procedure discussed in Section 6.2. The total pressure distribution obtained from the computations is compared with the target pressure distribution at all the eight sample points. The difference can be quantified in terms of root-mean-square error (*RMSE*) defined as (Hubble and Smith 1979)

$$RMSE = \sqrt{\frac{\sum_{i=1}^{n}\left(\frac{p_{0,\,obtained}}{p_{0,\,target}} - 1\right)^2}{n}} \times 100\,\% \qquad (7.1)$$

where $n = 8$ is the number of sampling points.

From these eight total pressure losses and by averaging the adjacent total pressure losses once again the data is reduced back to four loss values. These four values are used to evaluate the new mass flow rates in the jets. The difference between the obtained and target total pressure loss is calculated for each of the four averaged total pressure loss values and this difference is multiplied by the slope of the $[1 - (p_{03}/p_{01})]$ versus $m_{2,j}$ curve; the new mass flow rates in the jets are the difference between the current mass flow rate and this value.

With the new mass flow rates in the jets the jet total pressures are calculated and computations are performed again. The total pressure distribution obtained from the

computations is compared with the target distribution and the procedure repeated till the *RMSE* converges.

The total pressure distribution at each of these iterations is plotted in Figure 7.4; the target total pressure distribution is also plotted in the same figure. The total pressure distribution at iteration 1 is away from the target distribution and that of the converged solution (iteration 2) quickly gets close to the target distribution and is indistinguishable.

The present flow case with equal mass flow rates in the jets rather being a simple example the procedure converges fairly rapidly in two iterations. The reduction of *RMSE* with iterations is shown in Figure 7.5. The *RMSE* after the second iteration is only 0.328 %.

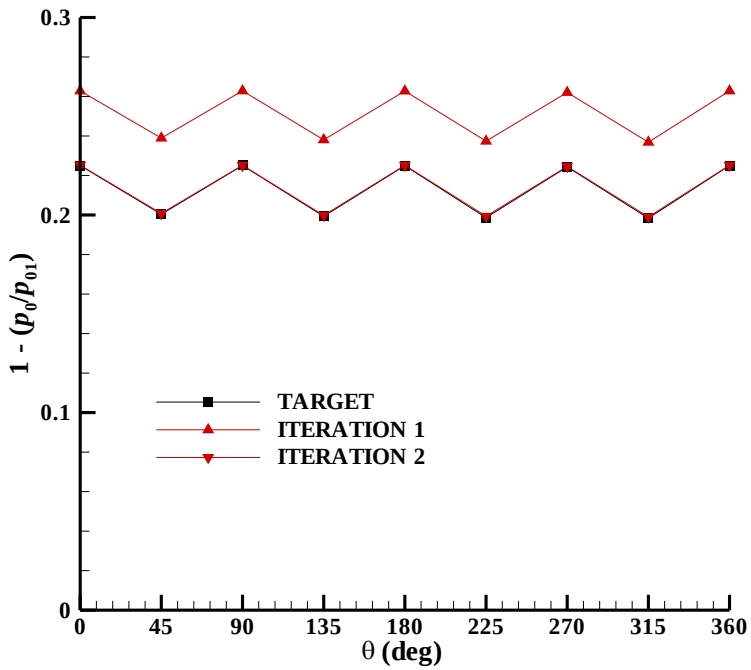

Figure 7.4 Total pressure loss distribution after each iteration compared with the target distribution. The distribution after the second iteration is indistinguishable from the target curve.

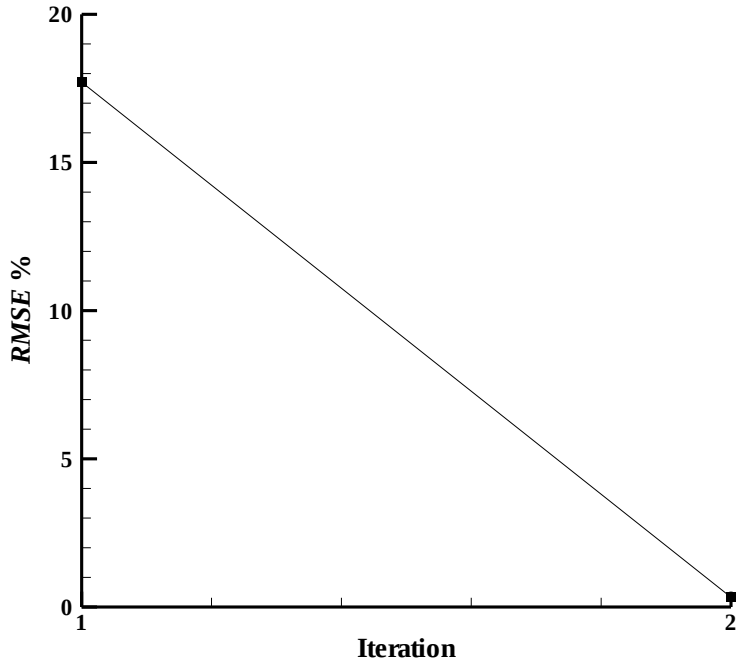

Figure 7.5 Convergence of *RMSE* with iterations.

Now the Mach number distribution corresponding to the total pressure distribution in Figure 7.3 is considered. This target distribution is shown in Figure 7.6 along with the distributions at each iteration. It may be noted that the average Mach number M_3 is 0.259. At each of the iterations the Mach number distribution is close to the target distribution. Though the total pressure distribution at iteration 1 is away from the target distribution the Mach number distribution is close to the target distribution. This is due to the fact that at iteration 1 the mass flow rate from the jets was high compared to the other iterations leading to higher total pressure loss and a Mach number distribution which is close to the target.

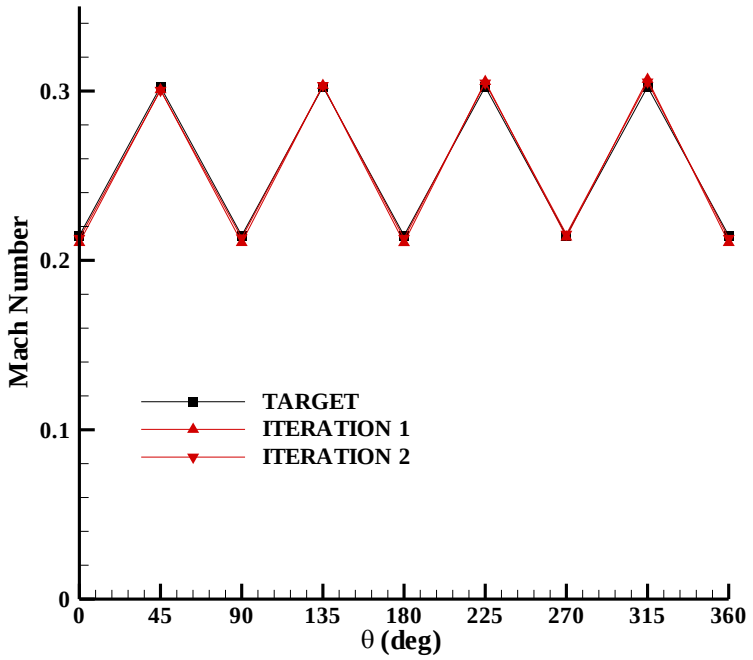

Figure 7.6 Mach number distribution corresponding to the target total pressure loss distribution in Figure 7.3 and the Mach number distribution after each iteration is shown in this figure.

The convergence of the mass flow rates in the jets is plotted in Figure 7.7. Since the flow case considered has equal mass flow rate in all the jets the target mass flow is shown by only one line in Figure 7.7. The mass flow in the jets start from a value away from the target and as the iterations progress converges to the target value.

The flow case in Example 1 was though simple and converges very fast it serves to indicate that a simple minded quasi-one-dimensional inviscid analysis approach used as a starting point is not adequate to generate the target total pressure distribution. Computations are necessary to complement the inviscid analysis and iteratively progress towards the target distribution.

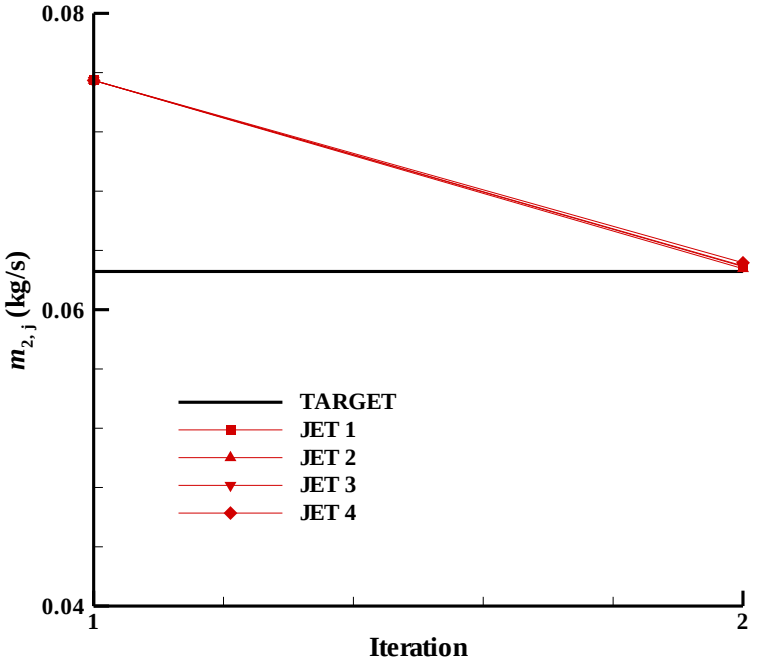

Figure 7.7 Convergence of mass flow rate in the jets to the target mass flow rate.

The total pressure loss contours at the *AIP* are plotted in Figure 7.8(a) for the target and achieved solutions. The distortion index *DI* for the target was 20.778 % and that achieved was 20.598 %. The ring-wise total pressure distribution normalised by the inlet total pressure for all the rings is plotted in Figure 7.8(b). The agreement between the target distribution and that achieved is excellent for all the rings. The circumferential and radial distortion components in the rings for the target and that achieved are also plotted in Figure 7.8(c) and (d), respectively. The comparison is very good. The methodology developed here is able to accurately reproduce not only the overall distortion level (in terms of the distortion index) but also the distribution of total pressure in the rings and the individual circumferential and radial distortion components in the rings.

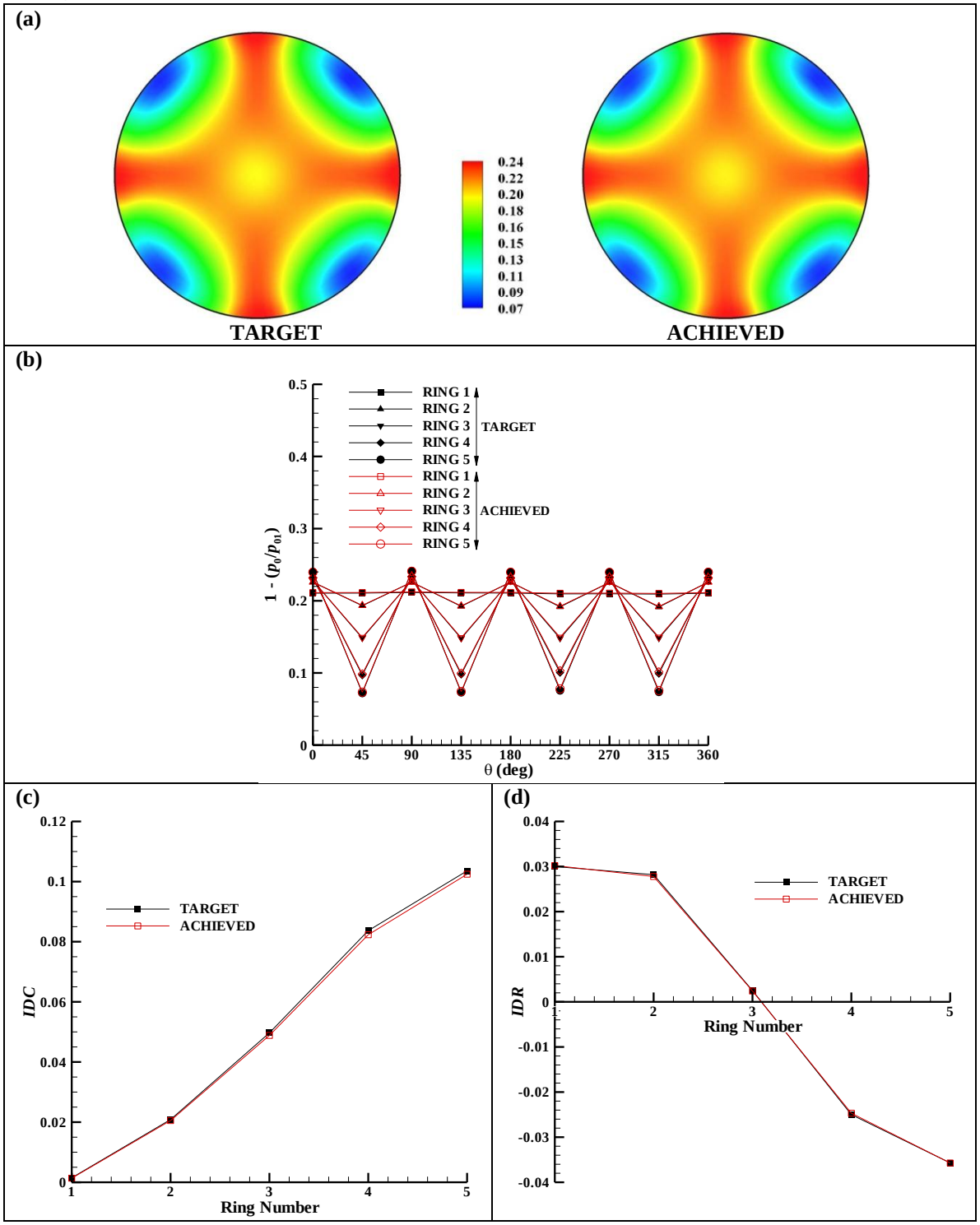

Figure 7.8 Distortion parameters at the *AIP* for Example 1. (a) Total pressure loss contours, (b) total pressure loss distribution in the rings, (c) circumferential distortion parameter *IDC* and (d) radial distortion parameter *IDR*.

7.3.2 Example 2

In the second example a flow case with unequal mass flow rates in the jets is considered. The flow case is the same one dealt extensively in Sections 6.4.2.1 to 6.4.2.3 and 6.4.2.6 in Figure 6.23(b). The mass flow rate $m_2/m_4 = 0.214$ and $M_3 = 0.315$. Without dwelling into the details again, the procedure similar to that explained for Example 1 (in Section 7.3.1) is followed.

The target total pressure distribution is shown in Figure 7.9. This is a difficult case compared to the previous case considered because of the unequal mass flow distribution and a sharp dip in the total pressure distribution at 225º.

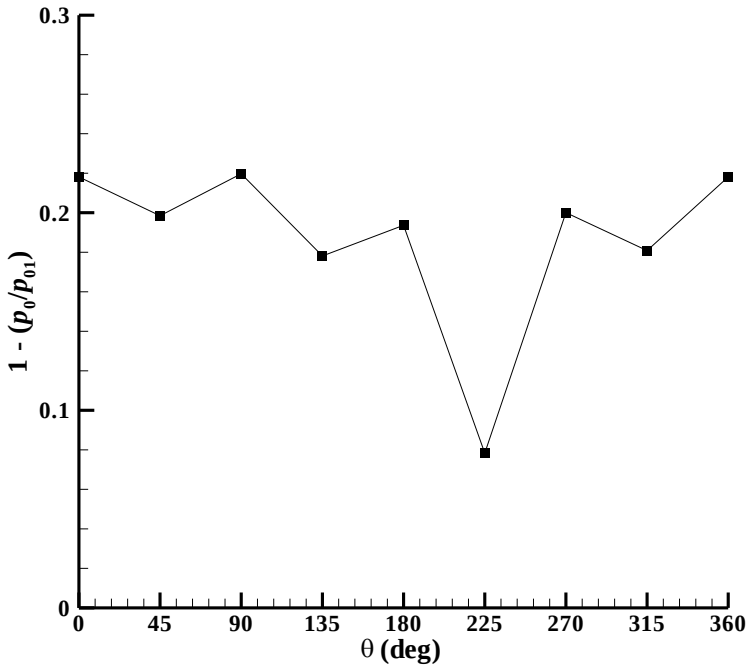

Figure 7.9 Target total pressure loss distribution at the *AIP* corresponding to Example 2.

However, the methodology developed is able to achieve this total pressure distribution. The total pressure distribution at each of the iterations is shown in Figure 7.10. As with the previous example the total pressure distribution at iteration 1 is away

from the target distribution and as the iterations progress the distribution gets close to the target.

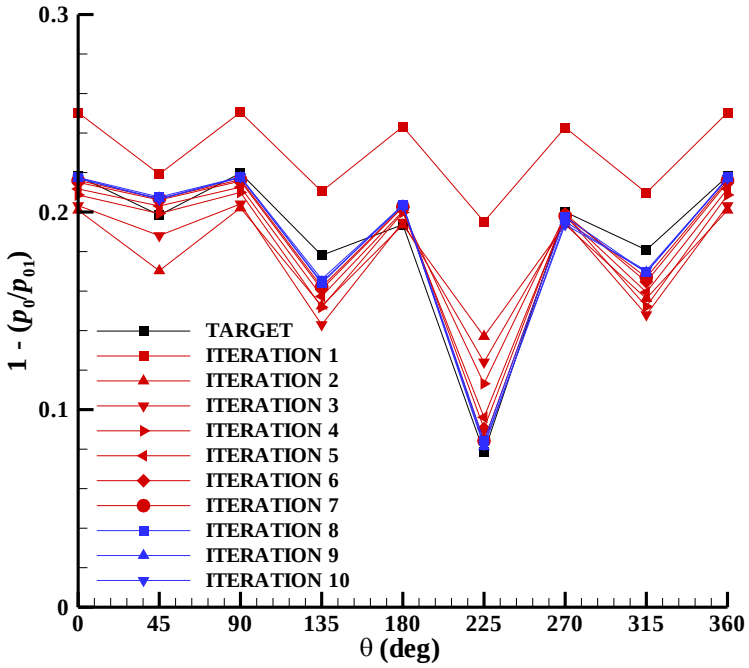

Figure 7.10 Total pressure loss distribution after each iteration compared with the target distribution.

The convergence of the *RMSE* is shown in Figure 7.11. Since the chosen target total pressure distribution was a difficult one the solution converges slowly compared to the previous example. The *RMSE* at tenth iteration is 4.443 %.

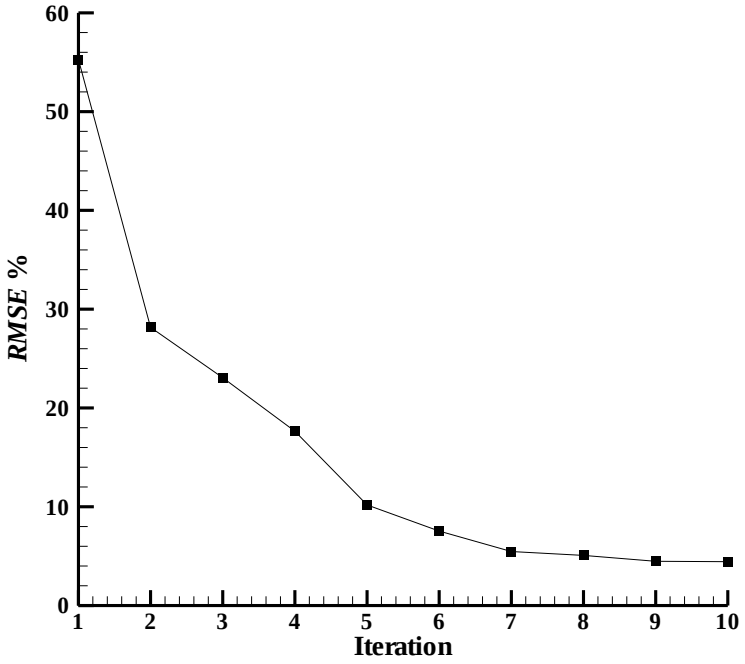

Figure 7.11 Convergence of *RMSE* with iterations.

The target Mach number distribution and that obtained at each iteration is plotted in Figure 7.12. At the tenth iteration the Mach number distribution is reasonably close to the target distribution. The convergence of the mass flow rates in the jets is shown in Figure 7.13. The mass flow rates converge though they do not reach the target values. It is interesting to note that the total pressure distribution converges whilst the mass flow distribution in the jets is slightly different than the target solution; this might have been the reason why the convergence in total pressure distribution is not as good and fast as that for Example 1.

It must be mentioned here that the target mass flow distribution in the jets as plotted in Figures 7.7 and 7.13 will not be available to the gas turbine test engineer. Since the two examples were chosen from the flow cases whose solution was already known (in Section 6.4.2) such comparisons of mass flow distribution are made. These comparisons are instructive and enable the study of convergence of the procedure for various parameters. The total pressure distribution and the average engine inlet Mach number

(M_3) only are known/provided to the test engineer and, indeed, these are the only parameters required for the methodology developed in this thesis.

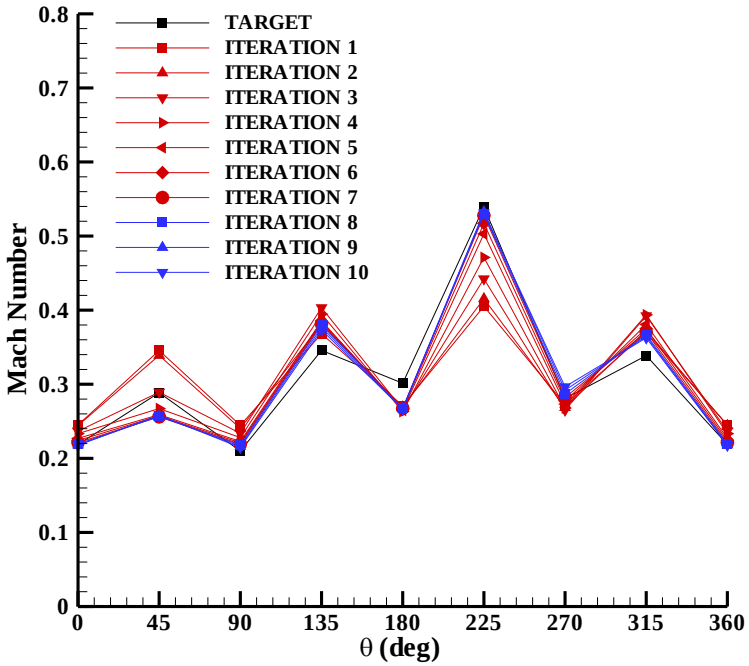

Figure 7.12 Mach number distribution corresponding to the target total pressure loss distribution in Figure 7.9 and the Mach number distribution after each iteration is shown in this figure.

This test case gives a hint that close to an exact solution, that is known to exist in this example, there may be approximate solutions and any search methodology, like the present one, may end up with one of them especially in a downstream plane. This is not surprising keeping in mind the evolving nature of the flow field which is governed by equations that are parabolic in nature. In such a system it is possible that two altogether different flow fields but with equal source strengths are likely to evolve into nearly same fully developed or nearly fully developed states that are very close. A methodology trying to search a source strength based on the fully developed state may end up with another source strength which is nearly as good since the final states are close.

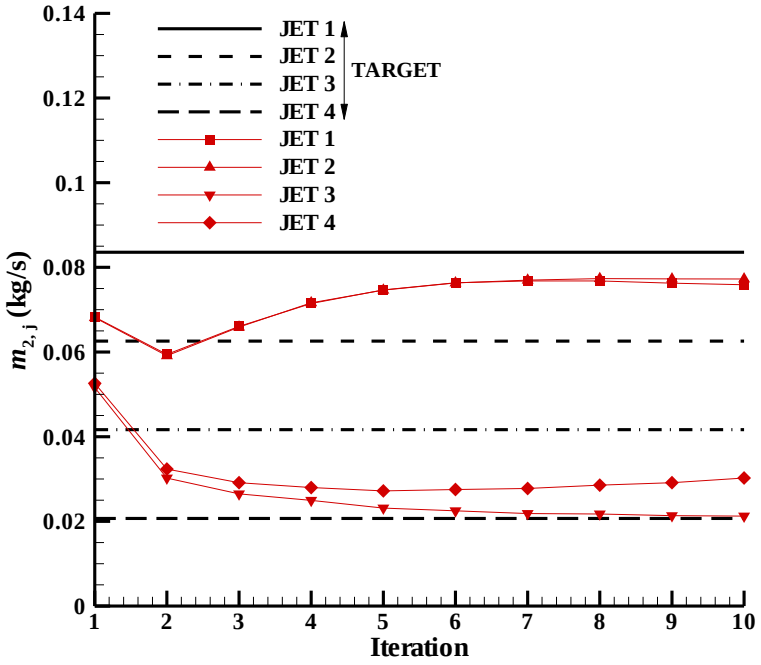

Figure 7.13 Convergence of mass flow rate in the jets to the target mass flow rate.

Now, the distortion parameters at the *AIP* are plotted in Figure 7.14. The total pressure loss contours at the *AIP* for the target and that obtained after convergence are shown in Figure 7.14(a). A good agreement between the patterns is observed. The distortion index for the target solution was 27.779 % and that achieved was 28.019 %. The total pressure distribution in the rings normalised by the inlet total pressure is plotted in Figure 7.14(b); the agreement is good at all the rings. The circumferential and radial distortion elements are plotted in Figure 7.14(c) and (d), respectively; again the agreement is good.

To summarise the developments so far, the methodology devised to produce a given total pressure pattern was successfully demonstrated for two flow cases, one with equal mass flow rates in the jets and another with unequal mass flow rates. For both the cases the total pressure loss distributions at the sampling points were reproduced with reasonable accuracy. The total pressure distortion pattern compared to the target pattern quantified in terms of *RMSE* was low. The overall distortion index, ring-wise total

pressure loss distribution and the circumferential and radial distortion elements were also reproduced accurately.

The methodology formulated here cannot and is also not expected to reproduce the given total pressure pattern identically (although the difference is quite small). This is due to several reasons: firstly, considering the complex non-uniform flow fields as those in Figures 7.8(a) and 7.14(a) (target distributions) that are to be simulated only eight sampling points were employed to retrieve the flow field. Furthermore, the values at these eight sampling points were appropriately averaged and reduced to four average losses to be commensurate with the number of jets. After averaging the total pressure losses the number of jets used to simulate the complex flow field is again finite. It thus seems plausible that increasing the number of jets and the number of sampling points in the system the simulated flow field can get closer to the target pattern, though, may not quite reproduce the target pattern identically.

In the subsequent sections of this chapter the methodology is tested further to generate a given flow field using twelve jets and later using twenty jets.

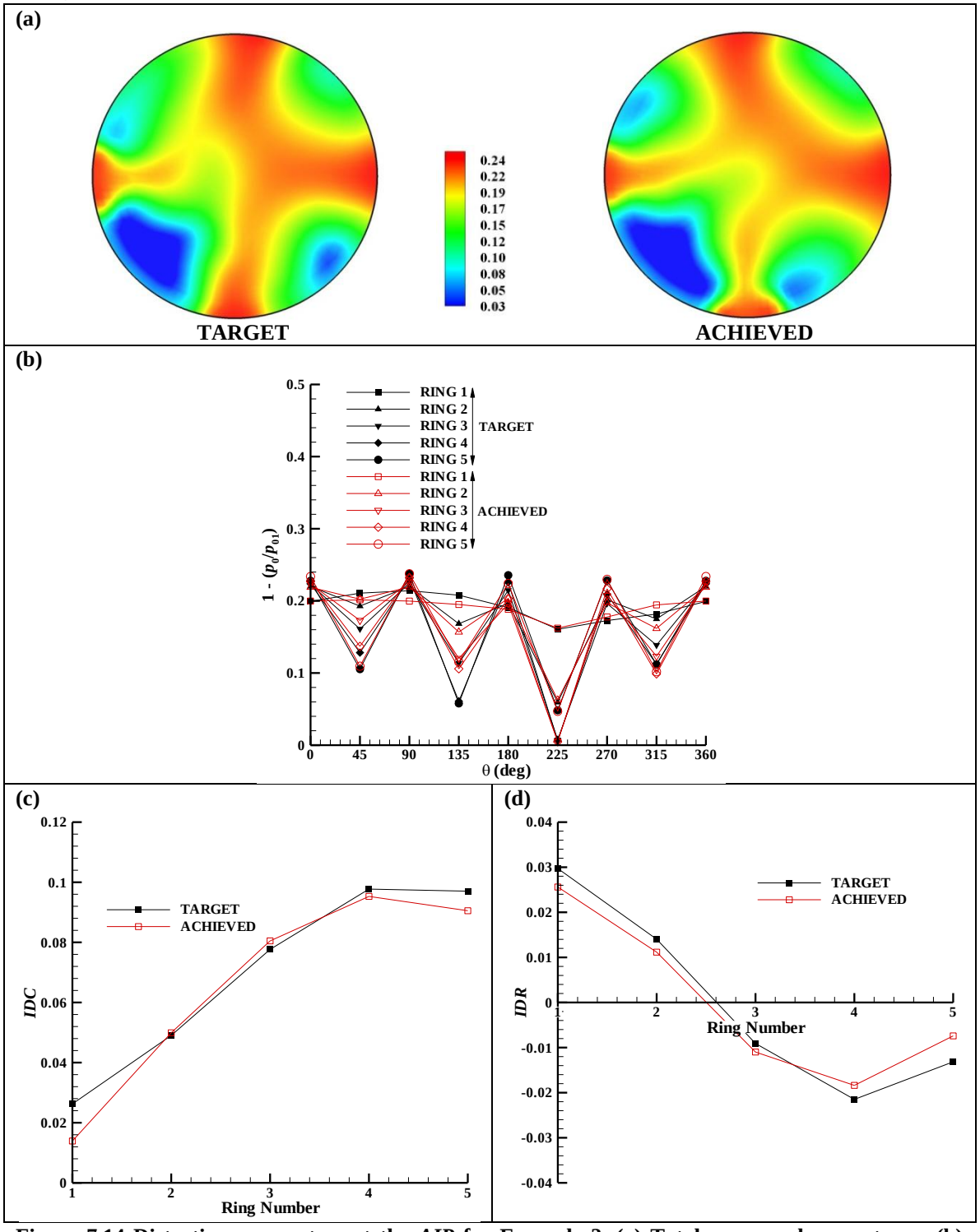

Figure 7.14 Distortion parameters at the *AIP* for Example 2. (a) Total pressure loss contours, (b) total pressure loss distribution in the rings, (c) circumferential distortion parameter *IDC* and (d) radial distortion parameter *IDR*.

7.4 Twelve Jet System

The methodology developed in Section 7.2 of this chapter is extended to a twelve jet flow system to achieve a better representation of the distorted field. In the next section it will be further improved with twenty jets. In the present section two flow cases are considered for demonstration – one with equal mass flow rates in all the twelve jets and another with unequal mass flow rates in the jets.

The twelve jets are arranged at two circumferential locations at radii 0.16 D_0 and 0.395 D_0, respectively, as shown in Figure 7.15. The jets are representative of equal area sectors. The inner diameter of the jets d_j = 4.33 mm and the duct diameter D_0 = 102 mm. The mass flow of the counterflow stream is $m_1 = \pi/4\ D_0^2\ \rho_0\ u_0$ and that at the jet exit is $m_j = \pi/4\ d_j^2\ \rho_j\ u_j$. The total mass flow rate from the jets is $m_2 = \sum_{j=1}^{N} m_{2,j}$, where N = 12 in the present case.

The station numbering is according to Figure 6.1 with the *AIP* at z = - 1 D_0 behind the jet injection plane.

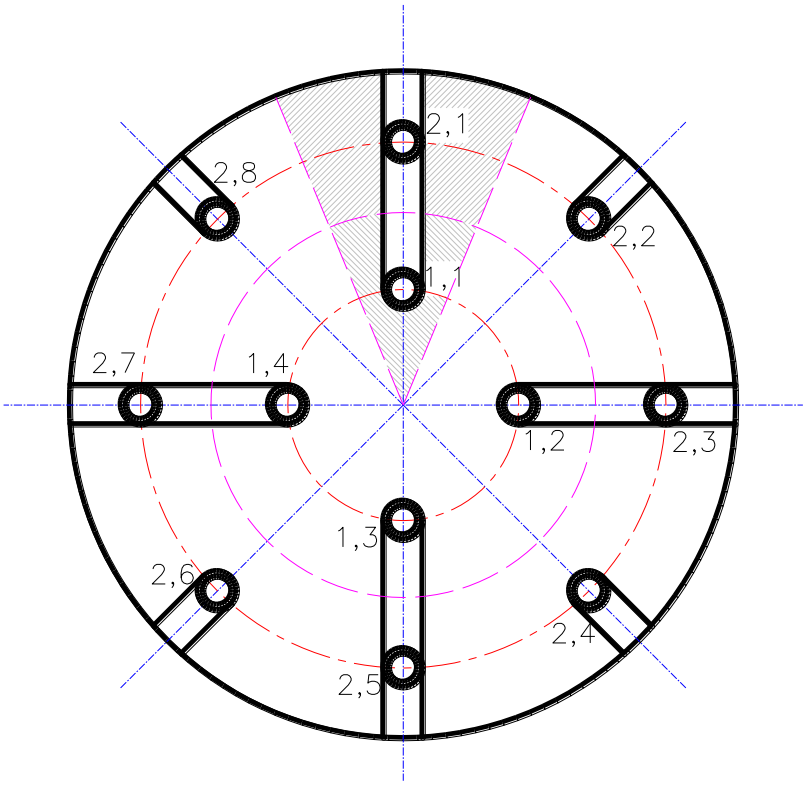

Figure 7.15 Schematic arrangement of the twelve jets in two circumferential locations.

The target flow cases were actually generated by computations similar to the procedure in Section 7.3 for the four jet system. The time-averaged computations were performed for one duct-to-jet diameter ratio (D_0/d_j = 23.6). The counterflow stream inlet and the combined flow outlet were placed at 4.9 D_0 and – 4.9 D_0 from the jet exit, respectively.

The three-dimensional computational domain consisted of 2,010,498 cells. The grid spacing was similar to that employed for the single jet case in Section 5.2. The total and static pressure boundary conditions were specified at the counterflow inlet and the jet exit. The pressure boundary conditions at the jet exit corresponded to sonic jet exit velocity. The exit static pressure was specified at the outlet boundary. The total temperature was specified (and equal) at the inlets and the outlet. On the main duct walls and on the walls of the jet stems the no-slip boundary condition was imposed. The k-ε

turbulence model was employed. All calculations were carried out in double-precision arithmetic.

7.4.1 Example 3

The total pressure loss distribution given in Figure 7.16 is considered as the target. It was obtained from computations for a flow case which had equal mass flow rate in all the jets. For this example m_2/m_4 = 0.197 and M_3 = 0.293. The total pressure loss distribution is plotted at two rings – ring A and B, at 0.32 D_0 and 0.79 D_0 at the *AIP*. The number of sampling points was, respectively, 8 and 16 at these rings. Again the number of sampling points is twice as that of the number of jets. The averaging of total pressure loss values in each ring to reduce them to the number of jets is similar to that done for the four jet cases.

The procedure to generate the given total pressure pattern is same as that discussed for the four jet system in Examples 1 and 2. The total pressure distribution at each of the iterations is shown in Figure 7.17(a) and (b), respectively, for rings A and B. The total pressure distribution at iteration 1 is away from the target distribution and as the iterations progress the distribution gets closer to the target.

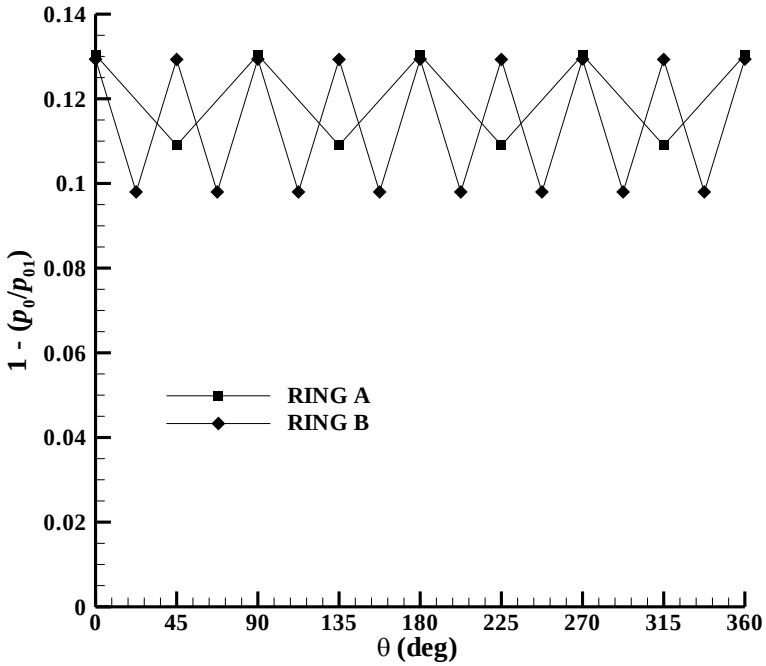

Figure 7.16 Target total pressure loss distribution at the *AIP* corresponding to Example 3 in rings A and B.

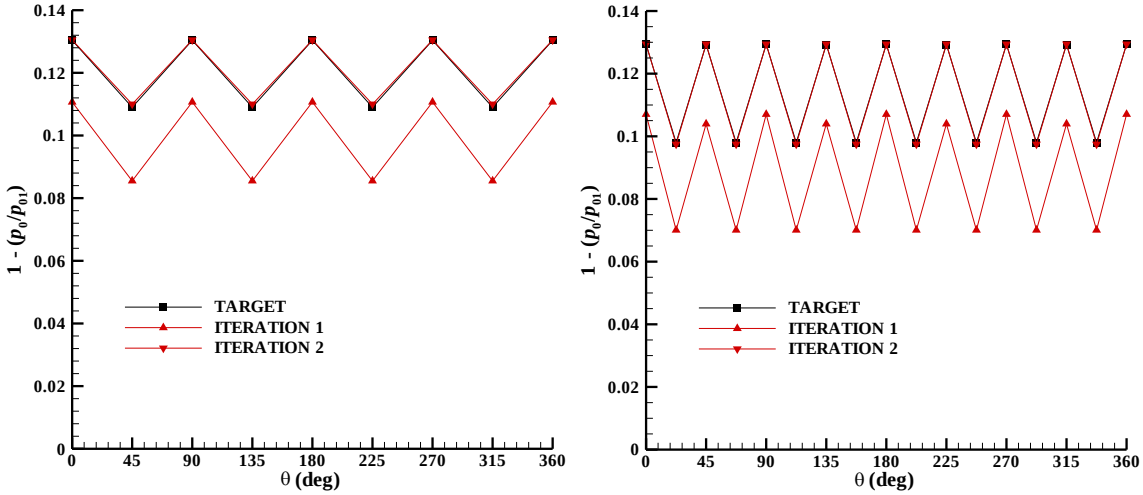

(a) **(b)**

Figure 7.17 Total pressure loss distribution after each iteration compared with the target distribution in (a) ring A and (b) ring B.

The convergence of the *RMSE* is shown in Figure 7.18. The present flow case with equal mass flow rates in the jets the procedure converges rapidly in two iterations. The *RMSE* after the second iteration is 0.490 % which is very small to be considered converged.

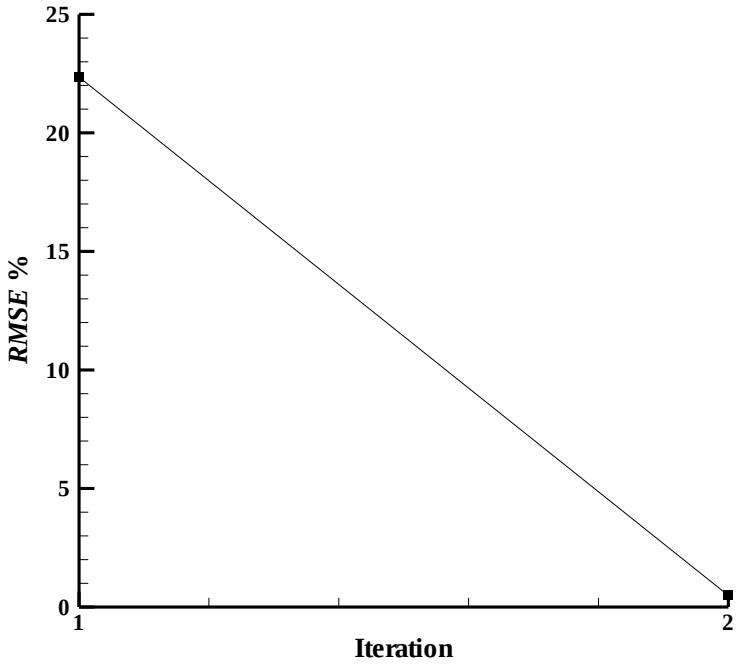

Figure 7.18 Convergence of *RMSE* with iterations.

The distortion parameters at the *AIP* are probed now. The total pressure loss contours at the *AIP* for the target and that obtained after convergence are shown in Figure 7.19(a). A good agreement between the patterns is observed. The distortion index for the target solution was 4.686 % and that achieved was 4.625 %. The total pressure loss distribution in the rings is plotted in figure 7.19(b); the agreement is good at all the rings. The circumferential and radial distortion elements are plotted in Figures 7.19(c) and (d); again the agreement is good.

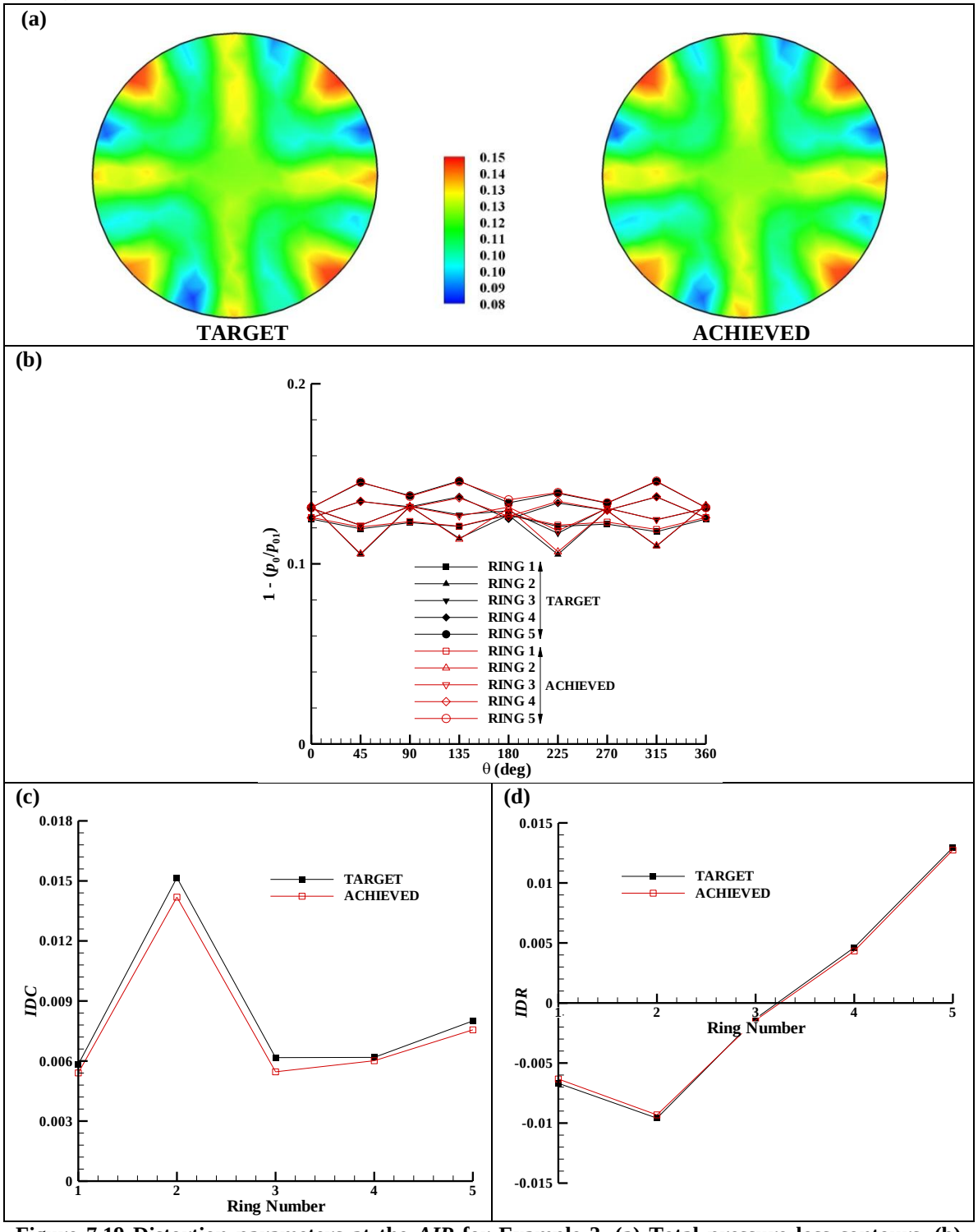

Figure 7.19 Distortion parameters at the *AIP* for Example 3. (a) Total pressure loss contours, (b) total pressure loss distribution in the rings, (c) circumferential distortion parameter *IDC* and (d) radial distortion parameter *IDR*.

7.4.2 Example 4

This example flow case had unequal mass flow rates in the twelve jets. The target total pressure distribution in the rings is shown in Figure 7.20. For this example m_2/m_4 = 0.197 and M_3 = 0.293, the same values as those used for Example 3.

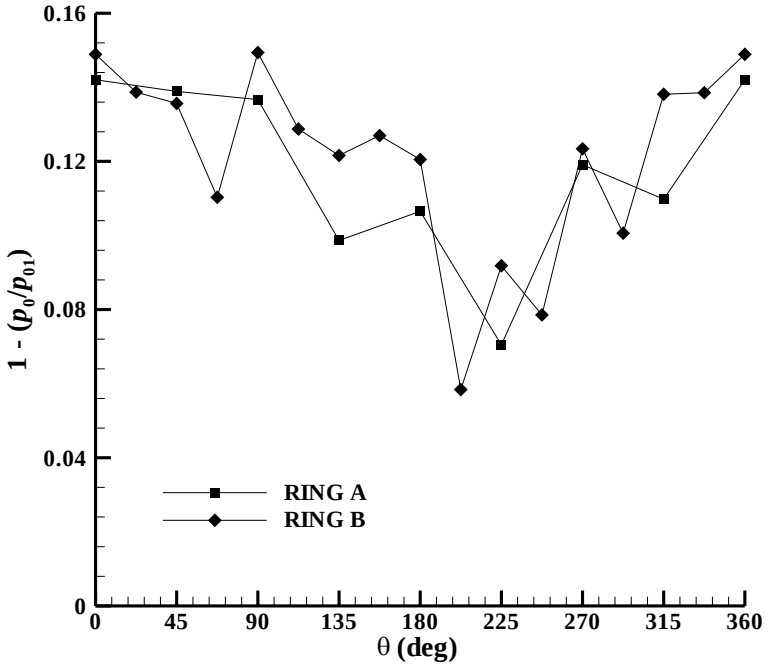

Figure 7.20 Target total pressure loss distribution corresponding to Example 4 in rings A and B at the *AIP*.

The procedure to generate the given total pressure pattern is same as that discussed Example 3. The total pressure distribution after each of the iterations is shown in Figures 7.21(a) and (b), respectively, for rings A and B. The total pressure loss distribution at iteration 1 is away from the target distribution and as the iterations progress the distribution gets closer to the target.

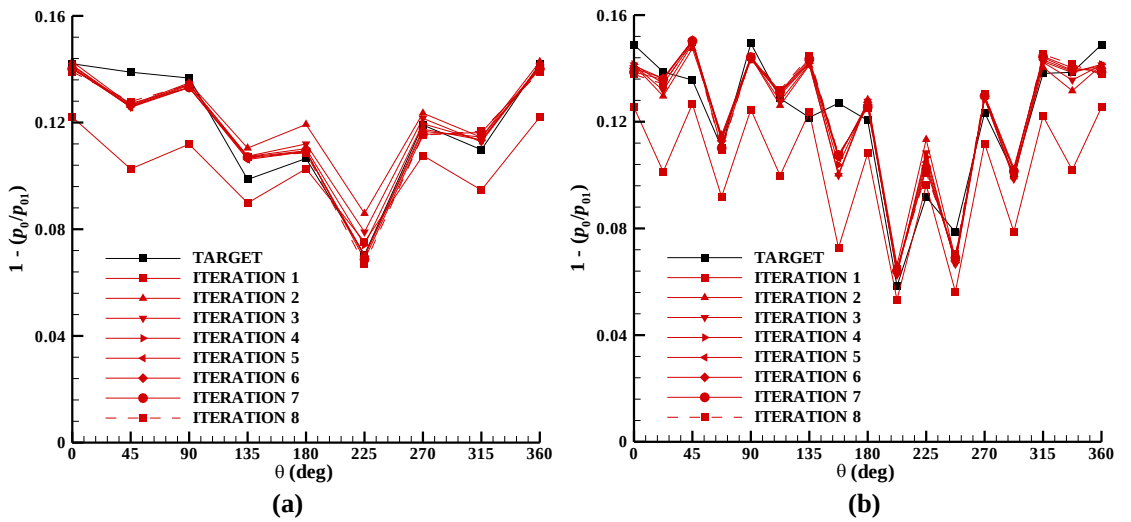

Figure 7.21 Total pressure distribution at each iteration compared with the target distribution in (a) ring A and (b) ring B.

The convergence of the *RMSE* is shown in Figure 7.22. The present flow case with unequal mass flow rates in the jets the procedure converges in eight iterations. The *RMSE* at the eighth iteration is 7.662 % and is considered converged.

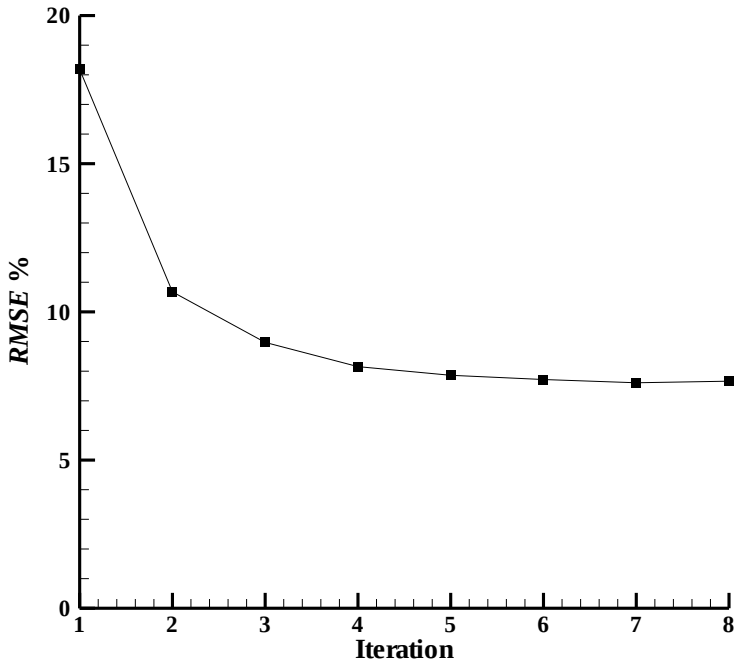

Figure 7.22 Convergence of *RMSE* with iterations.

The distortion parameters at the *AIP* are examined. The total pressure loss contours at the *AIP* for the target and that obtained after convergence are shown in Figure 7.23(a). A good agreement between the patterns is observed. The distortion index for the target solution was 11.261 % and that achieved was 12.153 %. The total pressure loss distribution in the rings is plotted in Figure 7.23(b); the agreement is good at all the rings. The circumferential and radial distortion elements are plotted in Figures 7.23(c) and (d); again the agreement is good.

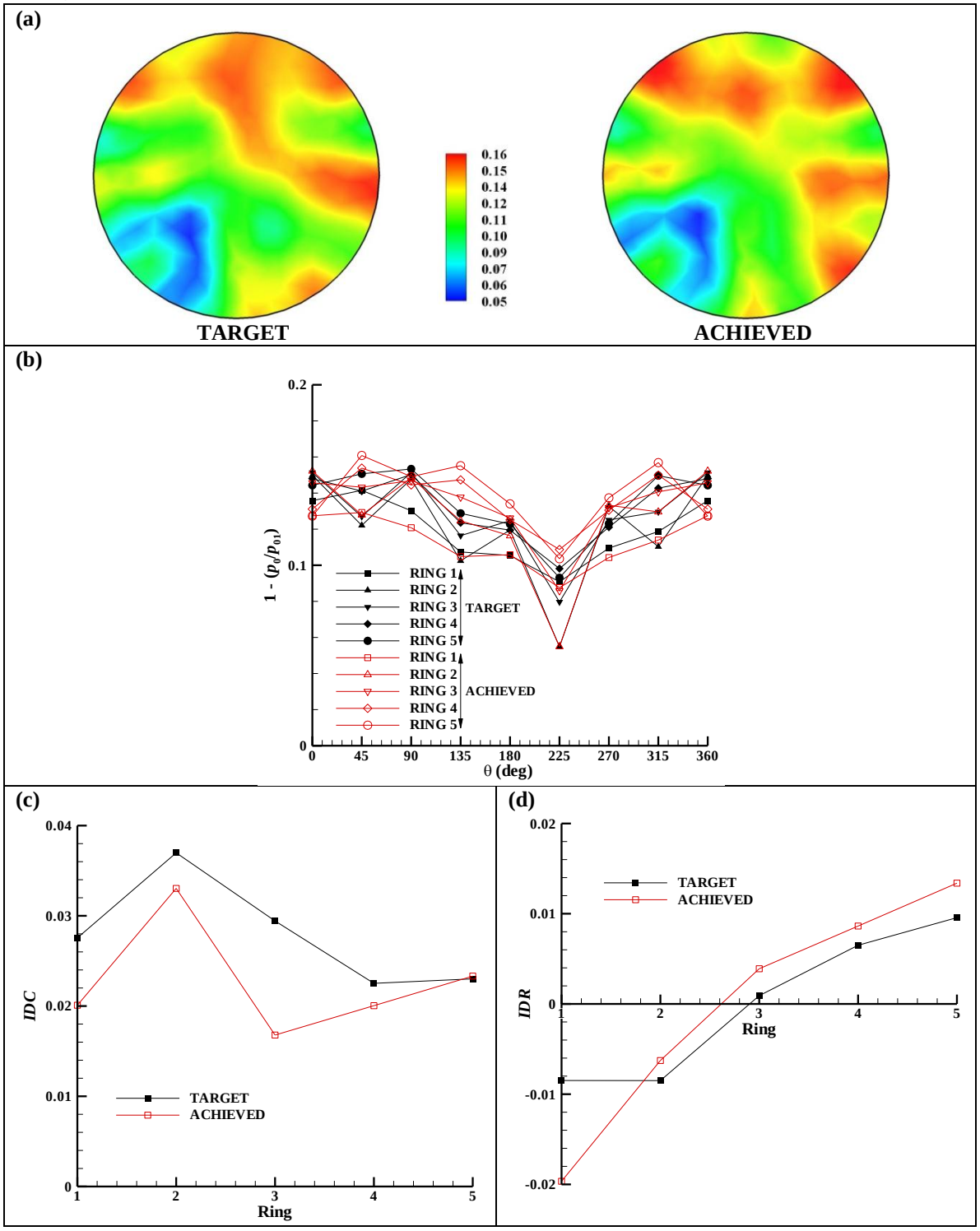

Figure 7.23 Distortion parameters at the *AIP* for Example 4. (a) Total pressure loss contours, (b) total pressure loss distribution in the rings, (c) circumferential distortion parameter *IDC* and (d) radial distortion parameter *IDR*.

Considering examples 3 and 4, both these cases had m_2/m_4 = 0.197 and M_3 = 0.293. However, by injecting the same amount of mass flow rate in the jets in an unequal manner the distortion index increased from 4.686 % to 11.261 % and the circumferential and radial distortion elements were also higher. Such observation was also noted in Meyer *et al.* (1970) in their ring-wise total pressure distribution by injecting unequal mass flow in the jets for the same value of overall mass flow ratio.

7.5 Simulating Aircraft Distortion Patterns

A methodology has been developed to generate a given total pressure distortion pattern. This methodology was demonstrated using four jets and later twelve jets for two example cases each. Two of these examples had equal mass flow rates in the jets and the other two had unequal mass flow rates. It was successfully demonstrated that the given total pressure distortion pattern can be generated accurately. It may be recalled that the target total pressure distortion patterns were known a priori by computing the flow fields. This was done to evaluate the methodology and assert if a known flow field can be generated.

In the present section, however, the methodology is deployed for two example cases whose solutions are not known. These examples represent distortion patterns typically measured in aircraft inlet / gas turbine engine testing. It is vital to see if the methodology can reproduce such patterns.

In this process of verifying the methodology, a twenty jet system is also employed apart from the four and twelve jet systems discussed earlier. The twenty jets are arranged circumferentially at three radii at 0.134 D_0, 0.305 D_0 and 0.443 D_0 as shown in Figure 7.24. The inner diameter of the jets d_j was 3.35 mm and the jets are representative of equal area sectors. The diameter of the duct D_0 is 102 mm, thus D_0/d_j = 30.45. The mass flow of the counterflow stream is $m_1 = \pi/4\ D_0^2\ \rho_0\ u_0$ and that at the jet exit is $m_j = \pi/4\ d_j^2\ \rho_j\ u_j$. The total mass flow rate from the jets is $m_2 = \sum_{j=1}^{N} m_{2,j}$, where N = 20 in this case.

The station numbering is according to Figure 6.1 with the *AIP* at z = - 1 D_0 behind the jet injection plane. The time-averaged computations were performed with the counterflow stream inlet and the combined flow outlet placed at 4.9 D_0 and – 4.9 D_0 from the jet exit, respectively.

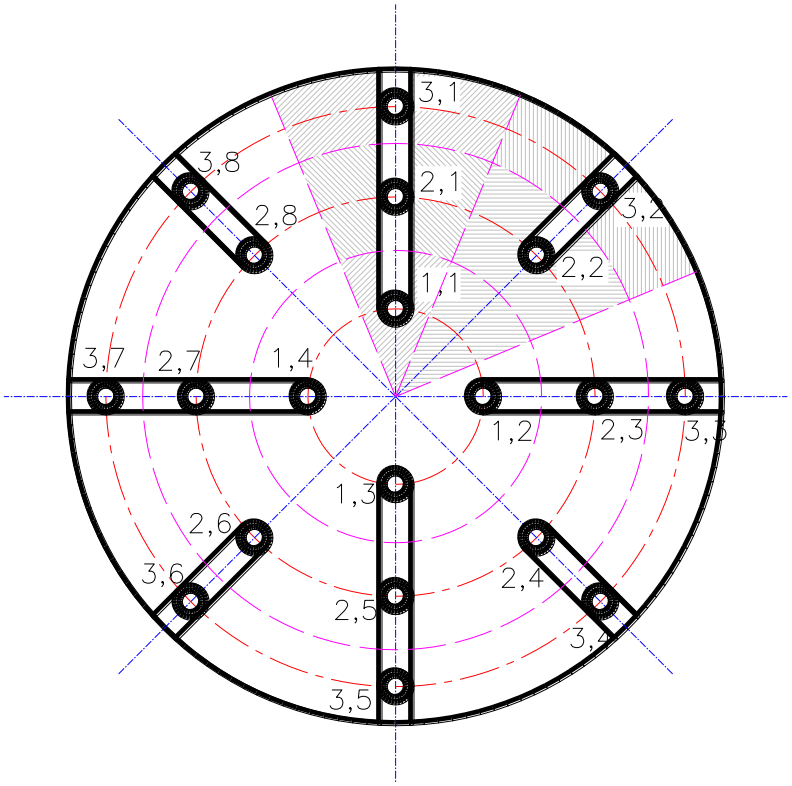

Figure 7.24 Schematic arrangement of the twenty jets in three circumferential locations.

The three-dimensional computational domain consisted of 1,980,440 cells. The grid spacing was similar to that employed for the single jet case in Section 5.2. The total and static pressure boundary conditions were specified at the counterflow inlet and the jet exit. The pressure boundary conditions at the jet exit corresponded to sonic jet exit velocity. The exit static pressure was specified at the outlet boundary. The total temperature was specified (and equal) at the inlets and the outlet. On the main duct walls and on the walls of the jet stems the no-slip boundary condition was imposed. The *k*-ε turbulence model was employed. All calculations were carried out in double-precision arithmetic.

Before the two examples are solved it is pertinent to consider some distortion descriptor elements as defined in SAE AIR1419 (1999) (see also Williams 1987). These distortion parameters are also relevant apart from the global parameter like distortion index (equation 5.4) and circumferential and radial distortion components (equations 5.5 and 5.6). The rationale for describing such distortion descriptors is well covered in AIR1419 (1999) and is not repeated here. Briefly, the distortion descriptor must be capable of describing the compressor's stability to the magnitude of circumferentially varying total pressure deficit, the time period a compressor blade spends in the low total pressure region, the number of low total pressure regions encountered by a blade in one revolution, the magnitude of radially varying total pressure defect, and the occurrence of the circumferential and/or the radial total pressure defect in the hub, mid-span or tip of the compressor.

The circumferential distortion in each ring is described by the magnitude of circumferentially varying total pressure deficit, the circumferential extent of the low total pressure region and the number of low total pressure regions in terms of intensity, extent and multiple-per-rev, respectively. These parameters are defined next.

The circumferential extent of the low total pressure region defined as intensity ($\Delta PC/P$) which indicates the magnitude of total pressure defect in each ring i.

$$\left(\frac{\Delta PC}{P}\right)_i = \frac{\left(p_{0,\,ring,ave}\right)_i - \left(p_{0,low,ave}\right)_i}{\left(p_{0,\,ring,ave}\right)_i} \tag{7.2}$$

where $p_{0,\,ring,\,ave}$ is the average total pressure in the ring and $p_{0,\,low,\,ave}$ is the average of the total pressures below the ring average total pressure. The counter i indicates the ring number; the number of rings is usually five (see Figure 5.3). The situation illustrated in Figure 7.25 adapted from AIR1419 (1999) would be useful in comprehending the definitions.

It is worth noting that the circumferential intensity ($\Delta PC/P$) is akin to *IDC* with $p_{0,\ ring,\ min}$ and $p_{0,\ face,\ ave}$ in the definition of *IDC* replaced by $p_{0,\ low,\ ave}$ and $p_{0,\ ave}$, respectively.

The circumferential distortion extent (θ^-) is the annular extent, in degrees, in which the total pressure is below the average total pressure in the ring. The extent is depicted graphically in Figure 7.26.

$$\left(\theta^-\right)_i = \theta_{2,i} - \theta_{1,i} \quad . \tag{7.3}$$

The circumferential intensity can also be determined by the ratio of the area of the curve under the average total pressure in the ring (shown by a shaded region in Figure 7.25) to the circumferential extent.

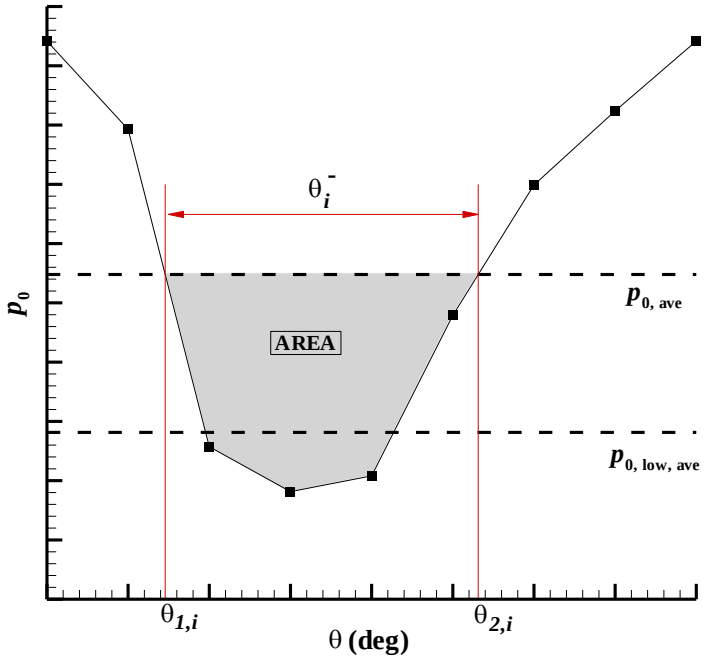

Figure 7.25 Circumferential total pressure distribution in i^{th} ring for a one-per-rev pattern.

The number of low total pressure regions in a ring is quantified by multiple-per-rev (*MPR*) parameter. For example, the total pressure distribution shown in Figure 7.25

has only one low pressure region below the average total pressure in the ring. Thus its *MPR* content is one, known as one-per-rev. Now consider the situation portrayed in Figure 7.26. This distribution clearly has two low total pressure regions for which case the *MPR* is greater than one. The *MPR* can be calculated as ratio of the sum of the areas of the low total pressure regions to the single largest area. From Figure 7.26, *MPR* = (area 1 + area 2) / (area 2). For such patterns the circumferential intensity corresponds to the maximum value of the ($\Delta PC/P$) and the circumferential extent ($\bar{\theta}$) is

$$\left(\bar{\theta}\right)_i = (\theta_{2,i} - \theta_{1,i}) + (\theta_{4,i} - \theta_{3,i}) \quad . \tag{7.4}$$

For the sake of completeness, it is mentioned here that if the low total pressure regions are separated by an angular extent less than some specified angle (approximately 25º) then the total pressure distribution can be considered as an equivalent one-per-rev.

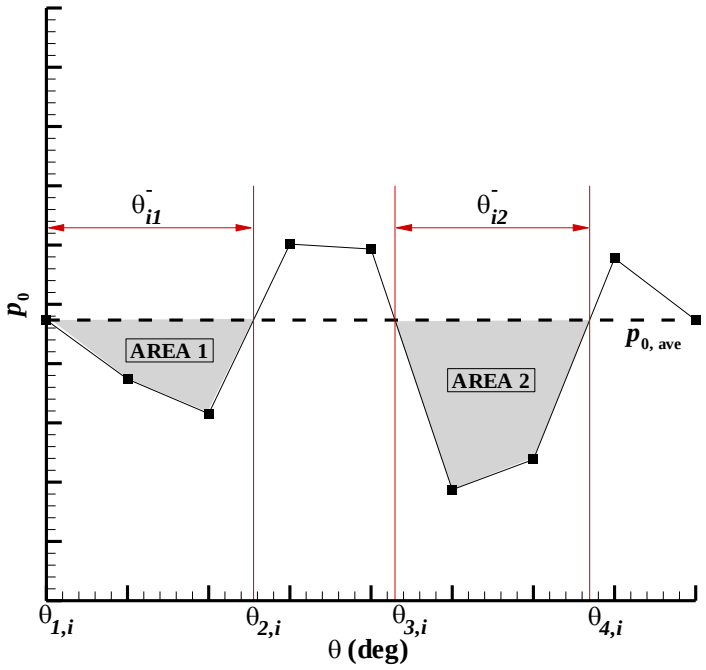

Figure 7.26 Circumferential total pressure distribution in *i*th ring for a multiple-per-rev pattern.

The radial distortion intensity is the difference between the average total pressure in the plane of interest and the ring average pressure divided by the average total pressure in the plane. The radial distortion ($\Delta PR/P$) is defined as

$$\left(\frac{\Delta PR}{P}\right)_i = \frac{p_{0,\,face,ave} - p_{0,ring,ave}}{p_{0,\,face,ave}} \quad . \tag{7.5}$$

It may be noted that ($\Delta PR/P$) is identical to *IDR* defined earlier in equation 5.6.

There is a great advantage of using the distortion descriptors defined above. This method avoids the otherwise cumbersome representation of the total pressure distribution by polynomial, spline or Fourier curve fit and results in consistently good correlations to an acceptable degree of accuracy (see Cousins 2004).

With the new distortion descriptors defined, now the two example flow cases can be considered.

7.5.1 Example 5

This example flow case is selected from Figure 19 of AIR1419 (1999). The total pressure measured at the 40 probes and non-dimensionalised by the average total pressure in the plane is listed in Table 7.1. From this data the target total pressure loss distribution [1-(p_0/p_{01})] (assuming p_{01}) that is to be generated at the *AIP* is shown in Figure 7.29(a).

The total pressure pattern listed in Table 7.1 and shown in Figure 7.29(a) is a 90º one-per-rev and tip radial combined distortion pattern. It has essentially uniform circumferential and angular extent distortion elements. This pattern was measured from a distortion screen test data. Though this pattern was meant to be a ‘classical’ distortion pattern that actually obtained by the screens was significantly different from the intended pattern.

Table7.1 Target total pressure distribution pertaining to Example 5.

Rake → / Ring ↓	1	2	3	4	5	6	7	8
1 (Hub)	0.987	0.962	0.982	1.068	1.086	1.061	1.076	1.069
2	0.961	0.939	1.091	1.072	1.086	1.064	1.080	1.064
3	0.911	0.913	1.020	1.034	1.010	1.046	1.012	1.026
4	0.878	0.873	0.989	1.002	0.984	0.987	0.985	0.997
5 (Tip)	0.872	0.858	0.970	0.983	0.981	0.985	0.972	0.961

The pattern shown in Figure 7.29(a) is the target total pressure loss distribution for simulation exercise using four, twelve and twenty jets. With 40 total pressure data given it is now only a matter of suitably averaging these pressure data and imposing the right amount of mass flow rate in the jets. The averaging procedure is illustrated for the four jet case as shown in Figure 7.27; the four jets and the 40 data points are superposed there. (For the numbering of the jets see Figure 6.1 and for probe locations see Figure 5.3.) The 40 total pressures have to be reduced to four sampling values equal to the number of jets. For an average total pressure corresponding to jet 1 the total pressures at the five rings and rakes (adjacent to jet 1) 1, 2 and 8 are averaged. This averaging is similarly done for the other jets.

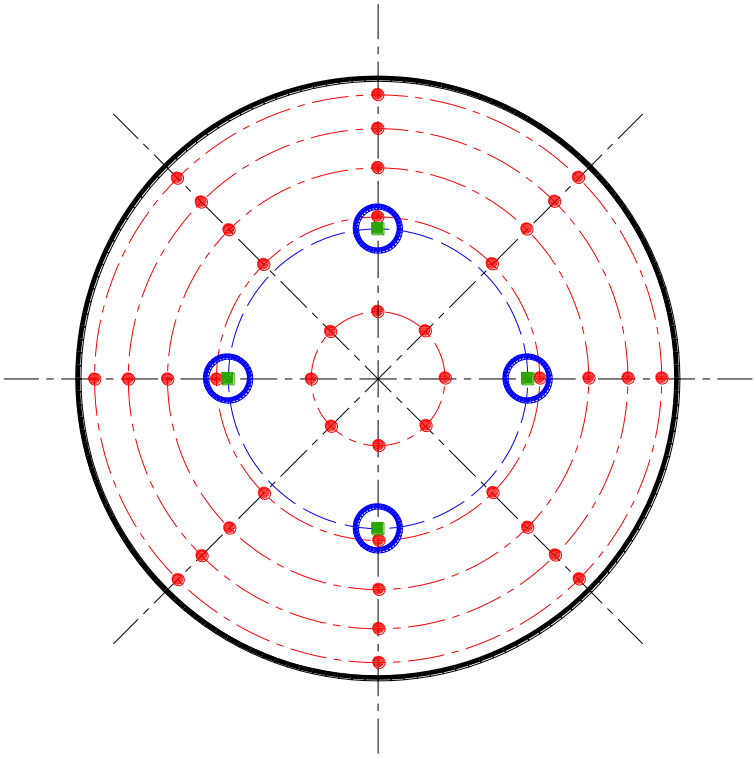

Figure 7.27 Procedure of averaging the 40 total pressures. The jets are denoted in blue, the locations where total pressure are known in red and the sampling points in green.

A similar procedure is followed for the twelve and twenty jet cases also with averaging carried out using the total pressures adjacent to the jets resulting in 12 and 20 sampling points, respectively. With the sampling points obtained after the averaging procedure the methodology to generate the total pressure pattern is initiated and computations performed. The convergence of the *RMSE* is shown in Figure 7.28. The convergence with twelve and twenty jets is faster than with four jets. Also the *RMSE* is lower using a larger number of jets. The *RMSE* after convergence with four jets is 5.924 %, and that with twelve and twenty jets are 4.434 % and 3.836 %, respectively.

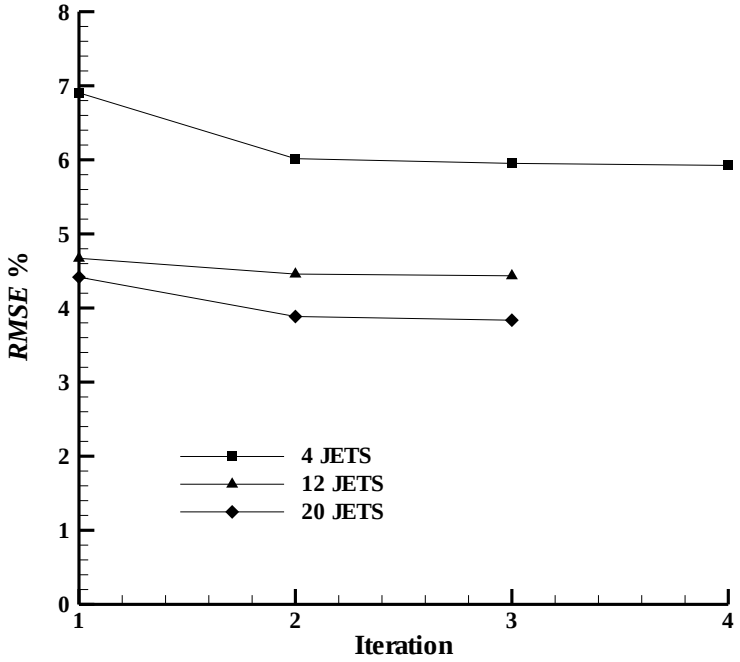

Figure 7.28 Convergence of *RMSE* with iterations.

The distortion parameters at the *AIP* after convergence are plotted in Figure 7.29. The distortion index for the target distribution was 21.426 % and that obtained was 11.576 %, 13.204 % and 12.267 %, respectively, with four, twelve and twenty jets. A visual inspection of the total pressure loss contours indicates that with twelve and twenty jets the pattern has similar regions of high and low total pressure region compared to the target pattern. The contour obtained with twenty jets appears closer to the target distribution. This can also be quantified by the total pressure distribution in the rings. The ring-wise total pressure loss distribution is plotted separately for the five rings for the sake of clarity. It was earlier mentioned that the target total pressure pattern was obtained with a screen. The distortion screens have a typical character of inducing sharp total pressure gradients at the edges of the screen from the distorted to undistorted section (Overall 1972). This sharp transition can be seen in the target distribution in all the rings from about 90º to about 315º. The jet systems are not able to reproduce these steep gradients. The air jet system not capturing the steep gradients was also reported in

Braithwaite, Dicus and Moss (1970). In all the rings the total pressure distribution obtained with twenty jets agrees reasonably well with the target distribution.

(a)TARGET

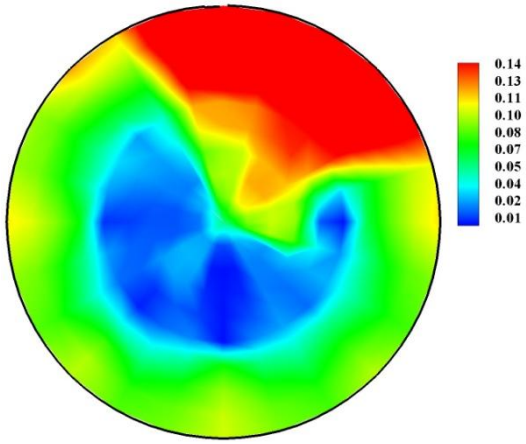

(b) ACHIEVED

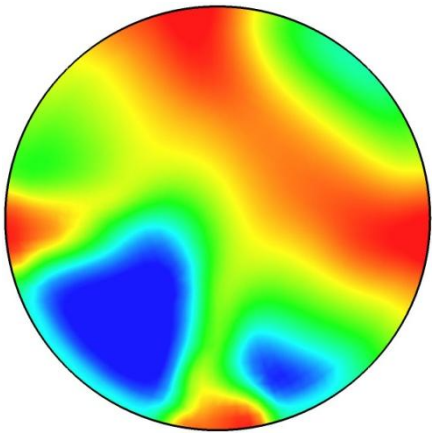

4 JETS

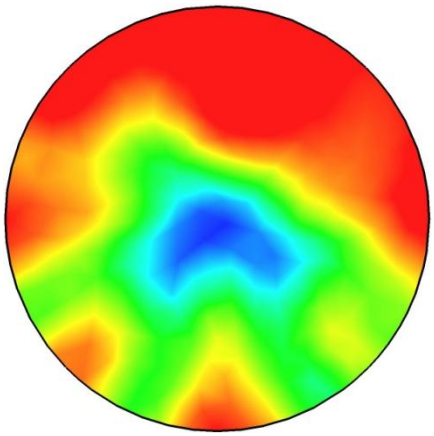

12 JETS

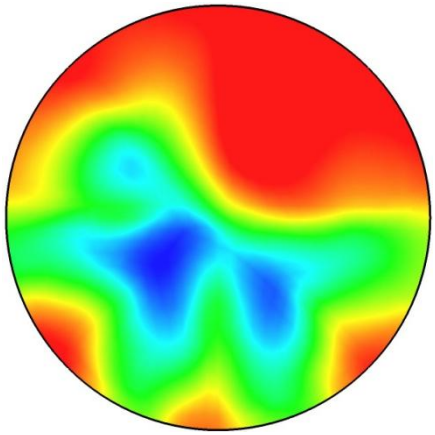

20 JETS

(c)

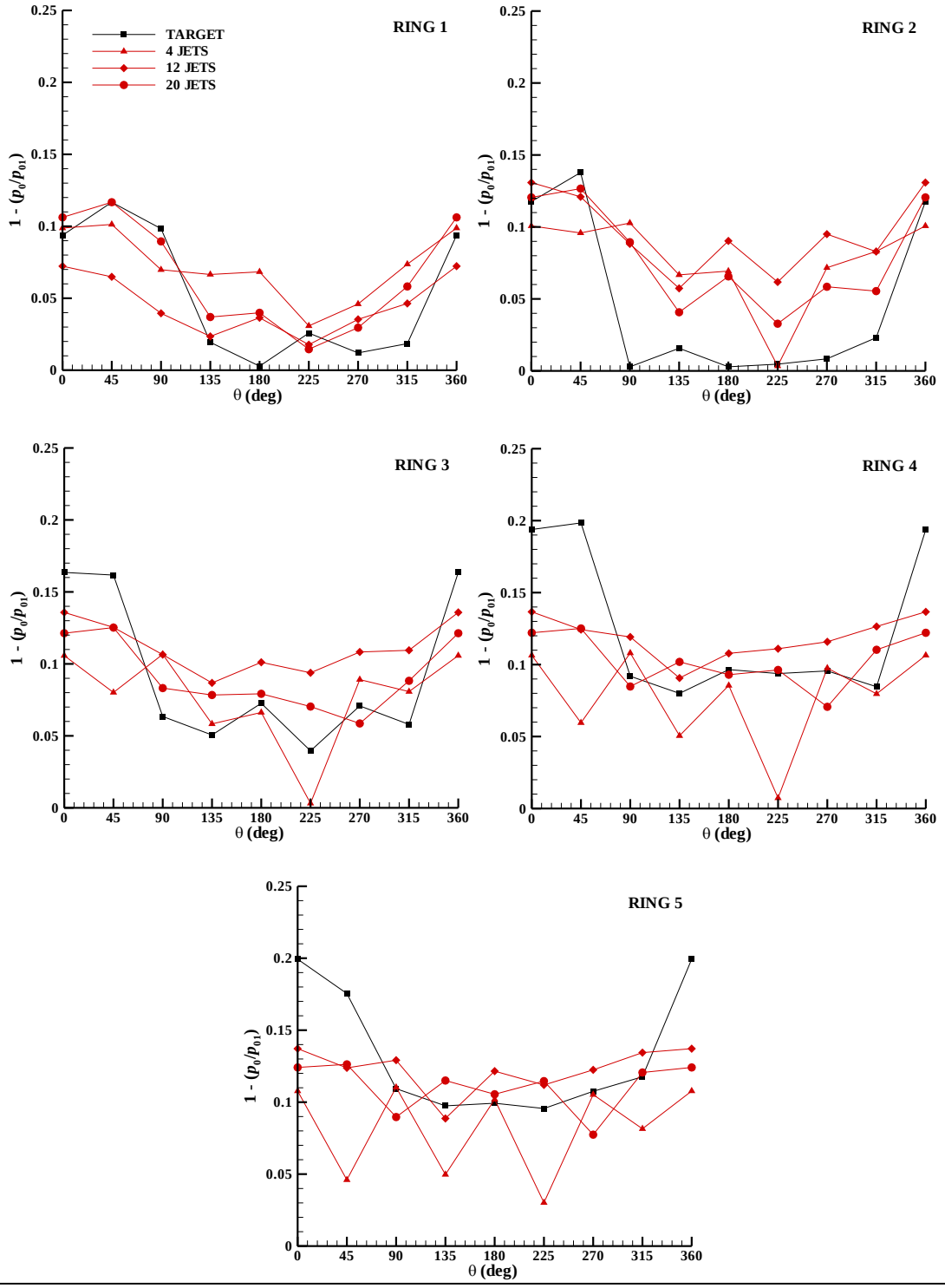
TARGET
4 JETS
12 JETS
20 JETS
RING 1
RING 2
RING 3
RING 4
RING 5
1 - (p0/p01)
θ (deg)
0
45
90
135
180
225
270
315
360
0.05
0.1
0.15
0.2
0.25

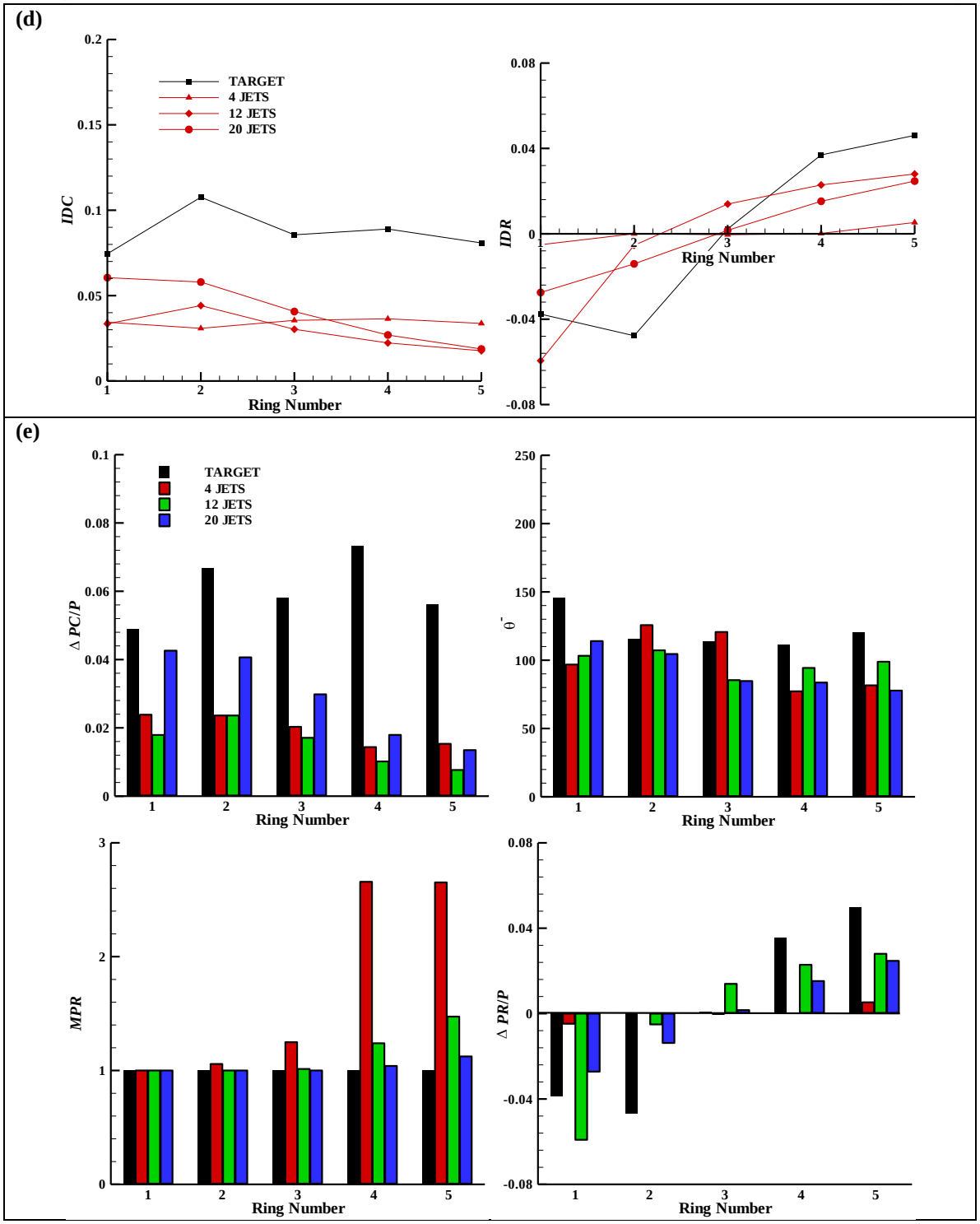

Figure 7.29 (a) Target total pressure loss distribution, (b) achieved total pressure loss distribution with four, twelve and twenty jets (c) ring-wise total pressure loss distribution (d) circumferential (*IDC*) and radial (*IDR*) distortion elements and (e) circumferential distortion intensity (Δ*PC*/*P*), circumferential extent (θ^-), multiple-pre-rev (*MPR*) and radial distortion intensity (Δ*PR*/*P*).

The circumferential and radial distortion components, *IDC* and *IDR*, are plotted in Figure 7.29(d). The *IDC* values of the air jet system are lower than the target values. In the hub region the *IDC* values from twenty jet system are closer to the target values while near the tip region the *IDC* of four jet system is larger than both the twelve and twenty jet systems. The *IDR* values for the target distribution are lower at the hub and higher near the tip compared with the values from twenty jet system. An inconsistent behaviour of *IDC* and *IDR* values were also reported in Hubble and Smith (1979).

The circumferential intensity for the target pattern was higher compared to the jet systems; however, the twenty jet system fares well in comparison. The circumferential extent is captured well by all the jet systems. The target pattern had no *MPR* content. But the four jet system has incurred *MPR* content in four rings. The twelve jet system has *MPR* content in the tip rings; the twenty jet system also has *MPR* content in the outer rings, but lower than that of the twelve jet system. The radial intensity with the four jet system is very small, and again the twenty jet system compares fairly well with the target values.

Overall, the twenty jet system is able to reproduce the target distribution reasonably well in terms of lower *RMSE* and other distortion parameters.

7.5.2 Example 6

Now, another example flow case, again, chosen from AIR1419 (Figure 22 in that document, slightly modified here) is used as a target pattern. The total pressure at the 40 probe locations s non-dimensionalised by the average total pressure in the plane is listed in Table 7.2. From this data the target total pressure loss distribution which is to be generated at the AIP is shown in Figure 7.32(a). This pattern is a typical aircraft-type pattern, perhaps, measured in an aircraft inlet test. This particular pattern has strong mid-span circumferential distortion and strong tip radial content. The circumferential distortion is of 180^{o} extent has no multiple-per-rev content.

Table 7.2 Target total pressure distribution pertaining to Example 6.

Rake → / **Ring ↓**	**1**	**2**	**3**	**4**	**5**	**6**	**7**	**8**
1 (Hub)	1.109	1.089	1.010	0.947	1.017	1.037	1.039	1.082
2	1.109	1.100	1.024	0.888	0.937	1.020	1.025	1.092
3	1.088	1.074	1.030	0.891	0.896	0.972	0.980	1.088
4	1.050	1.027	1.008	0.938	0.893	0.989	0.948	1.029
5 (Tip)	0.949	0.945	0.953	0.897	0.902	0.913	0.904	0.972

As with the previous example, the target pattern is simulated using four, twelve and twenty jets. The procedure of averaging the 40 total pressure data is also similar to the previous example. With the respective sampling points calculated the methodology is started and computations performed. The convergence of the *RMSE* is shown in Figure 7.30. The scheme converges quicker with twelve and twenty jets compared to the four jet case. The *RMSE* at convergence with four jets is 5.802 %, and that with twelve and twenty jets are 4.496 % and 4.479 %, respectively. The *RMSE* with twenty jets is only marginally lower compared to the twelve jet case.

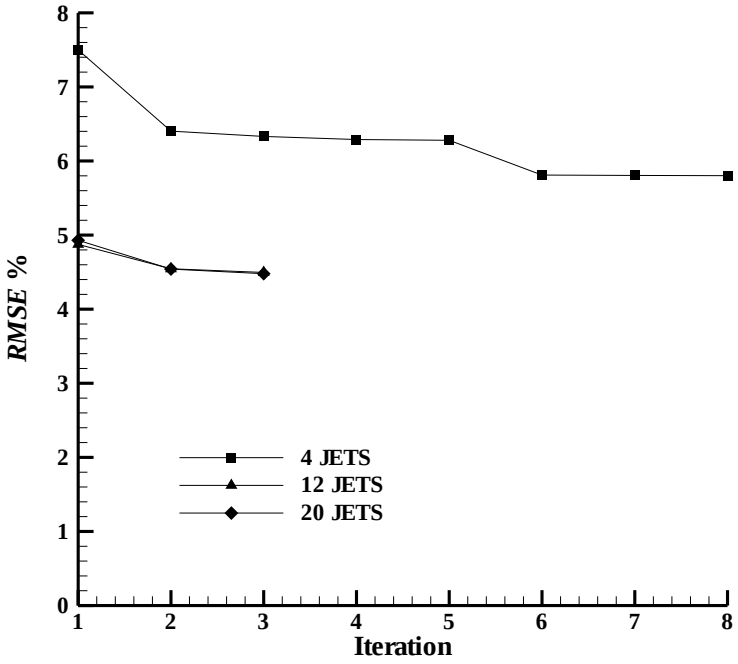

Figure 7.30 Convergence of *RMSE* with iterations.

The distortion parameters at the *AIP* after convergence are plotted in Figure 7.31. The distortion index for the target distribution was 22.177 % and that obtained was 15.375 %, 15.496 % and 14.029 %, respectively, with four, twelve and twenty jets. An inspection of the total pressure loss contours indicates that with twelve and twenty jets the pattern has nearly similar regions of high and low total pressure region compared to the target pattern. The contours obtained with twenty jets appear closer to the target distribution. The ring-wise total pressure loss distribution for the five rings is plotted in Figure 7.31(c). The total pressure loss distribution achieved with all the jet systems are nearly close to each other (except in ring 1) and the distribution in all the rings are reasonably close to the target distribution as well.

The circumferential and radial distortion components, *IDC* and *IDR*, are plotted in Figure 7.31(d). The *IDC* values with the jets are lower than the target values. The *IDR* values from four jet system are considerably lower than the target values. However, the

(a)

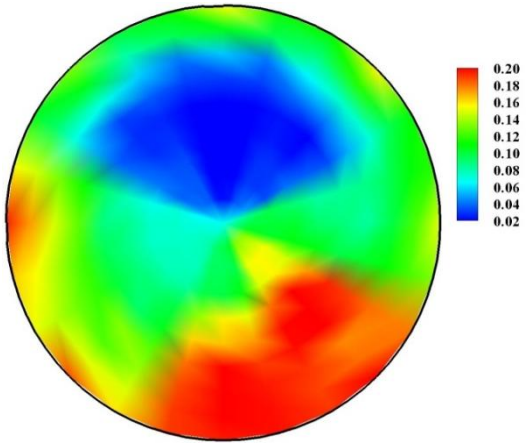

TARGET

(b)

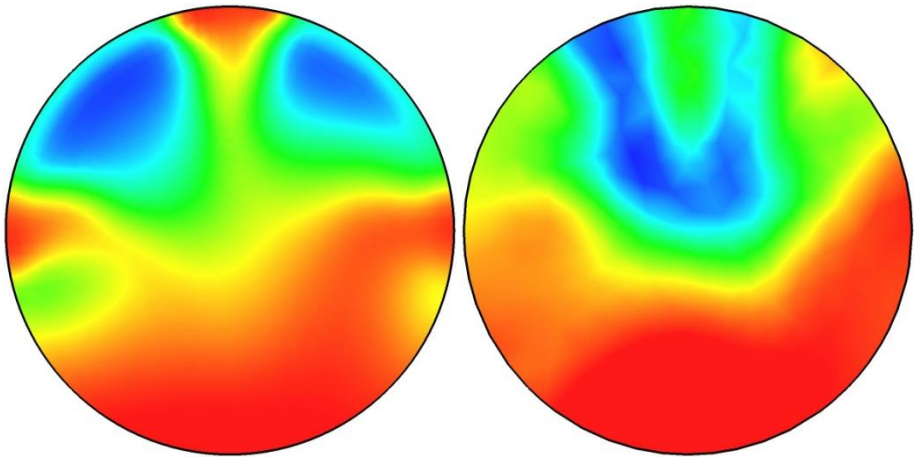

4 JETS **12 JETS**

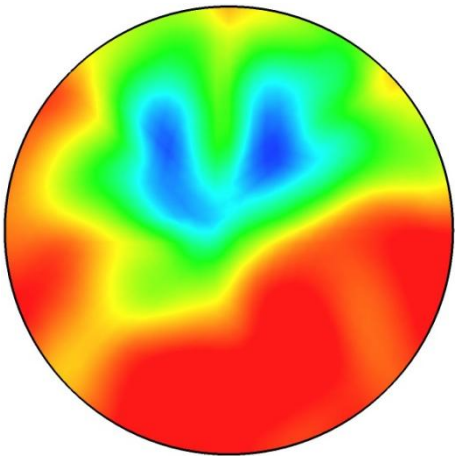

20 JETS

(c)

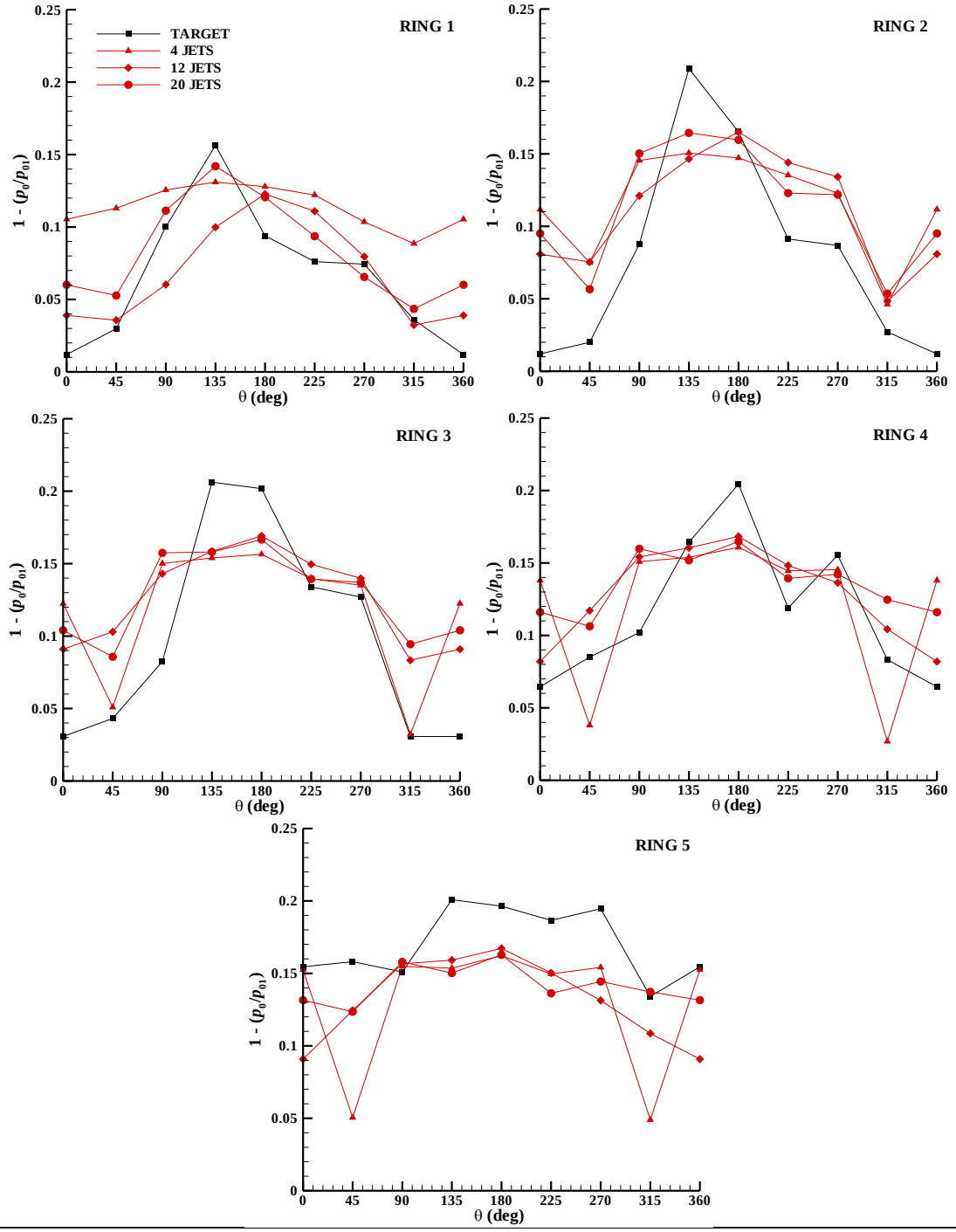
RING 1
RING 2
RING 3
RING 4
RING 5
TARGET
4 JETS
12 JETS
20 JETS
1 - (p0/p01)
θ (deg)
0
45
90
135
180
225
270
315
360
0.05
0.1
0.15
0.2
0.25

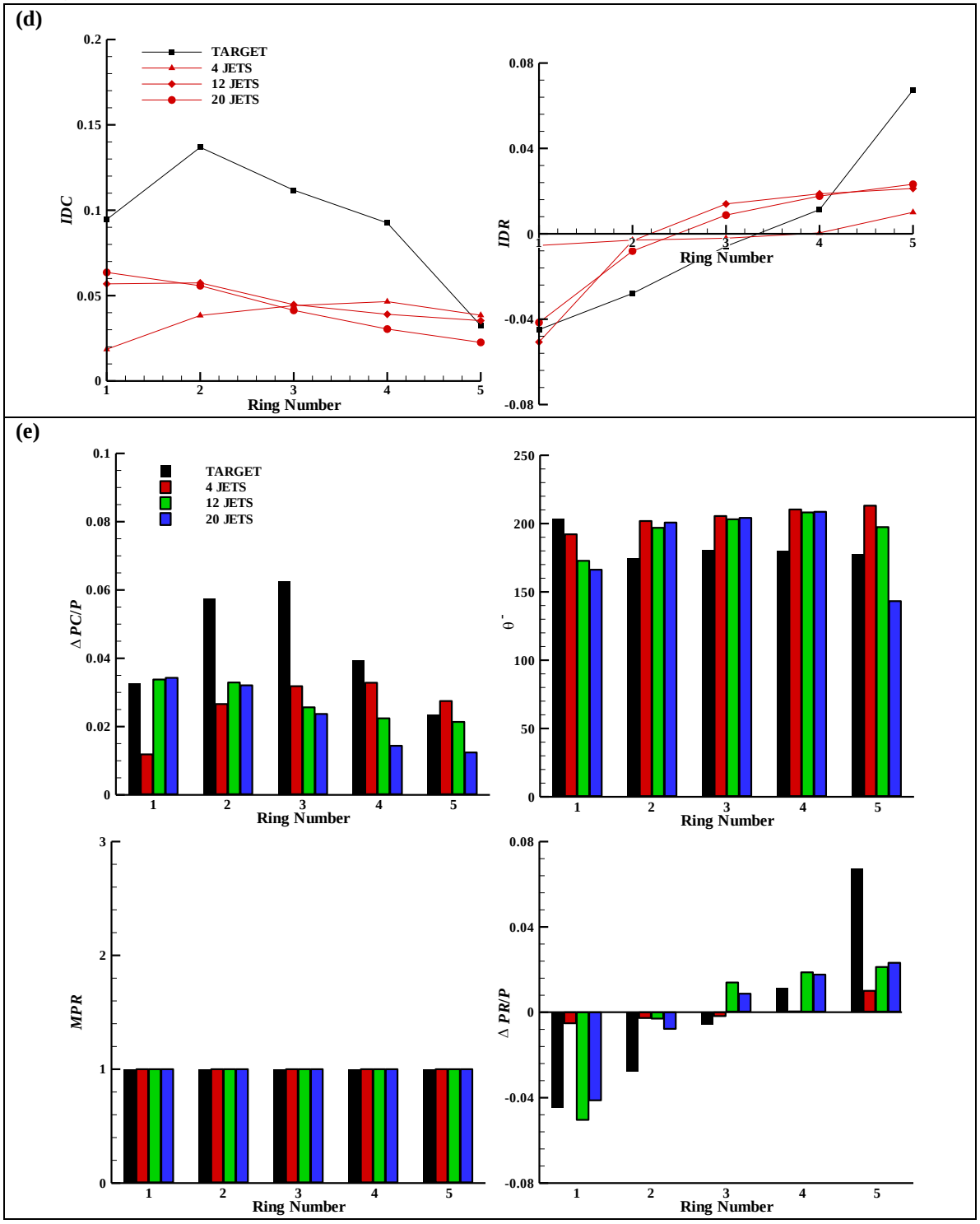

Figure 7.31 (a) Target total pressure loss distribution, (b) achieved total pressure loss distribution with four, twelve and twenty jets (c) ring-wise total pressure loss distribution (d) circumferential (*IDC*) and radial (*IDR*) distortion elements and (e) circumferential distortion intensity (Δ*PC*/*P*), circumferential extent ($\bar{\theta}$), multiple-pre-rev (*MPR*) and radial distortion intensity (Δ*PR*/*P*).

IDR values from the twelve and twenty jet systems are close and comparable to the target values except at the tip.

The circumferential distortion intensity for the target pattern was higher compared to the jet systems, except for the four jet system where the ring 5 value is higher. The circumferential extent is captured well by all the jet systems. The target pattern had no *MPR* content and the jet systems also do not have any *MPR* content. The radial intensity with the four jet system is very small, and the twelve and twenty jet systems compares fairly well with the target values. Thus a complex aircraft-type distortion pattern was simulated reasonably well with twelve and twenty jet systems.

Now, considering examples 5 and 6, a careful visual inspection of the target total pressure loss contours and those achieved with the jet systems indicate they do not very truthfully represent the target patterns. But it may be recalled that the *RMSE* of the jets systems compared with the target pattern were quite low as summarised in Table 7.3.

Table 7.3 *RMSE* values of the jet systems compared with the target distribution.

Sl. No.	No. of jets	Example 5 *RMSE* %	Example 6 *RMSE* %
1.	4	5.924	5.802
2.	12	4.434	4.496
3.	20	3.836	4.479

Before addressing the question of why the total pressure loss contour patterns for the target and those achieved with the jet systems look different despite the low values of *RMSE*, brief mention is made here on the effect of the screen and air jet generated distortion patterns on the gas turbine engine performance. To illustrate this, an example is taken from Hubble and Smith (1979). Performance tests were conducted on a General Electric F101-GE-100 turbofan engine, first with distortion screens, and then the same patterns were reproduced with an air jet distortion generation system. These patterns are

shown in Figure 7.32. The *DI* (see equation 5.4) for the screen generated pattern was reported to be 23.4 % and that for the air jet generated pattern was 17.5 %. However, the *RMSE* between these patterns was only 2.552 %, notwithstanding the perceptible difference in these patterns, particularly in the air jet generated pattern the region of low total pressure loss spans half the plane. With the screen and air jet generated patterns, as shown in Figure 7.32, the compressor surge pressure ratio comparison was only 0.4 %. This difference was calculated as,

$$\frac{PRS_{air\ jet} - PRS_{screen}}{PRS_{screen}} \times 100 \qquad (7.6)$$

where *PRS* is the compressor pressure ratio at surge. The engine surge response to screen and air jet generated patterns was reported to agree within an average of one percent for all the patterns tested in this experimental programme. In an earlier programme of NASA using the Pratt & Whitney TF30-P-1 turbofan engine, the engine response to the distortion patterns generated by screens and air jets were reported to be in good agreement (Braithwaite, Dicus and Moss 1970). However, they had employed a different distortion factor, K_{D2}, developed by Pratt & Whitney to quantify the distortion patterns. Thus the engine response to similar distortion patterns generated by the screens and air jets do not vary significantly, and is, in fact, well within "engine-to-engine and facility-to-facility tolerances" (Hubble and Smith 1979).

(a) **(b)**

Figure 7.32 Total pressure loss contours generated by (a) Screen and (b) air jet distortion generation system (Hubble and Smith 1979).

Now the question of why the total pressure loss contours look different despite the low values of *RMSE* can be addressed. In addition to the *RMSE* values in Table 7.3, to further aid in the interpretation of the results, the *RMSE* were calculated in the individual rings (see Figure 5.4) using equation 7.1 with n = 8. A summary of the results for examples 5 and 6 for the data plotted in Figures 7.29(c) and 7.31(c) are presented in Table 7.4. A general observation is that the *RMSE* values for the individual rings decrease with an increase in the number of jets which is consistent with the observation in Table 7.3 for the overall *RMSE*. It can be reasoned that though the *RMSE* is a good quantity for comparative purposes it does not portray the differences in the two patterns compared. The *RMSE* was used here for comparative purposes, and the very nature of the definition of *RMSE*, as in equation 7.1, is to reduce the comparison between two data sets to a single number. The *RMSE* is defined for a point-by-point comparison (40 points are used in the present study; see Figure 5.4 for locations of these points) and the circumferential and radial total pressure loss gradients are not accounted for in *RMSE*. Thus the contours look different, even though the *RMSE* values are low. These circumferential and radial total pressure gradients can be important as the aircraft gas turbine compressor can respond differently to different gradients. In the present thesis it was only the *RMSE* which was minimised by increasing the number of jets. Thus, while the use of *RMSE* and its interpretation are debatable and subjective, the aircraft gas turbine industry routinely uses this simplistic metric for the sake of convenience and consistency.

Table 7.4 *RMSE* values of the jet systems compared with the target distribution in the individual five rings.

	Ring →	1	2	3	4	5
Example 5 *RMSE* %	4 jets	3.927	5.890	4.859	8.093	7.703
	12 jets	3.681	6.333	4.372	4.709	3.893
	20 jets	2.257	4.579	3.167	4.808	4.316
Example 6 *RMSE* %	4 jets	5.680	5.865	5.263	4.967	6.699
	12 jets	3.483	5.259	5.115	3.386	5.049
	20 jets	2.436	4.973	5.534	4.069	4.471

Considering again the individual data sets of the total pressure loss values for the target and the jet systems the statistical quantities like mean and standard deviation (S. D.) were calculated and tabulated in Table 7.5. From this table it is observed that the individual data points are spread out widely around the mean, indicated by large values of S. D., for the target patterns for both examples 5 and 6, and such a spread is not seen in the jets systems. The measure of association of the data sets was calculated by a linear correlation coefficient, *r*, which is defined below:

$$r = \frac{\sum A_{p_0} B_{p_0}}{\sqrt{\sum A_{p_0}} \sqrt{\sum B_{p_0}}} \qquad (7.7)$$

where

$$A_{p_o} = \left\{ \left[1 - \frac{p_0}{p_{01}} \right]_j - \left[1 - \frac{p_0}{p_{01}} \right]_{ave} \right\}_{target}$$

$$B_{p_o} = \left\{ \left[1 - \frac{p_0}{p_{01}} \right]_j - \left[1 - \frac{p_0}{p_{01}} \right]_{ave} \right\}_{achieved}$$

and the summation is over the 40 data points. The calculated values of *r* are tabulated in Table 7.5. It is seen that as the number of jets increases the value of *r* also increases indicating a good correlation among the data sets.

Table 7.5 Statistical quantities for the target and jet systems data sets.

		Mean	S. D.	*r*
Example 5	Target	0.083	0.058	---
	4 jets	0.074	0.030	0.343
	12 jets	0.096	0.034	0.701
	20 jets	0.087	0.032	0.842
Example 6	Target	0.112	0.063	---
	4 jets	0.119	0.041	0.573
	12 jets	0.117	0.040	0.783
	20 jets	0.123	0.036	0.828

The frequency of occurrence of the total pressure loss values for the target and jet systems data sets were calculated and plotted in Figure 7.33 for both examples 5 and 6. As was noted earlier a wide spread of data points are seen for the target set, whereas such a spread is not observed in the data sets of the jet systems.

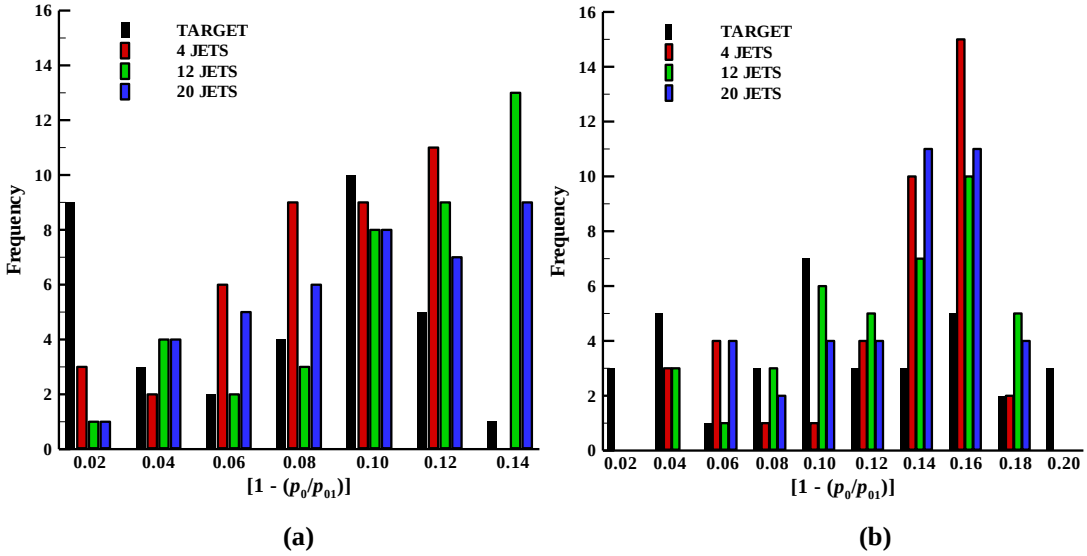

Figure 7.33 Frequency histogram of total pressure loss values for (a) example 5 and (b) example 6.

The parameter Distortion Index, *DI*, considered earlier (see equation 5.4), was a gross metric to quantify the total pressure non-uniformity and a useful descriptor for quick comparisons between two patterns. The *DI* values for the target patterns and those achieved with the jets systems are summarised in Table 7.6. Though the *DI* had the disadvantage of not being able to distinguish between circumferential and radial distortion components, the differences between the target and jet systems are easily discerned with this parameter. The $p_{0,max}$ and $p_{0,min}$ values non-dimensionalised by $p_{0,ave}$, whose difference is the *DI*, are also tabulated in Table 7.6. The high and low values of $(p_{0,max}/p_{0,ave})$ and $(p_{0,min}/p_{0,ave})$, respectively, in the target distributions are not obtained with the jets systems leading to a difference in the *DI* values. This observation is consistent with the earlier finding in Table 7.5 of large values of S. D. for the target data set.

Table 7.6 Distortion Index (*DI*) and ($p_{0,max}/p_{0,ave}$) and ($p_{0,min}/p_{0,ave}$) values for the target and jet systems.

		DI %	$p_{0,max}/p_{0,ave}$	$p_{0,min}/p_{0,ave}$
Example 5	Target	21.426	1.087	0.873
	4 jets	11.576	1.077	0.961
	12 jets	13.204	1.086	0.954
	20 jets	12.268	1.079	0.956
Example 6	Target	22.177	1.113	0.891
	4 jets	15.375	1.105	0.951
	12 jets	15.497	1.096	0.941
	20 jets	14.029	1.090	0.950

The discussions in the preceding paragraphs sheds light on why the total pressure loss contour patterns for the target and those achieved with the jet systems look different despite the low values of *RMSE*. The *RMSE* was used here to compare two data sets by reducing to a single number, and the very definition of *RMSE* suppresses the significant differences between the data sets. The *RMSE* does not account for the gradients in the total pressure. Also, in examples 5 and 6 the individual data points for the target distribution are spread out widely around the mean, indicated by large values of S. D., whereas such a spread is not seen in the data distributions of the jets systems; this observation is also true for the difference in the *DI* values.

A number of distortion parameters were used in this thesis for describing the distortion parameters. Each of them had its own merits and shortcomings. The *DI*, for example, though simple, is a rather crude descriptor and can have the same value for many widely differing flow patterns. The *RMSE* is simplistic, but suppresses the significant differences between the data sets compared. The SAE distortion descriptors are elaborate, but require separate descriptors for different distortion elements.

The most important requirements for the distortion parameters are they should describe well the magnitude and extent of circumferentially varying total pressure defect, the number of such defects in a ring and the magnitude of radially varying total pressure defect. The distortion parameters should also be able to lead to a good qualitative and quantitative comparison of two distortion patterns. As was seen earlier in this study the distortion patterns look distinct but their *RMSE* values are very close. This is because the parameters like *DI* and *RMSE* do not account for the characteristics that make the parameters distinct; for example, only the value of a function but not its derivatives being accounted for. A good distortion descriptor should handle such details keeping in mind also the geometric scales (like the compressor blade size and spacing) involved.

Another crucial aspect of the distortion parameters is that in addition to an accurate description of the various distortion elements they should also be able to be used in a gas turbine engine stability assessment programme to evaluate the engine compressor response to distorted conditions and result in consistently good correlations with the engine test data. It is to be mentioned here that SAE AIR1419 (1999) remarked that "a universal distortion descriptor is beyond the state-of-the-art". The all-encompassing distortion parameters do not exist now; but a clear need for the development of such metrics is emphasised. The present study indicates the possibility of describing more detailed metrics and their practical achievement. Such metrics would be useful to the gas turbine engine community.

7.6 Summary

A methodology was developed to generate a given total pressure pattern at the *AIP* through multiple jets at an upstream station and in the opposite direction. The number of jets is chosen and computations give the total pressure distribution at the *AIP*. The inputs required for the computations are obtained from a quasi-one-dimensional inviscid analysis keeping in mind the constraints of the problem. The inviscid analysis also provides a direction to perform the iterative procedure at the end of each computational step to achieve the target total pressure distribution at the *AIP*. The

methodology is presented first using four jets and subsequently demonstrated with twelve and later twenty jets. It was first done with simple examples and then with total pressure patterns typical of use in aircraft gas turbine engine testing.

The *RMSE* error with the air jet system demonstrated here are lower than those normally obtained with complex distortion screens. For instance, a complex distortion screen designed based on the methodology of Ramamurthy *et al*. (1998) was analysed computationally by Sivapragasam (2007) and the *RMSE* between the design intent and that actually obtained was about 11.4 %.

Further, the values of *RMSE* after convergence obtained here, for example, with twenty jets are lower than those reported in Hubble and Smith (1979), whose maximum *RMSE* for complex distortion patterns was about 6.3 %; it may be noted that they had used 56 jets in their system.

CHAPTER 8

CONCLUSIONS AND RECOMMENDATIONS FOR FURTHER WORK

In this chapter the major findings from this thesis are summarised, reviewed and discussed. The conclusions drawn from these results are presented along with certain recommendations for further course of work.

Incompressible Axisymmetric Turbulent Jet in Confined Counterflow

In Chapter 4 an incompressible axisymmetric jet issuing into a confined counterflow was investigated computationally. This study provided the basis for gaining an understanding into the characteristics of a turbulent jet issuing in an opposing stream. The computations were performed for different duct-to-jet diameter ratios and various jet-to-counterflow velocity ratios. The flow field was dominated by a large recirculation zone due to the interaction of the jet and the counterflow. The jet in confined counterflow behaves differently from a jet in unconfined counterflow. The jet penetration length and the jet width are reduced and a linear relationship between the velocity ratio and the jet length ceases to be valid. At very high values of momentum flux ratio between the jet and the counterflow corresponding to the confinement, the jet penetration length reaches an asymptotic limit of about 3.57 times the confining duct diameter. This conclusion is contrary to the existing results which predict indefinite growth.

Single Jet in Confined Counterflow

In Chapter 5 a single circular compressible turbulent jet in confined counterflow was investigated experimentally and computationally for various jet-to-counterflow mass flow ratios ranging from 0.090 to 0.332. The loss in total pressure due to the jet interacting with the counterflow was quantified by a total pressure loss parameter λ_{p0}. The total pressure loss increased with increasing mass flow ratio. The total pressure loss distribution was evaluated at several locations behind the jet injector. The total pressure non-uniformity quantified by Distortion Index (*DI*) was found to be highest at a location just downstream of the jet injector and at far downstream locations low values of *DI* were

observed. The *DI* increased with an increase in mass flow ratio at all the planes. At the highest mass flow ratio in this study m_2/m_4 = 0.322 the *DI* at z/D_0 = - 0.82 was about 3.504 % decreasing to about 0.907 % at z/D_0 = - 4.9.

The total pressure distribution and total pressure distortion parameters at the *AIP* were examined for three typical mass flow ratios m_2/m_4 = 0.130, 0.230 and 0.332. In general, the total pressure loss increased with increasing mass flow ratio. The circumferential total pressure distribution was nearly uniform for all the mass flow ratio cases and the dip in the total pressure distribution at one circumferential location was due to the wake from the jet stem. The circumferential and radial distortion parameters also increased with increase in mass flow ratio.

Four Jets in Confined Counterflow

In Chapter 6 four jets circumferentially arranged and issuing into confined counterflow was investigated experimentally and computationally for various jet-to-counterflow mass flow ratios ranging from 0.190 to 0.352. The mass flow rates in the four jets were equal in the first part of the study and in the second part they were unequal.

The loss in total pressure due to the jets interacting with the counterflow was, again, quantified by a total pressure loss parameter λ_{p0}. The total pressure loss increased with increasing mass flow ratio. The total pressure loss distribution was evaluated at several locations behind the jet injector. Distortion Index (*DI*) was found to be highest at a location just downstream of the jet injector and at far downstream locations low values of *DI* were observed. The *DI* increased with an increase in mass flow ratio at all the planes. At the highest mass flow ratio for the equal mass flow rates in the jets m_2/m_4 = 0.197 the *DI* at z/D_0 = - 0.82 was about 18.596 % decreased to about 3.713 % at z/D_0 = - 4.9. Correspondingly for the unequal mass flow rates in the jets, with m_2/m_4 = 0.193 the *DI* at z/D_0 = - 0.82 was about 29.285 % decreasing to about 8.988 % at z/D_0 = - 4.9.

The total pressure distribution and total pressure distortion parameters at the *AIP* were examined for three typical mass flow ratios m_2/m_4 = 0.110, 0.165 and 0.197 with equal mass flow rates in the jets and m_2/m_4 = 0.110, 0.214 and 0.268 with unequal mass flow rates in the jets. The total pressure loss increases with increasing mass flow ratio resulting in steeper dips in the ring-wise total pressure loss distribution. The circumferential and radial distortion parameters also increased with increase in mass flow ratio.

Methodology to Generate a Prescribed Total Pressure Distortion Pattern

From the understanding gained with a single jet and four jets in counterflow a methodology has been developed to generate a given total pressure distortion pattern at the *AIP* in Chapter 7. The methodology was based on the computational procedure for multiple jets in counterflow and the quasi-one-dimensional inviscid analysis is used as the starting point to estimate the overall total pressure loss. The average Mach number and the required total pressure loss distribution at the *AIP* are used as inputs for the inviscid analysis. The inlet Mach number, M_1, and the mass flow ratio, m_2/m_4, necessary to exert the required total pressure loss are estimated. From the overall total jet mass flow rate, the mass flow rates in the individual jets are calculated by dividing the flow field into a number of streamtubes equal to the number of jets, and with the inviscid calculations now done for the individual streamtubes. The target total pressure was achieved iteratively. In the iterative process at the end of each computational step the mass flow rates in the jets need to be changed. These changes in the mass flow rates were estimated by inviscid analysis.

The methodology developed was demonstrated with two examples with the four jet system. The first example had equal mass flow rates in the jets and the second had unequal mass flow rates. With equal mass flow rates in the jets the total pressure field generated was close to the target total pressure distribution with *RMSE* as low as 0.328 % and with unequal mass flow rates in the jets the *RMSE* was 4.443 %.

The methodology was further demonstrated on a twelve jet system with two examples – one with equal mass flow rates in the jets and another with unequal mass flow rates. The total pressure field generated for the equal mass flow rates case was close to the target distribution with the *RMSE* as 0.490 % and with unequal mass flow rates in the jets the *RMSE* was 7.662 %.

Further this methodology was extended to twenty jet case and tested for satisfactory convergence. The procedure was employed to generate total pressure distortion patterns typically used in aircraft engine testing. In the first example the total pressure distortion to be generated was a 90º one-per-rev and tip radial combined distortion pattern which has essentially uniform circumferential and radial distortion elements. The *RMSE* at convergence was 5.924 %, 4.434 % and 3.836 % with the four, twelve and twenty jet systems, respectively. In the second example the target total pressure distribution had a strong mid-span circumferential distortion and tip radial content. The *RMSE* at convergence with four, twelve and twenty jet systems were 5.802 %, 4.496 % and 4.479 %, respectively.

Thus the methodology was demonstrated to generate total pressure distortion patterns typical of aircraft distortion tests using four, twelve and twenty jets. In the two example cases selected the total pressure distortion pattern and the distortion elements were found to be generated well with the twenty jet system. The accuracy in values of *RMSE* obtained in the present method with only twenty jets is better than what the AJDG at the AEDC had achieved with 56 jets. Thus increasing the number of jets for further improvement in accuracy appears not needed.

A methodology has been developed from rigorous fluid dynamics principles involving a quasi-one-dimensional inviscid analysis to generate a complex total pressure distortion pattern. This methodology is demonstrated using twenty jets to generate total pressure patterns typical of use in aircraft gas turbine engine testing. The *RMSE* for the complex total pressure distortion pattern generated in the two example flow cases were

3.84 % and 4.48 % with twenty jets. The *RMSE* error with the air jet system demonstrated here are lower than those normally obtained with complex distortion screens. Further, the *RMSE* obtained here are with only twenty jets are lower than those obtained with 56 jets. A complex total pressure distortion pattern can be generated by the present methodology to simulate aircraft inlet flow distortion in gas turbine engine test facilities and is an original contribution from this thesis.

Recommendations for further work

Some recommendations are made for further work in the following paragraphs.

The study of the dynamics of the jet in counterflow is recommended to understand this flow system better. Large eddy simulation (LES) was used to investigate the dynamics of the jet flow field by Duwig and Revstedt (2009) and Li *et al*. (2013). It may be mentioned that both these work consider the counterflow to be unconfined. The confinement is expected to alter the dynamics of the flow field which can make an interesting study.

The jet penetration length was shown in Chapter 4 to asymptotically reach a value of about 3.57 D_0 [see Figure 4.7(b)]. The jet was incompressible in this case; for a compressible jet the jet length may also reach an asymptotic limit. The indefinite growth of u_{max}/u_0 in Figure 4.8 may not happen in the compressible flow case and it is postulated that the maximum Mach number in the neighbourhood of the jet may reach a sonic value thus choking the flow. This study can also be undertaken.

These studies can be done to gain a better fundamental understanding of this flow system and render it useful for various practical applications.

As regards the air jet distortion system itself the following studies are recommended.

The air jet distortion system has the potential of generating dynamic total pressure distortion patterns. The air jet distortion systems at NASA and AEDC had provision for pulsing the jets. The air jets can be pulsed at discrete frequencies to generate dynamic distortion at the *AIP*. A research can be undertaken to study the dynamic characteristics of total pressure distortion.

The performance of a fan/compressor can be studied in the presence of inlet total pressure distortion generated by the air jet system.

The use of *RMSE* as a comparative descriptor for comparing two distortion patterns was seen to be debatable and subjective. However, the aircraft gas turbine industry routinely uses this simplistic metric for the sake of convenience and consistency. Several other distortion parameters were used in this thesis for describing the distortion parameters; each of them had its own merits and shortcomings. A need was emphasised for the development of superior metrics for the description of total pressure distortion. The development of such metrics should be undertaken.

APPENDIX – 1

SIMILARITY SOLUTION FOR A TURBULENT JET IN COUNTERFLOW

It was mentioned in Section 4.1 that a similarity solution exists in region 2 (see Figure 4.1) for the jet in unconfined counterflow. In this appendix this similarity solution is revisited in the light of the present computational results. A simple modification of the similarity solution provides a convenient framework for presenting the results of the flow field and jet penetration length.

The similarity solution for a turbulent jet in an unconfined counterflow obtained by Oron and Abuaf (1977) is briefly summarised. The governing equations for the axisymmetric flowfield are written below following the usual boundary layer assumptions:

$$\left(u\frac{\partial u}{\partial x}+v\frac{\partial u}{\partial r}\right)=\frac{1}{\rho}\frac{1}{r}\frac{\partial}{\partial r}\left(r\,\mu_t\frac{\partial u}{\partial r}\right) \qquad \text{(A1.1)}$$

$$\frac{\partial}{\partial x}(ru)+\frac{\partial}{\partial r}(rv)=0, \qquad \text{(A1.2)}$$

subject to the boundary conditions

$$v=0,\ \frac{\partial u}{\partial r}=0 \ \text{ at } r=0, \text{ and} \qquad \text{(A1.3)}$$

$$u = -\,u_0 \text{ as } r\rightarrow\infty. \qquad \text{(A1.4)}$$

At the jet exit ($x = 0$),

$$m_j=\rho\int_0^{r_j}2\pi\,u(0,r)\,r\,dr, \quad \text{and} \quad u(0,r_j)=0. \qquad \text{(A1.5)}$$

Here, ρ is the density of the fluid, m_j is the jet mass flow rate and $r_j = d_j/2$, is the radius of the jet nozzle. The turbulent viscosity, μ_t, is modeled using a modified version of the Prandtl mixing length model for free shear flows (see Schlichting 1979).

A similarity solution is attempted assuming that the streamfunction ψ is of the form

$$\psi = U\,\Delta\, f(\eta). \tag{A1.6}$$

Here, Δ is a characteristic cross-sectional mixing area in the radial direction, $\eta = \Gamma/\Delta$, and U is the relative velocity defined as $U = u_c + u_0$; u_c is the axial velocity along the x-axis and is a function of x only.

Also, Γ is a new variable defined as

$$\Gamma = \int_0^r r\,dr = \frac{r^2}{2}.$$

Substituting the assumed form of the similarity solution (A1.6) in equations (A1.1) and (A1.2), the following expression was obtained for the variation of axial velocity along the jet centreline:

$$\frac{l_p - x}{d_j} = \frac{1}{2\lambda}\frac{e^{\eta_j - 1}}{\sqrt{2\eta_j}}\left[1 - \frac{u_0}{U}\exp\left(1 - \frac{u_0}{U}\right)\right], \tag{A1.7}$$

where η_j is the value of η at the starting location of the jet similarity and $\lambda = 0.075$ is the non-dimensional value of mixing length in the jet.

If at $x = 0$, the relative velocity $U = U_0$, the jet penetration length, l_p, can be obtained from:

$$\frac{l_p}{d_j} = \frac{1}{2\lambda}\frac{e^{\eta_j - 1}}{\sqrt{2\eta_j}}\left[1 - \exp\left(1 - \eta_j - e^{-\eta_j}\right)\right]. \tag{A1.8}$$

A1.1 Application of Similarity Solution to Nozzles with Uniform Velocity Profiles

It is to be noted that in the derivation of the expressions (A1.7) and (A1.8) above, Oron and Abuaf (1977) assumed a fully developed velocity profile at the nozzle exit. They also extended their analysis to nozzles with a uniform velocity profile at the jet exit. The velocity ratio, u_j/u_0, was related to η_j through an approximation

$$\eta_j = \ln\left(1+\frac{u_j}{u_0}\right). \tag{A1.9}$$

A hypothetical nozzle was defined at the end of the developing region which can be used to evaluate the penetration length beyond this location from equation (A1.8). Hence in equations (A1.7) and (A1.8) d_j is actually the diameter of the hypothetical nozzle d_h, which needs to be replaced by the physical diameter d_j. This was done in Oron and Abuaf (1977) by approximating

$$\frac{d_h}{d_j} = \sqrt{2\eta_j}\ . \tag{A1.10}$$

Thus, equations A1.7 and A1.8 get modified, respectively, to

$$\frac{l_p - x}{d_j} = \frac{1}{2\lambda} e^{\eta_j - 1}\left[1-\frac{u_0}{U}\exp\left(1-\frac{u_0}{U}\right)\right], \tag{A.11}$$

and

$$\frac{l_p}{d_j} = \frac{1}{2\lambda} e^{\eta_j - 1}\left[1-\exp\left(1-\eta_j - e^{-\eta_j}\right)\right]. \tag{A.12}$$

The jet penetration lengths calculated from the Oron and Abuaf (1977) model using equations (A1.8) and (A1.12) using the actual and hypothetical nozzle diameters are plotted in Figure A1.1 and compared with the present computational results for the highest diameter ratio D_0/d_j = 100 in this study. It can be seen that the Oron and Abuaf (1977) model highly under-predicts the jet penetration length.

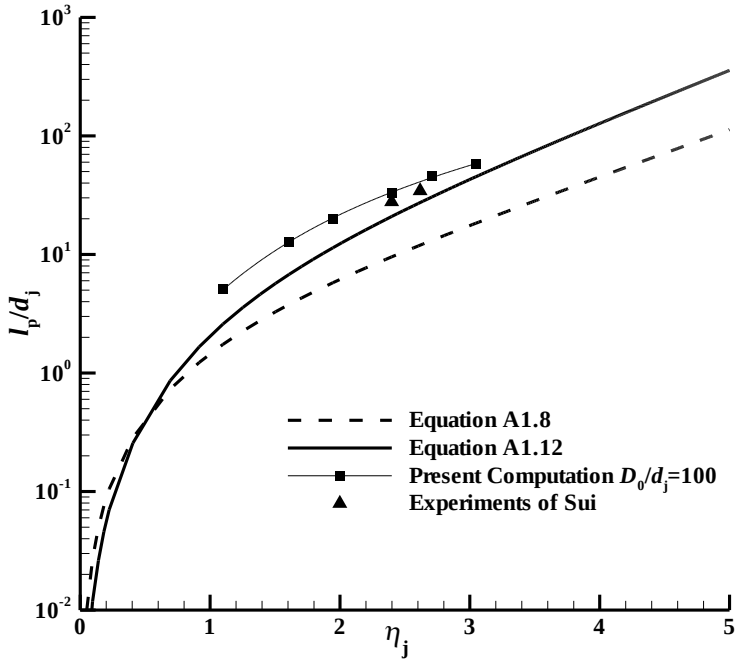

FigureA1.1 Non-dimensional jet penetration, l_p/d_j, as a function of η_j from Oron and Abuaf (1977). The dashed line is equation (A1.8) and the dark continuous curve is equation (A1.12) accounting for the hypothetical nozzle diameter given by equation (A1.10).

A major difficulty in this comparison is not knowing where exactly the hypothetical nozzle is to be located and hence the approximation given by equation (A1.10) is inadequate. Also, the penetration length starts from this hypothetical nozzle and such data will neither be easy nor convenient to a designer or an experimenter. Even though Oron and Abuaf (1977) claim a good agreement with modified experimental data of Sui (taken from Sekundov 1969), they had to curtail a significant portion of the jet length (more than 50% in some cases).

To overcome this difficulty the distinct potential core of length l_c is accounted (see equation A1.14) and also the approximations given by equations (A1.11) and (A1.12) are modified by introducing a scaling factor α to write

$$\frac{l_p - x}{d_j} = \frac{\alpha}{2\lambda} e^{\eta_j - 1} \left[1 - \frac{u_0}{U} \exp\left(1 - \frac{u_0}{U} \right) \right]. \qquad \text{(A1.13)}$$

Further, the procedure is simplified in this model assuming that similarity starts from the distinct location where the potential core ends; the determination of the length of the potential core is straightforward. This enables the addition of the potential core to the length of the similarity region to obtain the jet penetration length.

Now the computational data are useful in the evaluation of the scaling factor α. This is shown in Figure A1.2. Again, the case of D_0/d_j=100, the highest diameter ratio computed is considered. There is a reasonably good agreement after a shift equivalent to the potential core length is made. The advantage here compared to the strategy of Oron and Abuaf (1977) is that this location is distinct and easily identified and the length of the potential core is not very sensitive to the velocity ratio u_j/u_0 (see Figure 4.4) for larger values of velocity ratios which are of practical interest.

Another superior feature of this procedure is that the overall jet penetration length is kept intact unlike in Oron and Abuaf (1977) where the comparison is made with a curtailed penetration length. The value of α used here is 1.3 for all cases of u_j/u_0.

A particularly important observation to be made in Figure A1.2 is when the centreline velocity, u_c/u_0, becomes negative after the curve reaches the stagnation point. This is given by a dotted curve and it does not represent the physical reality. The results shown by equations (A1.7), (A1.11), or (A1.13) do not have validity beyond the penetration length. The tangent to this curve at the stagnation point is, in fact, vertical and this shows the difficulty in achieving good agreement between the actual and similarity solutions in this neighbourhood. This difficulty, of course, is not unexpected since the boundary layer assumptions themselves fail in the neighbourhood of the stagnation point.

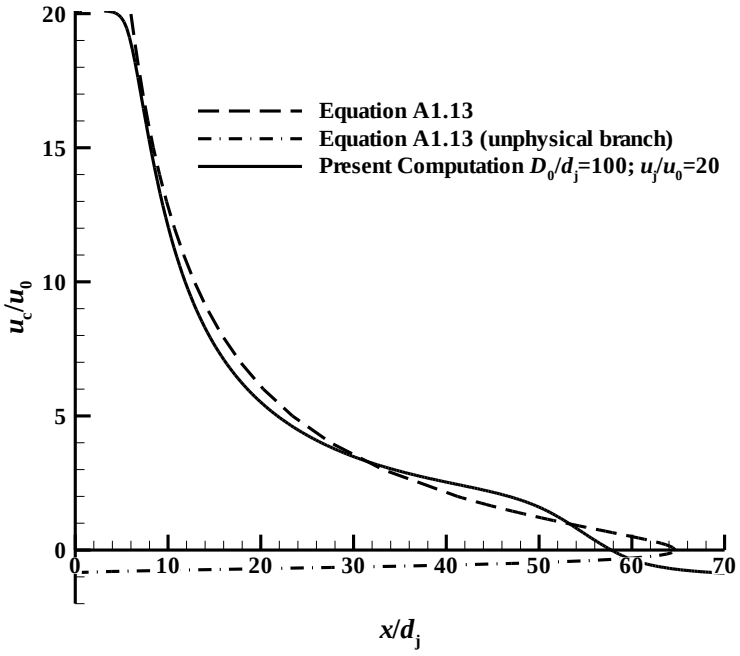

Figure A1.2 Variation of axial velocity, u_c/u_0, along the jet centreline; u_j/u_0=20. The variation of jet centreline velocity given by Oron and Abuaf (1977) modified by a scaling factor as given in equation (A1.13) is plotted here. This equation does not give values beyond the stagnation point and gives negative centreline velocity which is not physical and is shown by a dotted curve.

A further insight into the similarity solution and the flow may be obtained by replotting Figure A1.2 on a logarithmic scale as shown in Figure A1.3 in order to examine if any power law exists for the decay of centreline velocity. The ordinate now chosen is the centreline axial velocity, u_c, non-dimensionalised by the relative velocity U ($U = u_c + u_0$). By plotting the reciprocal of u_c a convincing power law with slope = 1 is seen and agreement between the computational and similarity solutions after the similarity solution is shifted to the right by the length of the potential core. The boundaries of the three regions shown schematically in Figure 4.1 can clearly be seen here. The similarity solution has difficulty in the vicinity of the stagnation point as explained above. The equivalent of the dotted line in Figure A1.2 is ignored here.

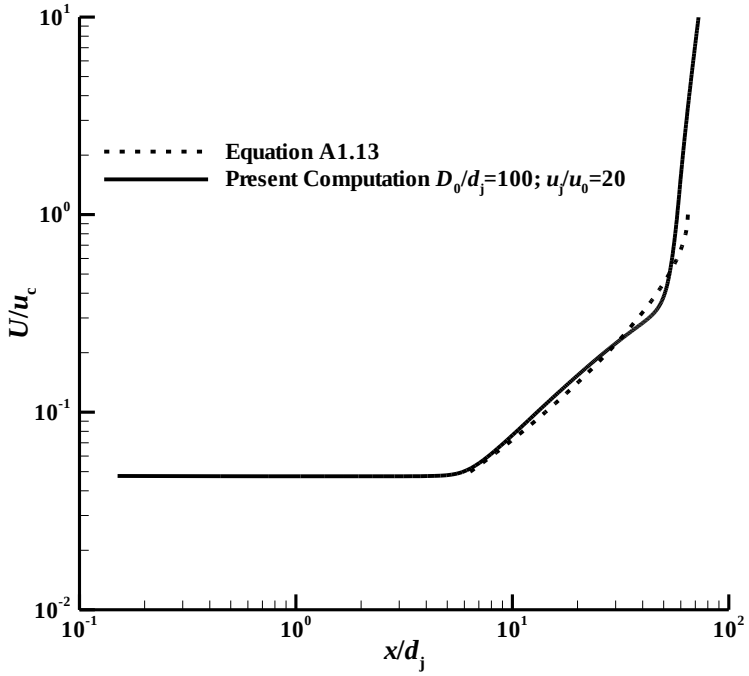

Figure A1.3 Variation of axial velocity along jet centreline plotted as a function of the axial location. Plotting the reciprocal of u_c helps to identify a power law-like variation in the similarity region.

A comment on the length of the interaction region (region 3 in Figure 4.1) is appropriate here. Oron and Abuaf (1977) estimate this region to extend from u_c/u_0 = 0.22 till the stagnation point. The present results are contrary to this observation. The interaction region starts where u_c/u_0 falls below 2 (see Figure 4.11). As mentioned above, this observation will not affect the overall results as this length constitutes only a small part of the jet penetration length.

Thus the modelled jet penetration length can finally be written as,

$$\frac{l_p}{d_j} = \frac{\alpha}{2\lambda} e^{\eta_j - 1}\left[1 - \exp\left(1 - \eta_j - e^{-\eta_j}\right)\right] + \frac{l_c}{d_j}. \qquad \text{(A1.14)}$$

Here, l_c is the potential core length whose values were evaluated from the present computational results. As mentioned earlier this length is not very sensitive to the velocity ratio, u_j/u_0.

The jet penetration length given by equation (A1.14) is plotted in Figure A1.4(a) along with the computational data for D_0/d_j = 100. There is a good agreement except at the last point with the largest value of η_j or l_p. This point violates the condition $D_0/l_p \geq 2$ (Sekundov 1969) [see Figure 4.7(a)] and hence the penetration length is seen to be shorter. An extension of this data set for larger η_j is bound to bring about a larger deviation. This feature should be more pronounced for smaller values of D_0/d_j as can be seen in Figure A1.4(b).

The modified model with the similarity solution provides a framework for plotting the jet penetration length as a function of velocity ratio even in the presence of confinement as shown in Figure A1.4(b). Though such a plot was used originally for unconfined counterflow, it has been extended now to represent data for all values of D_0/d_j including those violating the condition $D_0/l_p \geq 2$.

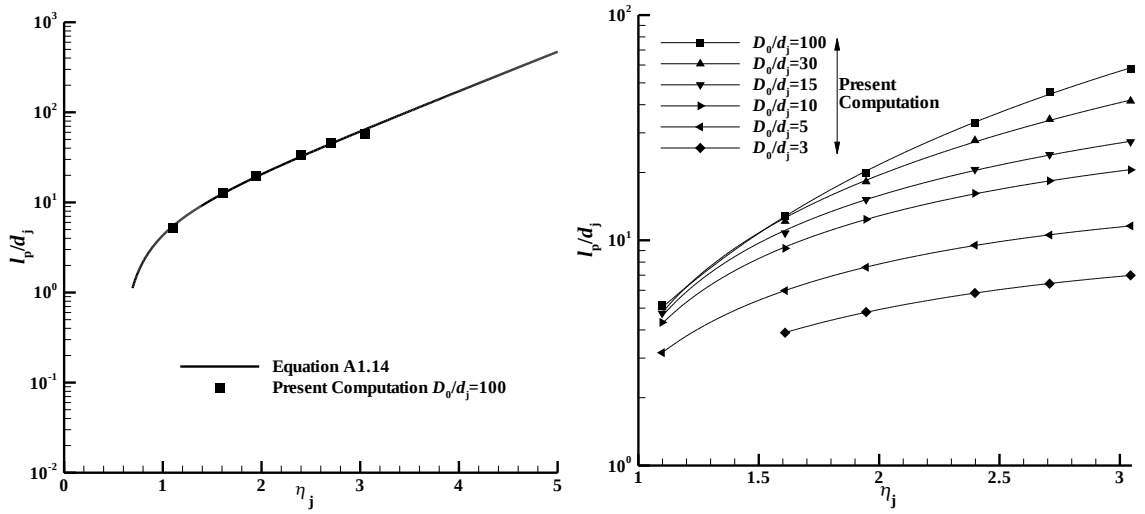

Figure A1.4 Non-dimensional jet penetration length, l_p/d_j, as a function of η_j from modified Oron and Abuaf (1977) similarity solution. (a) Comparison of present results for the highest diameter ratio considered in this study D_0/d_j = 100 with the modified Oron and Abuaf (1977) solution. (b) Present computational results for all diameter ratios.

The results of Oron and Abuaf (1977) for an unconfined counterflow using a similarity solution provided a theoretical framework for presenting the present computational results. However, the developing region of the jet with the potential core does not form a part of this similarity region. After adding the length of the developing region, a good agreement with the similarity results of Oron and Abuaf (1977) was seen. It is instructive to see the effects of confinement also in the same plot. By extending the range of the two parameters involved some interesting observations are made.

APPENDIX – 2

INVISCID ANALYSIS OF TOTAL PRESSURE LOSS

A quasi-one-dimensional inviscid analysis of total pressure loss due to momentum imbalance between the jet and the counterflow stream is presented in this appendix. Consider a jet issuing opposite to a uniform air stream as shown in Figure A2.1. The momentum imbalance between the two streams leads to total pressure loss at a location downstream of the jet injection. In this study stations 1 and 4 are far upstream and far downstream of the jet injection, respectively and the jet is injected at station 2. The case of two co-flowing streams was solved in Bird, Stewart and Lightfoot (2002: 460-461) and here this analysis is adapted and extended to counterflowing streams.

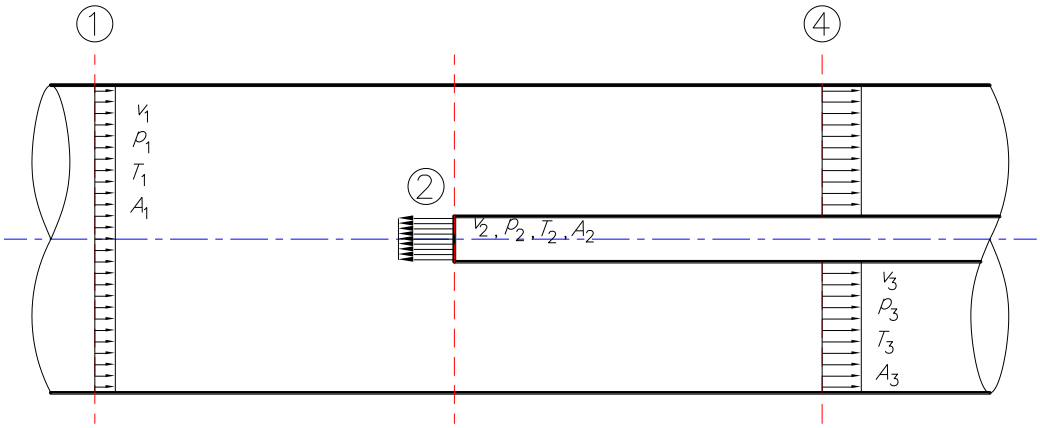

Figure A2.1 Schematic of the flow system involving counterflowing streams.

It is assumed that the velocity profiles are uniform at stations 1 and 2 and the shear stresses on the walls are neglected. The fluids are assumed to be perfect gases and the flow system operates adiabatically. The mass, momentum and energy conservation equations, respectively, can be written as,

$$m_4 = m_1 + m_2 \tag{A2.1}$$

$$m_4 v_4 + p_4 A_4 = \left(m_1 v_1 + p_1 A_1\right) - \left(m_2 v_2 + p_2 A_2\right) \tag{A2.2}$$

$$m_4\left(C_p T_4 + \frac{1}{2} v_4^2\right) = m_1\left(C_p T_1 + \frac{1}{2} v_1^2\right) + m_2\left(C_p T_2 + \frac{1}{2} v_2^2\right) \tag{A2.3}$$

where A is the area, p the static pressure, T the static temperature and v the velocity at the appropriate stations. Equations (A2.1), (A2.2), and (A2.3) are supplemented by the equation of state

$$p_4 = \rho_4 R T_4 . \qquad \text{(A2.4)}$$

The right hand sides of equations (A2.1), (A2.2) and (A2.3) are known and they are denoted as m, M, and E, respectively. Now, p_4 and A_4 can be eliminated from (A2.2) using the equation of state giving

$$v_4 + \frac{R T_4}{v_4} = \frac{M}{m} . \qquad \text{(A2.5)}$$

Next, T_4 can eliminated between (A2.3) and (A2.5) giving

$$v_4^2 - \left[2\left(\frac{\gamma}{\gamma+1} \right) \frac{M}{m} \right] v_4 + 2\left(\frac{\gamma-1}{\gamma+1} \right) \frac{E}{m} = 0 \qquad \text{(A2.6)}$$

where γ is the ratio of the specific heats. Equation (A2.6) is quadratic in v_4 whose solutions are

$$v_4 = \frac{M}{m}\left(\frac{\gamma}{\gamma+1} \right) \left[1 \pm \sqrt{1 - 2\left(\frac{\gamma^2-1}{\gamma^2} \right) \frac{m E}{M^2}} \right] . \qquad \text{(A2.7)}$$

One of the solutions for v_4 is subsonic and the other is supersonic. Only the subsonic solution is meaningful and is considered here. It is interesting to note that when the term in square parenthesis is unity v_4 is sonic.

Once v_4 is obtained p_4 and T_4 can be calculated from (A2.2) and (A2.5), respectively. The total quantities can then be calculated from the static quantities using the isentropic relations

$$\frac{T_0}{T} = 1 + \frac{\gamma-1}{2} M^2$$

$$\frac{p_0}{p} = \left(1 + \frac{\gamma-1}{2} M^2 \right)^{\gamma/\gamma-1} \qquad \text{(A2.8)}$$

where M is the Mach number and is given by $M = v / (\gamma R T)^{0.5}$.

APPENDIX – 3

DESIGN AND CALIBRATION OF TEST FACILITY

The design, installation and calibration of the test facility for delivering primary air to the test section are described in this Appendix. The instrumentation and measuring techniques for the calibration of the test facility are also reported in this Appendix. The present design is a typical low-speed blower tunnel of the open circuit-type and the design method of Mehta and Bradshaw (1979) is followed. A schematic of the test facility designed and built is shown in Figure A3.1 (see Table A3.1 for description of the numbered parts) and the individual components are explained in the following paragraphs. A photograph of the test facility is depicted in Figure A3.2.

A3.1 Description of the Components

A3.1.1 Centrifugal Blower

A centrifugal blower usually runs with good flow steadiness over a wide operating range and at high efficiency. The blower employed for the present design is Fläkt Woods model HCHB-3-20-1-3-1. Air enters the blower axially through a specially-designed smoothly-contoured inlet bellmouth designed in accordance with Ower and Pankhurst (1966: 242-243). The inlet bellmouth aids in delivering a uniform flow to the blower and reduces inlet losses.

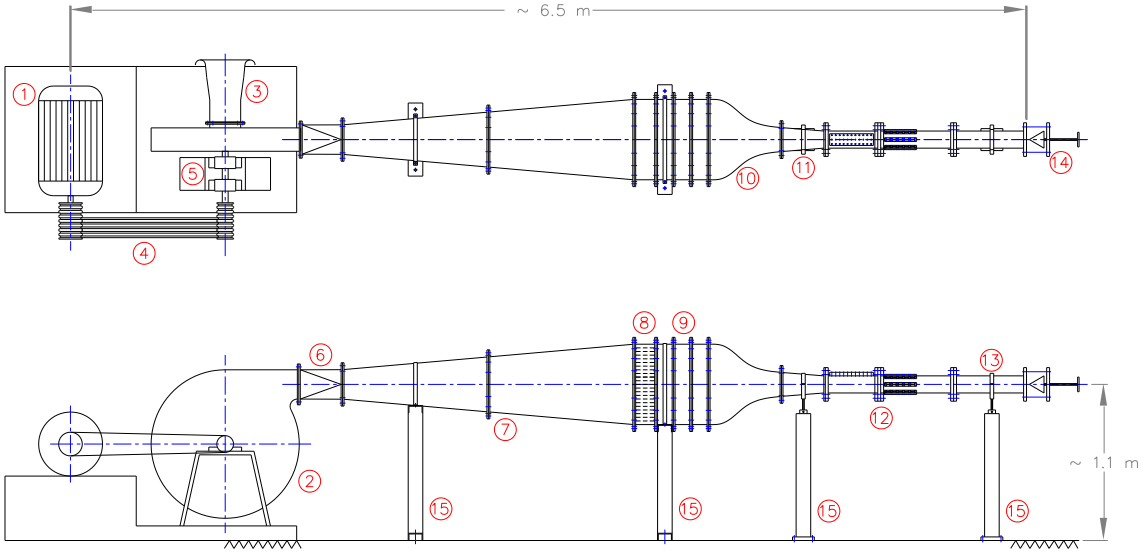

Figure A3.1 Test facility layout. See Table A3.1 for a description of the numbered components.

Figure A3.2 Photograph of the test facility. See Table A3.1 for a description of the numbered components.

Table A3.1 Description of test facility components.

Sl. No.	Component	Description
1.	Electric motor	AC Induction Motor, 18.5 kW
2.	Centrifugal blower	Fläkt Woods HCHB-3-20-1-3-1
3.	Inlet bellmouth	Smoothly-contoured inlet lip
4.	V-belts	Driving the blower
5.	Bearings	Two 2309K double row taper-bore grease-lubricated self-aligning ball bearings
6.	Transition section	Rectangular section at blower exit to circular section at diffuser inlet
7.	Diffuser	Area ratio = 7.56, Length = 2 m
8.	Honeycomb	25 mm circular cells, Length-to-diameter ratio = 6
9.	Screens	Two screens, each of porosity 61 %
10.	Contraction section	Contraction ratio = 14, Length = 0.5 m
11.	Contraction cone	Contraction ratio = 2, Length = 0.3 m
12.	Test section	Diameter = 102 mm, Length = 0.88 m
13.	Exit section	Diameter = 102 mm, Length = 0.48 m
14.	Exit throttle	Conical throttle with lead screw mechanism
15.	Support stands	Four number, rigidly grouted to the ground

A3.1.2 Driving Arrangement

The blower is driven by an AC-induction motor of 18.5 kW capacity and was mounted next to the blower. The pulley attached to the end of the motor shaft drove the blower through V-belts. The motor ran at a constant speed of 2900 rpm. However, the diameter ratio between the motor pulley and blower pulley was about 1.4 thus enabling the blower to run at about 4000 rpm.

A3.1.3 Transition Section

The compressed air from the blower exits through a transition section where the flow is smoothly guided from a rectangular section at the blower exit to a circular section at the diffuser inlet.

The primary loss in the transition section is due to friction (neglecting secondary losses) and can be calculated from

$$K = f\frac{L}{D_h} \tag{A3.1}$$

where $K = \dfrac{\Delta p}{1/2\,\rho V^2}$ henceforth.

The friction loss was be evaluated from Prandtl's famous formula for the friction factor which he had derived assuming a logarithmic velocity profile (see, White 2008: 360).

$$\frac{1}{\sqrt{f}} = 2.0\log\left(\mathrm{Re}_d\sqrt{f}\right) - 0.8 \tag{A3.2}$$

where Re_d is the Reynolds number (based on a suitable hydraulic diameter).

A3.1.4 Diffuser

The pressure losses occurring anywhere in the tunnel are proportional to the velocity cubed. Hence it is vital to reduce the stream speed which is usually done through a diffuser. The diffuser reduces the kinetic energy of the flow exiting from the blower thereby resulting in a pressure rise.

A conical diffuser was installed at the exit of the transition section. The included cone angle of the diffuser was conservatively set to 5º. The area ratio (ratio of diffuser exit-to-inlet area) was approximately 7.56. This rather high value of area ratio was chosen to later have a high contraction ratio in the contraction section as explained

subsequently. Though the diffuser angle was 5º a high area ratio was obtained by having a long diffuser which was 10 times the diffuser inlet diameter.

The losses in a diffuser are due to skin friction and expansion. The frictional loss can be evaluated from

$$K_f = \frac{f}{8\sin\theta}\left(1-\frac{1}{A_R^2}\right) \qquad \text{(A3.3)}$$

by taking an average value of friction coefficient *f*.

The expansion loss can be calculated from

$$K_{ex} = K_\theta(\theta)\left(\frac{A_R^2-1}{A_R^2}\right)^2 \qquad \text{(A3.4)}$$

A_R is the area ratio (as defined earlier) in both the relations.

K_θ (θ) is found from empirical correlation given by Eckert, Mort, and Jope (1976), which strongly depends on the diffuser cross-sectional shape. For the present circular cross-section shape with θ = 5º,

K_θ (θ) = 1.70925 x 10^{-1} – 5.84932 x 10^{-2} (2θ) + 8.14936 x 10^{-3} (2θ)^2 + 1.34777 x 10^{-4} (2θ)^3 – 5.67258 x 10^{-5} (2θ)^4 – 4.15879 x 10^{-7} (2θ)^5 + 2.10219 x 10^{-7} (2θ)^6. (A3.5)

A3.1.5 Settling Chamber

The settling chamber contains one honeycomb and two screens which (along with the downstream contraction) favourably manipulate the mean flow and turbulence characteristics of the flow entering the test section. Since the honeycomb and screens produce high pressure drop they are located in the settling chamber where the flow speed is the lowest thereby minimising their pressure loss contribution to the total tunnel power loss.

A3.1.5.1 Honeycomb

The low speed flow exiting the diffuser enters the settling chamber which first consists of the honeycomb. A honeycomb effectively straightens the flow and inhibits mean flow variations in cross-stream components and also suppresses the level of turbulence in the mean flow (Loehrke and Nagib 1976). The cross-sectional shape of the present honeycomb cells were circular and had a length-to-diameter ratio of 6. The honeycomb was fabricated by bundling 25 mm (1") aluminum tubes rigidly held together and to the walls of the settling chamber by applying an epoxy-based adhesive (Araldite). The honeycomb loss coefficient can be found from Barlow, Rae, and Pope (2010: 90)

$$K = \lambda\left(3 + \frac{L_h}{D_h}\right)\left(\frac{1}{\beta_h}\right)^2 + \left(\frac{1}{\beta_h} - 1\right)^2 \qquad \text{(A3.6)}$$

where L_h and D_h are the length and diameter of honeycomb cell and β_h is the honeycomb porosity. λ is the honeycomb friction coefficient and is evaluated based on the roughness, ε, of the cell as

$$\lambda = 0.214\left(\frac{\varepsilon}{D_h}\right)^{0.4} \quad . \qquad \text{(A3.7)}$$

A3.1.5.2 Screens

Screens have long been used to attain a uniform flow and suppress turbulence fluctuations in wind tunnels. It is also known that the passage of a stream through a screen causes nearly homogeneous and isotropic turbulent flow field downstream (Batchelor 1993). Prandtl (1933) gave an elegant description of honeycombs and screens and had apparently first suggested their use to improve flow quality in wind tunnels (Groth and Johansson 1988).

The screens chosen for the present design were made of stainless steel metal wires interwoven to form square meshes. The screen geometry is defined by its porosity (or its complement solidity) which is the ratio of open to total mesh area.

$$\beta = \left[1 - \left(\frac{d}{l}\right)\right]^2 \qquad \text{(A3.8)}$$

where d is the diameter of the wire and l is the mesh size. In the present screen d is 0.7 mm and l is 3.2 mm. Thus the porosity of both the screens was approximately 61 %. It is advantageous to have a number of screens with low or moderate pressure drop than a single screen with very high resistance. The honeycomb and screens were axially separated by distance of 0.2 settling chamber diameters. This separation is required for the turbulence generated by the grid to decay (which is usually approximately about 20 mesh lengths). The flow upon passing through the screens is subjected to significant strain and is allowed to relax to isotropy before entering the contraction in a constant area portion which is again 0.2 settling chamber diameters long.

The honeycomb and screens are always used in conjunction to obtain a good quality flow in the test section (Loehrke and Nagib 1972, Scheiman and Brooks 1981, Tan-atichat, Nagib, and Loehrke 1982, and Farell and Youssef 1996).

The screen pressure loss coefficient K is a function of the screen porosity and Reynolds number. In the Taylor – Batchelor theory (1949) the screen was modeled by the loss coefficient K and a deflection coefficient α which relates the incidence angle θ (measured from the normal), and the corresponding exit angle, φ as,

$\varphi = \alpha\, \theta$

where α is a constant varying from 0 and 1. Now, K is related to α by (see Schubauer, Spangenberg, and Klenaboff 1950),

$$\alpha = \frac{1.1}{\sqrt{1+K}} \quad . \qquad \text{(A3.9)}$$

The screen loss coefficient can be determined from the screen solidity β and a Reynolds number based on the wire diameter (Re_d).

$$K = f\left(\mathrm{Re}_d\right)\frac{1-\beta^2}{\beta^2} \quad . \qquad \text{(A3.10)}$$

The function f is high and strongly depends on Re_d for values below 100, but attains a constant value of 0.45 for Re_d above 100 (Groth and Johansson 1988).

The suppression of the streamwise and transverse turbulence components may be estimated from the Taylor – Batchelor theory (1949)

$$\frac{u_2'}{u_1'} = \frac{1+\alpha-\alpha K}{1+\alpha+K}$$

$$\frac{v_2'}{v_1'} = \frac{1.1}{\sqrt{1+K}} \qquad \text{(A3.11)}$$

where the subscripts 1 and 2 refer to the fluctuating components before and after the screen, respectively. It can be readily seen that u_2'/u_1' becomes zero for K=1+1/α. The present screens are estimated to suppress the streamwise turbulence by about 46 % and the normal turbulence component by nearly 83 %.

A3.1.6 Contraction Section

The contraction section is the final flow quality improvement device before the flow enters the test section. The flow accelerates through the contraction and the mean velocity is increased in the test section. The contraction also improves the uniformity of the mean flow. Again, Prandtl (1933) appears to be the first to give a qualitative explanation of the working of contraction sections. The now classical experiments of Comte-Bellot and Corrsin (1966) (and much subsequent work by various workers) amply demonstrate that the isotropy of turbulence is improved in passing through an axisymmetric contraction located downstream of the screens.

A comprehensive method of design of axisymmetric contractions was presented by Morel (1975). At first sight, it may seem rather easy to design a contraction section to accelerate the flow since the device operates in a favourable pressure gradient. However, this is not the case because of chances of flow separation along the wall both at the inlet and exit due to local transverse pressure gradients. Thus a careful design of the

contraction wall shape is essential to ensure a uniform flow being delivered to the test section.

The present design was of a cubic wall contour; this design was recommended by Hussain and Ramjee (1976) (see also Ramjee and Hussain 1976). This contraction "has the smallest inlet curvature and the mildest inlet adverse pressure gradient." The contraction ratio (ratio of contraction inlet-to-exit area) for the present design was approximately 14. The contraction section length was 1.1 times the inlet diameter.

At the downstream end of the contraction section a further contraction cone was fitted. Though this was primarily done to increase the versatility of the test facility[2], this had the added advantage of further improving the flow quality to the test section. The contraction ratio of this contraction cone was nominally around 2. The contraction section length was twice the cone inlet diameter. The overall contraction ratio including the conventional contraction and the contraction cone was approximately 29.

The contraction loss coefficient can be estimated as

$$K_n = 0.32 \frac{f\,L}{D_s} \qquad \text{(A3.12)}$$

where f is an average value of friction coefficient, L is the length of the contraction section and D_0 is the diameter of the test section. The loss coefficients were separately evaluated for the conventional contraction section and the contraction cone.

The improvement in mean flow uniformity caused by the contraction is proportional to c^2 for the streamwise component and $c^{0.5}$ for the transverse and azimuthal components, where c is the contraction ratio as explained earlier. Thus for an overall

[2] The test section diameter at the end of the contraction cone was 102 mm (4" nominal diameter). If this cone is removed a test section of 154 mm (6" nominal diameter) can be accommodated at the end of the conventional contraction section, thus increasing the versatility of the test facility. However, for all the test measurements reported in this dissertation only the 102 mm test section was employed.

contraction ratio of 29 the reduction in mean streamwise velocity variation is 841 whereas that for the crosswise components is about 5.4.

The reduction of the streamwise and transverse (and azimuthal) turbulence intensities are as follows (Batchelor 1993):

$$\frac{\left(u'/u\right)_2}{\left(u'/u\right)_1} = \frac{1}{c^2}\sqrt{\frac{3}{4}\left[\ln\left(4c^3\right)-1\right]}$$

$$\frac{\left(v'/v\right)_2}{\left(v'/v\right)_1} \; or \; \frac{\left(w'/w\right)_2}{\left(w'/w\right)_1} = \sqrt{\frac{4}{3c}} \quad . \qquad \text{(A3.13)}$$

Hence, the reduction factors for streamwise and crosswise turbulence intensities are approximately 300 and 4.7, respectively.

A3.1.7 Test Section

The test section should have constant flow characteristics along its entire section. The flow at the entry to this section should be steady and uniform, and must have low turbulence levels.

The present design demanded certain specific features of the test section and in turn dictated its design. The test section shown in Figure A3.3 (the numbered parts are described in Table A3.2) was of constant diameter (102 mm). A close-up photograph of the test section is shown in Figure A3.4. The test section was conveniently divided and termed as upstream section and downstream section, ahead of and behind the jet injector location, respectively. First, the length of the upstream section was calculated based on the available literature on jet penetration length. The test section inlet was placed sufficiently ahead of the jet length so that entry effects do not influence the jet propagation. The pressure loss due to jet mixing was to be measured behind the jet injection and the downstream section was suitably designed.

The test section being of constant diameter its loss coefficient is found from

$$K = f\frac{L}{D} \quad . \qquad \text{(A3.14)}$$

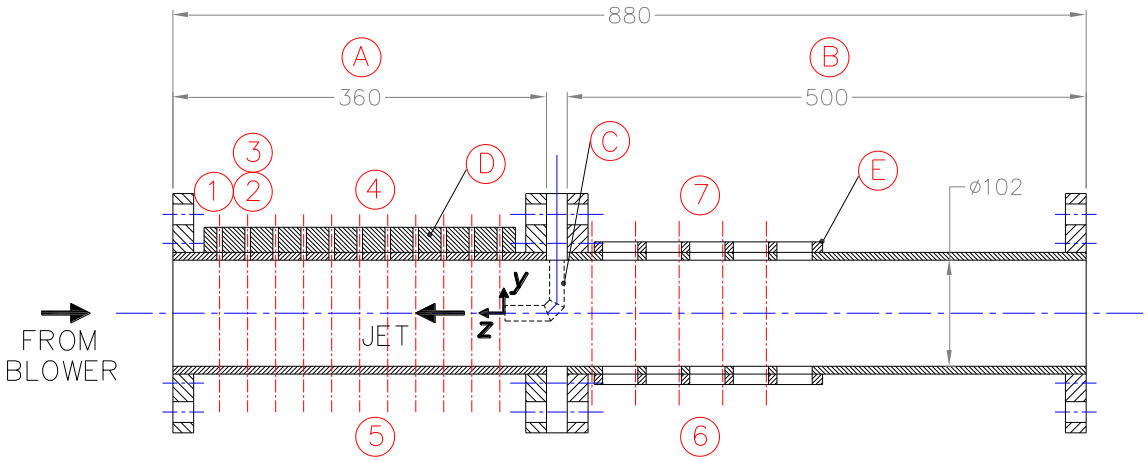

Figure A3.3 Layout of the test section. See Table A3.2 for a description of the components and Table A3.3 for a description of the instrumentation details.

Table A3.2 Description of the test section components.

Sl. No.	Description	Comments
A.	Upstream test section	To measure velocity profiles in the jet(s)
B.	Downstream test section	To measure downstream total pressure profiles
C.	Jet injector	Shown for reference only
D.	Metal block	Provisioned to accommodate the traverse mechanism to traverse through the jet(s) velocity profiles
E.	Metal blocks	Eight numbers circumferentially welded where total pressure rakes can be positioned to measure total pressure profiles

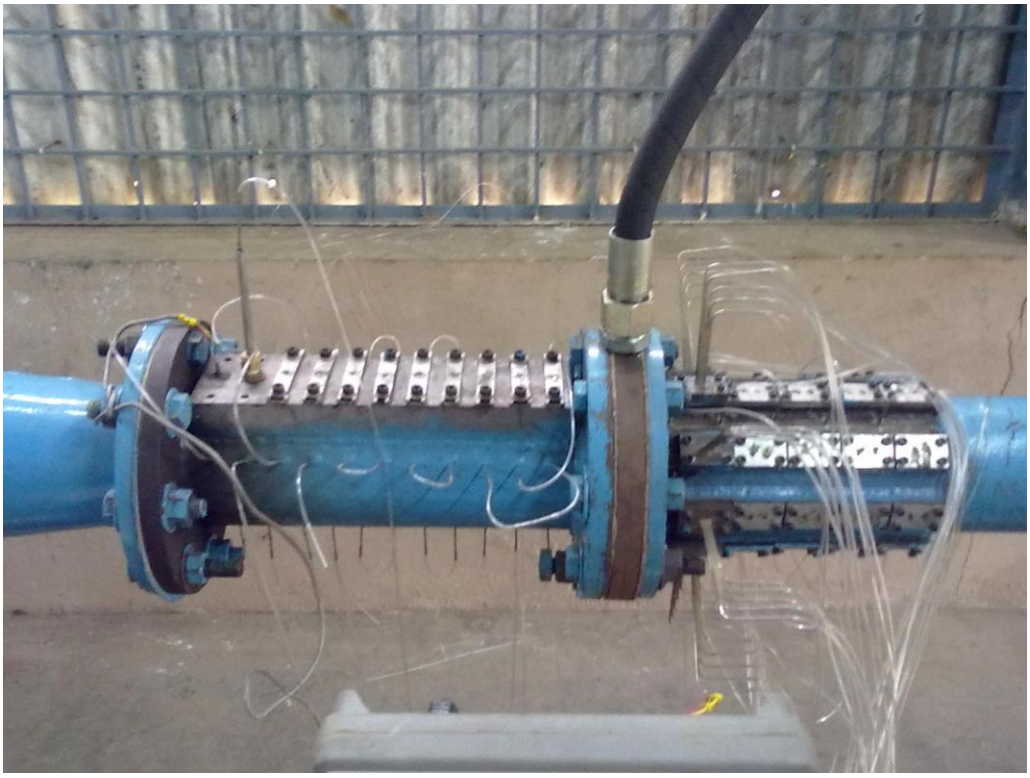

Figure A3.4 Photograph of the test section. See Table A3.2 for a description of the test section components and Table A3.3 for test section instrumentation details.

A3.1.8 Exit Section

The flow exited from the test section through a constant diameter section whose length was about 7.7 times the test section diameter. The exit section loss coefficient is evaluated as in equation (A3.14).

A3.1.9 Exit Throttle

A conical throttle was placed at the exit of the test facility at 10.2 D_0 downstream of the jet injection location. The primary mass flow from the blower can be controlled by this throttle which can be moved axially by means of a lead screw mechanism.

The total pressure loss at the exit of the facility due to expelled flow is calculated from

$$K = \frac{2\left\{\left[1+\left(\frac{\gamma-1}{2}M^2\right)\right]^{\gamma/\gamma-1}-1\right\}}{\gamma M^2} \qquad \text{(A3.15)}$$

where M is the exit Mach number and γ is the ratio of specific heats. In this calculation the presence of the exit throttle was ignored.

A3.2 Total Losses in the Test Facility

The loss at every section in the test facility can be referenced to that at the test section by the following relation

$$K_0 = K\left[\frac{A_0\,M}{A\,M_0}\right]\sqrt{\frac{1+\left(\frac{\gamma-1}{2}M_0^2\right)}{1+\left(\frac{\gamma-1}{2}M^2\right)}} \qquad \text{(A3.16)}$$

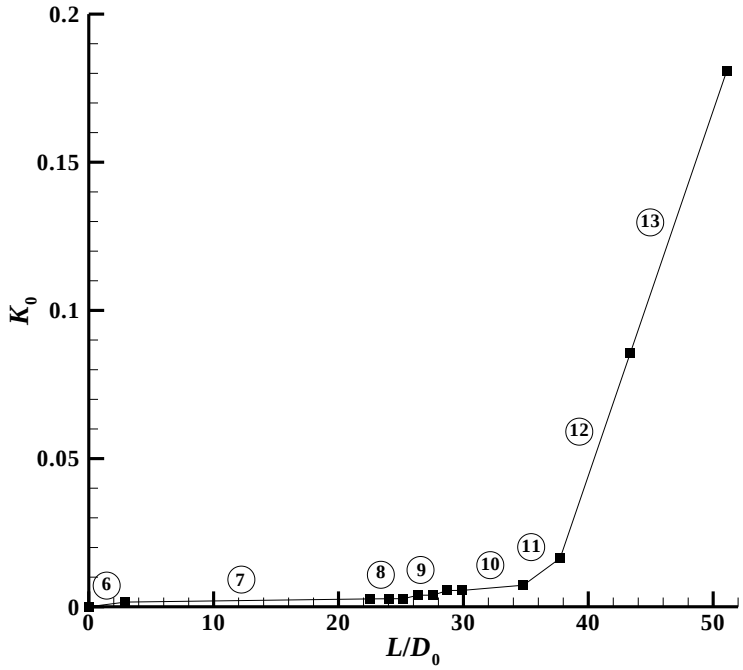

Figure A3.5 Cumulative pressure losses in various components in the test facility. See Figure A3.1 for test facility layout and Table A3.1 for a description of the numbered parts.

where A_0, and M_0, are the area of the test section and test section Mach number, respectively, and A and M are the area, and Mach number at any local station, respectively.

The local loss and the loss referenced to the test section value are tabulated in Table A3.3 for each section in the test facility. The cumulative total loss in the test facility is plotted in Figure A3.5 starting from the transition section till the exit for a test section velocity of 100 m/s.

The total losses in the facility can be expressed as 'power ratio' or 'energy ratio' as widely expressed in the literature. This measure is basically the ratio of energy of flow stream at the test section to the energy supplied to the driving unit (the centrifugal blower in this case). The present facility had an energy ratio of about 5.54 which is typical of such facilities.

Table A3.3 Local loss and loss referenced to test section value for each component of the test section.

Component. No.	Component	K	K_s
6.	Transition section	0.0240	0.001592
7.	Diffuser	0.1227	0.001076
8.	Honeycomb	0.0420	0.000050
a.	Spacer 1	0.0037	0.000004
9. a.	Screen 1	0.7580	0.001193
b.	Spacer 2	0.0035	0.000005
9. b.	Screen 2	0.7580	0.001583
c.	Spacer 3	0.0033	0.000007
10.	Contraction section	0.0053	0.001785
11.	Contraction cone	0.0091	0.009074
12.	Test section	0.0691	0.069100
13.	Exit section	0.0952	0.095178

A3.3 Test Facility Fabrication and Installation

The major components of the test facility were fabricated from commercial mild steel material except the contraction section which was CNC-milled from an aluminium block. The components fabricated from mild steel were coated with epoxy primer and enamel paint to prevent corrosion. The various components were connected together by flanges welded at their respective ends and fastened by bolts and nuts.

The centrifugal blower and the motor were rigidly mounted on a common machine foundation and the other sections were placed on suitably designed support stands (see Figure A3.1).

A3.4 Test Section Instrumentation

The test section is depicted in Figure A3.3. The measurement details are also shown in this figure and the associated instrumentation is described in Table A3.3.

The inlet to the test section was at $z = 2.7\ D_0$ upstream of the jet injector. A metal block was welded to the top of this section to accommodate the traverse mechanism for measuring the velocity profiles in the jet(s). The probes can enter the test section through holes drilled in this block. These holes were of 5.5 mm diameter. The first hole was placed at a distance of $0.05\ D_0$ and the subsequent 10 holes were drilled at equal axial distances of $0.26\ D_0$. The velocity profile at any desired location can be measured by traversing a suitable probe radially while all other holes can be blanked. At each of the 11 axial locations three wall static pressure taps circumferentially spaced 120º apart were drilled (total of 33 wall static pressure taps). The static pressure taps were of 0.8 mm diameter.

A Chromel-Alumel thermocouple was used to measure the inlet total temperature and was inserted at $z = 2.7\ D_0$ at a radial location of $0.25\ D_0$ above the duct centreline. This location was chosen so that the wakes from the thermocouple is not ingested by the Pitot probe which was located just downstream. The Pitot probe was placed at $2.4\ D_0$ to

measure the inlet total pressure. This probe was at the centre of the duct. As explained earlier static pressure measurements were made at this location through the three wall static pressure tappings. The inlet mass flow rate to the test section was calculated from the measured total and static pressures.

Table A3.4 Description of the test section instrumentation. See Figure A3.3 for instrumentation locations.

Sl. No.	Description	Instrument
1.	Inlet total temperature	Chromel-Alumel thermocouple
2.	Inlet total pressure	Pitot probe
3.	Inlet static pressure	Wall static pressures at three circumferential locations
4.	Velocity profiles in the jet(s)	Direction probes
5.	Local static pressure	Wall static pressures at three circumferential positions at each location of jet velocity profile traverse
6.	Total pressures	Eight total pressure rakes each containing five total pressure Pitot probes
7.	Local static pressure	Wall static pressures at two circumferential positions at each location of total pressure profile measurement

The downstream test section had provision to mount total pressure rakes. To enable this mounting eight metal block were welded circumferentially around this section. The rakes can be fastened to these metal blocks and the first downstream axial location was at 0.8 D_0 and the subsequent four locations were equally spaced at 0.26 D_0. Two wall static pressure taps were drilled at each of these 5 axial locations circumferentially spaced at 180º (total of 10 wall static pressure taps). These taps were of 0.8 mm diameter.

The total and static pressures were measured by two numbers of ESP-32HD miniature electronic differential pressure measurement unit each having 32 independent

pressure ports. All 64 transducers were individually calibrated by a GE Druck DPI 605 pressure calibrator.

The signals from the pressure scanner were acquired by Agilent 34970A Data Acquisition / Switch Unit and on-line data processing was done by a program written in LabVIEW 8.2 software interfaced through RS-232.

A3.5 Test Facility Calibration

The test section was calibrated after the construction of the test facility to ensure steady, uniform and low turbulence characteristics. There were various tests conducted to establish these primary requirements and other experiments were performed aiming some specific objectives; they are described in the following paragraphs.

A3.5.1 Performance Characteristic of Centrifugal Blower

The performance characteristic of the centrifugal blower was obtained to assess its performance and to ensure the blower is not operated in a stalled regime. The blower's characteristic can be plotted in terms of its mass flow and pressure rise capability. This can also be expressed as flow coefficient, φ, and pressure rise coefficient, ψ, defined as follows (Lakshminarayana 1996: 65):

$$\phi = \frac{V_a}{U_{b,m}} \quad ,$$

$$\psi = \frac{\Delta p_0}{\rho U_{b,m}^2} \quad , \qquad \text{(A3.17)}$$

where V_a is the axial flow velocity at the impeller inlet, $U_{b,m}$ is the impeller speed at the mean diameter, Δp_0 is the total pressure rise, and ρ is the fluid density.

The inlet mass flow was calculated with a Pitot probe positioned at the centre of the bellmouth and three wall static pressure measurements. The blower exit total pressure was measured by a Pitot probe located at the centre of the transition section. The

measured blower performance characteristic is shown in Figure A3.6. It is seen that the blower enters stall condition (though not severe) at mass flow rate below about 0.3 kg/s when the exit throttle was very nearly closed. The blower was never operated in this condition during experiments.

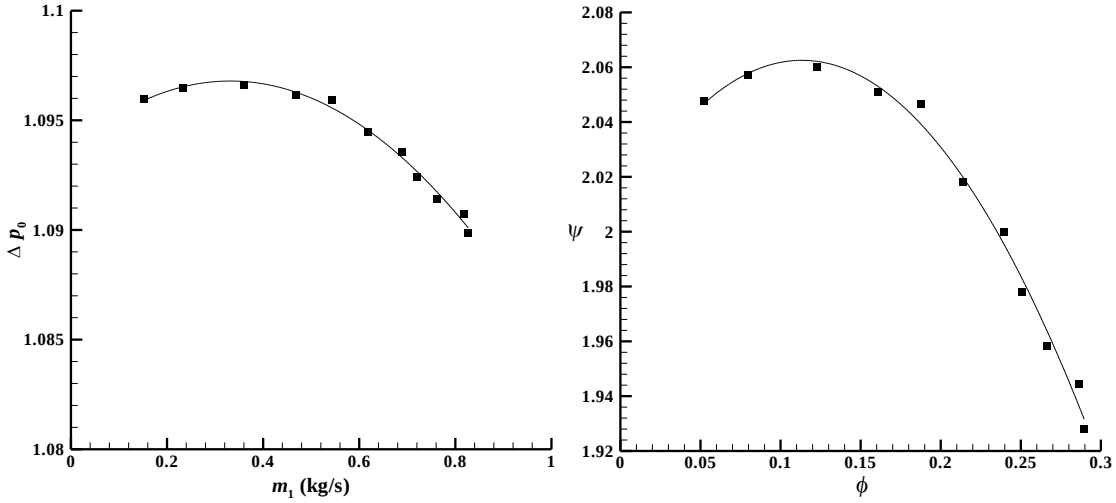

(a) **(b)**

Figure A3.6 Performance characteristic of the centrifugal blower. (a) Δp_0 is the pressure rise, the ratio of exit-to-inlet total pressure which was obtained for varying inlet mass flow rate. (b) φ, and ψ are the flow and pressure rise coefficients, respectively, as defined in equations (A3.17).

A3.5.2 Inlet Bellmouth Mass Flow Rate

The mass flow rate entering the centrifugal blower was measured as this would be the mass flow rate delivered to the test section. The mass flow rate was calculated from total and static pressure measurements made in the bellmouth. The total pressure was measured by a Pitot probe located at the bellmouth centerline. The Pitot probe was made from a 1.7 mm outside diameter (inside-to-outside diameter ratio was about 0.5) stainless steel hypodermic tube bent to a right angle with the square-ended open end facing the stream whose length was 15 times the probe diameter. At this location wall static pressure measurements were made at two locations at 180º circumferential interval. The total and static pressure difference was measured by a Furness Control FCO 510-3 Microprocessor Manometer. The total pressure was measured separately by a U-tube

water manometer. The mass flow rate was calculated from the total and static pressure measurements. The calculated mass flow rate is plotted as a function of total and static pressure difference in mm of water column in Figure A3.7.

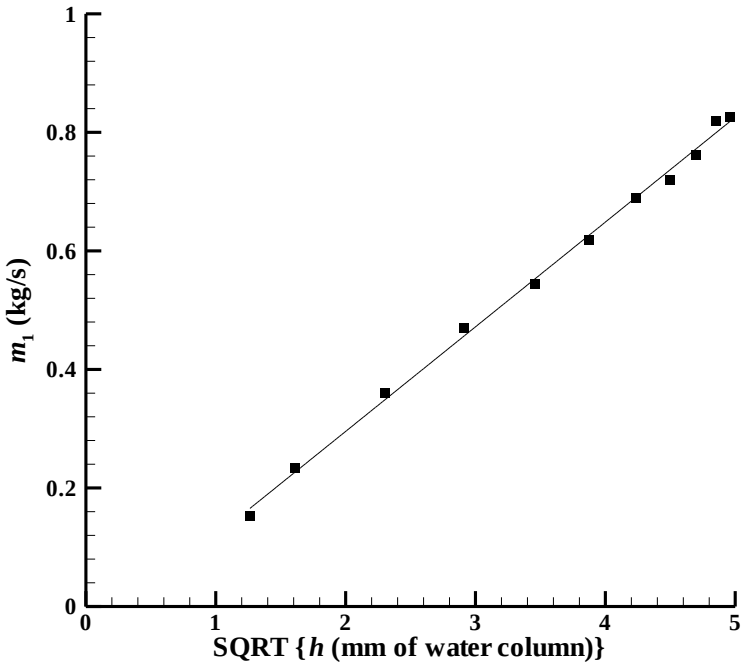

Figure A3.7 Mass flow rates calculated from measurements made in inlet bellmouth plotted as a function of total and static pressure difference in mm of water column.

A3.5.3 Test Section Inlet Velocity Profile

It is desirable to have a uniform and axisymmetric velocity profile at the test section inlet. The velocity profile was measured by a Pitot probe with its leading edge flattened. The 1.7 mm outside diameter hypodermic tube was used for constructing this probe. After flattening the inside-to-outside height ratio was 0.6 and the width-to-outside height ratio was 1.6. The length of the open end facing the stream was 10 times the outside diameter of the tube. At this location wall static pressure measurements were made at three circumferential positions spaced 120º apart. The total and static pressures were measured by a calibrated ESP-32HD electronic pressure scanner.

The measured velocity profile at the test section inlet is plotted in Figure A3.8 for a test section centerline velocity of 87.7 m/s. The velocities are normalised by the

centreline velocity. It can be readily seen that the velocity profile at the inlet to the test section is both uniform and axisymmetric except for the thin boundary layer along the duct walls. The boundary layer thickness was calculated to be about 1.44 mm.

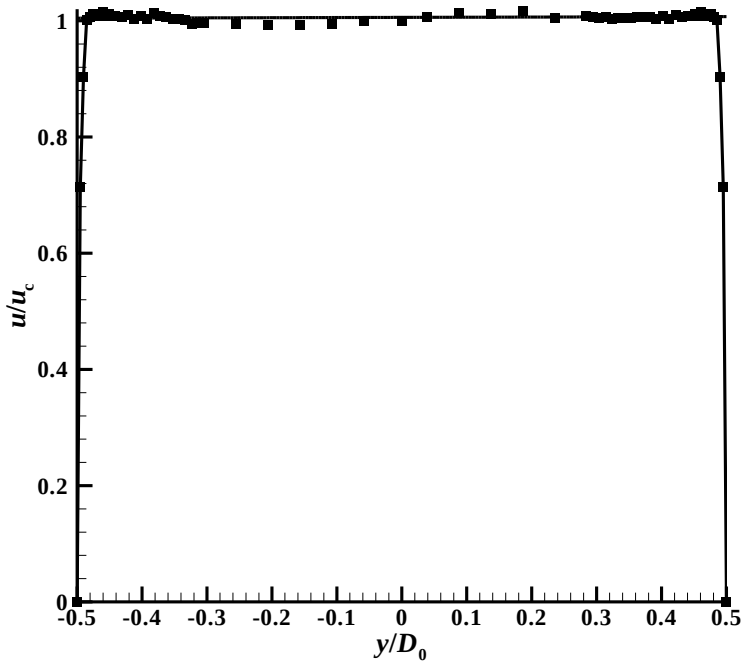

Figure A3.8 Velocity profile at inlet of the test section. The velocities are normalised by the centerline velocity and the radial distance by the test section diameter.

A3.5.4 Wall Static Pressure Measurements

The wall static pressure was measured at various locations in the test section. These locations are described in the Section A3.4. There were wall static pressure taps circumferentially spaced 120º apart at each of the 11 axial location thus totaling 33 measurements. These pressures were normalised by the atmospheric pressure and shown in Figure A3.9. It can be seen that the static pressure is nearly uniform along the test section.

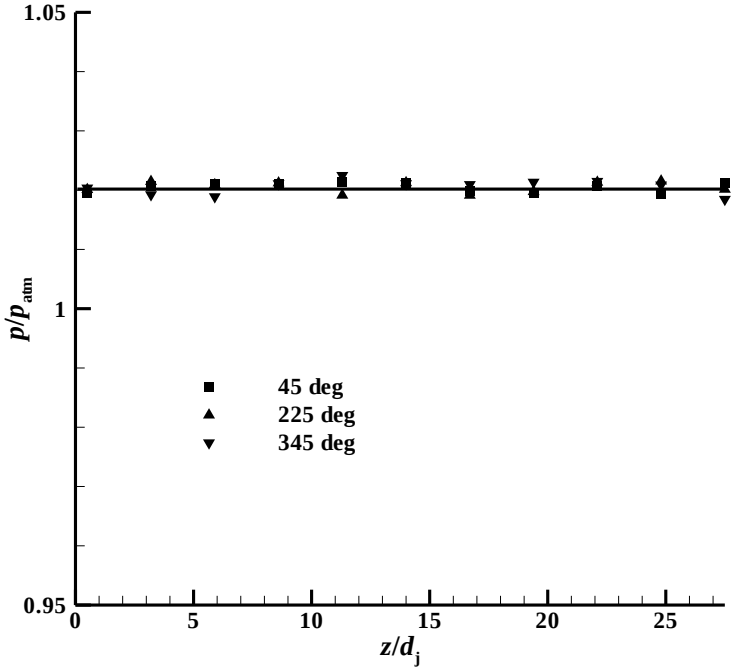

Figure A3.9 Static pressures normalised by the atmospheric pressure at various stations in the test section. See Figure 3 and Table 2 for the measurement locations.

A3.5.5 Total Pressure Measurements

The total pressure measurements were obtained in the test section using the total pressure rakes. Each rake had five total pressure probes and eight such rakes were employed thus enabling forty total pressures to be measured. Each probe was made from 1.7 mm outside diameter hypodermic tubes bent at right angles with the stream-facing end nearly 15 to 20 times the diameter of the tube. Each probe was fixed in position and to the rake platform by applying an epoxy-based adhesive. These probes can be fixed by screws to the metal block welded to the test section. The total pressure probes in the rake were radially spaced such that each probe would be located at centres of equal areas of the test section diameter. The test section diameter was divided into forty equal areas, thus forty total pressure probes would measure the total pressure distribution in any section of interest. The fabricated total pressure rake is shown in Figure A3.10 and the probe locations in the test section are shown in Figure 5.3

Figure A3.10 Total pressure rake fabricated from hypodermic tubes. Each rake had five total pressure probes and eight rakes were used for measurement of the total pressure profiles.

The total pressure uniformity at the test section is quantified by distortion index as defined in equation 5.4. The present distortion indices for varying inlet mass flow rates are plotted in Figure A3.11. The highest distortion index of about 0.3 % occurred for the highest inlet mass flow rate and is considered acceptable.

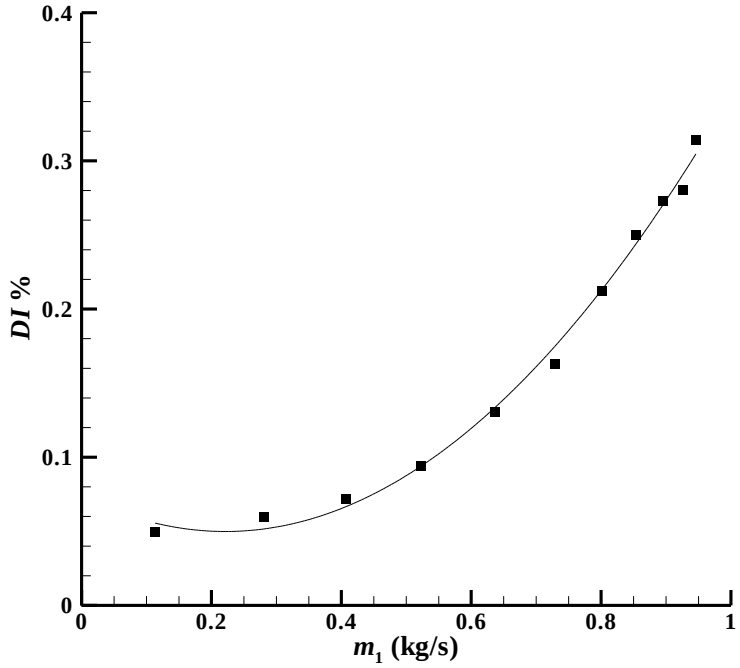

Figure A3.11 Total pressure distortion index plotted for varying mass flow rates. The distortion index was calculated from the forty total pressure measurements.

A3.5.6 Inlet Turbulence Intensity

The inlet turbulence level is another important parameter in assessing the quality of flow at the test section. As explained in several previous paragraphs various techniques were employed to obtain a low turbulence level in the test section like installation of turbulence reduction screens and contraction section.

The turbulence intensity at the inlet to test section was measured by a DANTEC 55P11 hot-wire anemometer. The hot-wire probe was used in conjunction with DISA 56C16 General Purpose Bridge and 56C01 CTA unit. The hot-wire anemometer was operated in constant-temperature mode.

The turbulence intensity measurements were made at the test section inlet centreline with the hot-wire placed normal to the stream. The calculated turbulence intensities are plotted in Figure A3.12 for varying mass flow rates. The turbulence intensity was found to be about 0.3 % for the mass flow rates of interest.

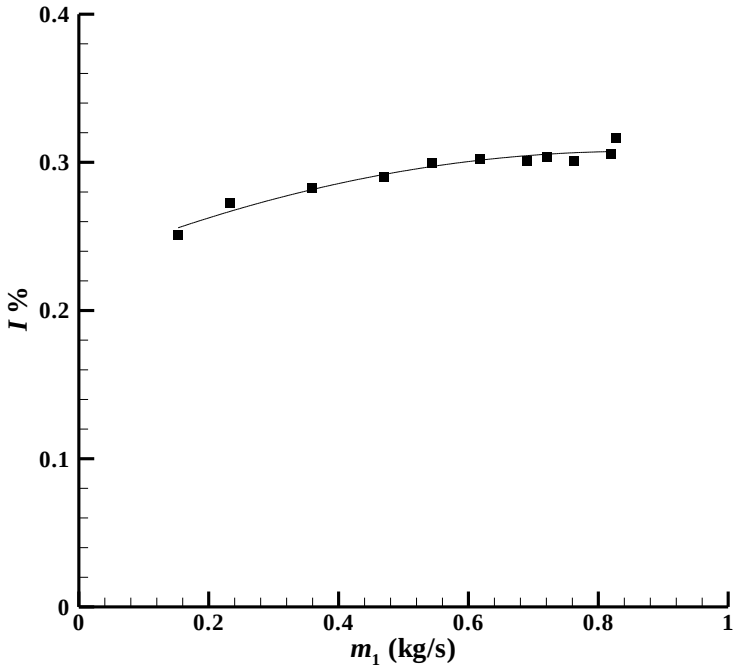

Figure A3.12 Turbulence intensity at the test section inlet centreline (z = 2.7 D_0) for varying mass flow rates.

A3.6 Summary

The test facility for delivering primary air to the section was designed based on guidelines for design of low-speed wind tunnels. The principal requirements for the design of this test facility were to deliver a steady, uniform and a low turbulence level flow to the test section.

The primary components of the test facility were a centrifugal blower driven by an electric motor, a diffuser, a settling chamber comprising honeycomb and screens, a contraction section and the test section. This test facility was employed for all the measurements reported in this dissertation.

APPENDIX – 4

RESEARCH PUBLICATIONS ASSOCIATED WITH THE THESIS

The following are the publications as an outcome of the present research:

Sivapragasam, M., and Ramamurthy, S. (2009) 'Inlet Flow Distortion Effects in Aircraft Gas Turbine Engine Compression Systems'. Technical Memorandum TM PR 0901. Bangalore: National Aerospace Laboratories

Sivapragasam, M., Ramamurthy, S., Desphande, M. D., and Sridhara, S. N. (2009) 'Computation of Turbulent Jets in Annular Counter-Flow'. *Proceedings of the 11th Annual CFD Symposium*. held 11-12 August 2009 at Indian Institute of Science, Bangalore

Sivapragasam, M., Ramamurthy, S., Desphande, M. D., and Sridhara, S. N. (2010) 'Numerical and Experimental Investigation on a Turbulent Jet in Annular Counter-Flow'. *Proceedings of the 37th National and 4th International Conference on Fluid Mechanics and Fluid Power*. held 16-18 December 2010 at Indian Institute of Technology – Madras, Chennai

Sivapragasam, M., Desphande, M. D., Ramamurthy, S., and White, P. (2012) 'Revisiting a Similarity Solution for a Turbulent Jet in Counterflow'. *Proceedings of the 14th Annual CFD Symposium*. held 10-11 August 2012 at Indian Institute of Science, Bangalore

Sivapragasam, M., Desphande, M. D., Ramamurthy, S., and White, P. (2013) 'Turbulent Jet in Confined Counterflow'. *Sādhanā* 39 (3), 713-729

Sivapragasam, M., Ramamurthy, S., Deshpande, M. D., and White, P. (2014) 'An Air Jet Distortion Generation System'. *International Journal of Rotating Machinery* 2014, 961452

APPENDIX – 5

LOW RISK RESEARCH ETHICS APPROVAL CHECKLIST

UARC Ethics Low Risk Projects 08-09 (2).doc Revision 1.05

Low Risk Research Ethics Approval Checklist

Applicant Details

Name M. SIVAPRAGASAM	E-mail msp@msrsas.org
Department	Date
Course	Title of Project NUMERICAL AND EXPERIMENTAL INVESTIGATIONS ON MULTIPLE AIR JETS IN COUNTERFLOW FOR GENERATING AIRCRAFT GAS TURBINE ENGINE INLET FLOW DISTORTION PATTERNS.

Project Details

Summary of the project in jargon-free language and in not more than 120 words:

- Research Objectives
- Research Design (e.g. Experimental, Desk-based, Theoretical etc)
- Methods of Data Collection

Participants in your research

1. Will the project involve human participants?	Yes	No ✓

If you answered **Yes** to this questions, this may **not** be a low risk project.

- If you are a student, please discuss your project with your Supervisor.
- If you are a member of staff, please discuss your project with your Faculty Research Ethics Leader or use the Medium to High Risk Ethical Approval or NHS or Medical Approval Routes.

Risk to Participants

2. Will the project involve human patients/clients, health professionals, and/or patient (client) data and/or health professional data?	Yes	No ✓
3. Will any invasive physical procedure, including collecting tissue or other samples, be used in the research?	Yes	No ✓
4. Is there a risk of physical discomfort to those taking part?	Yes	No ✓
5. Is there a risk of psychological or emotional distress to those taking part?	Yes	No ✓
6. Is there a risk of challenging the deeply held beliefs of those taking part?	Yes	No ✓
7. Is there a risk that previous, current or proposed criminal or illegal acts will be revealed by those taking part?	Yes	No ✓
8. Will the project involve giving any form of professional, medical or legal advice, either directly or indirectly to those taking part?	Yes	No ✓

If you answered **Yes** to **any** of these questions, this may **not** be a low risk project.

- If you are a student, please discuss your project with your Supervisor.
- If you are a member of staff, please discuss your project with your Faculty Research Ethics Leader or use the Medium to High Risk Ethical Approval or NHS or Medical Approval Routes.

Registry Research Unit Page 6 of 9 01/04/2011

Risk to Researcher

9. Will this project put you or others at risk of physical harm, injury or death?	Yes	No ✓
10. Will project put you or others at risk of abduction, physical, mental or sexual abuse?	Yes	No ✓
11. Will this project involve participating in acts that may cause psychological or emotional distress to you or to others?	Yes	No ✓
12. Will this project involve observing acts which may cause psychological or emotional distress to you or to others?	Yes	No ✓
13. Will this project involve reading about, listening to or viewing materials that may cause psychological or emotional distress to you or to others?	Yes	No ✓
14. Will this project involve you disclosing personal data to the participants other than your name and the University as your contact and e-mail address?	Yes	No ✓
15. Will this project involve you in unsupervised private discussion with people who are not already known to you?	Yes	No ✓
16. Will this project potentially place you in the situation where you may receive unwelcome media attention?	Yes	No ✓
17. Could the topic or results of this project be seen as illegal or attract the attention of the security services or other agencies?	Yes	No ✓
18. Could the topic or results of this project be viewed as controversial by anyone?	Yes	No ✓

If you answered **Yes** to **any** of these questions, this is **not** a low risk project. Please:

- If you are a student, discuss your project with your Supervisor.
- If you are a member of staff, discuss your project with your Faculty Research Ethics Leader or use the Medium to High Risk Ethical Approval route.

Informed Consent of the Participant

19. Are any of the participants under the age of 18?	Yes	No ✓
20. Are any of the participants unable mentally or physically to give consent?	Yes	No ✓
21. Do you intend to observe the activities of individuals or groups without their knowledge and/or informed consent from each participant (or from his or her parent or guardian)?	Yes	No ✓

If you answered **Yes** to **any** of these questions, this may **not** be a low risk project. Please:

- If you are a student, discuss your project with your Supervisor.
- If you are a member of staff, discuss your project with your Faculty Research Ethics Leader or use the Medium to High Risk Ethical Approval route.

Participant Confidentiality and Data Protection

22. Will the project involve collecting data and information from human participants who will be identifiable in the final report?	Yes	No ✓
23. Will information not already in the public domain about specific individuals or institutions be identifiable through data published or otherwise made available?	Yes	No ✓
24. Do you intend to record, photograph or film individuals or groups without their knowledge or informed consent?	Yes	No ✓
25. Do you intend to use the confidential information, knowledge or trade secrets gathered for any purpose other than this research project?	Yes	No ✓

If you answered **Yes** to **any** of these questions, this may **not** be a low risk project:

- If you are a student, discuss your project with your Supervisor.
- If you are a member of staff, discuss your project with your Faculty Research Ethics Leader or use the Medium to High Risk Ethical Approval or NHS or Medical Approval routes.

Gatekeeper Risk

26. Will this project involve collecting data outside University buildings?	Yes	No ✓
27. Do you intend to collect data in shopping centres or other public places?	Yes	No ✓
28. Do you intend to gather data within nurseries, schools or colleges?	Yes	No ✓
29. Do you intend to gather data within National Health Service premises?	Yes	No ✓

If you answered **Yes** to **any** of these questions, this is **not** a low risk project. Please:

- If you are a student, discuss your project with your Supervisor.
- If you are a member of staff, discuss your project with your Faculty Research Ethics Leader or use the Medium to High Risk Ethical Approval or NHS or Medical Approval routes.

Other Ethical Issues

30. Is there any other risk or issue not covered above that may pose a risk to you or any of the participants?	Yes	No ✓
31. Will any activity associated with this project put you or the participants at an ethical, moral or legal risk?	Yes	No ✓

If you answered **Yes** to these questions, this may **not** be a low risk project. Please:

- If you are a student, discuss your project with your Supervisor.
- If you are a member of staff, discuss your project with your Faculty Research Ethics Leader.

Principal Investigator Certification

If you answered **No** to **all** of the above questions, then you have described a low risk project. Please complete the following declaration to certify your project and keep a copy for your record as you may be asked for this at any time.

Agreed restrictions to project to allow Principal Investigator Certification

Please identify any restrictions to the project, agreed with your Supervisor or Faculty Research Ethics Leader to allow you to sign the Principal Investigator Certification declaration.

Participant Information Leaflet attached.
Informed Consent Forms attached.

Principal Investigator's Declaration

Please ensure that you:

- Tick all the boxes below and sign this checklist.
- Students must get their Supervisor to countersign this declaration.

I believe that this project **does not require research ethics approval**. I have completed the checklist and kept a copy for my own records. I realise I may be asked to provide a copy of this checklist at any time.	
I confirm that I have answered all relevant questions in this checklist honestly.	
I confirm that I will carry out the project in the ways described in this checklist. I will immediately suspend research and request a new ethical approval if the project subsequently changes the information I have given in this checklist.	

Signatures

If you submit this checklist and any attachments by e-mail, you should type your name in the signature space. An email attachment sent from your University inbox will be assumed to have been signed electronically.

Principal Investigator

Signed M. Sivaprasanna (Principal Investigator or Student)

Date 01.04.2011

Students storing this checklist electronically must append to it an email from your Supervisor confirming that they are prepared to make the declaration above and to countersign this checklist. This-email will be taken as an electronic countersignature.

Student's Supervisor

Countersigned (Supervisor)

Date 01.04.2011

I have read this checklist and confirm that it covers all the ethical issues raised by this project fully and frankly. I also confirm that these issues have been discussed with the student and will continue to be reviewed in the course of supervision.

REFERENCES

Abramovich, G. N. (1963) *The Theory of Turbulent Jets*. Massachusetts: The MIT Press

Agüí, J. C., and Hesselink, L. (1988) 'Flow Visualization and Numerical Analysis of a Coflowing Jet: A Three-Dimensional Approach'. *Journal of Fluid Mechanics* 191, 19-45

Anderson, R. E. (1983) 'Aircraft Engine Inlet Pressure Distortion Testing in a Ground Test Facility'. AIAA Paper No. 83-1233

Andreopoulos, J. (1985) 'On the Structure of Jets in a Crossflow'. *Journal of Fluid Mechanics* 157, 163-197

Antonia, R. A., and Bilger, R. W. (1973) 'An Experimental Investigation of an Axisymmetric Jet in a Co-Flowing Air Stream'. *Journal of Fluid Mechanics* 61 (4), 805-822

Arendt, J., Babcock, H. A., and Schuster, J. (1956) 'Penetration of a Jet into a Counterflow'. *Journal of Hydraulics Division* 82, 1038-8-11

Asendrych, D. (2007) 'Active Flow Control by Countercurrent Jets'. *Journal of Theoretical and Applied Mechanics* 45, 463-477

Asendrych, D., and Favre-Marinet, M. (2004) 'Diffusion of Jets with Annular Counterflow and Small Diameter Ratio'. *AIAA Journal* 42, 2385-2387

Barlow, J. B., Rae, Jr. W. H., and Pope, A. (2010) *Low-Speed Wind Tunnel Testing*. 3rd edn. New Delhi: Wiley India

Batchelor, G. K. (1993) *The Theory of Homogeneous Turbulence*. Reprinted edn. Cambridge: Cambridge University Press

Baumbick, R. J. (1970) 'Device for Producing Dynamic Distortion Patterns at Inlets of Air-Breathing Engines'. NASA TM X-2026. Washington: National Aeronautics and Space Administration

Beale, D. K., Cramer, K. B., and King, P. S. (2002) 'Development of Improved Methods for Simulating Aircraft Inlet Distortion in Turbine Engine Ground Tests'. AIAA Paper 2002-3045

Beltaos, S., and Rajaratnam, N. (1973) 'Circular Turbulent Jet in an Opposing Infinite Stream'. in *Proceedings of the 1st Canadian Hydrotechnical Conference*, Edmonton, 220-237

Bernero, S. (2000) *A Turbulent Jet in Counterflow*. PhD thesis. Berlin: Technical University of Berlin

Biesiadny, T. J., Braithwaite, W. M., Soeder, R. H., and Abdelwahab, M. (1987) 'Summary of Investigations of Engine Response to Distorted Inlet Conditions'. in *Engine Response to Distorted Inflow Conditions*. Conference Proceedings CP 400. Advisory Group for Aerospace Research and Development Neuilly sur Seine: North Atlantic Treaty Organization

Bird, R. B., Stewart, W. E., and Lightfoot, E. N. (2002) *Transport Phenomena*. 2nd edn. New York: John Wiley & Sons

Biswas, S., Kumar, J., Ganeshachar, M. D., Babu, S. N. N., and Ramachandra, S. (2013) 'Fatigue Failure of a Distortion Screen During Testing'. *Procedia Engineering* 55, 487-492

Bloch, G. S. (1992) 'An Assessment of Inlet Total-Pressure Distortion Requirements for the Compressor Research Facility'. Final Report WL-TR-92-2066. Ohio: Wright Laboratory, Wright-Patterson Air Force Base

Boguslawski, A., Asendrych, D., Drobniak, S., and Kubacki, S. (2002) 'CFD Simulations of Concentric Jets with External Counterflow'. *QNET Network Newsletter* 1, 27-30

Bowditch, D. N., and Coltrin, R. E. (1983) 'A Survey of Inlet/Engine Distortion Compatibility'. AIAA Paper No. 83-1166

Braithwaite, W. M., Dicus, J. H., and Moss, J. E. Jr. (1970) 'Evaluation with a Turbofan Engine of Air Jets as a Steady-State Inlet Flow Distortion Device'. NASA TM X-1955. Washington: National Aeronautics and Space Administration

Brinkworth, B. J. (1999) 'Discussion to "Lam, K. M., and Chan, H. C. (1997) 'Round Jet in Ambient Counterflowing Stream'. *Journal of Hydraulic Engineering* 123 (10), 895-903". *Journal of Hydraulic Engineering* 125, 430-431

British Standards Institution (2003) *Measurement of Fluid Flows by Means of Pressure Differential Devices Inserted in Circular-Cross Section Conduits Running Full. Part 2: Orifice Plates*. BS EN ISO 5167-2. London: British Standards Institution

Celik, I. B., Ghia, U., Roache, P. J., Freitas, C. J., Coleman, H., and Raad, P. E. (2008) 'Procedure for Estimation and Reporting of Uncertainty due to Discretization in CFD Applications'. *Journal of Fluids Engineering* 130, 078001

Chan, C. H. C., and Lam, H. K. (1998) 'Centerline Velocity Decay of a Circular Jet in a Counterflowing Stream'. *Physics of Fluids* 10 (3), 637-644

Chan, C. H. C., Lam, H. K., and Bernero, S. (1999) 'On the Penetration of a Round Jet into a Counterflow at Different Velocity Ratios". in *Environmental Hydraulics*. ed. by Lee, J. H. W., Jayawardena, A. W., and Wang, Z. Y. Rotterdam: Balkema, 229-234

Chan, H. C. (1999) *Investigation of a Round Jet into a Counterflow*. PhD thesis. Hong Kong: University of Hong Kong

Chen, F., Li, W., Wang, Z., and Cong. M. (1985) 'An Experimental Investigation of Response of a Turbojet Engine to Inlet Distortion'. Beijing International Gas Turbine Symposium and Exposition, Beijing

Comte-Bellot, G., and Corrsin, S. (1966) 'The Use of a Contraction to Improve the Isotropy of Grid-Generated Turbulence'. *Journal of Fluid Mechanics* 25 (4), 657-682

Cousins, W. T. (2004) 'History, Philosophy, Physics, and Future Directions of Aircraft Propulsion System / Inlet Integration'. ASME GT2004-54210

Cousins, W. T., Dalton, K. K., Andersen, T. T., and Bobula, G. A. (1994) 'Pressure and Temperature Distortion Testing of a Two-Stage Centrifugal Compressor'. *Journal of Engineering for Gas Turbines and Power* 116 (3), 567-573

Cousins, W. T., Georges, M. J., and Rezaei, H. (2003) 'Inlet Distortion Testing and Analysis of a High-Bypass Ratio Turbofan Engine'. *Proceedings of the 16th International Symposium on Air Breathing Engines*.

Davis, M. W., Jr., Hale, A. A., and Klepper, J. (2010) '40 Years of AEDC Development, Evolution and Application of Numerical Simulations for Integrated Test and Evaluation of Turbine Engine Turbomachinery Operability Issues'. AEDC-TR-09-T-19. Tennessee: Arnold Engineering Development Center

Donaldson, C. D., and Snedeker, R. S. (1971) 'A Study of Free Jet Impingement. Part 1. Mean Properties of Free and Impinging Jets'. *Journal of Fluid Mechanics* 45 (2), 281-319.

Duwig, C., and Revstedt, J. (2009) 'Large Scale Dynamics of a Jet in a Counter Flow'. in *Advances in Turbulence XII*. ed. by Eckhardt, B. Berlin: Springer

Eckert, W. T., Mort, K. W., and Jope, J. (1976) 'Aerodynamic Design Guidelines and Computer Program for Estimation of Subsonic Wind Tunnel Performance'. NASA TN D 8243. Washington: National Aeronautics and Space Administration

Elghobashi, S. E., Samuelsen, G. S., Wuerer, J. E., and LaRue, J. C. (1981) 'Prediction and Measurement of Mass, Heat, and Momentum Transport in a Nonreacting Turbulent Flow of a Jet in an Opposing Stream'. *Journal of Fluids Engineering* 103 (1), 127-132

Farell, C., and Youssef, S. (1996) 'Experiments on Turbulence Management Using Screens and Honeycombs'. *Journal of Fluids Engineering* 118 (1), 26-32

Flitcroft, J. E., Dunham, J., and Abbott, W. A. (1987) 'Transmission of Inlet Distortion through a Fan'. Report No. P964500. Farnborough: Royal Aircraft Establishment

Fric, T. F., and Roshko, A. (1994) 'Vortical Structure in the Wake of a Transverse Jet'. *Journal of Fluid Mechanics* 279, 1-47

Groth, J., and Johansson, A. V. (1988) 'Turbulence Reduction by Screens'. *Journal of Fluid Mechanics* 197, 139-155

Hah, C., Rabe, D. C., Sullivan. T. J., and Wadia, A. R. (1998) 'Effects of Inlet Distortion on the Flow Field in a Transonic Compressor Rotor'. *Journal of Turbomachinery* 120 (2), 233-246

Hamed, A., and Numbers, K. (1997) 'Inlet Distortion Considerations for High Cycle Fatigue in Gas Turbine Engine'. AIAA Paper No. 97-3364

Haven, B. A., and Kurosaka, M. (1997) 'Kidney and Anti-Kidney Vortices in Crossflow Jets'. *Journal of Fluid Mechanics* 351, 27-64

Hercock, R. G., and Williams, D. D. (1974) 'Aerodynamic Response'. *Distortion Induced Engine Stability*, in Lecture Series LS 72. Advisory Group for Aerospace Research & Development. Neuilly sur Seine: North Atlantic Treaty Organization

Hinze, J. O. (1975) *Turbulence*. 2nd edn. New York: McGraw-Hill

Holman, J. P. (2001) *Experimental Methods for Engineers*. 7th edn. New Delhi: Tata McGraw-Hill

Hopkins, D. F., and Robertson, J. M. (1967) 'Two-Dimensional Incompressible Fluid Jet Penetration'. *Journal of Fluid Mechanics* 29 (2), 273-287

Huang, J., Wu, H., and. Du, W. H. (2009) 'Experimental Investigation and Analysis of an Axial Compressor Stage with 45° Circumferential Inlet Flow Pressure Distortion'. *New Trends in Fluid Mechanics Research* 7, 503

Hubble, J. D., and Smith, R. E. (1979) 'Evaluation of an Airjet Distortion Generator Used to Produce Steady-State, Total-Pressure Distortion at the Inlet of a General Electric

F101-GE-100 Turbofan Engine'. AEDC-TR-78-73. Tennessee: Arnold Engineering Development Center

Hussain, A. K. M. F., and Ramjee, V. (1976) 'Effects of the Axisymmetric Contraction Shape on Incompressible Turbulent Flow'. *Journal of Fluids Engineering* 98 (1), 58-68

Hussein, H. J., Capp, S. P., and George, W. K. (1994) 'Velocity Measurements in a High-Reynolds Number, Momentum-Conserving, Axisymmetric, Turbulent Jet'. *Journal of Fluid Mechanics* 258, 31-75

Kelso, R. M., Lim, T. T., and Perry, A. E. (1996) 'An Experimental Study of Round Jets in Cross-Flow'. *Journal of Fluid Mechanics* 306, 111-144

King, R. W., Schuerman, J. A., and Muller, R. G. (1976) 'Analysis of Distortion Data from TF30-P-3 Mixed Compression Inlet Test'. NASA CR-2686. Washington: National Aeronautics and Space Administration

König, O., and Fiedler, H. E., (1991) 'The Structure of Round Turbulent Jets in Counterflow: A Flow Visualization Study'. in *Advances in Turbulence III*. ed. by Johansson, A. V., and Alfredsson, P. H. Berlin: Springer, 61-66

Lam, K. M., and Chan, H. C. (1997) 'Round Jet in Ambient Counterflowing Stream'. *Journal of Hydraulic Engineering* 123 (10), 895-903

Launder, B. E. (1989) 'Second-Moment Closure: Present ... and Future?'. *International Journal of Heat and Fluid Flow* 10, 282-300

Launder, B. E., and Spalding, D. B. (1972) *Lectures in Mathematical Models of Turbulence*. London: Academic Press

Launder, B. E., and Spalding, D. B. (1974) 'The Numerical Computation of Turbulent Flows'. *Computer Methods in Applied Mechanical Engineering* 3, 269-289

Launder, B. E., Reece, G. J., and Rodi, W. (1975) 'Progress in the Development of a Reynolds-Stress Turbulence Closure'. *Journal of Fluid Mechanics* 68, 537-566

Laws, E. M., and Livesey, J. L. (1978) 'Flow Through Screens'. *Annual Review of Fluid Mechanics* 10, 247-266

Li, Z. H., Huai, W. X., and Qian Z. D. (2013) 'Large Eddy Simulation of a Round Jet into a Counterflow'. *Science China Technological Sciences* 56 (2), 484-491

Liepmann, H. W., and Roskho, A. (1957) *Elements of Gas Dynamics*. New York: John Wiley & Sons

Loehrke, R. I., and Nagib, H. M. (1972) 'Experiments on Management of Free-Stream Turbulence'. Report No. 598. Advisory Group for Aerospace Research & Development. Neuilly sur Seine: North Atlantic Treaty Organization

Loehrke, R. I., and Nagib, H. M. (1976) 'Control of Free-Stream Turbulence by Means of Honeycombs: A Balance Between Suppression and Generation'. *Journal of Fluids Engineering* 98 (3), 342-351

Longley, J. P., and Greitzer, E. M. (1992) 'Inlet Distortion Effects in Aircraft Propulsion System Integration'. in *Steady and Transient Performance Prediction of Gas Turbine Engines*. Lecture Series LS 183. Advisory Group for Aerospace Research and Development Neuilly sur Seine: North Atlantic Treaty Organization

Longley, J. P., Shin, H. –W., Plumley, R. E., Silkowski, P. D., Day, I. J., Greitzer, E. M., Tan, C. S., and Wisler, D. C., (1996) 'Effects of Rotating Inlet Distortion on Multistage Compressor Stability'. *Journal of Turbomachinery* 118 (2), 181-188

Majumdar, S., and Bhaduri, D. (1981) 'On Recirculating Flow in an Opposed Jet Flame Holder'. *Applied Mathematical Modelling* 5 (3), 179-184

Manickam, M. D., and Murugesan, K. (1978) 'Calibration Characteristics of Various Types of Two Dimensional Yaw Probes, used in Cascade Tunnel'. Technical Memorandum TM-PR-304.2-78. Bangalore: National Aeronautical Laboratory

Manwaring, S. R., and Fleeter, S. (1990) 'Inlet Distortion Generated Periodic Aerodynamic Rotor Response' *Journal of Turbomachinery* 112 (2) 298-307

Manwaring, S. R., Rabe, D. C., Lorence, C. B., and Wadia, A. R. (1997) 'Inlet Distortion Generated Forced Response of a Low-Aspect-Ratio Transonic Fan'. *Journal of Turbomachinery* 119 (4), 665-676

Margason, R. J. (1969) 'The Path of a Jet Directed at Large Angles to a Subsonic Stream'. NASA TN D-4919. Washington: National Aeronautics and Space Administration

McIlveen, M. W. (1979) 'Further Test Results with the Airjet Distortion Generator: A New Tool for Aircraft Turbine Engine Testing'. AIAA Paper No. 79-1185

Mehta, R. D., and Bradshaw, P. (1979) 'Design Rules for Small Low Speed Wind Tunnels'. *The Aeronautical Journal* 83 (827), 443-449

Meyer, C. L., McAulay, J. E., and Biesiadny, T. J. (1970) 'Technique for Inducing Controlled Steady-State and Dynamic Inlet Pressure Disturbances for Jet Engine Tests'. NASA TM X-1946. Washington: National Aeronautics and Space Administration

Morel, T. (1975) 'Comprehensive Design of Axisymmetric Wind Tunnel Contractions'. *Journal of Fluids Engineering* 97 (2), 225-233

Morgan, W. D., Brinkworth, B. J., and Evans, G. V. (1976) 'Upstream Penetration of an Enclosed Counterflowing Jet'. *Industrial & Engineering Chemistry Fundamentals* 15 (2), 125-127

Naseri, A., Boroomand, M., and Tousi, A. M. (2012) 'The Effect of Inlet Flow Distortion on Performance of a Micro-Jet Engine: Part 1 – Development of an Inlet Simulator'. in ASME 2012 International Mechanical Engineering Congress and Exposition. Volume 1. Advances in Aerospace Technology

Nickels, T. B., and Perry, A. E. (1996) 'An Experimental and Theoretical Study of the Turbulent Coflowing Jet'. *Journal of Fluid Mechanics* 309, 157-182

Nie, C., Zhang, J., Tong, Z., and Zhang, H. (2006) 'The Response of a Low Speed Compressor on Rotating Inlet Distortion'. *Journal of Thermal Science* 15 (4), 314-318

Or, C. M., Lam, K. M., and Liu, P. (2011) 'Potential Core Lengths of Round Jets in Stagnant and Moving Environments'. *Journal of Hydro-environment Research* 5 (2), 81-91

Oron, A., and Abuaf, N. (1977) 'Jet Expanding into a Uniform Counterflow'. *Israel Journal of Technology* 15, 239-245

Overall, B. W. (1972) 'A Procedure for the Design of Complex Distortion Screen Patterns for Producing Specified Steady-State Total Pressure Profiles at the Inlet of Turbine Engines'. AEDC-TR-72-10. Tennessee: Arnold Engineering Development Center

Overall, B. W., and Harper, R. E. (1977) 'The Airjet Distortion Generator System: A New Tool for Aircraft Turbine Engine Testing'. AIAA Paper No. 77-993

Ower, E., and Pankhurst, R. C. (1966) *The Measurement of Air Flow*. 4th edn. Oxford: Pergamon Press

Pai, S. I. (1954) *Fluid Dynamics of Jets*. New York: van Nostrand

Panchapakesan, N. R., and Lumley, J. L. (1993) 'Turbulence Measurements in Axisymmetric Jets of Air and Helium. Part 1. Air Jet'. *Journal of Fluid Mechanics* 246, 197-223

Patankar, S. V. (1980) *Numerical Heat Transfer and Fluid Flow*. New York: Hemisphere

Peck, R. E. (1981) 'Aerodynamics of a Round Jet in a Counterflowing Wind'. *Journal of Aircraft* 18 (1), 61-62

Perry, A. E., and Tan, D. K. M. (1984) 'Simple Three-Dimensional Vortex Motions in Coflowing Jets and Wakes'. *Journal of Fluid Mechanics* 141, 197-231

Pope, S. B. (2000) *Turbulent Flows*. New Delhi: Cambridge University Press

Povolny, J. H. (1970) 'Stall and Distortion Investigation of a YTF30-P-1 Turbofan Engine'. in *Proceedings of the Air Force Airframe-Propulsion Compatibility Symposium*. AFAPL-TR-69-103. Ohio: Wright-Patterson Air Force Base

Prandtl, L. (1933) 'Attaining a Steady Air Stream in Wind Tunnels'. NACA TM 726. trans. from 'Herrstellung Einwand freier luftströme im Windkanäle'. *Handbuch der Experimentalphysik* IV (2). Washington: National Advisory Committee for Aeronautics

Rabe, D., Bolcs, A., Russler, P. (1995) 'Influence on Inlet Distortion on Transonic Compressor Blade Loading'. AIAA Paper No. 95-2461

Rajaratnam, N. (1976) *Turbulent Jets*. Amsterdam: Elsevier

Ramamurthy, S., Murugesan, K., Sankaranarayanan, S., and Ramachar, D. (1998) 'Design and Development of Distortion Screens for a Gas Turbine Engine Intake'. in *Air Breathing Engines and Aerospace Propulsion*. Bangalore: Interline Publishing

Ramjee, V., and Hussain, A. K. M. F. (1976) 'Influence of the Axisymmetric Contraction Ratio on Free-Stream Turbulence'. *Journal of Fluids Engineering* 98 (3), 506-515

Rathakrishnan, E. (2008) *Gas Dynamics*. 2nd edn. New Delhi: Prentice Hall India

Reid, C. (1969) 'The Response of Axial-Flow Compressors to Intake-Flow Distortion'. ASME Paper 69-GT-29

Ricou, F. P., and Spalding, D. B., (1961) 'Measurements of Entrainment by Axisymmetrical Turbulent Jets'. *Journal of Fluid Mechanics*, 11, 21-32

Rivero, A., Ferré, J. A., and Giralt, F. (2001) 'Organized Motions in a Jet in Crossflow'. *Journal of Fluid Mechanics* 444, 117-149

Sahgravani, S. F., and Ramamurthy, A. S. (2010) 'Penetration Length of Confined Counter Flowing Free Jets'. *Journal of Hydraulic Engineering* 136, 179-182

Salunkhe, P. B., and Pradeep, A. M. (2010a) 'Stall Inception and its Control in an Axial Flow Fan under Dynamic Inflow Distortion'. *Proceedings of the Institution of Mechanical Engineers, Part A: Journal of Power and Energy* 224 (3), 383-398

Salunkhe, P. B., and Pradeep, A. M. (2010b) 'Stall Inception Mechanism in an Axial Flow Fan under Clean and Distorted Inflows'. *Journal of Fluids Engineering* 132 (12), 121102

Salunkhe, P. B., Reddy, V., and Pradeep, A. M. (2009) 'Tip Injection as a Means for Rotating Stall Control in an Axial Flow Fan'. *Proceedings of the Institution of Mechanical Engineers, Part A: Journal of Power and Energy* 223 (1), 55-70

Sankaranarayanan, S. Murugesan, K., and Rao, K. V. L., (1994) 'Simulation of Distorted Flow Through an Engine Intake Using Mesh Combinations'. in *Air Breathing Engines and Aerospace Propulsion*. Bangalore: Interline Publishing

Saravanamuttoo, H. I. H., Rogers, G. F. C., and Cohen, H. (2001) *Gas Turbine Theory*. 5th edn. New Delhi: Pearson

Scheiman, J., and Brooks, J. D. (1981) 'Comparison of Experimental and Theoretical Turbulence Reduction from Screens, Honeycomb and Honeycomb-Screen Combinations'. *Journal of Aircraft* 18 (8), 638-643

Schlichting, H., (1979) *Boundary-Layer Theory*. 7th edn. New York: McGraw-Hill

Schneider, W. (1985) 'Decay of Momentum Flux in Submerged Jets'. *Journal of Fluid Mechanics* 154, 91-110

Schubauer, G. B., Spangenberg, W. G., and Klenaboff, P. S. (1950) 'Aerodynamic Characteristics of Damping Screens'. NACA TN 2001. Washington: National Advisory Committee for Aeronautics

Seddon, J., and Goldsmith, E. J. (1999) *Intake Aerodynamics*. 2nd edn. Oxford: Blackwell

Sekundov, A. N. (1969) 'The Propagation of a Turbulent Jet in an Opposing Stream'. in *Turbulent Jets of Air, Plasma and Real Gas.* ed. by Abramovich, G. N. New York: Consultants Bureau, 99-109

Serovy, G. K. (1985) 'Axial Flow Compressor Aerodynamics'. in *Aerothermodynamics of Aircraft Engine Components*. ed. by Oates, G. C. New York: American Institute of Aeronautics and Astronautics

Shapiro, A. H. (1953) *The Dynamics and Thermodynamics of Compressible Fluid Flow*. Vol. I. New York: The Ronald Press Company

Sivaapragasam, M. (2007) *Numerical and Experimental Investigation on Flow Distortion in an Aero Engine Air Intake*. MSc [Engg.] thesis. Bangalore: M. S. Ramaiah School of Advanced Studies, in collaboration with Coventry University, Coventry

Sivapragasam, M., and Ramamurthy, S. (2009) 'Inlet Flow Distortion Effects in Aircraft Gas Turbine Engine Compression Systems'. Technical Memorandum TM PR 0901. Bangalore: National Aerospace Laboratories

Society of Automotive Engineers (1999) *Inlet Total-Pressure-Distortion Considerations for Gas-Turbine Engines*. Warrendale: SAE International

Society of Automotive Engineers (2002) *Gas Turbine Engine Inlet Flow Distortion Guidelines*. Warrendale: SAE International

Strykowski, P. J., and Niccum, D. L. (1991) 'The Stability of Countercurrent Mixing Layers in Circular Jets'. *Journal of Fluid Mechanics* 227, 309-343

Strykowski, P. J., and Wilcoxon, R. K. (1993) 'Mixing Enhancement Due to Global Oscillations in Jets with Annular Counterflow'. *AIAA Journal* 31, 564-570

Strykowski, P. J., Krothapalli, A. and Jendoubi, S. (1996) 'The Effect of Counterflow on the Development of Compressible Shear Layers'. *Journal of Fluid Mechanics* 308, 63-96

Tan-atichat, J., Nagib, H. M., and Loehrke, R. I. (1982) 'Interaction of Free-Stream Turbulence with Screens and Grids: A Balance between Turbulence Scales'. *Journal of Fluid Mechanics* 114, 501-528

Taylor, G. I., and Batchelor, G. K. (1949) 'The Effect of Wire Gauze on Small Disturbances in a Uniform Stream'. *Quarterly Journal of Mechanics and Applied Mathematics* 2 (1), 1-29

Tennekes, H., and Lumley, J. L. (1972) *A First Course in Turbulence*. Massachusetts: The MIT Press

Torres, L. A., Mahmoudi, M., Fleck, B. A., Wilson, D. J., and Nobes, D. (2012) 'Mean Concentration Field of a Jet in a Uniform Counter-Flow'. *Journal of Fluids Engineering* 134, 014502

Townsend, A. A. (1980) *The Structure of Turbulent Shear Flow*. 2nd edn. Cambridge: Cambridge University Press

Tsunoda, H., and Saruta, M. (2003) 'Planar Laser-Induced Fluorescence Study on the Diffusion Field of a Round Jet in a Uniform Counter-Flow'. *Journal of Turbulence* 4, N13.

Tsunoda, H., and Takei, J. (2006) 'Statistical Characteristics of the Cross-Sectional Concentration Field in a Round Counter Jet'. *Journal of Fluid Science and Technology* 1 (2), 105-113

van Schalkwyk, C. M., Paduano, J., Greitzer, E. M., and Epstein, A. H. (1998) 'Active Stabilization of Axial Compressors with Circumferential Inlet Distortion'. *Journal of Turbomachinery* 120 (3), 431-439

Versteeg, H. K., and Malalasekara, W. (2007) *An Introduction to Computational Fluid Dynamics: The Finite Volume Method*. 2nd edn. New Delhi: Pearson

Villermaux, E., and Rehab, H. (2000) 'Mixing in Coaxial Jets'. *Journal of Fluid Mechanics* 425, 161-185

Wadia, A. R. (2010) 'Forward Swept Rotor Studies in Multistage Fans including the Effect on Performance with Inlet Distortion'. in *Proceedings of the 27th International Congress of the Aeronautical Sciences*. Nice: France

Wallace, R. M., King, P. S., and Kenyon, J. (2010) 'Assessing Fan and Compressor Blade HCF Sensitivity to Non-Uniform Inlet Flows'. ASME Paper No. GT2004-54264

Walsh, P. P., and Fletcher, P. (2004) *Gas Turbine Performance*. 2nd edn. Oxford: Blackwell

White, F. M. (2008) Fluid Mechanics. 6th edn. New Delhi: Tata McGraw-Hill

Williams, D. D. (1987) 'Review of Current Knowledge on Engine Response to Distorted Inflow Conditions'. in *Engine Response to Distorted Inflow Conditions*. Conference Proceedings CP 400. Advisory Group for Aerospace Research and Development Neuilly sur Seine: North Atlantic Treaty Organization

Williams, D. D., and Surber, L. (1993) 'Intake/Engine Compatibility'. in *Practical Intake Aerodynamic Design*. ed. by Seddon, J. and E. L. Goldsmith. Oxford: Blackwell Scientific Publishing

Yoda, M., and Fiedler, H. E. (1996) 'The Round Jet in a Uniform Counterflow: Flow Visualization and Mean Concentration Measurements'. *Experiments in Fluids* 21 (6), 427-436

Yüceil, K. B., and Ötügen, M. V. (2002) 'Scaling Parameters for Underexpanded Supersonic Jets'. *Physics of Fluids* 14 (12), 4206-4215

Zaman, K. B. M. Q. (1999) 'Spreading Characteristics of Compressible Jets from Nozzles of Various Geometries'. *Journal of Fluid Mechanics* 383, 197-228

Zhang, S., and Gao, S. (1983) 'Experiments and Mathematical Simulation of Plate Distortion Simulators'. in *Proceedings of the Sixth International Symposium on Air Breathing Engines*. held 6-10 June 1983 at Paris